INVESTIGATION OF THE ROLE OF BREAK-UP PROCESSES IN HEAVY ION REACTIONS BELOW 7 MeV/nucleon

ABSTRACT

of

the thesis submitted for the award of

Doctor of Philosophy

in

PHYSICS

(Experimental Nuclear Physics)

2010

by

DEVENDRA PAL SINGH

Under the supervision of

PROF. B. P. SINGH

DEPARTMENT OF PHYSICS
ALIGARH MUSLIM UNIVERSITY,
ALIGARH (U. P.)-202 002, INDIA

ABSTRACT

Nuclear Physics has been an important subject due to its impact on the related fields of investigation. Becquerel's discovery of penetrating radiation led to contemplate the nature of the nucleus [1]. In 1897, British physicist J. J. Thomson conjectured that electrons are embedded in a spherical matrix of positive charge [2]. The experiments [3] of Rutherford and his co-workers indicated that all the positive charge and almost total mass of the atom is concentrated in a very small and tiny central part of the atom called the nucleus. The experiments of Rutherford, Cock-Croft & Walton, Curie & Juliet and Fermi on the nuclear transmutation developed new ideas to solve basic problems regarding the nuclear structure, nuclear properties, nuclear forces, energy states of nuclei, transition probabilities etc., and considerably motivated the nuclear reaction studies [4, 5]. The study of nuclear reactions has been used as a tool to understand the properties of nuclei and to investigate the nature of nuclear interactions, decay characteristics of excited nuclei etc.

In nuclear reactions the identity of nuclides may be changed by altering the structure of atomic nucleus. In principle, the incident particle must approach the range of nuclear forces of the target nucleus for a nuclear reaction to occur. Once the nucleons of the incident nucleus are within the range of nucleons of the target nucleus, the strongly attractive nuclear forces become effective, merging the incident particle with the target nucleus. In a nuclear reaction, all the properties of the interacting partners of the system are known, before and after the reaction has taken place. However, what exactly happens during the nuclear reaction is still not well understood. It is mainly because the time scales involved are very short (i.e., $\approx 10^{-22}$ to 10^{-16} sec.) in the occurrence of a reaction. Since, the exact process of a nuclear reaction is not known, therefore, simplified theories and models are developed for explaining the mechanism of the reaction. In order to explain the nuclear reaction mechanism, Bohr [6] proposed the compound nucleus (CN) reaction model. According to this model, a nuclear reaction takes place in two distinct stages. The first stage is the formation of the compound nucleus and the second stage is its decay. Both these steps are assumed to be independent of each other. In the first stage, when a projectile ($E > B_{fus}$) interacts with the target nucleus, it is captured by

the target nucleus, the total kinetic energy and angular momentum of the projectile are shared statistically among all the nucleons of the composite system leading to the establishment of thermodynamic equilibrium. Once the equilibrium is established, the CN forgets its history of formation and may then decay. However, in the second stage, after a long time ($\approx 10^{-16}$ sec.), somehow sufficient amount of energy, more than the separation energy, may get accumulated on a nucleon or on a group of nucleons which may be emitted from the CN, leaving behind a residual nucleus. As a matter of fact, the lapse time between the formation of composite system and its decay is too large, and hence, no trace is left to decide its mode of formation [6]. Another approach to describe the nuclear reaction is the direct reaction mechanism. The time scales involved in the direct reactions is $\approx 10^{-22}$ sec. In direct reactions, only a few degrees of freedom are excited. Such reactions are likely to occur at considerably higher energies. In the CN reaction mechanism it is assumed that the emission of light nuclear particle(s)/cluster(s) takes place, after the establishment of thermodynamic equilibrium and the state of compound nucleus is achieved by a series of two body residual interactions between the nucleons of the composite system. However, both the intuition and the results of a large number of experiments indicate that the emission of nuclear particle(s) may also take place even before the establishment of thermodynamic equilibrium of the composite system [7] and the process is referred to as PE-emission and the mechanism is referred to as pre-compound reaction mechanism [8]. With the availability of modern accelerators, it has now become possible to accelerate heavy-ions (HI) at energies from a few MeV/nucleon to many GeV/nucleon, and has opened an entirely new field of research which is not possible using the light ion beams.

Heavy ion (HI) collisions are said to occur when two nuclei interact with each other within the range of nuclear forces. With the availability of particle accelerators it has become possible to accelerate nuclei to energies where they can overcome the Coulomb repulsion and the nuclear reaction occurs. During the last few decades or so major research work in experimental nuclear physics involved the use of protons, deuterons and alpha particles. These studies explained several important aspects of the nuclei and nuclear reactions. In general, when two heavy ions are brought in contact, a variety of phenomena may take place. By appropriately selecting the target and the projectile nuclei it may be possible to excite

different degrees of freedom. Collisions which bring the two nuclei into rather intimate contact may lead to a combined nuclear system which is excited to a state of relatively high angular momentum. Collisions between HIs have been studied for a range of target-projectile combinations but detailed interpretation of reaction dynamics is still lacking. The experience gathered from these experiments leads to a consistent picture when the reactions are classified into categories, such as grazing collisions, deep inelastic collisions, fusion processes etc.

The study of HI-induced reactions is quite complex due to the involvement of a large number of nucleons. Further, the interacting partners have large Coulomb barrier (B_{fus}). The study of reactions involving HIs tend to differ from the light ion induced reactions in many ways. The de-Broglie wavelength associated with relative motion of the interacting heavy-ions is much shorter than that for light ions. Since, the associated de-Broglie wavelength (λ) of the HIs is very small, therefore, the HI-induced reactions can be described using semi-classical approach. The HIs consist of larger mass in comparison to the light ions and their angular momentum with respect to the centre of mass is very large. An important feature of HI reactions is, (since, a HI is a multi-nucleon system), that a variety of reactions may occur even at energies near and well above the B_{fus}. Therefore, the HI induced reactions provide a possibility of producing and studying the nuclei with high excitation energy and spin. The HI reactions can be described in terms of the distance of closest approach r_{min} [9].

In case of complete fusion (CF) reactions, the incident nucleus completely fuses with the target nucleus. Further, for the fusion to occur the projectile and target nuclei should have mass and the input angular momentum of the entrance channel which should be sustainable by the composite nuclear system. In the CF process, the attractive nuclear potential overcomes the sum of repulsive Coulomb and centrifugal potentials during the projectile-target interaction. This implies large transmission probability, even for higher partial waves ($\ell \leq \ell_{crit}$). As a result, the target nucleus hugs the projectile with all nucleonic degrees of freedom essentially at projectile energies comparable to the B_{fus} or well above it. The CF reactions are said to occur probably at zero/small values of impact parameters and for the input angular momenta range $0 \leq \ell \leq \ell_{crit}$, where the probability of CF is considered to be maximum. Further, in case of CF processes, the total

linear momentum of the projectile is transferred to the composite system and hence the nuclei recoil forward and may traverse a relatively large range in a given stopping medium. In case of CF, the mass of the composite system is nearly equal to the sum of the masses of interacting partners i.e., projectile and the target nucleus. In this case, the kinetic energy of projectile is converted into the excitation energy of the CN and distributed statistically among all accessible internal degrees of freedom until the memory of its mode of formation is lost. At a later stage, the CN thus formed, de-excites by the evaporation of light nuclear particle(s) alongwith characteristic γ-radiations. As a result, a definite amount of excitation energy is reduced by the evaporation of every particle from the equilibrated system. Further, at higher ℓ-values ($\ell > \ell_{crit}$) or at relatively higher values of impact parameters, minimum mass overlap between projectile and target nuclei takes place. This is obvious, when a grazing collision involves only the tails of nuclear matter, where fusion incompleteness may take place, where an in-completely fused composite system is formed as a result of partial linear momentum transfer (LMT) from the projectile to the target nucleus. Such in-complete fusion (ICF) reactions may be described in terms of the projectile energies and the impact parameter. Under the influence of centrifugal force field, the driving angular momenta exceed its critical limit (ℓ_{crit}) for CF. As such, the attractive nuclear potential is not strong enough to capture the entire projectile. Eventually, an in-completely fused composite system (a part of projectile + target nucleus) appears with less charge and mass as compared to that of CF population. It may, however, be pointed out that in case of ICF, most of the time either α-particle or cluster of α-particles (i.e., ^{8}Be or ^{12}C) depending on the incident ion, escape as unfused spectator. Nonetheless, the viscous forces between interacting partners also play an important role in the occurrence of fusion and fusion-like (ICF) processes [10]. It has been experimentally observed that there is no sharp boundary of input angular momentum for CF and ICF to occur. Both the processes are found to contribute significantly below and above their input angular momentum limits. Some of the prominent features of ICF reactions, which have emerged from qualitative observation of recent experimental results are;

- the ICF processes mainly take place for the $\ell > \ell_{crit}$ for CF, meaning thereby the lower ℓ-values don't contribute to ICF [11],

- the fused system is formed with less charge and mass as compared to the total charge and mass of interacting partners [12],

- the contribution of ICF increases with projectile energy,

- the forward recoil velocity of the reaction products, formed via ICF, has been observed to be less than those populated via CF, due to partial linear momentum transfer [13],

- the ICF has been observed to be more prominent for relatively more mass asymmetric systems as compared to the mass symmetric systems [14-16] etc.

For many years, the study of HI induced reactions has been used to understand the reaction dynamics at energies near and above the Coulomb barrier (CB) [12, 17-19]. One of the main reasons has been to understand the ICF processes at energies ≈4-7 MeV/nucleon, where only complete fusion (CF) is expected to be dominant. It is now experimentally established that complete fusion (CF) and in-complete fusion (ICF) are the dominant modes of reaction processes at these energies [20-25]. The evidence of ICF reaction dynamics was observed from experiments [26, 27] on different projectile-target combinations at energies from ≈ 7-10 MeV/nucleon. The results of these experiments suggested that the main process involved in the production of fast-α-particles is the projectile break-up, in the nuclear field of target nucleus, in a hard grazing interaction. It has also been observed [28] that ICF processes compete with CF at the bombarding energies above 7 MeV/nucleon. Further, ICF becomes more and more dominant as the projectile energy increases [29-34]. The different modes of reactions may also be understood on the basis of driving input angular momenta imparted into the system. The CF occurs for the input angular momenta values $\leq \ell_{crit}$, as per the sharp cutoff approximation. However, at relatively higher projectile energies and/or at larger impact parameters, ICF starts competing with the CF. It may, further, be pointed out that the multitude of driving input angular momenta may vary with the projectile energy and/or with the impact parameter. However, there is no sharp boundary for the CF and ICF processes; both the processes have

been observed below and/or above the limiting value of input angular momenta [35].

In order to explain the ICF reaction dynamics a variety of dynamical models/theories, like the Break-up Fusion (BUF) model [36], the SUMRULE model [37], the Promptly Emitted Particles (PEPs) model [38], the EXCITON model [7], the Hot Spot model [39], the Multistep Direct Reaction theory [40], the Overlap model [41-43] etc., have been proposed. In the SUMRULE model of Wilczynski et. al., [37], the in-complete fusion processes are considered to be mainly originated from peripheral interactions and are localized in the angular momentum space above the critical angular momentum (ℓ_{crit}) for the CF. The peripheral nature of ICF reaction dynamics has also been emphasized by Trautmann et. al., [44], and Inamura et. al., [45, 46]. The BUF-model of Udagawa and Tamura [36], employs the Distorted Wave Born Approximation (DWBA) formalism for elastic breakup, where the projectile is assumed to break-up into its constituent α-clusters (e.g., ^{16}O may break-up into $^{12}C + \alpha$ and/or $^{8}Be + {}^{8}Be$) as it approaches the nuclear field of target nucleus. One of the fragments of the projectile is assumed to fuse with target nucleus to form an in-completely fused composite (IFC) system which continues to move in the forward cone with almost projectile velocity. Moreover, the leading-particle model of Natowitz et. al., [47], Fermi-jet model [48, 49], and Moving-Source model [50] have also been proposed and seem to explain some of the experimental data related to ICF at relatively higher projectile energies. Apart from the above mentioned dynamical models, Morgenstern et. al., [16, 51] investigated the mass asymmetry dependence of the ICF contribution. It may, however, be pointed out that these models may predict the magnitude of ICF contribution, to some extent, at energies ≥10 MeV/nucleon, but none of these models/theories is able to successfully explain the ICF data at energies of ≈4–7 MeV/nucleon. Even though, there are several models, a clear picture of the mechanism of ICF is yet to emerge, particularly at energies, below 7 MeV/nucleon, where the systematic studies are lacking. As such, in order to have better understanding of CF and ICF reaction dynamics, it is required to further investigate these processes.

In the present work, in order to explore some of the important issues related to the ICF reaction dynamics at energies near and just above the

Coulomb barrier (i.e., ≈4-7 MeV/nucleon), the information of considerable value has been obtained from the measurements of (i) excitation functions (EFs) [25, 33, 52], as an indication of ICF reaction dynamics wherein the relative contributions of CF and ICF processes have been deduced, (ii) forward recoil range distributions (RRDs) [53], as a proof of fractional linear momentum transfer in which significant fusion incompleteness, associated with fractional degree of linear momentum transfer (LMT) in ICF processes has been observed. In the complementary experiment on the angular distribution information regarding ICF has also been obtained. The experiments for these measurements have been performed at the Inter-University Accelerator Center (IUAC), New Delhi, India. In the first set of experiments, the measurements have been carried out to understand the influence of incomplete fusion on complete fusion at energies near and above the Coulomb barrier. For the excitation function measurements, $^{16}O+^{181}Ta$, $^{16}O+^{103}Rh$ and $^{16}O+^{27}Al$ systems have been studied. A list of reactions for which EFs have been measured is given below;

$^{181}Ta(O, 3n)^{194}Tl^{g}$,	$^{181}Ta(O, 3n)^{194}Tl^{m}$,	$^{181}Ta(O, 4n)^{193}Tl^{g}$,
$^{181}Ta(O,4n)^{193}Tl^{m}$,	$^{181}Ta(O,5n)^{192}Tl^{g}$,	$^{181}Ta(O, 5n)^{192}Tl^{m}$,
$^{181}Ta(O, p3n)^{193}Hg^{g}$,	$^{181}Ta(O, p3n)^{193}Hg^{m}$,	$^{181}Ta(O, p4n)^{192}Hg$,
$^{181}Ta(O, p5n)^{191}Hg^{g}$,	$^{181}Ta(O, p5n)^{191}Hg^{m}$,	$^{181}Ta(O, \alpha n)^{192}Au^{g}$,
$^{181}Ta(O, \alpha 2n)^{191}Au^{g}$,	$^{181}Ta(O, \alpha 3n)^{190}Au^{g}$,	$^{103}Rh(O, p3n)^{115}Te^{g}$,
$^{103}Rh(O, p3n)^{115}Te^{m}$,	$^{103}Rh(O, p4n)^{114}Te$,	$^{103}Rh(O, 2\alpha n)^{110}In^{g}$,
$^{103}Rh(O, 2\alpha n)^{110}In^{m}$,	$^{103}Rh(O, 2\alpha 3n)^{108}In^{g}$,	$^{103}Rh(O,2\alpha 3n)^{108}In^{m}$,
$^{103}Rh(O, 3\alpha 4n)^{103}Ag^{g}$,	$^{27}Al(O, 2\alpha n)^{34}Cl$,	$^{27}Al(O, 3\alpha 3p)^{28}Mg$,
$^{27}Al(O, 3\alpha 3pn)^{27}Mg$,	$^{27}Al(O, 4\alpha 2pn)^{24}Na$ and	$^{27}Al(O, 4\alpha 3p)^{24}Ne$.

Experimental data on EFs have been compared with the predictions of the statistical model code PACE4. Sizable enhancement in the experimentally measured production cross-sections has been observed in case of α-emitting channels over the theoretical predictions, which has been attributed to be coming from in-complete fusion of projectile at these energies. Analysis of experimental data indicates that in-complete fusion is in competition with the complete fusion, and is observed to be a dominant mode of reaction at higher energies. As such, an attempt has been made to estimate the fraction of in-complete fusion F_{ICF} in reactions for ^{16}O + ^{181}Ta and ^{16}O + ^{103}Rh systems. The F_{ICF} has been found to be sensitive to the projectile energy and mass asymmetry of interacting partners. A detailed discussion of these

measurements is presented [25, 33, 52]. Further, in order to confirm the findings of the measurements and analysis of EFs presented and also to investigate the fusion in-completeness due to fractional linear momentum transfer from the projectile to the target nucleus, most probable forward recoil ranges for the reactions viz., ^{181}Ta(O, 3n)^{194}Tl, ^{181}Ta(O, 4n)^{193}Tl, ^{181}Ta(O,5n)^{192}Tl, ^{181}Ta(O,p3n)^{193}Hg^{g}, ^{181}Ta(O,p3n)^{193}Hg^{m}, ^{181}Ta(O,p4n)^{192}Hg, ^{181}Ta(O,p5n)^{191}Hg^{g}, ^{181}Ta(O,p5n)^{191}Hg^{m}, ^{181}Ta(O,αn)^{192}Au^{g}, ^{181}Ta(O,α2n)^{191}Au^{g}, ^{181}Ta(O,α3n)^{190}Au^{g} and ^{181}Ta(O,2α3n)^{186}Ir^{g}, produced via CF and/or ICF in ^{16}O + ^{181}Ta system have been measured [53] at three different projectile energies i.e., $\approx$81, 90 and 96 MeV, respectively. In the present work, the analysis of forward recoil ranges for different radio-nuclides have been performed within the framework of degree of linear momentum transfer from the projectile to the target nucleus by adopting break-up fusion model considerations. Different full and fractional linear momentum transfer components corresponding to the fusion of ^{16}O and/or ^{12}C and ^{8}Be from the projectile to the target nucleus have been observed. An attempt has been made to separate out the relative percentage contributions of CF and ICF processes. Further, with a view to get complementary information on ICF reactions, an attempt has been made to measure the angular distribution of residues produced in ^{16}O + ^{27}Al system at incident beam energy $\approx$85 MeV. To the best of our knowledge most of the presently measured EFs, RRDs and ADs are being reported for the first time.

The thesis is organized in the five Chapters. The Chapter-I introduces the field of nuclear reactions in general, and heavy ion physics in particular. Some relevant terminology and a brief summary of the literature is also given in this Chapter. Chapter II, focuses on the experimental procedure adopted to carry out different experiments at the Inter University Accelerator Centre, New Delhi, India. In Chapter III, various theoretical models that may be used to analyze the experimental results are discussed, while in Chapter IV details of measurements are presented. In Chapter V, the details of the data analysis in the form of results and discussion are presented followed by the summary and the conclusions drawn from the present work. The references are given at the end of each Chapter.

References

[1] A. H. Becquerel; Comp. Rend., 122, 450 (1896).
[2] J. J. Thomson; Phil. Mag., 44, 293 (1897).
[3] E. Rutherford; Phil. Mag., 21, 669 (1911).
[4] E. Rutherford; Phil. Mag., 37, 537 (1919).
[5] E. Rutherford; Phil. Mag., 37, 581 (1919).
[6] N. Bohr; Nature 137, 344 (1936).
[7] M. Blann; Phys. Lett. 27, 337 (1971).
[8] M. Blann; Phys. Rev. C31, 1245 (1985).
[9] P.E. Hodgson; Nuclear Heavy-Ion Reactions, Chapter 1, Clarendon Press Oxford (1978).
[10] A. C. Berriman; Nature, 413, 144 (2001).
[11] J. Wilczynski, K. Siwek-Wilczynska, J.; Nucl. Phys. A373, 109 (1982).
[12] E. Gadioli et al., Nucl. Phys. A641, 271 (1998).
[13] D.J. Parker, P. Vergani, E. Gadioli, J.J. Hogan, F. Vettore, E. Gadioli Erba, E. Fabrici and M. Galmarini; Phys. Rev. C44, 1528 (1991).
[14] H. Morgenstern, W. Bohne, W. Galster, K. Grabisch, and A. Kyanowski; Phys. Rev. Lett. 52, 1104 (1984).
[15] H. Morgenstern, W. Bohne, K. Grabisch, H. Lehr, W. Stoeffler; Z. Phys. A313, 39 (1983).
[16] H. Morgenstern, et al., Phys. Lett. B113, 463 (1982).
[17] M. Cavinato, E. Fabrici, E. Gadioli, E. Gadioli Erba, P. Vergani, M. Crippa, G. Colombo, I. Redaelli, and M. Ripamonti; Phys. Rev. C 52, 2577 (1995).
[18] P. Vergani, E. Gadioli, E. Vaciago, E. Fabrici, E. Gadioli Erba, M. Galmarini, G. Ciavola and C. Marchetta; Phys. Rev. C 48, 1815 (1993).
[19] F. Schussler et al., Nucl. Phys. A584, 704 (1995).
[20] Pushpendra P. Singh, B. P. Singh, Manoj Kumar Sharma, Unnati, Devendra P. Singh, R. Prasad, Rakesh Kumar and K. S. Golda; Eur. Phys. J. A 34, 29 (2007).
[21] R. H. Siemsen et al., Nucl. Phys. A400, 245c (1983).
[22] D. J. Parker, J. Asher, T. W. Conlon and I. Naqib; Phys. Rev. C 30, 143 (1984).
[23] Ch. Ngo; Prog. Part. Nucl. Phys. 16, 139 (1985).
[24] D. R. Zolnowski et al., Phys. Rev. Lett. 41, 92 (1978).
[25] Devendra P. Singh, Unnati, Pushpendra P. Singh, Abhishek Yadav, Manoj Kumar Sharma, B. P. Singh, K. S. Golda, Rakesh Kumar, A. K. Sinha, and R

Prasad; Phys. Rev. C 80, 014601 (2009).
[26] R. Kauffmann and R. Wolfgang; Phys. Rev. 121, 206 (1961).
[27] H. C. Britt and A. R. Quinton; Phys. Rev. 124, 877 (1961).
[28] J. Galin, B. Gatty, D. Guerreau, C. Rousset, U. C. Schlotthauer-Voos, and X Tarrago; Phys. Rev. C9, 1126 (1974).
[29] Manoj Kumar Sharma, B. P. Singh, Sunita Gupta, M. M. Musthafa, H. D. Bhardwaj, R. Prasad and A. K. Sinha; J. Phys. Soc. Jpn. 72, 1917 (2003).
[30] Manoj Kumar Sharma, Unnati, B.K. Sharma, B.P. Singh, H.D. Bhardwaj, Rakesh Kumar, K. S. Golda and R. Prasad; Phys. Rev. C70, 044606 (2004)
[31] Manoj Kumar Sharma, Unnati, B.P. Singh, Rakesh Kumar, K.S. Golda, H.D. Bhardwaj, R. Prasad; Nucl. Phys. A776, 83 (2006).
[32] Sunita Gupta, B. P. Singh, M. M. Muthafa, H. D. Bhardwaj and R. Prasad; Phys. Rev. C61, (2000) 064613.
[33] Unnati Gupta, Pushpendra P. Singh, Devendra P. Singh, Manoj Kumar Sharma, Abhishek Yadav, Rakesh Kumar, B.P. Singh, R. Prasad; Nucl. Phys. A811, 77(2008). References therein.
[34] Pushpendra P. Singh, B. P. Singh, Manoj Kumar Sharma, Unnati, R. Kumar, K. S. Golda, D. Singh, R. P. Singh, S. Muralithar, M. A. Ansari, R. Prasad, and R. K. Bhowmik; Phys. Rev. C 78, 017602 (2008).
[35] I. Tserruya, V. Steiner, Z. Fraenkel and P. Jacobs; Phys. Rev. Lett. 60, 14 (1988).
[36] T. Udagawa and T. Tamura, Phys. Rev. Lett. 45, 1311 (1980).
[37] J. Wilczynski, K. Siwek-Wilczyńska, J. van Driel, S. Gonggrijp, D. C. J. M. Hageman, R. V. F. Janssens, J. Łukasiak, and R. H. Siemssen; Phys. Rev. Lett. 45, No. 8, 606 (1980).
[38] J. P. Bondrof et al., Nucl. Phys. A333, 285 (1980).
[39] R. Weiner et al., Nucl. Phys. A286, 282 (1977).
[40] V. I. Zagrebaev; Ann. Phys. (NY) 197, 33 (1990).
[41] B. G. Harvey; Nucl. Phys. A444, 498 (1985).
[42] M. H. Simbel and A. Y. Abdul Magd; Z. Phys. A 294, 277 (1980).
[43] A. Y. Abdul Magd; Z. Phys. A 298, 143 (1980).
[44] W. Trautmann, Ole Hansen, H. Tricoire, W. Hering, R. Ritzka, and W. Trombik; Phys. Rev. Lett., 53, 1630 (1984).
[45] T. Inamura et al., Phys. Lett., B 84, 71 (1982).
[46] T. Inamura, A. C. Kahler, D. R. Zolnowski, U. Garg, T. T. Sugihara and M. Wakai; Phys. Rev., C 32, 1539 (1985).
[47] J. B. Natowitz, S. Leray, R. Lucas, C. Ngo, E. Tomasi and C. Volant; Z Phys A 325, 467 (1986).

[48] D. H. E. Gross and J. Wilczynski; Phys. Lett. B67, 1 (1977).
[49] H. Tricoire, et al., Z. Phys. A312, 221 (1983).
[50] T. C. Awes, G. Poggi, C. K. Gelbke, B. B. Back, B. G. Glagola, H. Breuer an V. E. Viola, Jr.; Phys. Rev. C24, 89 (1981).
[51] H. Morgenstern, W. Bohne, W. Galster and K. Grabisch; Z. Phys. A 324, 443 (1986).
[52] Manoj Kumar Sharma, Unnati, Devendra P. Singh, Pushpendra P. Singh, B. P. Singh, H. D. Bhardwaj and R. Prasad; Phys. Rev. C75, 064608(2007).
[53] Devendra P. Singh, Unnati, Pushpendra P. Singh, Abhishek Yadav, M. K. Sharma, B. P. Singh, K. S. Golda, Rakesh Kumar, A. K. Sinha and R. Prasad; Phys. Rev. C, Communicated, (2009). References therein.

INVESTIGATION OF THE ROLE OF BREAK-UP PROCESSES IN HEAVY ION REACTIONS BELOW 7 MeV/nucleon

A thesis submitted for the award of
DOCTOR OF PHILOSOPHY

in

PHYSICS

(Experimental Nuclear Physics)

2010

by

DEVENDRA PAL SINGH

Under the supervision of

PROF. B. P. SINGH

DEPARTMENT OF PHYSICS
ALIGARH MUSLIM UNIVERSITY,
ALIGARH (U. P.)-202 002, INDIA

Thesis Supervisor: **Prof. Bhanu Prakash SINGH*[1]**

Experimental Collaborators:

Prof. R. Prasad[1]
Dr. (Mrs.) Unnati Gupta[1]
Mr. Abhishek Yadav[1]
Dr. Pushpendra P. Singh[2]
Dr. M. K. Sharma[3]
Dr. H. D. Bhardwaj[4]
Mr. Rakesh Kumar[5]
Ms. K. S. Golda[5]
Dr. A. K. Sinha[6]

*email: bpsinghamu@gmail.com
[1]*Department of Physics, Aligarh Muslim University, Aligarh-202 002, India.*
[2]*INFN-Laboratori Nazionali di Legnaro (LNL), Legnaro (PD) -35020, Italy.*
[3]*Department of Physics, Sri Varshney (PG) College, Aligarh-202 002, India.*
[4]*Department of Physics, DSN College, Unnao, India.*
[5]*Nuclear Physics Group, Inter-University Accelerator Center, New Delhi-110 067, India.*
[6]*UGC-DAE-CSR, Bidhan Nagar, Kolkata-700 098, India.*

The work presented in this thesis is from the results of several experiments carried out at the Inter-University Accelerator Center (IUAC), New Delhi-67, India, using 15UD-Pelletron accelerator facilities
(http://www.iuac.ernet.in)

This thesis is dedicated to

My teachers.....

for systematization of my knowledge at every stage of life, and

My parents....

for their endless love, deep affection & inventive inspiration.

DEPARTMENT OF PHYSICS
ALIGARH MUSLIM UNIVERSITY
ALIGARH-202002 (U.P.) INDIA

Dr. B. P. Singh
Professor

Phone & Fax: +91-571-2701001, Cell :+91-9412133929, e-mail: bpsinghamu@gmail.com

CERTIFICATE

Certified that the work presented in this thesis entitled "Investigation of the role of break-up processes in heavy ion reactions below 7 MeV/nucleon" is the original work done by Mr. Devendra Pal Singh under my supervision.

BP Singh
29th Jan 2010

(Prof. B. P. Singh)

ACKNOWLEDGEMENTS

In the accomplishment of the present work, I have received generous cooperation, help and guidance from several individuals and teachers. I shall be failing in my duties if I do not put on record my sincere obligations and humble regards to them.

First of all, I utilize this fortunate opportunity and privilege to express my profound gratitude to my supervisor Prof. B. P. Singh, Department of Physics, Aligarh Muslim University, Aligarh for his decisive guidance, constructive criticism, inspiring suggestions, constant encouragement and keen interest since the beginning of my research career. This thesis would have never been accomplished without his support and enthusiasm. Above all, his humble character and attractive personality is what made it a great pleasure to be his student.

Next, I wish to acknowledge my deepest sense of gratitude to Prof. R. Prasad, Emeritus fellow (U.G.C), Department of Physics, Aligarh Muslim University, Aligarh for his inspiring, enthusiastic, analytical guidance, critical, scientific discussions and suggestions throughout the work. His enthusiasm and relentless curiosity about the subject has always been an inspiration.

My special thanks are due to Dr. Unnati Gupta, Research Associate, C.S.I.R., for her appreciation, immense help in all kind of computational work and for always being available with her critical comments and suggestions. I also thank to Dr. M. K. Sharma, Dr. Pushpendra Pal Singh, Mr. Abhishek Yadav and Mr. Vijay Raj Sharma for their critical suggestions in the laboratory and a reason for me to look into things deeper than I usually would. They all have been good friends and patient colleagues. They have managed to keep the lab interesting for the long hours we spent together. It is a great pleasure to extend regards to Dr. A. K. Sinha, Director, IUC-DAE-CSR, Kolkata for his support and discussions during the experiments and otherwise.

I wish to express my sincere regards to Dr. Amit Roy, Director, IUAC, New Delhi for providing me the experimental facilities for this work. I am

indebted from the core of my heart to Dr. R. K. Bhowmik, Mr. Rakesh Kumar and Ms. K. S. Golda, Scientists, Inter University Accelerator Centre (IUAC), New Delhi for all their support, enthusiasm and for always being ready to discuss the instrumentation. I am very much thankful to Mr. S. Murlithar and Mr. R. P. Singh, IUAC for helping us in setting up the experimental arrangement, and always being available with their comments and suggestions for the improvement of the present work. I equally thank to Mr. J. J. Das, Mr. N. Madhavan, Mr. S. Nath, Mr. J. Gehlot for their help and encouraging attitude. Mr. E. T. Subramanium, Mr. P. Barua, Mr. R. Abhilash, Ms. Kusum Rani, and Mr. M. Archunan from IUAC are also thankfully acknowledged for their help at various stages. A considerable support from Dr. H. D. Bhardwaj, Department of Physics, DSN College, Unnao during this work is also acknowledged.

I warmly thank to Prof. M. Zafar, Chairman, Department of Physics, AMU, Aligarh for facilitating me with all the departmental requirements from time to time in different ways for carrying out this work. I am also thankful to the technical staff in the Departmental Workshop as well as non-teaching staff for becoming available to help me. I owe a lot to them.

The best part of my Ph. D duration has been all the people I have spent time with, both on and off the court. My childhood friends Mr. Ajeet Arya, Mr. Anil Verma and Ms. Seema Mittal have been a source of endless friendship. I am also thankful to Dr. D. K. Gupta, Dr. Suman Bala and all those who remembered and wished me on every success, without their endless strife and blessings it would have been impossible for me to pursue this work. I owe a debt of gratitude to my family and relatives whose continuous moral support led me to complete this work. I definitely would not be here without their support and I am forever indebted to them. I am deeply grateful to Mrs. Seema-Mr. Santosh for their affection. And saving the best for the end, my words fail to thank Pinkey, Richa, Rajat, Jatin and Jeet for continuous, unwavering, and unconditional support throughout these trying years, their love has always been a reason to smile.

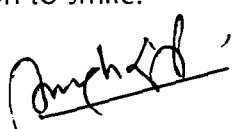

(Devendra Pal Singh)

List of Publications

(a) International Journals

1. Investigation of the role of break-up processes on the fusion of ^{16}O induced reactions: Devendra P. Singh, Unnati, Pushpendra P. Singh, A. Yadav, M. K. Sharma, B. P. Singh, K. S. Golda, Rakesh Kumar, A. K. Sinha and R. Prasad; Phys. Rev. C 80, 014601 (2009).

2. Observation of a large incomplete fusion in $^{16}O+^{103}Rh$ system at ≈40-85 MeV; Unnati, Pushpendra P. Singh, Devendra P. Singh, Manoj K. Sharma, B. P. Singh, and R. Prasad; Nucl. Phys. A 811, 77-92 (2008).

3. A study of reaction mechanism in $^{16}O+^{27}Al$ system: Measurement and analysis of excitation functions and angular distributions.; Manoj K. Sharma, Unnati, Devendra P. Singh, Pushpendra P. Singh, B. P. Singh, and R. Prasad; Phys. Rev. C75, 064608 (2007).

4. Energy dependence of in-complete fusion processes in $^{16}O+^{181}Ta$ system: Measurement and analysis of forward recoil range distributions at $E_{lab} \leq 7$ MeV/A; Devendra P. Singh, Unnati, Pushpendra P. Singh, A. Yadav, M. K. Sharma, B. P. Singh, K. S. Golda, Rakesh Kumar, A. K. Sinha and R. Prasad; Communicated in Journal Phys. Rev. C (2009).

5. Disentangling of full and partial linear momentum transfer events in $^{16}O + ^{169}Tm$ system at $E_{beam} \leq 5.4$ MeV/nucleon: Unnati, Pushpendra P. Singh, Devendra P. Singh, Manoj Kumar Sharma, Abhishek Yadav, B. P. Singh, and R. Prasad; Phys. Rev. C 80, 024613(2009).

6. Role of high ℓ-values in the onset of incomplete fusion; Pushpendra P. Singh, Abhishek Yadav, Devendra P. Singh, Unnati Gupta, Manoj K. Sharma, R. Kumar, D. Singh, R. P. Singh, S. Muralithar, M. A. Ansari, B. P. Singh, R. Prasad and R. K. Bhowmik; Phys. Rev. C 80, 064603 (2009).

7. Influence of incomplete fusion on complete fusion: Observation of large incomplete fusion fraction at E/A ≈5-7 MeV; Pushpendra P. Singh, B. P. Singh, Manoj K. Sharma, Unnati, Devendra P. Singh, Rakesh Kumar, K. S. Golda and R. Prasad; Phys. Rev. C77, 014607 (2008).

8. Large pre-equilibrium emission in $\alpha+^{nat}Ni$ interaction at ≈ 8-45 MeV; Abhishek Yadav, Pushpendra P. Singh, M. M. Musthafa, Devendra P. Singh, Unnati, Manoj K. Sharma, B. P. Singh, and R. Prasad; Phys. Rev. C 78, 044606 (2008).

9. Observation of complete and in-complete-fusion components in ^{159}Tb, $^{169}Tm(^{16}O,x)$ reactions: Measurement and analysis of forward recoil ranges at E/A≈6 MeV.; Pushpendra P. Singh, Manoj K. Sharma, Unnati, Devendra P. Singh, Rakesh Kumar, B. P. Singh, and R. Prasad; Euro. Phys. J. A 34, 29-39 (2007).

(b) International/national Conferences/Symposia

1. Measurement and analysis of excitation functions in $^{16}O+^{103}Rh$ system at E* =2-4MeV/nucleon; Devendra P. Singh, Unnati, Manoj Kumar Sharma, Pushpendra P. Singh, Sunita Gupta, B. P. Singh, Rakesh Kumar, H. D. Bhardwaj and R. Prasad; DAE-BRNS, Nucl. Phys. Symp., V51, 365 (2006).

2. A study of energy dependence of complete and in-complete fusion in $^{16}O+^{169}Tm$ system below 6 MeV/nucleon using recoil range distribution technique; Unnati, Manoj Kumar Sharma, B. P. Singh, Pushpendra P. Singh, Devendra P. Singh, Rakesh Kumar, K. S. Golda, H. D. Bhardwaj, Sunita Gupta and R. Prasad; DAE-BRNS symposium, 51, 441 (2006).

3. Measurement and analysis of cross-sections for some residues produced in $^{16}O+^{27}Al$ system; Manoj Kumar Sharma, Unnati, Devendra P. Singh, Pushpendra P. Singh, Rakesh Kumar, K. S. Golda, H. D. Bhardwaj, B. P. Singh and R. Prasad; DAE-BRNS, Nucl. Phys. Symp., V51, 431 (2006).

4. Influence of in-complete fusion on complete fusion: Observation of large fusion suppression at ≈5-7 MeV/nucleon; Pushpendra P. Singh, Devendra P. Singh, Unnati, Manoj Kumar Sharma, Rakesh Kumar, K. S. Golda, H. D. Bhardwaj, B. P. Singh and R. Prasad; DAE-BRNS, Nucl. Phys. Symp., V51, 359 (2006).

5. Pre-equilibrium emission studies in some light ion induced reactions; B. P. Singh, Manoj K. Sharma, Unnati, Pushpendra P. Singh, Devendra P. Singh, H. D. Bhardwaj and R. Prasad; International Workshop on "Physics for ADS for Energy and Transmutation" held at University of Rajasthan, Jaipur, India. 23rd-26th Feb. 2006.

6. A study of reaction mechanism in heavy ions at energies ≈5-7MeV/A; Manoj Kumar Sharma, Unnati, Pushpendra P. Singh, Devendra P. Singh, B. P. Singh and R. Prasad; 11th International Conference on Nuclear Reaction Mechanisms, Varenna (Italy), Villa Monastero, June12-16, 2006.

7. Complete and in-complete fusion studies for the $^{16}O+^{181}Ta$ system using x-ray detection technique; Devendra P. Singh, Unnati, Manoj K. Sharma, Pushpendra P. Singh, B. P. Singh, K. S. Golda, A. K. Sinha, and R. Prasad; DAE-BRNS, Nucl. Phys. Symp., V51, 379 (2007).

8. Isotopic mass distribution of fission products in $^{16}O+^{197}Au$ reactions at ≈6 MeV/nucleon; Manoj K. Sharma, Devendra P. Singh, Unnati, Pushpendra P. Singh, B. P. Singh, K. S. Golda and R. Prasad; DAE-BRNS, Nucl. Phys. Symp., V51, 433 (2007).

9. Measurement and analysis of radio-active nuclides produced in the interaction of $^{16}O+^{130}Te$ system over the energy range ≈3.8-5.6MeV/A; Unnati, Manoj K. Sharma, Devendra P. Singh, Pushpendra P. Singh, Sunita Gupta, H. D. Bhardwaj, Rakesh Kumar, B. P. Singh, and R. Prasad; DAE-BRNS, Nucl. Phys. Symp., V51, 343 (2007).

10. Absorptive break-up of ^{16}O projectile in interaction with ^{nat}Tm: Observation of fast projectile-like fragments in forward cone; Pushpendra P. Singh, B. P. Singh, Unnati, Manoj K. Sharma, Devendra P. Singh, Rakesh Kumar, P. D. Shidling, D. Singh, P. S. Rao, S. Muralithar, R. P. Singh, K. S. Golda, M. A. Ansari, H. D. Bhardwaj, R. Prasad and R. K. Bhowmik; International Nuclear Physics Conference 2007 (INPC07), 3-8th June 2007, Tokyo, Japan.

11. Spin distribution and feeding intensity measurement: Disentangling of fusion and Incomplete fusion dynamics at E/A ≈ 4-7MeV; Pushpendra P. Singh, B. P. Singh, Unnati, Manoj Kumar Sharma, Devendra P. Singh, R. Kumar, D. Singh, R. Ali, P. D. Shidling, D. Negi, R. P. Singh, S. Muralithar, H. D. Bhardwaj, M. Afzal Ansari, R. Prasad, and R. K. Bhowmik; DAE-BRNS Symposium, 52, 327 (2007).

12. Complete versus in-complete fusion in $^{159}Tb(^{16}O, x)$ reactions: Forward recoil ranges measurement of heavy slow residues at Erecoil < 0.05 MeV/nucleon; Pushpendra P. Singh, Devendra P. Singh, Unnati, Manoj Kumar Sharma, Rakesh Kumar, K. S. Golda, H. D. Bhardwaj, B. P. Singh and R. Prasad; DAE-BRNS Symposium, 52, 403 (2007).

13. Fusion and in-complete fusion studies in ^{16}O +^{181}Ta in the energy range ≈4.7- 6.2 MeV; Devendra P. Singh, Abhishek Yadav, Pushpendra P. Singh, Unnati, Manoj Kumar Sharma, B. P. Singh, K. S. Golda, Rakesh Kumar, A. K. Sinha and R. Prasad; DAE-BRNS Symposium, 53, 429 (2008).

14. Thin layer activation analysis of α-induced reactions for surface wear studies in some natural isotopes; Devendra P. Singh, Abhishek Yadav, Pushpendra P. Singh, Unnati, Manoj Kumar Sharma, B. P. Singh, K. S. Golda, Rakesh Kumar, A. K. Sinha and R. Prasad; DAE-BRNS Symposium, 53, 431 (2008).

15. Investigation of in-complete fusion fraction in ^{16}O +^{169}Tm system below 6 MeV/A; Unnati, Manoj Kumar Sharma, Devendra P. Singh, Pushpendra P. Singh, Abhishek Yadav, Sunita Gupta, H. D. Bhardwaj, Rakesh Kumar, B. P. Singh and R. Prasad; DAE-BRNS Symposium, 53, 395 (2008).

16. Isomeric yield ratios for some reactions in ^{16}O +^{169}Tm system; Manoj Kumar Sharma, Pushpendra P. Singh, Devendra P. Singh, Unnati, Abhishek Yadav, Akshaya Behra, Rakesh Kumar, K. S. Golda, H. D. Bhardwaj, B. P. Singh and R. Prasad; DAE-BRNS Symposium, 53, 469 (2008).

17. Study of in-complete fusion dynamics: Measurement and analysis of forward recoil range distributions at ≈5-6 MeV/nucleon; Devendra P. Singh, Abhishek Yadav, Unnati, Pushpendra P. Singh, Manoj Kumar Sharma, Sunita Gupta, K. S. Golda, R. Kumar, A. K. Sinha, B. P. Singh and R. Prasad; DAE-BRNS Symposium, 54, 334 (2009).

18. Isomeric ratios for several residues in the interaction of ^{16}O with ^{181}Ta and ^{103}Rh; Devendra P. Singh, Abhishek Yadav, Unnati, Pushpendra P. Singh, Manoj Kumar Sharma, Sunita Gupta, K. S. Golda, R. Kumar, A. K. Sinha, B. P. Singh and R. Prasad; DAE-BRNS Symposium, 54, 336 (2009).

19. A study of Pre-equilibrium emission in some proton induced reactions: Measurement of cross-sections; B. P. Singh, M. M. Musthafa, H. D. Bhardwaj, Devendra P. Singh, Pushpendra P. Singh, Abhishek Yadav, Unnati, Manoj Kumar Sharma and R. Prasad; International Topical Meeting on Nuclear Research Applications and Utilization of Accelerators, Vienna, Austria, 48 May, 66 (2009).

20. Measurement of cross-sections in some reactions in $^{16}O+^{181}Ta$ system at energies $\approx$5 MeV/ nucleon; R. Prasad, Devendra P. Singh, Abhishek Yadav, Pushpendra P. Singh, Unnati, Manoj Kumar Sharma, B.P. Singh, R. Kumar, K. S. Golda and A. K. Sinha; International Topical Meeting on Nuclear Research Applications and Utilization of Accelerators, Vienna, Austria, 48 May, 71 (2009).

(c) Scientific/Technical Reports

1. Fusion and in-complete fusion studies with heavy targets using ^{16}O beam; Devendra P. Singh, Unnati, Manoj Kumar Sharma, Pushpendra P. Singh, Abhishek Yadav, B. P. Singh, K. S. Golda, Rakesh Kumar, A. K. Sinha and R. Prasad; Annual Report, Inter-University Accelerator Center (IUAC), New Delhi, India, Year 2007-08, page No. 130.

2. Disentangling of fusion and in-complete fusion: spin distribution measurement at ≈4-7 MeV/nucleon; Pushpendra P. Singh, B. P. Singh, Unnati, Manoj K. Sharma, Devendra P. Singh, Rakesh Kumar, P. D. Shidling, D. Singh, Abhishek Yadav, R. Ali, R. P. Singh, S. Muralithar, M. A. Ansari, H. D. Bhardwaj, R. Prasad and R. K. Bhowmik; Annual Report, Inter-University Accelerator Center (IUAC), New Delhi, India, year 2007-08, page No. 124.

3. Spin distribution studies at E/A ≈4-7MeV: a sensitive probe for in-complete fusion dynamics; Pushpendra P. Singh, B. P. Singh, Unnati, Manoj K. Sharma, Devendra P. Singh, Rakesh Kumar, P. D. Shidling, D. Singh, J. K. Rana, P. S. Rao, R. Ali, R. P. Singh, S. Muralithar, M. A. Ansari, H. D. Bhardwaj, R. Prasad and R. K. Bhowmik; Annual Report, Inter-University Accelerator Center (IUAC), New Delhi, India, year 2006-07, page No. 133.

4. Spin distribution studies of evaporation residues produced through complete and in-complete fusion in the collision of ^{16}O + ^{160}Gd @ 90 MeV; R. Ali, D. Singh, D. Pouchri, M. A. Ansari, Manoj K. Sharma, Unnati, Pushpendra P. Singh, Devendra P. Singh, P. D. Shidling, B. P. Singh, Rakesh Kumar, R. P. Singh, S. Muralithar, R. Prasad and R. K. Bhowmik; Annual Report, Inter-University Accelerator Center (IUAC), New Delhi, India, year 2007-08, page No. 127.

Contents

List of Figures

List of Tables

Chapter 1

INTRODUCTION

1.1 OVERVIEW

Nuclear Physics is not only an important subject in its own right, but is significant also for its impact on the related fields of investigation. By the early 20th century, there was rather compelling evidence that matter is composed of atoms. This provided a consistent and unified picture for almost all known physical and chemical processes at that time. In 1896, A.H. Becquerel discovered penetrating radiation and led to contemplate the nature of the nucleus [1]. In 1897, British physicist J. J. Thomson contemplated that in an atom electrons are embedded in a spherical matrix of positive charge [2]. An important breakthrough came in 1911, when Ernest Rutherford and his coworkers conducted an experiment [3] which indicated that all the positive charge and almost total mass of the atom is concentrated in a very small and tiny central part of the atom, the nucleus. The electrons are assumed to revolve around the nucleus in nearly circular orbits and make the atom electrically neutral. The results of Rutherford's experiment were astounding. Later in 1919, the first artificial radioactivity [4] was produced. Further, the experiments of Rutherford, Cock-Croft & Walton, Curie & Juliet and of Fermi on the nuclear transmutation developed new ideas to solve basic problems regarding the nuclear structure, nuclear properties, nuclear forces, energy states of nuclei, transition probabilities etc., which considerably motivated nuclear reaction studies [4, 5]. Soon after the establishment of the presence of neutron(s) inside the nucleus, nuclear reactions were used as a tool to understand the properties of nuclei in various physical conditions. Some of the basic aims of nuclear physics research are to investigate the structure of the nucleus, the nature of the nuclear interactions, decay characteristics of excited nuclei and more recently to explore the possibilities of producing the super heavy nuclei [6].

In general, a nuclide 'A', when interacts with a nuclear particle 'a', forms a new nucleus 'B' and emits a nuclear particle of the type 'b' [7]. The energetic incident particle 'a', may be taken either from radio-active decay or from the particle accelerators. The above reaction may be represented as;

$$a + A \rightarrow B + b \tag{1.1}$$

or in the short form as;

$$A(a, b)B \tag{1.2}$$

where, 'a' and 'b' are the projectile and emitted particles, while 'A' & 'B' are the target and residual nuclei respectively.

An important parameter involved in the nuclear reactions is the Q-value of the reaction, which refers to the energy balance of a nuclear reaction and may be written for a binary reaction of the type A(a, b)B as;

$$Q = (M_a + M_A)c^2 - (M_b + M_B)c^2 \tag{1.3}$$

where, M_a and M_A are the masses of projectile and target nuclei in the entrance channel, while M_b and M_B are the masses of ejectile and residual nuclei in the exit channel and 'c' is the speed of light in vacuum.

On the basis of Q-value, the nuclear reactions may be classified as; (a) Exoergic reactions ($Q>0$), in which energy is evolved, and (b) Endoergic reactions ($Q<0$), in which energy is absorbed. Since, there is a net deficit of energy in the endoergic reaction, therefore, energy must be supplied to initiate such a reaction, which usually comes from the kinetic energy of the incident particle. Based on the energy region of interest, a broad classification of nuclear reaction studies may be given as; (i) Low Energy Nuclear Reactions, (ii) Medium Energy Nuclear Reactions, and (iii) High Energy Nuclear Reactions. In nuclear reactions the identity of elements or nuclides may be changed by altering the structure of atomic nuclei. Changes in the nuclei can be in the form of energy, number of nucleons etc. Ideally, the energetic incident nuclear particle must approach within the range of nuclear field of the target nucleus for a nuclear reaction to occur. Particles such as protons, and light nuclides with a positive charge experience repulsion. The repulsion results in the rise of potential energy, reaching its maximum value as Coulomb barrier, when two nuclei nearly touch each other. In order that a nuclear reaction takes place, the incident particles must carry enough energy to overcome the Coulomb barrier/fusion barrier (B_{fus}). Once within the nuclear range of the target nucleus, the strong forces become effective, merging the incident particle with the target nucleus. In a nuclear reaction, all the properties of the interacting partners of the system

are known, before and after the reaction has taken place. However, what exactly happens during the nuclear reaction is still not well understood. It is mainly because the time scales involved in the occurrence of a reaction are very short (i.e., $\approx 10^{-22}$ to 10^{-16} sec). Since, the exact process of a nuclear reaction is not well known, therefore, simplified theories and models are developed for explaining the mechanism of the reaction. A major step in understanding nuclear reaction dynamics was made when Neil's Bohr [8] proposed first such model for nuclear reactions, called the compound nucleus (CN) reaction model, which has been extremely useful in describing a typical nuclear reaction. Although, the CN model was proposed to explain observed resonances in thermal and low energy neutron cross-sections, but the concept was extended to reactions at higher energies as well.

According to Bohr, a nuclear reaction takes place in two distinct stages. The first stage is the formation of the compound nucleus and the second stage is the disintegration of the compound nucleus into the products of the reaction. Both these steps are assumed to be independent of each other. In the first stage, when a projectile ($E>B_{fus}$) interacts with the target nucleus, it is captured by the target nucleus, the total kinetic energy and angular momenta of the projectile are shared statistically among all the nucleons of the composite system leading to the establishment of thermodynamic equilibrium. Once the equilibrium is established, the CN forgets its history of formation and may then decay. However, in the second stage, after a long time ($\approx 10^{-16}$ sec.), somehow sufficient amount of energy, more than the separation energy, may be accumulated on a nucleon or on a group of nucleons which may be emitted from the CN, leaving behind a residual nucleus [8]. In 1950, the validity of "Bohr's independence hypothesis" has been experimentally verified by S. N. Ghoshal [9]. Another approach to describe a nuclear reaction is the direct reaction mechanism. The time scale of the direct reactions is $\approx 10^{-22}$ sec., which is typically the time taken by the energetic projectile to cross the target nucleus diameter. In direct reactions, only a few degrees of freedom are excited. The direct reactions may further be sub-divided into three categories, viz., (1) knock-out reactions, where the incident particle hits a nucleon or a cluster of nucleons at the surface of the target nucleus which is then ejected, (2) pick-up reactions, where the incident particle picks-up a nucleon/nucleons from the target nucleus and (3) stripping reactions, where the incident projectile loses one or few

nucleons, which are captured by the target nucleus. Such reactions are likely to occur at considerably higher energies.

In the CN reaction mechanism it is assumed that the emission of light nuclear particle(s)/cluster(s) takes place, after the establishment of thermodynamic equilibrium and this state of the compound nucleus is achieved by a series of two body residual interactions between the nucleons of the composite system. However, both the intuition and the results of a large number of experiments indicate that the emission of nuclear particle(s) may also take place even before the establishment of thermodynamic equilibrium of the composite system [10]. The particles which are emitted before the equilibration of composite system are called pre-equilibrium (PE) particle(s) and the process is referred to as PE-emission and the mechanism is referred to as pre-compound reaction mechanism [11]. It may not be out of place to mention that the PE-emission serves as a bridge between the direct and the CN reactions. Such studies have mostly been carried out for light ion induced reactions. Further, with the availability of modern accelerators, it has now become possible to accelerate heavy-ions (HI) at energies from few MeV/nucleon to many GeV/nucleon. The HI induced reactions are significantly different from that of the light ion induced reactions. This is because of the fact that the charge and mass of the HIs are larger than the light ions, thus energy and momentum carried in by the HIs are relatively large, which makes the HI induced reactions more complex. A brief description of HI induced reactions and how they differ from light ion induced reactions is given here.

1.2 NUCLEAR PHENOMENA IN HEAVY ION COLLISIONS

Heavy ion collisions deal with the phenomena that occur when two nuclei are brought in contact with each other within the range of nuclear forces. Various heavy nuclei that exist in nature, particularly, never come in contact with each other at the temperatures that occur in nature, the only exception being reactions produced by cosmic rays. In recent years, particle accelerators have been constructed which are capable to accelerate nuclei to energies where they can overcome the Coulomb repulsion and the nuclear reaction occurs. During the last few decades or so, major research efforts have gone into the study of nuclei by means of probes which excite

them in a moderate way, mainly by bombardment with light ions such as protons, deuterons and alpha particles. These investigations led to a rather detailed picture of nuclei close to their ground state, and have shown a rich variety of phenomena displayed by the nuclear many body system. In general, when two nuclei are brought in contact, a variety of phenomena can arise. By appropriately selecting the target, the projectile and the incident energy it is possible to excite different degrees of freedom. On the other hand, collisions which bring the two nuclei into more intimate contact lead to a combined nuclear matter system which at a later stage of the reaction may look like a normal nucleus which has been excited to a state of relatively high angular momentum. The transition from the situation in which the two nuclei maintain their identity to the situation in which they become a composite system is the main theme of research in the field of HI physics. Collisions between HIs have been studied for a range of target-projectile combinations but detailed interpretation of reaction dynamics is still lacking. The experience gathered from these experiments leads to a consistent picture when the reactions are classified into categories, such as grazing collisions, deep inelastic collisions, fusion processes etc.

The study of HI-induced reactions is quite complex due to the involvement of many nucleons and interacting partners having large B_{fus}. The study of reactions involving HIs tend to differ from the light ion induced reactions in many ways. The de-Broglie wavelength associated with relative motion of the interacting heavy ions is much shorter than that for light ions, typically an order of magnitude smaller than the size of the nuclei and can be expressed by the relation;

$$\lambda = \frac{1}{2\pi}\left[\frac{h^2}{2mE_{lab}}\right]^{1/2} . \qquad (1.4)$$

Since, the associated de-Broglie wavelength (λ) of the HIs is very small, therefore, the HI-induced reactions can be described using semi-classical approach. In semi-classical approach, one considers radial motion of the ions classically and angular motion quantum mechanically in central force field. The HIs consist of larger mass in comparison to the light ions and their angular momentum with respect to the centre of mass is very large.

An important feature of HI reactions is (since, a HI is a multi-nucleon system) that a variety of reactions may occur at energies near and well above the B_{fus}. Therefore, the HI induced reactions provide a possibility of producing nuclei with high excitation energy and spin. Nuclei far away from the neutron drip line may also be produced in HI interactions. Thus, it allows the study of those nuclei that do not exist naturally. The HI induced reactions have also been used to produce super heavy elements (SHE). With the availability of accelerated beams of heavy ions, the study of nuclear reactions initiated by HIs has acquired central place in nuclear physics research. The HI reactions can be described in terms of the distance of closest approach r_{min}, which is related to the impact parameter 'b' by the relation [12].

$$r_{min} = \frac{b}{\sqrt{\left[1 - \frac{V(r_{min})}{E_{cm}}\right]}} \tag{1.5}$$

where, $V(r_{min})$ is the nuclear potential between the target and projectile, and E_{cm} is the center of mass energy.

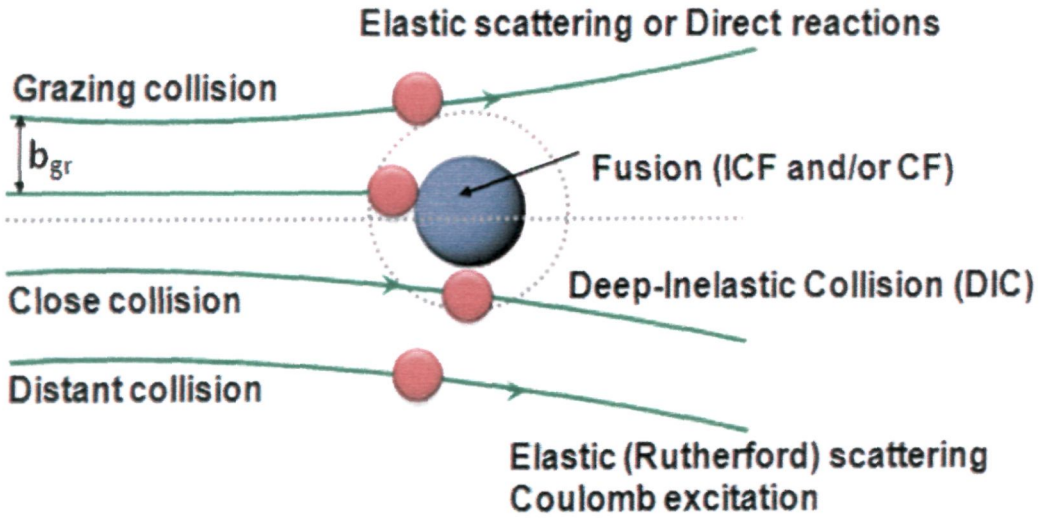

Figure 1.1: A typical representation of heavy-ion interaction trajectories.

The classical trajectories of projectile leading to the different modes of reactions may be classified on the basis of impact parameters shown in Fig. 1.1. As can be seen from the Fig. 1.1, at projectile energies well below the Coulomb barrier, the projectile does not touch the target nucleus and is elastically scattered through the Coulomb field, at large values of impact parameter leading to the 'distant collisions'. In such type of reactions, no mass is transferred from the projectile to the target nucleus and/or vice-versa, and the Coulomb forces exclusively determine the process (elastic scattering and Coulomb excitation). However, when the projectile and target nuclei come into close contact then the nuclear interactions will set in. Meaning thereby, if the impact parameter is comparable to the sum of the radii of the interacting partners, 'grazing collision' may takes place and the projectile can be elastically or in-elastically scattered. Moreover, when the projectile interacts with the target nucleus at smaller values of impact parameter with relatively high bombarding energies (just enough to enter in the nuclear field range of target nucleus) then 'deep inelastic collisions' (DIC) dominate. Here, the projectile interacts strongly with the target nucleus. In such a case, the nuclear density rises very rapidly in the surface region of target nucleus, and a few nucleons may get transferred from the projectile to the target nucleus, which is also referred to as the 'massive transfer reaction'. Further, if the projectile interacts with the target nucleus very strongly at still smaller values of impact parameters, the projectile fuses with target nucleus resulting into the formation of a compound nucleus (CN). The typical ranges of impact parameters associated with different processes are summarized in Table.1.1.

Table 1.1: Values of distance of closest approach (impact parameter) and angular momentum representing different types of heavy-ion reactions.

Distance of closest approach (r_{min})	Angular momentum (ℓ)	Nuclear reaction of the type
b or $r_{min} > R_N (= R_1 + R_2)$	$\ell > \ell_N$	Rutherford (elastic) scattering or Coulomb excitation
$R_F < r_{min} \leq R_{DIC}$	$\ell_{DIC} > \ell > \ell_N$	Deep in-elastic scattering or close collision
$R_{DIC} < r_{min} \leq R_N$	$\ell_N > \ell > \ell_{DIC}$	Transfer reactions (elastic and in-elastic scattering)
$0 \leq r_{min} \leq R_F$	$\ell < \ell_F$	Fusion reaction (Compound nucleus formation)

Here, R_N is the grazing range of nuclear force, R_{DIC} is the minimum distance for the deep inelastic collision, while R_F is the minimum distance for fusion reactions.

As already described, in case of HI induced reactions, when the center of mass energy of the interacting partners is higher than the B_{fus}, they overcome the barrier and may lose some of the relative energy through friction to get trapped in the pocket of the potential and ultimately, it may lead to the formation of the compound nucleus. In general, the total cross-section for these reactions may be estimated as,

$$\sigma = \pi R^2 = \pi \lambda^2 \ell^2 \tag{1.6}$$

The cross-sections for the fusion reaction and for the deep in-elastic scattering may be represented by using the equation (1.6) as;

$$\sigma_F = \pi \lambda^2 \ell_F^2 \tag{1.7}$$

and $$\sigma_{DIC} = \pi \lambda^2 \left(\ell_{DIC}^2 - \ell_F^2\right) \tag{1.8}$$

The partial reaction cross-section for such a collision at a given energy E, may be given by [12],

$$\sigma_\ell^R (E) = \pi \lambda^2 (2\ell + 1) T_\ell (E) \tag{1.9}$$

where, T_ℓ (E) is the transmission coefficient of the ℓ^{th} partial wave for the potential V_ℓ (r) at energy E.

A qualitative picture of the reaction probability as a function of entrance channel angular momentum (ℓ) is given in Fig. 1.2, for different type of collisions discussed above. As can be observed from this figure, the area below the respective solid curves give the reaction cross-section for CN formation (σ_{CN}), deep in-elastic collision (σ_{DIC}), direct reactions (σ_D) and towards the extreme right the area for elastic collisions and/or Coulomb excitation follow. As indicated in this figure, different regions are overlapping in ℓ-values. At present, it is not clear, how large the

overlapping regions are for an individual mode of reaction. In the simplest form, one can set an assumption of effective nuclear potential V_{eff}, that depends on the relative separation (r) of two interacting nuclei. The $V_{eff}(r)$, as a function of 'r' and relative angular momenta may be written as the sum of Coulomb, nuclear and centrifugal potential terms and may be given as,

$$V_{eff}(r) = V_{Coul}(r) + V_{nucl}(r) + V_{cent}(r) \tag{1.10}$$

where, $V_{Coul}(r)$ is the Coulomb potential, $V_{nucl}(r)$ is the nuclear potential and $V_{cent}(r)$ is the centrifugal potential.

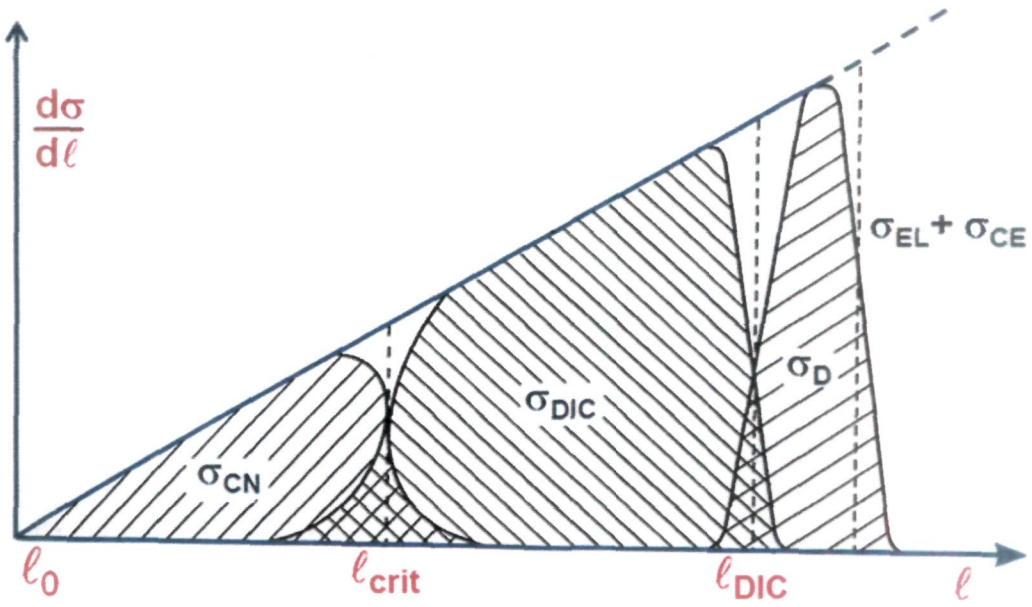

Figure 1.2: A typical picture of the distribution of reaction probability for fusion (σ_{CN}), deep in-elastic collisions (σ_{DIC}), direct reactions (σ_D), etc., as a function of entrance channel input angular momentum.

The repulsive Coulomb potential $V_{Coul}(r)$ may be given as,

$$V_{Coul}(r) = \frac{1}{4\pi\varepsilon_0} \frac{Z_P Z_T e^2}{r} \text{ ; for } r \geq (R_P + R_T) \tag{1.11}$$

and

$$V_{Coul}(r) = \frac{1}{4\pi\varepsilon_0}\frac{Z_P Z_T e^2}{2R_{Coul}}\left(3 - \frac{r^2}{R_{Coul}^2}\right); \text{ for } r \leq (R_P + R_T) \quad (1.12)$$

Here, Z_P and Z_T are the atomic numbers, while, R_P and R_T are the radii of the projectile and the target nuclei, respectively.

The complex short-range attractive nuclear potential $V_{nucl}(r)$ has been described in different forms. Wood-Saxon form is the simplest form for the nuclear potentials and is given as;

$$V_{nucl}(r) = \frac{V_0}{1 + \exp\left(\frac{r - R}{a}\right)} \quad (1.13)$$

where, $R = r_o\left(A_T^{1/3} + A_P^{1/3}\right)$, and V_0 is the depth of the potential, 'a' is the diffuseness parameter and $r_0 = 1.31$ fm.

The repulsive centrifugal potential $V_{cent}(r)$ is given by,

$$V_{cent}(r) = \frac{\hbar^2}{2\mu}\frac{\ell(\ell+1)}{r^2} \quad (1.14)$$

here, ℓ is the angular momentum and μ the reduced mass of the interacting nuclei. The effective potential $V_{eff}(r,\ell)$ for the entrance channel can be written as;

$$V_{eff}(r_b, \ell) = V_b(r_b) + V_n(r_b) + \frac{\ell(\ell+1)\hbar^2}{2\mu r_b^2} \quad (1.15)$$

where, the terms used have their usual meanings. It may be observed that the magnitude of μr_b^2 strongly affects the contribution of the centrifugal potential to the effective interaction for each partial wave.

It may, further, be noticed that at lower energies and larger impact parameters, when the two ions pass through each other at distances larger than the range of the nuclear interaction, they interact only through their Coulomb fields. As a result, elastic scattering may take place as only V_{Coul} and V_{cent} are important. In such type of interactions no dissipation of the kinetic energy takes place, and hence, the nuclear interaction is only a small perturbation on the Coulomb interaction. For grazing impact parameters (b_{gr}), processes like, in-elastic scattering and a few nucleon transfer may take place from the projectile to the target nucleus. This may be due to the overlapping of the tails of nuclear wave functions. On further reduction of impact parameter, the wave functions of the two interacting nuclei overlap considerably and a part of the relative kinetic energy may be converted into internal excitation before the two nuclei separate into target and projectile like systems. These deep in-elastic collisions take place at energies of the order of a few MeV/A above the B_{fus}. At still lower values of impact parameter, the two ions may come close to each other within the range of nuclear interactions, where large dissipation of energy takes place forming a fully thermalized composite system. The study of HI induced reactions has been used as an important tool to understand the reaction dynamics and the decay characteristics of excited compound nuclei at energies near and above the Coulomb barrier (CB) [13-17]. It is now experimentally established that complete fusion (CF) and incomplete fusion (ICF) are the dominant modes of reaction processes at these energies [18-22]. A brief description of these processes is presented here.

1.2.1 COMPLETE FUSION

In case of complete fusion (CF), the projectile nucleus completely fuses with the target nucleus leading to the formation of fully equilibrated compound nucleus (CN). For such reactions to take place, the incident energy of the projectile must be sufficient enough to overcome the B_{fus} of the projectile-target combination. In the centre of mass frame, the B_{fus} is given as;

$$B_{fus} = \frac{1.44\ Z_p\ Z_T}{r_0\,(A_T^{1/3} + A_p^{1/3})}\ \text{MeV} \qquad (1.16)$$

where, the symbols used have their usual meaning.

Further, for the CF to occur the input angular momentum should be such that can be sustained by the composite system. In the CF reaction all nucleonic degrees of freedom are involved. A typical representation of the CF reaction dynamics, formation of CN and its subsequent decay is shown in Fig. 1.3. The CF reactions are said to occur probably at zero/small values of impact parameters and for the input angular momenta range $0 \leq \ell \leq \ell_{crit}$. Another way of describing the CF processes is on the basis of linear momentum transfer from the projectile to the target nucleus. In case of CF process, the total linear momentum of the projectile is transferred to the composite system. The mass of the composite system is essentially equal to

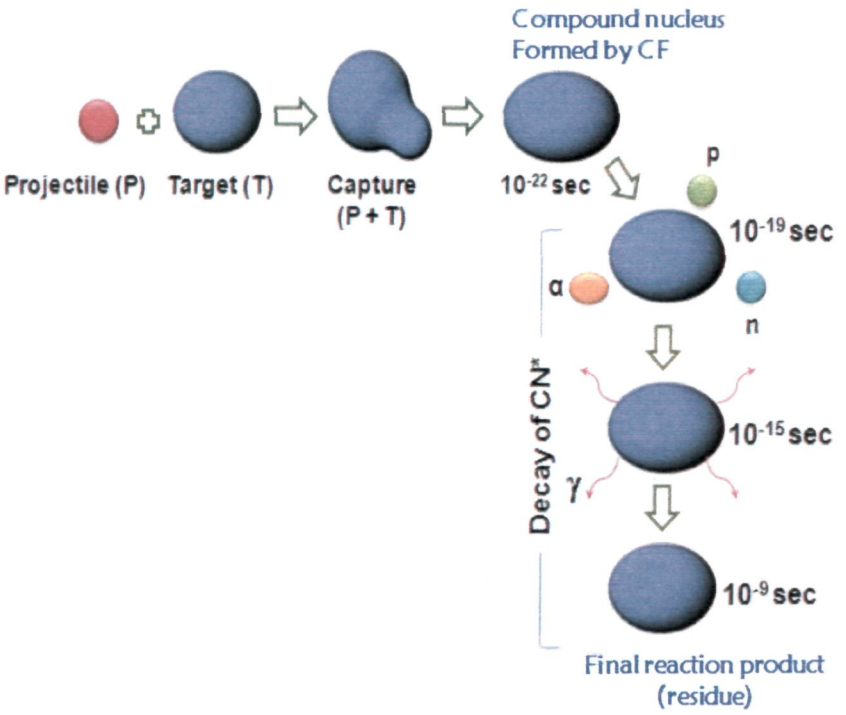

Figure 1.3: A typical representation of compound nucleus (CN) formation and its decay via complete fusion (CF) process. The CN first decays by the evaporation of neutrons, protons and/or α-particles. Eventually, it may lose the rest of its excitation energy and almost all of its initial angular momentum by emission of γ-rays.

the sum of the masses of interacting partners i.e., projectile and the target nucleus. The CN formed by complete fusion may de-excite by the evaporation of light nuclear particle(s), alongwith characteristic γ-radiations leaving a residue recoiling essentially in the forward cone. At higher ℓ-values ($\ell > \ell_{crit}$) the overlap between the target nucleus and the incident ion is less and may lead to in-complete fusion.

1.2.2 IN-COMPLETE FUSION

In case of in-complete fusion (ICF), a part of the projectile fuses with the target nucleus while the remnant moves with the same velocity as that of the incident ion. It is assumed that the un-fused part does not interact and behaves as a spectator. In case of ICF, partial linear momentum transfer (LMT) from the projectile to the target nucleus takes place and relatively less nucleonic degrees of freedom are excited as compared to the CF. A typical representation of ICF reaction dynamics is shown in Fig. 1.4. At relatively higher projectile energies and at finite values of impact parameter, CF gradually gives way to ICF. For large impact parameter, the driving angular momenta exceed its critical limit (ℓ_{crit}) for CF, as such the attractive nuclear potential (V_{nucl}) is not strong enough to capture the entire projectile. Eventually, an in-completely fused composite (IFC) system (a part of projectile + target nucleus) appears with less charge and mass as compared to that of CF population. It may, however, be pointed out that in case of ICF, most of the time either α-particle or clusters of α-particles (i.e., ^{8}Be or ^{12}C) depending on the incident ion, escape as un-fused spectator. Nonetheless, the viscous forces between interacting partners also play an important role in the occurrence of fusion and fusion-like (ICF) processes [24]. However, it has experimentally been observed that there is no sharp boundary of input angular momentum for CF and ICF to occur. Both the processes are found to contribute significantly below and above their input angular momentum limits. Some of the prominent features of ICF reactions, which have emerged from qualitative observations of recent experimental results, are summarized as;

- the ICF processes mainly take place for the $\ell > \ell_{crit}$ for CF, meaning thereby that the lower ℓ-values don't contribute to ICF [23],

- the fused system is formed with less charge and mass as compared to the total charge and mass of interacting partners [16],

- the contribution of ICF increases with projectile energy. At relatively higher beam energies ICF contributes a significant fraction to the total fusion cross-section [16, 25],

- the forward recoil velocity of ICF residues has been observed to be less than those populated via CF, due to partial linear momentum transfer [26],

- the ICF has been observed to be more prominent for relatively more mass asymmetric systems as compared to the mass symmetric systems [27-29].

- The spin distribution of the residues formed via ICF processes is found to be distinctly different from that for CF population [30].

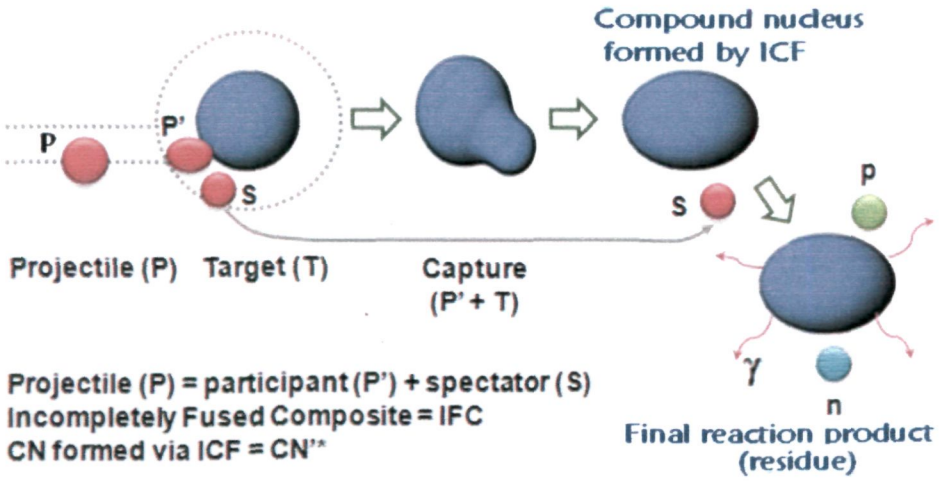

Figure 1.4: A typical representation of in-complete fusion (ICF) process. As shown, one of the fragments fuses with target nucleus called participant (P'), leading to the formation of an IFC system, while the remnant moves in the forward cone as spectator(s) with almost the projectile velocity. The IFC system de-excites in the similar fashion as the CN decay in CF.

1.3 HISTORICAL PERSPECTIVE AND MOTIVATION OF THE PRESENT WORK

For many years, the study of HI reactions has been used as an important tool to understand the reaction dynamics and the decay characteristics of excited compound nuclei at energies near and above the Coulomb barrier (CB) [13-16, 31]. The evidence of ICF reactions was observed from experiments [32, 33] on different projectile target combinations at energies from ≈7-10 MeV/nucleon. The results of these experiments suggested that the main process involved in the production of fast α-particles is the projectile break-up in the nuclear field of the target nucleus in a hard grazing interaction. Later, similar experimental evidences were put forward by Galin et. al., [34], where it has been observed that ICF processes compete with CF at the bombarding energies above 7 MeV/nucleon. Recently, it has been observed that ICF becomes more and more dominant as the projectile energy increases [35-40]. The different modes of reactions can be understood on the basis of driving input angular momenta imparted into the system. The CF occurs for the input angular momenta values $\leq \ell_{crit}$, as per the sharp cut-off approximation. However, at relatively higher projectile energies and/or at larger impact parameters, ICF starts competing with the CF. It may, further, be pointed out that the multitude of driving input angular momenta may vary with the projectile energy and/or with the impact parameter. However, there is no sharp boundary for the CF and ICF processes; both the processes have been observed below and/or above the limiting value of input angular momenta [41]. A few reports have indicated that ICF can selectively populate high spin states in the final reaction products at low bombarding energies and can be used as spectroscopic tool as well [42, 43]. The ICF reactions have been employed to populate neutron-rich nuclei compared to conventional fusion-evaporation reactions, and hence opening the possibilities for the study of nuclei along the neutron rich side of the line of stability [44].

A variety of dynamical models/theories, like the Break-up Fusion (BUF) model [45], the SUMRULE model [46], the Promptly Emitted Particles (PEPs) model [47], the EXCITON model [10], the Hot Spot model [48], the Multistep Direct Reaction theory [49], the Overlap model [50-52] etc., have been proposed to explain some of the characteristics of ICF reactions.

The SUMRULE model of Wilczynski et. al., [46], considers that ICF processes mainly originate from peripheral interactions and are localized in the angular momentum space above the critical angular momentum (ℓ_{crit}) for the CF. Apart from the above mentioned dynamical models, Morgenstern et. al., [29, 53] investigated the mass asymmetry dependence of the ICF contribution. The peripheral nature of ICF reaction dynamics has also been emphasized by Trautmann et. al., [54], and Inamura et. al., [55, 56]. The BUF-model of Udagawa and Tamura [45], is based on the Distorted Wave Born Approximation (DWBA) formalism for elastic break-up, where the projectile is supposed to break-up into its constituent α-clusters (e.g., ^{16}O may break-up into $^{12}C + \alpha$ and/or $^{8}Be + {}^{8}Be$) as it approaches the nuclear field of target nucleus. One of the fragments of the projectile is assumed to fuse with target nucleus to form an in-completely fused composite system and un-fused fragment continues to move un-deflected or slightly deflected in the forward cone with almost projectile velocity. However, in PEP's model [47], the particles are assumed to be transferred from the projectile to the target nucleus and get accelerated in the nuclear field of target nucleus and hence, acquire extra velocity to escape from the surface of composite system before the establishment of thermodynamical equilibrium. Moreover, the leading particle model of Natowitz et. al., [57], Hybrid model of Blann [11], Fermi-jet model [47, 58, 59], and Moving Source model [60] have also been proposed and seem to explain some of the experimental data related to ICF at relatively higher projectile energies. It may, however, be pointed out that these models predict the magnitude of ICF, to some extent, at energies $\geq$10 MeV/nucleon, but none of these models/theories is able to successfully explain the ICF data at energies $\approx$4 –7 MeV/nucleon. Despite the existence of so many models, a clear picture of the mechanism of ICF is yet to emerge, particularly at relatively low bombarding energies, i.e., below 7 MeV/nucleon, where the systematic studies are available only for a few projectile-target combinations. As such, the study of ICF is still an active area of investigation.

In order to explore some of the important issues, related to the CF and ICF reactions at energies near and above the Coulomb barrier, several experiments have been performed at the Inter-University Accelerator Center (IUAC), New Delhi, India. The measurements of excitation functions

[31, 39, 61], which give an indication of ICF processes below 7 MeV/nucleon; forward recoil range distributions [62], which is considered to be one of the direct proofs of ICF processes, indicating fusion incompleteness associated with fractional degree of linear momentum transfer (LMT) and angular distribution of residues [61] have been carried out.

The present chapter introduces the field of nuclear reactions in general, and heavy ion physics in particular. Some relevant terminology and a brief summary of the literature is also given. Consequently, the rest of the thesis is organized as follows; the Chapter II, focuses on the experimental procedure adopted to carry out different experiments at the Inter University Accelerator Centre, New Delhi, India. In Chapter III, various theoretical models that may be used to analyze the experimental results are discussed, while in Chapter IV details of measurements are presented. Chapter V gives the details of the data analysis in the form of results and discussion. Summary and the conclusions drawn from the present work are given at the end. The references are given at the end of each Chapter.

References

[1] A. H. Becquerel; Comp. Rend., 122, 450 (1896).
[2] J. J. Thomson; Phil. Mag., 44, 293 (1897).
[3] E. Rutherford; Phil. Mag., 21, 669 (1911).
[4] E. Rutherford; Phil. Mag., 37, 537 (1919).
[5] E. Rutherford; Phil. Mag., 37, 581 (1919).
[6] R. D. Herzberg, P. T. Greenlees, P. A. Butler, G. D. Jones and M. Venhart; Nature, 442, 896 (2006).
[7] P. E. Hodgson; Introductory Nuclear Physics, Chapter 23, Clarendon Press, Oxford (1997).
[8] N. Bohr; Nature 137, 344 (1936).
[9] S. N. Ghoshal; Phy. Rev. 80, 939 (1950).
[10] M. Blann; Phys. Lett. 27, 337 (1971).
[11] M. Blann; Phys. Rev. C31, 1245 (1985).
[12] P.E. Hodgson; Nuclear Heavy-Ion Reactions, Chapter 1, Clarendon Press, Oxford (1978).
[13] M. Cavinato, E. Fabrici, E. Gadioli, E. Gadioli Erba, P. Vergani, M. Crippa, G. Colombo, I. Redaelli, and M. Ripamonti; Phys. Rev. C 52, 2577 (1995).
[14] P. Vergani, E. Gadioli, E. Vaciago, E. Fabrici, E. Gadioli Erba, M. Galmarini, G. Ciavola and C. Marchetta; Phys. Rev. C 48, 1815 (1993).
[15] F. Schussler et. al.; Nucl. Phys. A584, 704 (1995).
[16] E. Gadioli et, al.; Nucl. Phys. A641, 271 (1998).
[17] Pushpendra P. Singh, Manoj Kumar Sharma, Unnati, Devendra P. Singh, Rakesh Kumar, K. S. Golda, B. P. Singh and R. Prasad; Phys. Rev. C 77, 014607 (2008).
[18] Pushpendra P. Singh, B. P. Singh, Manoj Kumar Sharma, Unnati, Devendra P. Singh, R. Prasad, Rakesh Kumar and K. S. Golda; Eur. Phys. J. A 34, 29 (2007).
[19] R. H. Siemsen et. al.; Nucl. Phys. A400, 245c (1983).
[20] D. J. Parker, J. Asher, T. W. Conlon and I. Naqib; Phys. Rev. C 30, 143 (1984).
[21] Ch. Ngo; Prog. Part. Nucl. Phys. 16, 139 (1985).
[22] D. R. Zolnowski et. al.; Phys. Rev. Lett. 41, 92 (1978).
[23] J. Wilczynski, K. Siwek-Wilczynska, J.; Nucl. Phys. A373, 109 (1982).
[24] A. C. Berriman, D. J. Hinde, M. Das Gupta, C. R. Morton, R. D. Butt & J. O. Newton; Nature, 413, 144 (2001).

[25] S. Chakrabarty, et. al.; Nucl. Phys. A678, 355 (2000).
[26] D.J. Parker, P. Vergani, E. Gadioli, J.J. Hogan, F. Vettore, E. Gadioli Erba, E. Fabrici and M. Galmarini; Phys. Rev. C44, 1528 (1991).
[27] H. Morgenstern, W. Bohne, W. Galster, K. Grabisch, and A. Kyanowski; Phys Rev. Lett. 52, 1104 (1984).
[28] H. Morgenstern, W. Bohne, K. Grabisch, H. Lehr, W. Stoeffler; Z. Phys. A313. 39 (1983).
[29] H. Morgenstern et. al.; Phys. Lett. B113, 463 (1982).
[30] Pushpendra P. Singh, B. P. Singh, M. K. Sharma, Unnati Gupta, Rakesh Kumar D. P. Singh, R. P. Singh, S. Murlithar, M. A. Ansari, R. Prasad and R. K. Bhowmik; Physics Letters B 671, 20 (2009).
[31] Devendra P. Singh, Unnati, Pushpendra P. Singh, Abhishek Yadav, Manoj Kumar Sharma, B. P. Singh, K. S. Golda, Rakesh Kumar, A. K. Sinha and R. Prasad; Phys. Rev. C 80, 014601 (2009).
[32] R. Kaufmann and R. Wolfgang; Phys. Rev. 121, 206 (1961).
[33] H. C. Britt and A. R. Quinton; Phys. Rev. 124, 877 (1961).
[34] J. Galin, B. Gatty, D. Guerreau, C. Rousset, U. C. Schlotthauer-Voos, and X. Tarrago; Phys. Rev. C9, 1126 (1974).
[35] Manoj Kumar Sharma, B. P. Singh, Sunita Gupta, M. M. Musthafa, H. D. Bhardwaj, R. Prasad and A. K. Sinha; J. Phys. Soc. Jpn. 72, 1917 (2003).
[36] Manoj Kumar Sharma, Unnati, B.K. Sharma, B.P. Singh, H.D. Bhardwaj, Rakesh Kumar, K. S. Golda and R. Prasad; Phys. Rev. C70, 044606 (2004).
[37] Manoj Kumar Sharma, Unnati, B.P. Singh, Rakesh Kumar, K.S. Golda, H.D. Bhardwaj, R. Prasad; Nucl. Phys. A776, 83 (2006).
[38] Sunita Gupta, B. P. Singh, M. M. Muthafa, H. D. Bhardwaj and R. Prasad; Phys. Rev. C61, 064613 (2000).
[39] Unnati Gupta, Pushpendra P. Singh, Devendra P. Singh, Manoj Kumar Sharma, Abhishek Yadav, Rakesh Kumar, B.P. Singh and R. Prasad; Nucl. Phys A811, 77(2008). References therein.
[40] Pushpendra P. Singh, B. P. Singh, Manoj Kumar Sharma, Unnati, R. Kumar, K S. Golda, D. Singh, R. P. Singh, S. Muralithar, M. A. Ansari, R. Prasad, and R. K. Bhowmik; Phys. Rev. C 78, 017602 (2008).
[41] I. Tserruya, V. Steiner, Z. Fraenkel and P. Jacobs; Phys. Rev. Lett. 60, 14 (1988).
[42] S. M. Mullins, A. P. Byrne, G. D. Dracoulis, T. R. McGoram, and W. A. Seale; Phys. Rev. C 58, 831 (1998).
[43] S. M. Mullins, G. D. Dracoulis, A. P. Byrne, T. R. McGoram, S. Bayer, R. A.

Bark, R. T. Newman, W. A. Seale, and F. G. Kondev; Phys. Rev. C 61, 044315 (2000).
[44] G. J. Lane, G. D. Dracoulis, A. P. Byrne, A. R. Poletti and T. R. McGoram; Phys. Rev. C 60, 067301 (1999).
[45] T. Udagawa and T. Tamura; Phys. Rev. Lett. 45, 1311 (1980).
[46] J. Wilczynski, K. Siwek-Wilczyńska, J. van Driel, S. Gonggrijp, D. C. J. M. Hageman, R. V. F. Janssens, J. Łukasiak and R. H. Siemssen; Phys. Rev. Lett. 45, No. 8, 606 (1980).
[47] J. P. Bondrof et al., Nucl. Phys. A333, 285 (1980).
[48] R. Weiner et al., Nucl. Phys. A286, 282 (1977).
[49] V. I. Zagrebaev; Ann. Phys. (NY) 197, 33 (1990).
[50] B. G. Harvey; Nucl. Phys. A444, 498 (1985).
[51] M. H. Simbel and A. Y. Abdul Magd; Z. Phys. A 294, 277 (1980).
[52] A. Y. Abdul Magd; Z. Phys. A 298, 143 (1980).
[53] H. Morgenstern, W. Bohne, W. Galster and K. Grabisch; Z. Phys. A 324, 443 (1986).
[54] W. Trautmann, Ole Hansen, H. Tricoire, W. Hering, R. Ritzka and W. Trombik; Phys. Rev. Lett., 53, 1630 (1984).
[55] T. Inamura et. al.; Phys. Lett., B 84, 71 (1982).
[56] T. Inamura, A. C. Kahler, D. R. Zolnowski, U. Garg, T. T. Sugihara and M. Wakai; Phys. Rev. C 32, 1539 (1985).
[57] J. B. Natowitz, S. Leray, R. Lucas, C. Ngo, E. Tomasi and C. Volant; Z Phys., A 325, 467 (1986).
[58] D. H. E. Gross and J. Wilczynski; Phys. Lett. B67, 1 (1977).
[59] H. Tricoire, et al., Z. Phys. A312, 221 (1983).
[60] T. C. Awes, G. Poggi, C. K. Gelbke, B. B. Back, B. G. Glagola, H. Breuer and V. E. Viola, Jr.; Phys. Rev. C24, 89 (1981).
[61] Manoj Kumar Sharma, Unnati, Devendra P. Singh, Pushpendra P. Singh, B. P. Singh, H. D. Bhardwaj and R. Prasad; Phys. Rev. C75, 064608(2007).
[62] Devendra P. Singh, Unnati, Pushpendra P. Singh, Abhishek Yadav, M. K. Sharma, B. P. Singh, K. S. Golda, Rakesh Kumar, A. K. Sinha and R. Prasad; Phys. Rev. C, Communicated, (2009). References therein.

Chapter II

THE EXPERIMENTAL TECHNIQUE

The experiments reported in this thesis have been carried out using the 15UD Pelletron accelerator [1, 2] of the Inter University Accelerator Centre (IUAC), New Delhi, India. Brief details of Pelletron accelerator at IUAC are presented in section 2.1. The details of the sample preparation for the measurement of excitation functions (EFs), forward recoil range distributions (FRRDs) and angular distributions (ADs) of reaction residues are presented in section 2.2. The activation technique used for the measurement of EFs, FRRDs and ADs is presented in the next section 2.3. The method of the irradiation of the samples is presented in section 2.4, while the post irradiation analysis including the calibration and efficiency determination of high purity Germanium spectrometer, discussion on the detection of residues, determination of production cross-section and finally the estimation of errors in the measurements are discussed in section 2.5.

2.1 PELLETRON ACCELERATOR AT IUAC

A particle accelerator is one of the most versatile instruments, used to study the nature of the matter and energy. The IUAC Pelletron is a 15UD, tandem electrostatic accelerator and is capable to accelerate any ion (independent of its mass and charge state) from proton to Uranium in the energy region from a few tens of MeV to a few hundred MeV, depending on the ion species. The installation of the accelerator is in a vertical configuration in a huge stainless steel tank of 26.5 meter in height and 5.5 meter in diameter. The tank is filled with a high di-electric constant gas SF_6 at ≈7-8 atmospheric pressure to insulate the high voltage terminal from the tank wall or to prevent the breakdown of high voltage. In the middle of the tank there is a high voltage terminal, which can hold potential from 4 to 16 million volts (MV). Since, 16 MV is quite high a potential, special technique of charging the terminal is adopted using the pelletron charging chain.

The basic principle of acceleration of charged particles with this accelerator is similar to that of Van de Graaff generator, except a novel feature that it uses the accelerating voltage twice and hence the name tandem accelerator. Once the terminal is charged to a high voltage, it may be used for accelerating any ion beam. A typical layout of Pelletron setup is shown in Fig. 2.1. By attaching an extra electron to the neutral atoms, negative

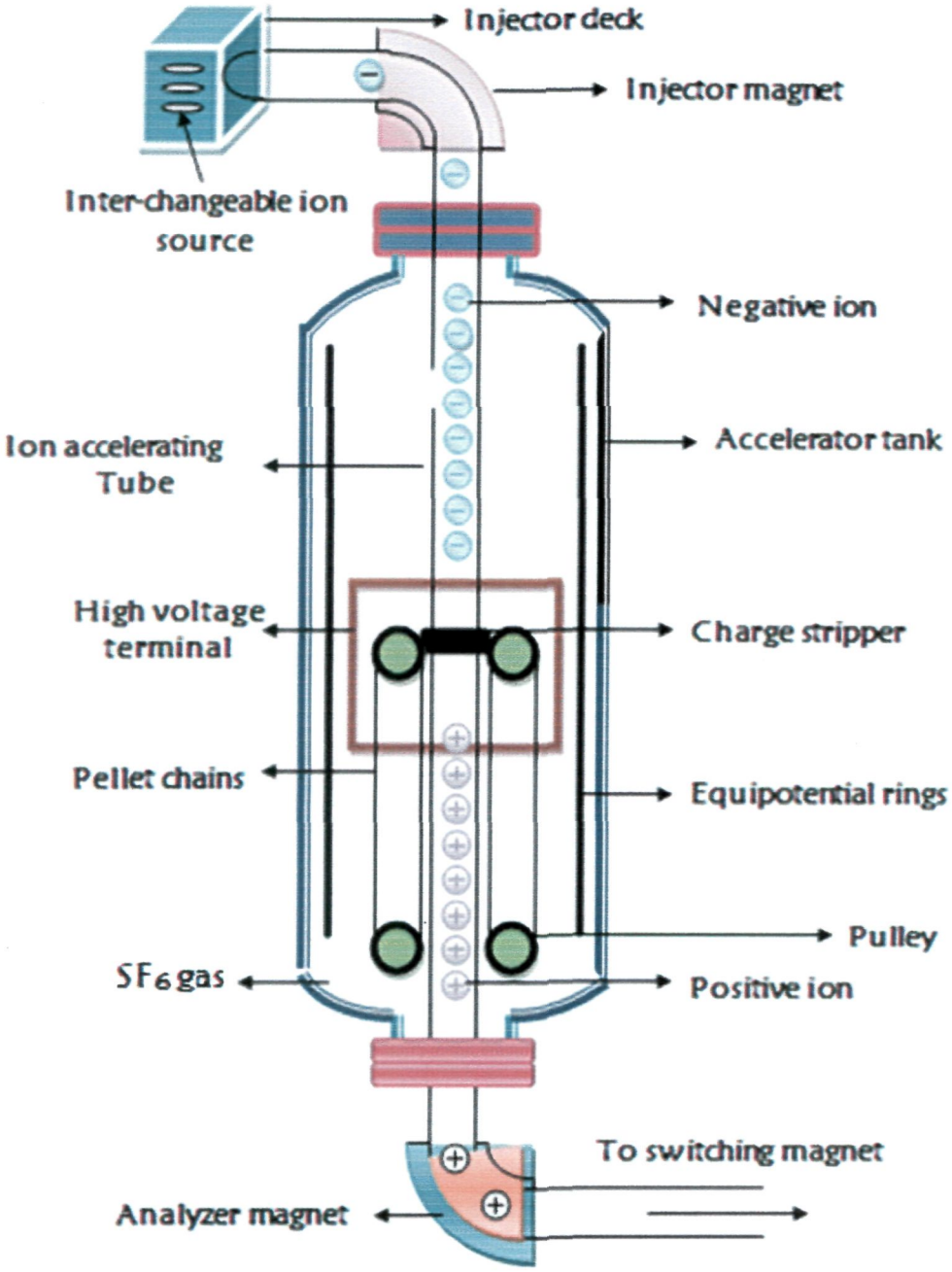

Figure 2.1: A schematic diagram of IUAC Pelletron Accelerator.

ions are produced in the ion source. The negative ions are injected at ground potential to the accelerator with the help of injector magnet and the beam is accelerated towards the terminal at high positive potential, increasing its energy to eV_t (where, V_t is the terminal potential in MV). At the terminal, these ions pass either through a thin foil or some gas used as stripper, which strips-off at least few electrons from each negative ion, thereby, converting them to positive ions. Since, the terminal is at high positive potential, the positive ions are now repelled and then accelerated below the terminal to ground potential. If the charge state of positive ion after passing through the stripper at the terminal is q, then the energy gained in the acceleration below the terminal to the ground potential is qV_t. Therefore, after passing through the two stages of acceleration the final energy of the ion beam is given by,

$$E_{final} = E_0 + (q+1)V_t \qquad (2.1)$$

where, E_0 is the energy of the ion before acceleration by terminal voltage V_t and q is the charge state of ion after stripping. Since, $E_0 << E_{final}$, it may be neglected. As such, the above equation may be written as;

$$E_{final} = (q+1)V_t \quad MeV \qquad (2.2)$$

2.2 SAMPLE PREPARATION

Samples for the measurements for different systems viz., $^{16}O+^{181}Ta$, $^{16}O+^{103}Rh$ and $^{16}O+^{27}Al$ have been prepared by different techniques. A brief description of the sample preparation for EF, FRRD and AD measurements are given in the following sub-sections.

2.2.1 Measurement of Excitation Functions

For the excitation function (EF) measurements, the targets of isotopically pure ^{181}Ta (≈99.99%), ^{103}Rh (≈100%) and ^{27}Al (≈99.99%) were prepared at the target laboratory of IUAC, New Delhi, using the rolling technique. To trap the recoiling products produced via different reaction processes, Al-catchers of appropriate thicknesses were also prepared by rolling. The Al-

backing of targets served both as energy degrader as well as catchers for the residues recoiling out of the target foil during the irradiations.

In case of ^{16}O + ^{181}Ta system, three stacks of samples containing four foils, three foils and one foil respectively were arranged. All the samples of Ta and Al-foils (used to trap recoiling reaction products) were prepared by the rolling technique. In the first stack, the thicknesses of four Ta samples were ≈1.25, 1.43, 1.42 and 1.22 mg/cm^2 while the thicknesses of corresponding Al-catchers were ≈1.16, 1.76, 2.01 and 1.24 mg/cm^2 respectively. In the second stack, the thicknesses of three Ta samples were ≈1.28, 2.03 and 1.76 mg/cm^2 while the thicknesses of corresponding Al-catchers were ≈1.81, 1.65, and 1.47 mg/cm^2 respectively. However, in the third one containing single foil, the thickness of Ta sample was ≈1.22 mg/cm^2 while the thickness of corresponding Al-catcher was ≈1.29 mg/cm^2.

In case of ^{16}O + ^{103}Rh system, two stacks each containing three samples of Rh and Al-foils sandwiched between them were used. All the samples of Rh and Al-foils were prepared by the rolling technique. The thicknesses of Rh samples used in the first stack were ≈2.41, 2.53 and 2.68 mg/cm^2, while the thicknesses of corresponding Al-foils were ≈1.83, 1.65 and 1.83 mg/cm^2. Further, in the second stack the thicknesses of three Rh samples were ≈2.49, 2.76 and 2.97 mg/cm^2, while, the thicknesses of Al-foils (catchers) used for energy degradation in this stack were ≈1.83, 1.83 and 1.04 mg/cm^2, respectively.

For the study of the system ^{16}O + ^{27}Al, four stacks were made for irradiations. In the first and second stacks, there were five Al-foil samples (of thickness ≈1.5 mg/cm^2) and Tm degraders (of thickness ≈0.6 mg/cm^2). In the other two stacks, there were five/four Al-samples (of thickness ≈2 mg/cm^2) and degraders of Tb (of thickness ≈1.8 mg/cm^2).

2.2.2 Measurement of Forward Recoil Range Distributions

In the present work, forward recoil range distributions (FRRDs) of several residues in ^{16}O+^{181}Ta system have been measured. For these measurements, isotopically pure samples of ^{181}Ta (abundance ≈99.99%) of thickness ≈150 μg/cm^2 were deposited by the electro-deposition technique on Al-backing

of thickness ≈1.1-1.5 mg/cm^2 prepared by rolling technique. The thin Al-catcher foils required for trapping the recoiling heavy residues produced via different processes were prepared by vacuum evaporation technique. Stacks of a number of thin Al-catcher foils with the total thickness (≈600 μg/cm^2), sufficient to stop most energetic residues, were placed just after the target. The heavy (slow) residues populated via CF and/or ICF processes in the target could be trapped at various thicknesses in the catcher foil stack.

2.2.3 Measurement of Angular Distributions

For the measurements of angular distribution of recoiling residues produced in ^{16}O + ^{27}Al system, an Al-target supported by Tm material of thickness ≈0.48 mg/cm^2 followed by a stack of thick annular concentric Al-catcher foils of thickness ≈0.3 mm was prepared. Here, the thick concentric annular Al-catchers of diameters 0.81, 1.29, 1.95, 2.64, 3.27, 5.46 and 6.4 cm were used to trap the recoiling nuclei emitted at different angles.

Since, a precise knowledge of the target thickness is crucial in the absolute cross-section measurements of different reaction products, therefore, the measurement of target thickness must be as accurate as possible. The thicknesses of each target and catcher foil, used for the EF, FRRD and AD measurements in all the above mentioned systems, were separately measured by the α-transmission method. The α-transmission method is based on the measurement of the energy lost by 5.487 MeV α-particles (obtained from standard ^{241}Am source) while passing through the target material. The targets were cut into the size of 1.2×1.2 cm^2 and were pasted on Al-holders having concentric hole of 1.0 cm diameter. The Al-holders were used for rapid heat dissipation during the irradiations.

2.3 STACKED FOIL ACTIVATION TECHNIQUE

Stacked foil activation technique [3] has been used for the measurement of cross-sections. Activation technique is a non destructive method of measuring concentration of constituents in a given sample by measuring the characteristic radiations emitted by the radioactive nuclides resulting from selected nuclear transformations. Activation technique is one of the simplest and powerful methods for measuring the EFs and to deduce important information about the nuclear reaction dynamics. In this technique, a stack

of targets backed by suitable catcher/degrader foils is irradiated by an energetic beam. After the irradiation, the activities induced in the target-catcher foil assembly are recorded off-line for a considerably long time depending on the half-lives of reaction products of interest. Some of the important advantages of the activation technique are given below;

• When a sample is irradiated, several nuclear reactions may take place simultaneously. Many of these reactions leave radioactive nuclides. Each radioactive nuclide has its characteristic half-life and decay mode. The technique provides the possibility of measuring cross-sections for several reactions at different projectile energies in a single irradiation, hence the beam-time requirements may be minimized.

• Measurement of induced activity may be done after the irradiation. Therefore, there is no possibility of contamination from the beam background.

• With the availability of high resolution detectors, it is now possible to separate out the activities of different reaction products decaying by γ-rays of nearly same energies, accurately. As a result, errors in these measurements are expected to be quite low. Further, often a given radio-active residue emits gamma rays of more than one energy. By measuring the intensities of these radiations, cross-section for the production of the residue can be determined in a self consistent way.

The activation technique is quite simple and accurate but sometimes it becomes complicated due to the presence of radiations (γ-rays) of almost similar energies for more than one reaction products. In case of mixing of γ-rays due to different isotopes, the contribution from each isotope can be separated out by analyzing their decay curves. The unique half-life of each radioactive isotope provides a specific way for its identification and measurement. It may, however, be pointed out that this technique is limited only for the reaction products having measureable half-lives.

2.4 IRRADIATION

In the present work, irradiations have been carried out using $^{16}O^{7+}$ beam delivered from the 15UD-Pelletron Accelerator at the IUAC, New Delhi,

India. Irradiations were performed in the General Purpose Scattering Chamber (GPSC) of 1.5 m diameter. This big chamber was selected because it has an in-vacuum transfer facility (ITF) i.e., the samples may be changed in the GPSC without disturbing the vacuum inside the chamber. Using this facility, the time lapse between the stop of the irradiation and the counting of the samples may be considerably reduced and thus induced activities of short half-lives may be recorded. Typical photographs of GPSC and ITF are given in Figs. 2.2. The flux of the incident ions (^{16}O) was determined from the total charge collected in the Faraday cup, placed behind the target-catcher foil assembly. In an auxiliary experiment two silicon surface barrier detectors D_1 and D_2 (Rutherford monitors) were kept at 30^0 with respect to the direction of the beam at the forward angles, to record the scattered incident ions for flux determination. Flux of incident beam determined from the counts of Rutherford monitors and from the integrated counts of Faraday cup were found to agree with each other within 5%. The activities produced in the samples after irradiation were recorded using a pre-calibrated, High Purity Germanium (HPGe) detector of 100 c.c. active volume coupled to a PC through CAMAC based FREEDOM software. In the present work, the targets backed by Al-catchers were placed normal to the beam direction so that the recoiling nuclei coming out of the target may be trapped in the catcher foil and hence there is no loss of activity from the sample, giving rise to better accuracy in the measurements.

2.4.1 Measurement of Excitation Functions

In $^{16}O+^{181}Ta$ system, for the measurement of EFs, three stacks, with four foils, three foils and one foil respectively, were irradiated at ≈100, 98, and 88 MeV beam energies to cover a wide energy range. As the incident beam passes through the stack, it loses its energy both in the target material and in the catcher/degrader material. As such, successive targets of the stack get irradiated at different energies. The energies of the incident ion on successive targets have been calculated using stopping power values obtained from code SRIM [4] based on the range-energy formulations. In the first stack, containing four foils, the incident energy on each foil after energy loss has been estimated to be 99 ± 0.9, 93 ± 1.1, 85 ± 1.2 and 76 ± 1.1 MeV, respectively. Further, in the second stack, containing three foils of the Ta-sample, the beam energies were 97 ± 1.0, 88 ± 1.6 and 80 ± 1.5 MeV, respectively. Similarly, in the third irradiation of single foil the

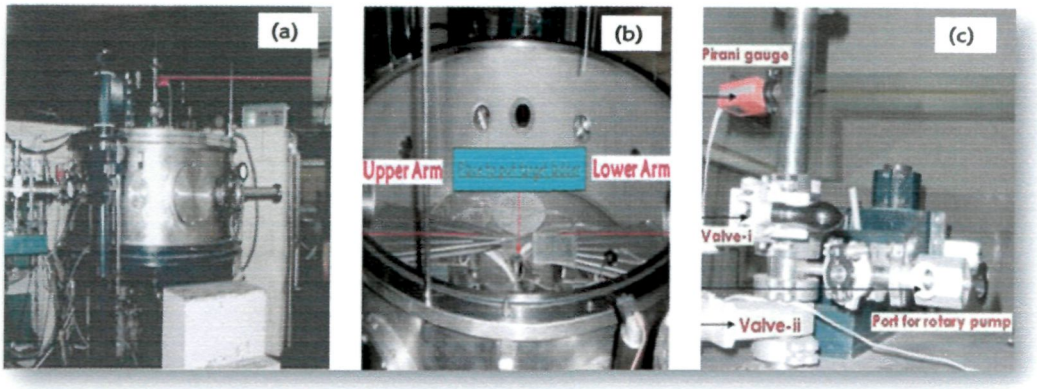

Figure 2.2: (a) The general purpose scattering chamber (GPSC), (b) its inside view and (c) typical arrangement of an in-vacuum transfer facility (ITF), used for in-vacuum transfer of irradiated samples.

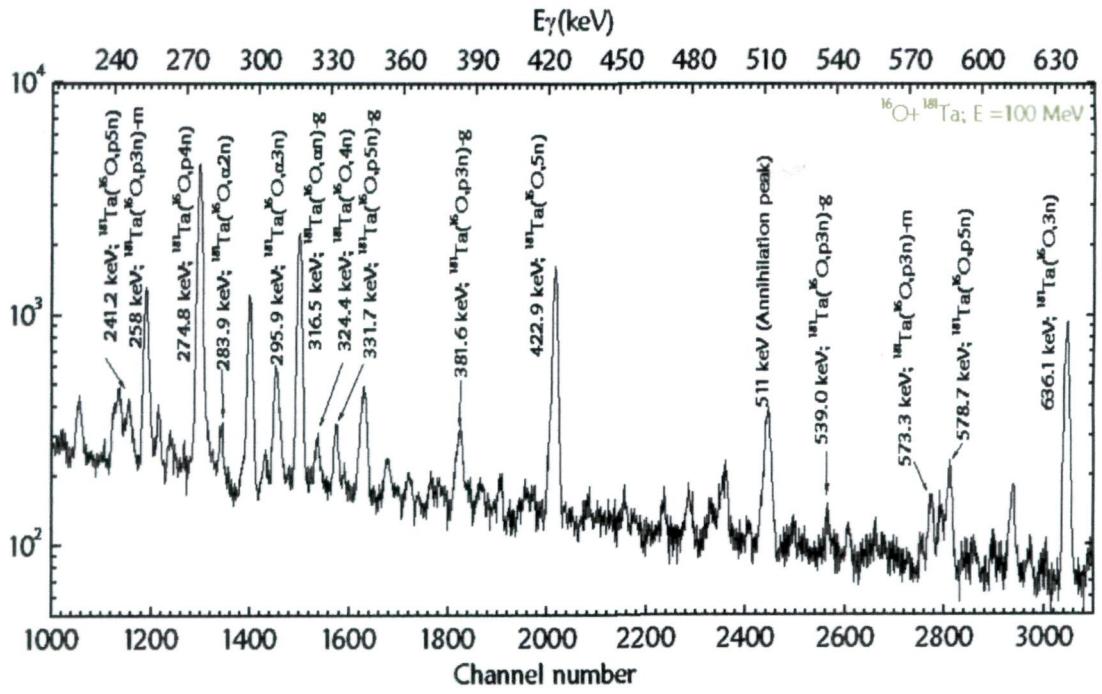

Figure 2.3: A typical γ-ray spectrum of $^{16}O+^{181}Ta$ system at ≈100 MeV.

incident energy was estimated to be 87 ± 1.0 MeV. As already mentioned, the stacks were placed normal to the beam direction, so that the recoiling products could be trapped in the catcher foil placed just behind the target and there would be no loss of activity. Keeping in view the half-lives of interest, irradiations were carried out for ≈8–10 hrs duration for each stack. The Pelletron crew provided a constant beam current ≈50 nA throughout the irradiations. A typical γ-ray spectrum for the $^{16}O+^{181}Ta$ system at ≈100 MeV is shown in Fig. 2.3, where various γ-peaks corresponding to different reaction products populated via different reaction modes are indicated. Further confirmation of the identification of reaction products has been made by the decay curve analysis. Identified evaporation residues along with their important spectroscopic properties are given in Chapter IV.

In case of $^{16}O+^{103}Rh$ system, two stacks containing three samples each were irradiated by ≈80 and 85 MeV $^{16}O^{7+}$ beam, respectively. The beam energy on each sample was calculated using the code SRIM [4]. In first stack, the incident energies on successive Rh samples were 77.38 ± 2.61, 65.44 ± 2.98 and 52.61 ± 3.48 MeV respectively. Further, in the second irradiation the incident energies on Rh samples were estimated to be 82.38 ± 2.63, 70.51 ± 3.13 and 56.90 ± 3.72 MeV respectively. Irradiations for each of the ^{103}Rh stacks were carried out for ≈4 hrs. The residual nuclei trapped in the samples and Al-catcher foils were counted together.

In case of $^{16}O+^{27}Al$ system, two stacks containing five alternate samples each of natural Tm and Al and another two stacks containing five and four alternate samples of natural Tb and Al, respectively, were used for the EF studies. The samples of Tm and Tb served as energy degraders. Four stacks containing in all nineteen ^{27}Al samples and an equal number of energy degraders were irradiated by the $^{16}O^{7+}$ beam at four different energies, i.e., 86, 88, 92, and 95 MeV. The irradiation of these stacks covered the desired energy range ≈58 to 95 MeV. The irradiation of each stack was carried out for ≈8 hrs duration. The beam currents were ≈50 nA. The activities induced in the various samples were recorded by counting the Al-samples as well as the degrader/catcher foils using a HPGe γ-ray spectrometer. The off-line γ-ray spectroscopy was employed to determine the cross-sections for various reaction residues.

2.4.2 Measurement of Forward Recoil Range Distributions

The forward recoil range distributions (FRRDs) for several residues have been measured at 81, 90 and 96 MeV energies in the system $^{16}O+^{181}Ta$. For these measurements, stacks of thin Al-catcher foils (with the total thickness sufficient to stop most energetic residues formed via full linear momentum transfer) have been prepared. The catcher stack stops heavy residues, produced by various reactions in target, at different distances (thicknesses) depending on their energies. As already mentioned, both the targets and the catchers were prepared by vacuum evaporation technique. The thin ($\approx$ 150 $\mu g/cm^2$) target of ^{181}Ta has been mounted in such a way that the Al-backing first faces the beam so that the recoiling nuclei, even of very short range, will not get stopped in the target backing thickness itself. A typical arrangement of target and stack of catcher foils for the FRRD measurements is shown in Fig. 2.4.

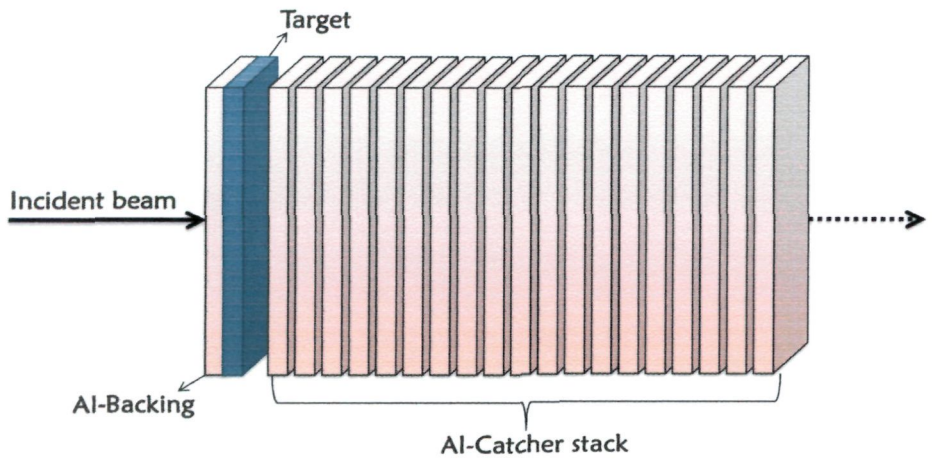

Figure 2.4: A typical stack arrangement for the forward recoil range distribution measurements.

The $^{16}O^{7+}$ beam energies in three separate irradiations for FRRD measurements were 85, 94 & 100 MeV. After an energy loss of $\approx$3.7, 3.9 & 3.5 MeV in the target backing ($\approx$1.06, 1.2 and 1.13 mg/cm^2, respectively), the incident energies on the targets are estimated to be respectively $\approx$81.3,

≈90.1 & ≈96.5 MeV. The irradiations have been carried out for the duration of ≈12 hrs each, with a beam current ≈50 nA. The residues populated via CF and/or ICF processes are supposed to be trapped at different catcher foil thicknesses, depending on the recoil velocity and/or the degree of LMT of the projectile associated with the mode of residue formation. The γ-ray spectra of each catcher foil were recorded at increasing times for the identification of the residues. A list of the radionuclides populated in $^{16}O+^{181}Ta$ system, energies of identified γ-rays alongwith their branching ratios are given in Chapter IV. The activities induced in each thin catcher foil were followed off-line using a pre-calibrated high resolution (≈2 keV for 1.33 MeV γ-ray of ^{60}Co) HPGe detector of 100 c.c. active volume of CANBERRA coupled to CAMAC based software FREEDOM [6] at the IUAC, New Delhi. The Al-catcher thicknesses used in the present experiment for the FRRD measurements at ≈81, 90 and 96 MeV are given in Table 2.1.

2.4.3 Measurement of Angular distributions

A separate experiment has been carried out to measure the angular distribution of recoiling residues in the system $^{16}O+^{27}Al$ at ≈85 MeV beam energy. In this experiment, Al-target supported by Tm material of thickness ≈0.48 mg/cm^2 followed by several thick annular concentric Al-catchers was prepared. The target was mounted normal to the beam direction in the irradiation chamber. Concentric annular Al-catchers of thickness ≈0.3 mm with diameters 0.81, 1.29, 1.95, 2.64, 3.27, 5.46 and 6.4 cm were used to trap the recoiling nuclei emitted at different angles. A typical arrangement of the target and catcher assembly used for the angular distribution measurements is shown in Fig. 2.5. The arrangement of annular catchers was placed 1.8 cm behind the target for collecting the residues emitted in seven different angular ranges, viz., 0°–13° (most forward cone), 13°–21°, 21°–30°, 30°–39°, 39°–45°, 45°–60°, and 60°–64°. The irradiation was carried out for about 11 hrs with a beam current of ≈50 nA. The activities induced in each annular catcher foil were followed off-line for a couple of days. Typical γ-ray spectra indicating the region of interest for different annular Al catcher rings covering the angular range from 0°–13° to 45°–60° is shown in Fig. 2.6.

Table 2.1: A list of Al-catcher thicknesses used for the RRD measurements.

S. No.	Thickness ($\mu g/cm^2$) for the irradiation at ≈85 MeV	Thickness ($\mu g/cm^2$) for the irradiation at ≈94 MeV	Thickness ($\mu g/cm^2$) for the irradiation at ≈100 MeV
1	9.96	23.33	10.01
2	15.19	23.52	16.17
3	30.86	23.78	18.17
4	30.94	23.89	18.32
5	31.05	24.35	19.00
6	31.15	25.06	19.29
7	32.05	25.35	19.90
8	32.05	26.56	21.59
9	32.09	29.08	23.33
10	32.27	29.08	40.16
11	32.31	29.40	40.17
12	33.21	35.45	40.56
13	33.50	36.07	50.70
14	33.53	36.35	50.73
15	33.53	54.04	50.89
16	33.55	54.74	51.68
17	33.59	54.94	56.77
18	41.47	55.02	64.40

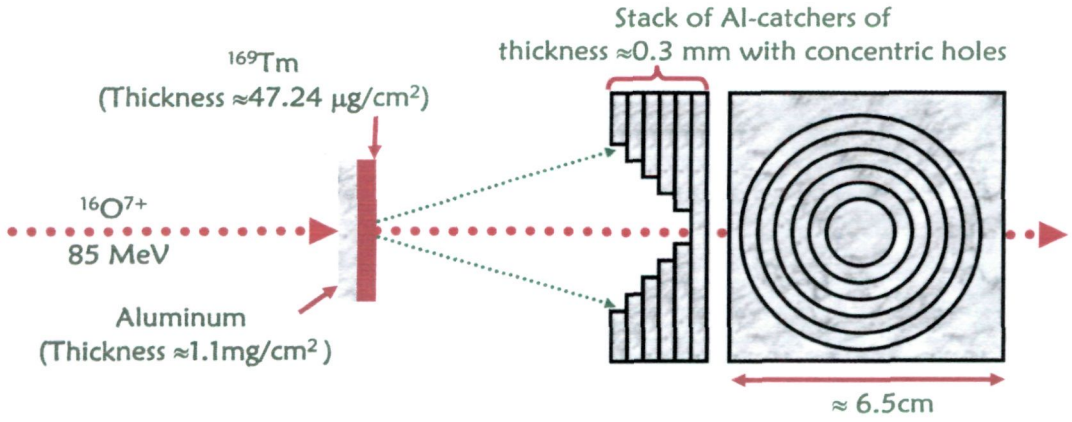

Figure 2.5: Typical arrangement of target-catcher assembly used for the angular distribution measurements covering the annular range from 0^0-13^0 to 45^0-60^0.

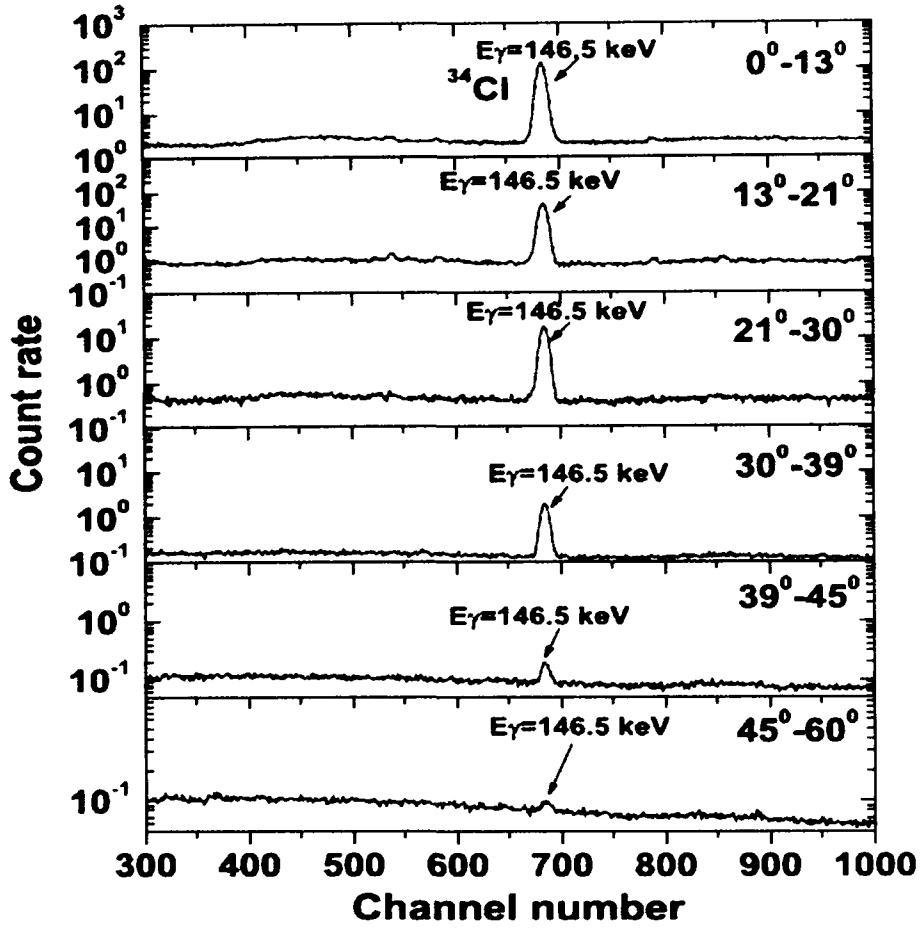

Figure 2.6: Typical γ-ray spectra of Al-catcher rings covering the annular range from 0°-13° to 45°-60°.

The peak in the observed γ-ray spectrum was assigned to the reaction residue on the basis of its characteristic γ-lines as well as measured half-life using decay curve analysis. Further, the intensities of the characteristic γ-rays were used to compute the reaction cross-sections at different angular ranges, using standard formula (equation 2.12) given in section 2.5.3, of this chapter. The efficiency of the detector was obtained for a point source. However, the annular catchers used for trapping the reaction residues had

a finite area, therefore, proper correction [7] was applied to deduce the cross-sections for the residues of interest.

2.5 POST IRRADIATION ANALYSIS

In order to identify the characteristic γ-rays of evaporation residues in the complex γ-ray spectra, a detector of good resolution and proper calibration is required. The post irradiation analysis has been carried out using γ-ray spectrometer with a HPGe Detector.

2.5.1 Calibration and Efficiency Determination of HPGe Detector

The HPGe detector was pre-calibrated both for energy as well as efficiency by using various standard γ-sources i.e., ^{22}Na, ^{60}Co, ^{133}Ba, ^{137}Cs and ^{152}Eu of known strengths. The prominent γ-rays of the standard ^{152}Eu source are given in Table 2.2, and have been used in the present measurements, both for energy calibration of the γ-ray spectrometer and for the determination of detector efficiency as a function of γ-ray energy.

Table 2.2: A list of γ-ray energies and absolute intensities of some of the prominent γ-rays from standard γ-source ^{152}Eu.

γ-ray energy (keV)	Absolute Intensity (%)
121.78	28.58
244.69	7.58
344.27	26.54
443.96	2.82
778.90	12.94
867.37	4.24
964.07	14.60
1089.73	1.72
1112.07	13.64
1212.94	1.42
1299.14	1.62
1408.00	21.00

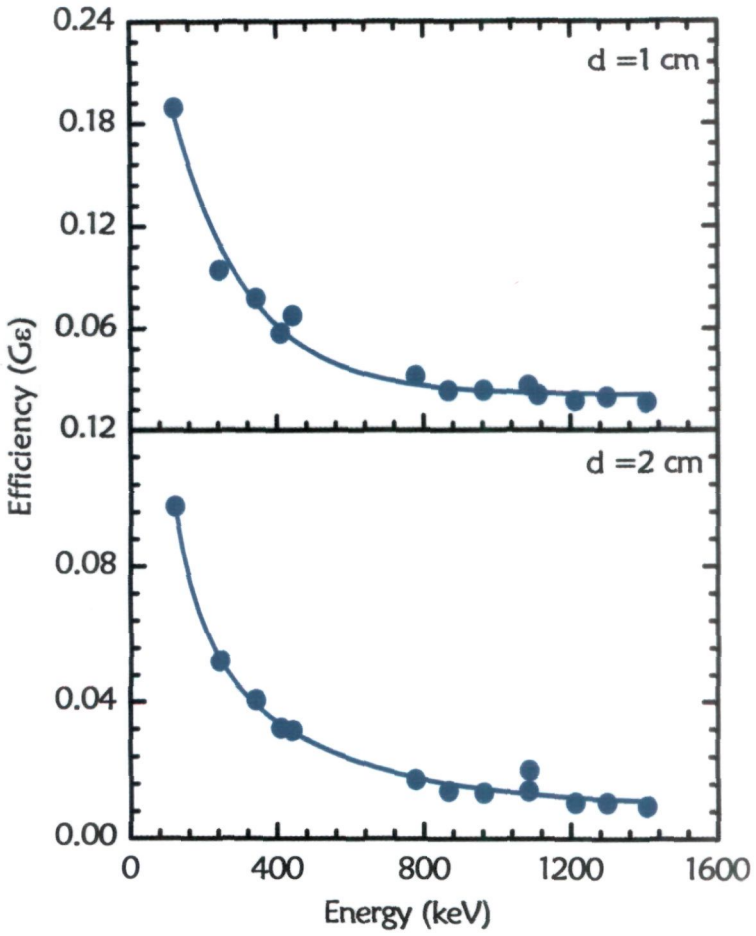

Figure 2.7: Geometry dependent efficiency curves as a function of γ-ray energy at source-detector separations (a) d=1 cm and (b) d=2 cm. Solid lines represent the best polynomial fit.

The geometry dependent efficiency (G_ε) of the HPGe detector at a given energy has been determined using the following expression;

$$G_\varepsilon = \frac{N_0}{N_{a0}\, e^{(-\lambda t)}\, \theta} \qquad (2.3)$$

where, N_o is the disintegration rate of the standard γ-source at the time of measurement, N_{ao} is the disintegration rate at the time of manufacture of the source, λ is the decay constant, t is the time lapse between the manufacture of the source and the start of the time of counting, and θ is the branching ratio of the characteristic γ-ray.

In order to keep the geometry dependent detector efficiency same for standard γ-sources and samples/catchers, the standard γ-sources and the irradiated sample foils were counted in the same geometry. However, the source-detector separations for various irradiated samples were kept different, depending on the intensity of the induced activities, in order to keep the dead time of counting less than 10%. Typical geometry dependent efficiency as a function of γ-rays energy and for two different source-detector separations (1 cm and 2 cm) are shown in Fig. 2.7.

Further, the geometry dependent efficiency curves are found to be best fitted with a 5th order polynomial function of the type;

$$G_\varepsilon = a_0 + a_1 E + a_2 E^2 + a_3 E^3 + a_4 E^4 + a_5 E^5 \qquad (2.4)$$

where, E is the energy of the γ-ray and a_0, a_1, a_2, a_3, a_4 and a_5 are the coefficients having different values for each source-detector separation.

2.5.2 Identification of Reaction Products

Once the irradiation has been completed, the stacks of targets alongwith catcher foils were taken out of the GPSC with the help of ITF. The intensities of identified γ-peaks were recorded at increasing times to get their decay curves. The analysis of decay curves give the half-lives of the residues and thus confirmed their identification. This is a very specific way for the identification of reaction products because each radioactive isotope has a unique decay mode. As a representative case, a typical decay curve of ^{193g}Tl ($T_{1/2}$ =21.6 m) identified by 324.4 keV γ-ray is shown in Fig. 2.8. List of reaction products identified are given in Tables 4.2, 4.6 and 4.9 in Chapter IV, alongwith their spectroscopic properties which have been taken from the Table of Isotopes [8].

Chapter IV, alongwith their spectroscopic properties which have been taken from the Table of Isotopes [8].

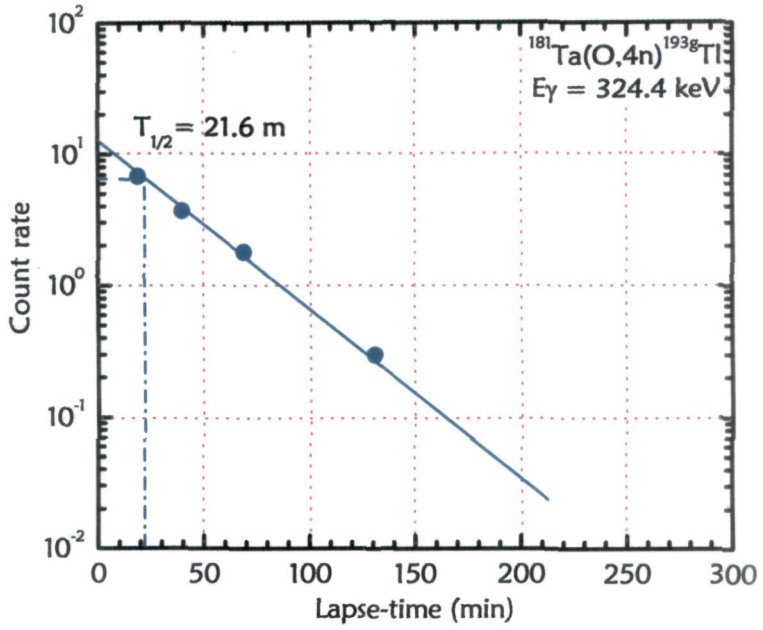

Figure 2.8: Experimentally observed decay curve; the count-rates have been plotted on semi-log graph as a function of lapse time, which indicates the half-life of corresponding residue produced in ^{16}O + ^{181}Ta system.

2.5.3 Determination of the nuclear reaction production cross-section

The production cross-section $\sigma_{X(a,b)}(E)$ is a measure of the probability of the formation of a particular reaction product. Experimentally, the cross-section for a reaction X(a, b)Y may be defined as the number of events of a given type X(a, b)Y per unit area per unit target nucleus per unit time. The cross-section is generally expressed in units of barn which is equal to 10^{-24} cm^2. As such, the reaction cross-section may be represented as;

$$\sigma_{X(a,b)}(E) = \frac{\text{Number of events } X(a,b)Y \text{ / area}}{N_0\ \phi t} \qquad (2.5)$$

where, N_o is the number of target nuclei in the sample, ϕ is the flux of incident beam and 't' is the time of irradiation of the samples.

In order to determine the production cross-section of a particular reaction product, the quantities given in the denominator of the above equation are known and the quantities in the numerator i.e., the number of events of a given type X(a,b)Y are required to be measured. The number of events of a given type may be obtained from (a) on-line measurements, by recording the outgoing particles directly using particle telescopes accommodated in the irradiation chamber, and/or by (b) off-line measurements, by following the activities induced in the irradiated samples, only in case the radio-active residues (Y) are of measurable half-lives. As has already been mentioned, the irradiation of a sample by a particle beam may initiate various reactions in it, and many isotopes are likely to be formed by the process of transmutation. The rate of formation (N) of a particular activation product may be given by the expression,

$$N = N_0 \phi \sigma_{X(a,b)} \tag{2.6}$$

where, ϕ is the flux of incident beam, N_0 is the initial number of nuclei in the sample, and $\sigma_{X(a,b)}$ is the reaction cross-section for that particular channel.

The disintegration rate of the induced activity in a sample after a time 't' from the stop of irradiation may be given as;

$$\left[\frac{dN}{dt}\right]_t = N\frac{[1-\exp(-\lambda t_1)]}{\exp(\lambda t)} \tag{2.7}$$

where, t_1 is the time of irradiation and λ is the decay constant of the induced activity given as;

$$\lambda = \frac{\ln 2}{t_{1/2}} \tag{2.8}$$

The factor [1- exp(-λt_1)] takes care of the decay of residues during the irradiation and is typically known as the saturation correction. The number of decays of the induced activity in a very small time 'dt' may be given as;

$$dN = N\frac{[1-\exp(-\lambda t_1)]}{\exp(\lambda t)}dt \qquad (2.9)$$

If the activity induced in the irradiated sample is recorded for time duration t_3 after a lapse time t_2, then the number of nuclei decayed in time between t_2 to (t_2+t_3) may be given as;

$$C = N\frac{[1-\exp(-\lambda t_1)][1-\exp(-\lambda t_3)]}{\lambda.\exp(\lambda t_2)} \qquad (2.10)$$

If the activity induced in the sample is recorded by a γ-ray spectrometer of efficiency G_ε, then absolute count rate 'C' and observed counting rate 'A' may be related as;

$$C = \frac{A}{\theta.K.G_\varepsilon} \qquad (2.11)$$

where, A is the total counts recorded during the accumulation time t_3 of the induced activity of decay constant λ, the term θ is the branching ratio of the characteristic γ-ray and $K=[\{1-\exp(-\mu d)\}/\mu d]$ is the self-absorption correction factor for the material of the sample of thickness d (gm/cm^2) and of absorption coefficient μ (cm^2/gm) and G_ε the geometry dependent efficiency of the detector.

Thus, $\sigma_{X(a,b)}$ can be written as,

$$\sigma_{X(a,b)}(E) = \frac{A.\lambda\exp(\lambda t_2)}{N_0.\phi.\theta.K.G_\varepsilon.[1-\exp(-\lambda t_1)][1-\exp(-\lambda t_3)]} \qquad (2.12)$$

Also, the count-rate at the time of stop of irradiation $C_{t=0}$ can be given as,

$$C_{t=o} = \frac{A\lambda \exp(\lambda t_2)}{[1-\exp(-\lambda t_3)]} \qquad (2.13)$$

The reaction cross-section $\sigma_{X(a,b)}$ may be written with the help of above equations as,

$$\sigma_r(E) = \frac{C_{t=0}}{N_0.\ \phi.\theta.K.G_\varepsilon.[1-\exp(-\lambda t_1)]} \qquad (2.14)$$

A FORTRAN program EXP-SIGMA based on the above formulations has been used for the determination of the reaction cross-sections of the reaction products.

2.5.4 Experimental Uncertainties; error analysis

Critical evaluation of uncertainties that are likely to introduce errors in the measured cross-sections reflects the quality of measurements. Some of the factors which may introduce errors in the present measurements are given in the following;

1. Non-uniform deposition of the target material and in-accurate estimate of the foil thickness may lead to uncertainty in the determination of the number of target nuclei in the sample. Though, it is hard to know the uncertainty in the target thickness, however, to check the uniformity of the sample, the thicknesses of the samples, prepared by evaporation technique, were measured at different locations of the same sample by the α-transmission method. It is estimated that the error in the target thickness is ≤1%.

2. During the irradiations, fluctuations in the beam current may result in the variation of the incident flux. Many tests were performed to check the time-integrated beam fluctuations and it was estimated that beam fluctuations may introduce errors of not more than 5% in the measured cross-sections.

3. Uncertainty in the determination of the geometry-dependent efficiency of the γ-ray spectrometer may give rise to error in the production cross-sections. The HPGe detector efficiency was measured before and very frequently during the experiment, using calibrated sources of ^{60}Co and ^{152}Eu. The efficiency curves were corrected for the acquisition system dead time. Statistical errors in counting of the standard sources may also give rise to errors in the efficiency, which were minimized by accumulating a large number of counts for comparatively larger times (≈ 5000 sec). Experimental data on the geometry-dependent efficiencies with γ-ray energy at a fixed source-detector separation has been fitted with a power law curve. The uncertainty due to the fitting of the efficiency curve is estimated to be less than 3%. The uncertainty in determining the efficiency may also appear due to the solid-angle effect, because the irradiated samples were not point sources like the standard source, but they had a diameter of ≈4 mm. It is estimated that the error in the efficiency due to the solid-angle effect is less than 5%.

4. The statistical errors in the evaluation of the γ-ray intensity and the background subtraction were different for different observed residues and were separately evaluated.

5. During the stack irradiation, the beam traverses the thickness of the material, thus the initial beam intensity may get reduced. It is found that the error due to the decrease in beam intensity is less than 2%.

6. Dead time of counting is likely to introduce errors in determining the count rates. In all the measurements, the dead time of the spectrometer was kept <10% by suitably adjusting the sample-detector distance and the corrections for it were applied to the counting rate.

7. The loss of the product nuclei recoiling out of the sample may introduce large errors in the measured cross-sections. In order to reduce it, the thickness of the catcher foils placed just behind the target in EF measurements was kept sufficient to stop even the most energetic residues. Moreover, in the present measurements both the

sample and the catcher foils were counted together and hence, the losses due to the recoiling of nuclei is further avoided.

Further, the uncertainties of the nuclear data like branching ratio, decay constant etc., which have been taken from the Table of Isotopes [8, 9] have not been taken into consideration. Considering all the possible sources of errors, the uncertainty in the absolute values of the cross-sections is estimated to be less than 15%, including statistical errors.

References

[1] G. K. Mehta and A. P. Patro; Nucl. Inst. and Meth. A268, 334 (1988).
[2] B. P. Ajithkumar et. al.; Nucl. Inst. and Meth. A343, 327 (1994).
[3] R. C. Kotch; Activation Analysis Handbook, Academic Press, New York and London, 1960.
[4] SRIM06; http://www.srim.org/
[5] L.C. Northcliffe and R.F. Schilling; At. Data Nucl. Data Tables A7, (1970) 264.
[6] FREEDOM; Data acquisition and analysis system designed to support the accelerator based experiments at the Inter University Accelerator Centre, New Delhi, India.
[7] R. P. Gardner and K. Verghese; Nucl. Inst. Methods 93, 163(1971).
[8] E. Browne and R.B. Firestone; Table of Radioactive Isotopes (Wiley, New York, 1986).
[9] Jagdish K. Tuli; Nuclear Wallet Cards, National Nuclear Data Center, Upton, New York, 2000.

Chapter III

COMPUTER CODES AND MODELS

In a compound nucleus reaction two nuclei fuse together to form an excited composite nucleus [1], which then decays either through particle and/or γ-ray emission or by the process of fission. Formation of the compound nucleus is inhibited primarily by the electrostatic repulsion between the collision partners. At energies above the Coulomb barrier, the analysis of a complex interaction such as the compound nucleus formation and its subsequent decay could be explained through the application of statistical theory. Various computer codes viz., PACE4 [2], CASCADE [3], ALICE91 [4] and SUMRULE [5] are available to perform such statistical model calculations. In the following sections, a brief description of these codes is presented.

3.1 PACE4

The statistical model code Projection-Angular-Momentum-Coupled-Evaporation (PACE4) [2] is derived from the original code called JULIAN. It uses a Monte-Carlo procedure to determine the decay sequence of an excited nucleus using the Hauser-Feshbach formalism. The main advantage of Monte-Carlo calculations is to provide correlations between various quantities, such as particles and gamma-rays, or angular distribution of particles. Sequential decays are considered until any further decay is prohibited due to the energy and angular momentum conservation laws. A random number selection determines the actual final state to which the nucleus decays to and the process is, then repeated for other cascades until all the nuclei reach the ground state. The transmission coefficients for light particle emission (n, p, α) are determined using optical model potentials [6, 7]. A fission decay mode is employed using a rotating liquid drop fission barrier routine [8]. The code also provides event by event trace back of the entire decay sequence from the compound nucleus into any one of the exit channels. The fusion cross-sections are obtained from the Bass model [9]. There are two default level density options that are essentially derived from the Fermi gas formalism and are identical to constant temperature formalism at low energies. These are i) the determination of the parameter 'a' and ii) 'a' is taken to be equal to A/K, where, A is the number of nucleons and K is constant factor. Independent of these options, rotational energy contribution $E_{rot}(J)$ can be selected in two ways viz., the spin cut-off parameter and the ground-state rotational energy of the finite-range rotating-drop model [10]. For values of A, Z or J beyond the range of

validity of Sierk's routine, the rotational energies are taken from the work of Cohen, Plasil and Swiatecki [11]. It has been observed that the code PACE4 is more accurate for high spins, close to the yrast line. The fission probability is calculated using the Bohr-Wheeler saddle point formalism [12]. The fission barriers are those of Sierk [10]. The code cannot be used for below barrier calculations. A special feature of the PACE4 code is its ability to provide information on energy and angular distributions of evaporated particles. This is obtained by tracking the distribution of projection through each cascade. The angular distribution of the emitted particles is determined at each stage of de-excitation. The code could be run with a large number of events (50,000) to obtain better statistics for the energy and angular distribution of residual nuclei.

The partial cross-section for CN formation at angular momentum (ℓ) and specific bombarding energy is given by,

$$\sigma_\ell = \frac{\pi\lambda^2}{4\pi^2}(2\ell+1)T_\ell \tag{3.1}$$

where, λ is the reduced wavelength and T_ℓ, the transmission coefficient given by,

$$T_\ell = [1+\exp(\ell-\ell_{max})/\delta]^{-1} \tag{3.2}$$

where, δ is the diffuseness parameter and ℓ_{max} is determined by the total fusion cross-section σ_F, since,

$$\sigma_F = \sum_{\ell=0}^{\infty}\sigma_\ell \tag{3.3}$$

It may be pointed out that code PACE4 performs only the statistical equilibrium model calculations and does not take pre-equilibrium (PE) and in-complete fusion processes into consideration.

3.2 CASCADE

The code CASCADE [3] is based on Hauser-Feshbach theory [13] for compound nucleus calculations and is frequently used to calculate the reaction cross-sections for heavy-ion interactions. It is assumed that the compound nucleus has lost memory about its formation by the time a thermodynamic equilibrium is attained. The code computes the reaction cross-sections for product nuclei, both stable and radioactive in the ground state formed by the de-excitation of the compound nucleus. The decay probabilities are determined by the level densities of the daughter nuclei and the barrier penetrability for the various channels. This code also does not take into account the possibility of pre-equilibrium emission and/or incomplete fusion. However, the present version of the code includes fission competition for which the liquid drop fission barrier is assumed. Some of the input parameters like the mass of nuclide and the transmission coefficients for the emitted particles are computed using subroutines MASS and TLCALC respectively, for the region of interest and are stored permanently on the disc. The optical model potentials of Becchetti and Greenlees [14] are used for calculating the transmission coefficients for p and n, while optical model potential of Satchler [15] is used for α-particles. Fermi gas model is used for calculating the level densities for the product nuclei. At low excitation energies, the parameters can be determined empirically, however, attention is required for the spin dependence of level densities in the region of high excitation. This is because of the high angular momenta involved in heavy ion reactions. The partial cross-section for the formation of the CN of spin J and parity π from a projectile and a target nuclei of spins J_P and J_T respectively, at the center of mass energy E is given by [16],

$$\sigma(J,\pi) = \frac{\lambda^2}{4\pi}\frac{(2J+1)}{(2J_P+1)(2J_T+1)}\sum_{S=|J_P-J_T|}^{J_P+J_T}\sum_{\ell=|J-S|}^{J+S} T_\ell(E) \qquad (3.4)$$

here, T_ℓ is the transmission coefficient which depends on the energy and the orbital angular momentum. $S=(J_P+J_T)$ is the channel spin. The T_ℓ as a function of angular momentum is approximated by a Fermi distribution;

$$T_\ell = \frac{1}{1+\exp[-(\ell-\ell_0)/d]} \tag{3.5}$$

where, ℓ_0 is the grazing angular momentum and d is the diffuseness parameter.

In case of even-even nuclei, the spins of the projectile and the target nuclei are taken as zero. The partial cross-section in that case is given as,

$$\sigma_\ell = \frac{\lambda^2}{4\pi}(2\ell+1)T_\ell(E) \tag{3.6}$$

while, the total cross-section (σ_t) is given by,

$$\sigma_t = \frac{\lambda^2}{4\pi}\sum_{\ell=0}^{\infty}(2\ell+1)T_\ell(E) \tag{3.7}$$

The total fusion cross-section for the maximum angular momentum ℓ_c of the CN is given by,

$$\sigma_f = \frac{\pi\lambda^2}{4\pi^2}\sum_{\ell=0}^{\ell_C}(2\ell+1)T_\ell(E) \tag{3.8}$$

In statistical model calculations, the critical angular momentum ℓ_c for CN fusion may have a sharp limit, or may have some overlap from ℓ_c to higher ℓ determined by the diffuseness parameter d.

The level density ρ at an excitation energy E and spin J is given by [17],

$$\rho(E,J) = \omega(E,M=J) - \omega(M=J+1) \tag{3.9}$$

with the level densities,

$$\omega(E,M) = \omega(E-M^2/aR,0), \omega(E,0) = \frac{1}{12\sqrt{Ra^2t^3}}\exp(2\sqrt{aU}) \tag{3.10}$$

and the equation of state,

$$U = E - \Delta = at^2 - \frac{3}{2}t \tag{3.11}$$

here, a is the level density parameter which determines the energy dependence, Δ is the pairing energy which determines the zero point of the effective excitation energy $U=E-\Delta$, and 't' is the thermodynamic temperature given by the equation of state. The spin dependence is determined by the parameter $aR = 2I/\hbar^2$, where, 'I' is the effective moment of inertia obtained from the low lying states. Generally, 'I' is taken as,

$$I = \frac{2}{5} mr^2 \tag{3.12}$$

with, $r = r_0 A^{1/3}$.

The level density formula implies a yrast line,

$$E_{rot}(J) = J(J+1)/aR + \Delta = \frac{J(J+1)\hbar^2}{2I} + \Delta. \tag{3.13}$$

When large range of excitation energies are involved, the parameters used should be energy dependent. Therefore, the entire energy region is divided into three groups viz., (i) for low excitation energy $E \leq 3$ to 4 MeV, shell effects and the pairing correction have to be taken into account. At $E^* \leq 2$ to 4 MeV, experimentally known levels are used particularly in the case of light nuclei, (ii) In the medium excitation energy ($4 \leq E \leq 10$ MeV) region, the analytic level density formula is applied. The parameters 'a' and 'Δ' can be determined empirically for each nucleus as was done by Vonach & Hillie et. al., [18] and Dilg et. al., [19] and (iii) However at high excitation energies $E \geq E_{LDM}$, it is assumed that all nuclei behave as predicted by liquid drop model (LDM). Analytical form of Fermi gas level density is used here and both the parities are assumed equi-probable. The parameter '$a=a_{LDM}$' is taken to be (1/8)A MeV^{-1}. The pairing shift 'Δ_{LDM}' is calculated assuming that the virtual ground state for the level density in this region should coincide with the ground state energy of a spherical liquid drop which can be calculated from one of the following options i.e., i) Myers-Swiatecki mass formula [20] ii) Dilg et. al. [19] and iii) Ramamurthy et. al. [21].

3.3 ALICE-91

The code ALICE-91 [4] is based on the Weisskopf-Ewing model [22] for compound nucleus reaction while the pre-equilibrium emission is simulated within the framework of Hybrid/Geometry Dependent Hybrid Model [23, 24]. In this code the possibility of in-complete fusion is not taken into account but it can compute statistical fission cross-sections using Bohr-Wheeler approach [12]. The code considers the emission of neutrons, protons, deuterons and/or α-particles. The code may calculate the reaction cross-sections for the residual nuclei upto 11 mass and 9 atomic number units away from the compound nucleus. Myers-Swiatecki/Lysekil mass formula [20] is used for calculating Q-values and binding energies of all the nuclei in the evaporation chain. The inverse reaction cross-sections used in the code are calculated using the optical model [25] subroutines. The transmission coefficients for heavy ions are calculated using the parabolic model of Thomas [26]. The pre-equilibrium calculations in this code are done assuming equipartition of energy among the initially excited particles and holes. The important input parameters required in this code are, the level density parameter a, the initial exciton number n_o and the mean free path (MFP) multiplier COST. The MFP for intra-nuclear transitions may be calculated from the optical model of Becchetti and Greenlees [14] or from Pauli corrected nucleon-nucleon cross-sections [27, 28]. The MFP multiplier COST is used to adjust the nuclear mean free path in order to reproduce the experimental data. It accounts for the difference, if any, between the calculated and the actual MFPs for two-body residual interactions. Level densities of the residues may be calculated either from the Fermi gas model or from the constant temperature form. The Fermi gas model gives [29],

$$\rho(U) = (U-\delta)^{-5/4}\, e^{2\sqrt{a(U-\delta)}} \tag{3.14}$$

where, δ is the pairing term and U is the excitation energy of the nucleus. The level density parameter a is taken as A/K, where, A is the mass number of the nucleus and K is an adjustable parameter. The level density ρ(U) in constant temperature approach is given as [30],

$$\rho(U) \propto \frac{1}{T}\varepsilon^{U/T} \tag{3.15}$$

The differential cross-section for emitting a particle of type ν with channel energy ε may be written as;

$$\frac{d\sigma}{d\varepsilon_\upsilon} = \frac{\pi\lambda^2}{4\pi^2}\sum_{l=|0|}^{\infty}(2l+1)T_l(2S_\upsilon+1)\sum_{\ell=|0|}^{\infty}T_\upsilon^\ell(\varepsilon)\sum_{J=|l-\ell|}^{l+\ell}\rho(\varepsilon,J)/D \qquad (3.16)$$

where, λ is the de-Broglie wavelength of the incident ion, T_l the transmission coefficient of the ℓ^{th} partial wave of the incident ion, ρ(ε,J) the spin dependent level density for the residual nucleus, D the integral of numerator over all particles and emission energies, ε the excitation energy of the compound nucleus. S_ν is the intrinsic spin of the particle ν, $T_\upsilon^\ell(\varepsilon)$ is the transmission coefficient for the particle ν with kinetic energy ε and orbital angular momentum ℓ.

In the Weisskopf-Ewing calculations, the nuclear moment of inertia is assumed to be infinite and hence there is no energy tied to rotation. As such, there is no level density cut-off at high spin. This code does not take into account the angular momentum involved in heavy ion reactions. However, the heavy ion projectile imparts large angular momentum to the composite system which has a finite moment of inertia. Hence, the composite nucleus has large rotational energy. Due to nuclear rotation, a nucleus with a given angular momentum J, cannot have energy below a minimum value E_J^{min}, which is given by,

$$E_J^{min} \approx J(J+1)\frac{\hbar^2}{2I} \qquad (3.17)$$

here, I being the moment of inertia of the composite nucleus.

If in the last stages of nuclear de-excitation, higher angular momentum of the nucleus inhibits particle emission more than it does γ-emission, then the peak of the excitation functions corresponding to particle emission mode will be shifted to higher energy [31]. A similar shift may also be produced if the mean energy of the evaporated particles increases with increasing nuclear spin. One way of obtaining an estimate of the overall energy shift is

from the nuclear rotational energy. Assuming the excited nucleus to be the rigid body, the rotational energy may be given by $E_{rot} \approx (m/M)E_{lab}$, where, m/M is the ratio of the projectile and target masses and E_{lab} is the incident energy [31]. To account for the large angular momentum imparted to the composite system in heavy ion reactions, it is desirable to shift the energy axis of excitation functions calculated with code ALICE-91 [3], by the amount of the rotational energy E_{rot}.

3.4 SUMRULE MODEL

The SUMRULE [5] model is based on the idea of partial statistical equilibrium and the generalized concept of critical angular momentum. With the help of this model, one can calculate absolute cross-sections for complete fusion, in-complete fusion and other binary reactions, which presumably proceed via the formation of di-nuclear system. Wilczynski et. al. [5], assumed that the transfer of mass may only take place if the angular momentum of relative motion of the captured fragment with respect to the absorbing nucleus is smaller than the critical angular momentum ($\ell \leq \ell_{cr}$). The critical angular momentum ℓ_{cr} (based on liquid drop model) is calculated with the help of the following formulation,

$$\left(\ell_{cr}+\frac{1}{2}\right)^2 \approx \frac{\mu(C_1+C_2)^3}{\hbar^2}\left[4\pi\gamma\frac{C_1C_2}{C_1+C_2}-\frac{Z_1Z_2e^2}{(C_1+C_2)^2}\right] \qquad (3.18)$$

where, C_1, C_2, Z_1 and Z_2 are the half-density radii and charges of two interacting nuclei, respectively, while γ is the surface tension coefficient. The half-density radii may be calculated using the expression [32],

$$C = R\left\{1-\frac{b^2}{R^2}+.....\right\} \qquad (3.19)$$

where, b=1 fm and $R = (1.28A^{1/3} - 0.76+0.8A^{1/-3})$ fm. The surface tension coefficient γ is given as,

$$\gamma = 0.95(1 - 1.78\ I^2)\ MeV.fm^2 \qquad (3.20)$$

As concluded by Bondorf et. al. [33], the reaction probability for a given channel P(i) is proportional to the following exponential factor,

$$P(i) \propto \left[\exp\frac{(Q_{gg}(i) - Q_C(i))}{T}\right] \tag{3.21}$$

where, Q_{gg} is the ground state Q-value, T the effective temperature and $Q_C(i)[=(Z_bZ_Y-Z_aZ_X)e^2/R_C]$ is the change in the Coulomb interaction energy due to the transfer of charge. The Z_a, Z_X, Z_b and Z_Y are, respectively the charges of the initial and of the final ions.

Under the assumption of the smooth cut-off in the ℓ space for each individual reaction channel i, the transmission coefficient $T_\ell(i)$ is given as,

$$T_\ell(i) = \left[1+ \exp\frac{(\ell - \ell_{lim}(i))}{\Delta}\right]^{-1} \tag{3.22}$$

Here, $\ell_{lim}(i)$ is the limiting angular momentum in the reference frame of entrance channel and Δ the diffuseness of the cut-off in the T_ℓ, distribution, respectively.

The absolute cross-section for a reaction channel (i) is given by the expression,

$$\sigma(i) = \pi\lambda^2 \sum_{\ell=0}^{\ell_{max}} (2\ell+1)\frac{T_\ell(i)P(i)}{\sum_j T_\ell(j)P(j)} \tag{3.23}$$

where, $\lambda=\frac{\hbar^2}{2\mu E}$ is the reduced wavelength associated with the entrance channel in the center of mass system and ℓ_{max} is the angular momentum that confines the range of partial waves leading to formation of the di-nuclear system.

The model contains three free parameters, one is the effective temperature T, second the effective Coulomb interaction radius R_C and the third is diffuseness Δ of the T_t distributions. The second and third parameters are purely empirical in nature, while T has no clear interpretation.

References

[1] N. Bohr; Nature 137, 344 (1936).
[2] A. Gavron; Phys. Rev. C21, 230 (1980).
[3] F. Puhlhofer; Nucl. Phys. A280, 267 (1977).
[4] M. Blann; NEA Data Bank, Gif-sur-Yvette, France, Report PSR- 014/91 (1991).
[5] J.Wilczynski, K. Siwek-Wilczynski, J. Van Driel, S. Gonggrijp, D. C. J. M. Hageman, R. V. F. Janssens, J. Lukasiak and R. H. Siemssen; Phys. Rev. Lett 45, No.8, 606 (1980).
[6] C. M. Perey and F. G. Perey; At. Nucl. Data Tables 17, 1 (1976).
[7] J. R. Huizenga and G. Igo, Nucl. Phys. 29, 462 (1962).
[8] Subroutine FISROT provided by courtesy of Dr. F. Plasil, Oak Ridge National Laboratory.
[9] R. Bass; Phys. Rev. Lett. 39, 265 (1977).
[10] A. J. Sierk; Phys. Rev. C 33, 2039 (1986).
[11] S. Cohen, F. Plasil and W. J. Swiatecki; Ann. of Phys. 82, 557 (1974).
[12] N. Bohr and J. A. Wheeler; Phys. Rev. 56, 426 (1939).
[13] W. Hauser and H. Feshbach; Phys. Rev. 87, 366 (1952).
[14] F.D. Becchetti and G.W. Greenlees; Phys. Rev. 182, 1190 (1969).
[15] G.R. Satchler; Nucl. Phys. 70, 177 (1965).
[16] J. M. Blatt and V. F. Weisskopf; Theoretical Nuclear Physics (Wiley, New York, 1952).
[17] J. Gilat; Phys. Rev. C1, 1432 (1970).
[18] H.K. Vonach and M. Hillie; Nucl. Phys. A127, 289 (1969).
[19] W. Dilg, W. Schantl, H. Vonach and M. Uhl; Nucl. Phys. A217, 343 (1973).
[20] W.D. Myers and W.J. Swiatecki; Ark. Phys. 36, 343 (1967).
[21] V.S. Ramamurthy, S.S. Kapoor and S.K. Kataria; Phys. Rev.Lett. 25, 386(1970).
[22] V.F. Weisskopf and D.H. Ewing; Phys. Rev. 57, 472, 935 (1940).
[23] M. Blann; Phys. Rev. Lett. 27, 337 (1971).
[24] M. Blann; Phys. Rev. Lett. 28, 757 (1972).
[25] M. Blann; Phys. Rev. C21, 1770 (1980).
[26] T.D. Thomas; Nucl. Phys. 53, 577 (1964).
[27] K. Kikuchi and M. Kawai; Nucl. Matter and Nucl. reactions, North Holland Publ. Co. (1968).
[28] M. Blann; Nucl. Phys. A213, 570 (1973).
[29] M. Blann and H.K. Vonach; Phys. Rev. C28, 1475 (1983).

[30] M. Blann, G. Reffo and F. Fabbri; Nucl. Instr. Methods A265, 490 (1988).
[31] D. Bodansky; Annu. Rev. Nucl. Sci. 12, 79 (1962).
[32] W.U. Schroder and J.R. Huizenga; Ann. Rev. Nucl. Sci. 27, 456 (1977).
[33] J.P. Bondorf, F. Dickmann, D.H.E Gross and P.J. Siemens; J.Phys. (Paris), Colloq. 32, C6-145 (1971).

Chapter IV

MEASUREMENTS

With a view to study the complete fusion (CF), in-complete fusion (ICF) and the role of break-up processes in nuclear reactions induced by energetic ^{16}O ions, experiments have been performed to measure the excitation functions (EFs), forward recoil range distributions (FRRDs) and angular distribution (AD) of the radio-nuclides populated via these processes. The systems studied, the type of measurements and the energy range covered in these measurements for different systems are mentioned in Table 4.1.

Table 4.1: A list of systems studied, type of measurements done alongwith the energy range covered.

S. No.	Systems Studied	Measurements	Energy Range (MeV)
1.	$^{16}O + {}^{181}Ta$	EFs	≈76-100
2	$^{16}O + {}^{103}Rh$	EFs	≈56-85
3.	$^{16}O + {}^{27}Al$	EFs	≈60-94
4.	$^{16}O + {}^{181}Ta$	FRRDs	≈81, 90 & 96
5.	$^{16}O + {}^{27}Al$	ADs	≈85

In the present work, EFs for twenty seven reactions viz.,

$^{181}Ta(O, 3n)^{194}Tl^{g}$, $^{181}Ta(O, 3n)^{194}Tl^{m}$, $^{181}Ta(O, 4n)^{193}Tl^{g}$,

$^{181}Ta(O,4n)^{193}Tl^{m}$, $^{181}Ta(O,5n)^{192}Tl^{g}$, $^{181}Ta(O, 5n)^{192}Tl^{m}$,

$^{181}Ta(O, p3n)^{193}Hg^{g}$, $^{181}Ta(O, p3n)^{193}Hg^{m}$, $^{181}Ta(O, p4n)^{192}Hg$,

$^{181}Ta(O, p5n)^{191}Hg^{g}$, $^{181}Ta(O, p5n)^{191}Hg^{m}$, $^{181}Ta(O, \alpha n)^{192}Au^{g}$,

$^{181}Ta(O, \alpha 2n)^{191}Au^{g}$, $^{181}Ta(O, \alpha 3n)^{190}Au^{g}$, $^{103}Rh(O, p3n)^{115}Te^{g}$,

$^{103}Rh(O, p3n)^{115}Te^{m}$, $^{103}Rh(O, p4n)^{114}Te$, $^{103}Rh(O, 2\alpha n)^{110}In^{g}$,

$^{103}Rh(O, 2\alpha n)^{110}In^{m}$, $^{103}Rh(O, 2\alpha 3n)^{108}In^{g}$, $^{103}Rh(O,2\alpha 3n)^{108}In^{m}$,

$^{103}Rh(O, 3\alpha 4n)^{103}Ag^{g}$, $^{27}Al(O, 2\alpha n)^{34}Cl$, $^{27}Al(O, 3\alpha 3p)^{28}Mg$,

$^{27}Al(O, 3\alpha 3pn)^{27}Mg$, $^{27}Al(O, 4\alpha 2pn)^{24}Na$ and $^{27}Al(O, 4\alpha 3p)^{24}Ne$,

have been measured using the activation technique. The details of these measurements for each reaction are given in section 4.1. Further, in order to determine the degree of linear momentum transfer and to study the energy dependence of CF and ICF processes, the FRRDs for the following twelve radio-nuclides produced in $^{16}O+^{181}Ta$ system at three different projectile energies ≈81, 90 and 96 MeV have been measured;

$^{181}Ta(O, 3n)^{194}Tl$, $^{181}Ta(O, 4n)^{193}Tl$, $^{181}Ta(O,5n)^{192}Tl$,

$^{181}Ta(O, p3n)^{193}Hg^{g}$, $^{181}Ta(O, p3n)^{193}Hg^{m}$, $^{181}Ta(O, p4n)^{192}Hg$,

$^{181}Ta(O, p5n)^{191}Hg^{g}$, $^{181}Ta(O, p5n)^{191}Hg^{m}$, $^{181}Ta(O, \alpha n)^{192}Au^{g}$,

$^{181}Ta(O, \alpha 2n)^{191}Au^{g}$, $^{181}Ta(O, \alpha 3n)^{190}Au^{g}$ and $^{181}Ta(O, 2\alpha 3n)^{186}Ir^{g}$.

In order to obtain complementary information about the linear momentum transfer from projectile to the target nucleus, AD of residues produced in $^{16}O + ^{27}Al$ system has also been measured at incident beam energy ≈85 MeV. The details of these FRRDs and angular distribution measurements are described in section 4.2 & 4.3 respectively. To the best of our knowledge most of the presently measured EFs and the RRDs are being reported for the first time.

4.1 THE EXCITATION FUNCTIONS

4.1.1 $^{16}O+^{181}Ta$ System:

The excitation functions (EFs) for fourteen reaction residues [1] in the system $^{16}O+^{181}Ta$, have been measured in the energy range ≈76 to 100 MeV. A list of the reactions, residues, their half-lives, characteristic γ-rays identifying the residue, spin-parity (J^{π}) and the corresponding branching ratios are given in Table 4.2. The residues have been identified by their characteristic γ-rays and also from the measured half-lives using decay curve analysis. In general, a residue populated via a specific reaction channel often emits several γ-rays of different energies. In such cases, the cross-sections for the individual channels have been determined from the measured intensities of several characteristic γ-rays and the value quoted is

the weighted average of cross-sections obtained for these γ-rays [2]. Each reaction has been discussed in detail in this section.

Table 4.2: A list of the reaction products populated (via CF and/or ICF) through different reaction channels and their spectroscopic properties.

S. No.	Reaction	Residue	Half-life ($T_{1/2}$)	Spin (J^{π})	Energy of γ.ray (keV)	Branching ratio (%)
1.	^{181}Ta(O, 3n)	^{194}Tl^{g}	33 m	2^-	636.1	15.3
2.	^{181}Ta(O, 3n)	^{194}Tl^{m}	32.8 m	7^+	636.1	99.0
3.	^{181}Ta(O, 4n)	^{193}Tl^{g}	21.6 m	$(1/2)^+$	324.4, 1044.7	15.2, 8.99
4.	^{181}Ta(O,4n)	^{193}Tl^{m}	2.1 m	$(9/2)^-$	365.0	90.1
5.	^{181}Ta(O,5n)	^{192}Tl^{g}	9.6 m	2^-	422.9	31.1
6.	^{181}Ta(O, 5n)	^{192}Tl^{m}	10.6 m	7^+	422.9	31.1
7.	^{181}Ta(O, p3n)	^{193}Hg^{g}	3.8 h	$(3/2)^-$	381.6, 539.0, 827.8, 861.1, 1118.8	11.0, 1.2, 4.0, 13.0, 8.3
8.	^{181}Ta(O, p3n)	^{193}Hg^{m}	11.8 h	$(13/2)^+$	258.1	60.0
9.	^{181}Ta(O, p4n)	^{192}Hg	4.85 h	0^+	274.8	50.4
10.	^{181}Ta(O, p5n)	^{191}Hg^{g}	49 m	$(3/2)^-$	224.6, 241.2, 331.7	17.4, 8.9, 11.24
11.	^{181}Ta(O, p5n)	^{191}Hg^{m}	50.8 m	$(13/2)^+$	420.3, 578.7	17.9, 17.0
12.	^{181}Ta(O, αn)	^{192}Au^{g}	4.94 h	1^-	295.5, 316.5	22.7, 58.0
13.	^{181}Ta(O, α2n)	^{191}Au^{g}	3.18 h	$(3/2)^+$	283.9, 399.8	6.3, 4.5
14.	^{181}Ta(O, α3n)	^{190}Au^{g}	42.8 m	1^-	295.9, 301.9	71.0, 25.1

(^{16}O, xn) Channels

In the case of xn channels, there is no likely-hood of ICF and, therefore, these channels are considered to be populated only by CF processes.

^{181}Ta(O, 3n) channel [Residue=^{194}Tl^{g}, $T_{1/2}$=33 m, $J^{\pi}=2^-$]
[Residue=^{194}Tl^{m}, $T_{1/2}$=32.8 m, $J^{\pi}=7^+$]

The evaporation residue ^{194}Tl is formed by the fusion of ^{16}O with ^{181}Ta forming an excited composite system ^{197}Tl, followed by the emission of three neutrons. The residual nucleus ^{194}Tl is populated in ground (^{194}Tl^{g}) as well as in the meta-stable state (^{194}Tl^{m}). From the analysis of the

experimental data, activities of the residues (corresponding to 3n channel) were identified. The identification was done both, on the basis of measured half-lives using decay curve analysis and also by the characteristic γ-ray energies of the residues. In both these cases, the meta-stable and ground states have γ-rays of nearly the same energy (but of different intensities) and half-lives. As such, the observed composite decay curve gives the contribution due to sum of both the states. Hence, individual production cross-sections for meta-stable and ground states of ^{194}Tl were obtained by dividing the measured composite cross-sections in the ratio of their γ-ray intensities [3, 4].

^{181}Ta(O, 4n) channel [Residue=^{193}Tl^{g}, $T_{1/2}$=21.6 m, $J^{\pi}=1/2^{+}$]
[Residue=^{193}Tl^{m}, $T_{1/2}$=2.1 m, $J^{\pi}=9/2^{-}$]

The evaporation residue ^{193}Tl is populated by the emission of four neutrons from the excited composite system ^{197}Tl produced in the interaction of ^{16}O with ^{181}Ta. The residual nucleus ^{193}Tl has two states, the ground state (^{193}Tl^{g}) as well as the meta-stable state (^{193}Tl^{m}). The meta-stable state of half-life ≈2.1 m decays to the ground state, which has a half-life of ≈21.6 m. Since, the counting of the irradiated samples was done after about 10 min., from the cessation of irradiation, the meta-stable state of this residue could not be observed. The measured cross-sections for the ground state also contain contribution (≤0.38%) from the meta-stable state. As such, an upper limit for the cross-sections for the independent production of the meta-stable state has been determined and is given in Table 4.3.

^{181}Ta(O, 5n) channel [Residue=^{192}Tl^{g}, $T_{1/2}$=9.6 m, $J^{\pi}=2^{-}$]
[Residue=^{192}Tl^{m}, $T_{1/2}$=10.6 m, $J^{\pi}=7^{+}$]

The evaporation residue ^{192}Tl (5n) is formed by the fusion of ^{16}O with ^{181}Ta forming an excited composite system ^{197}Tl, followed by the emission of five neutrons. The residual nucleus ^{192}Tl has both the ground state as well as the meta-stable state. The meta-stable and the ground states of ^{192}Tl decay with γ-rays of nearly the same energy (422.9 keV), same intensities and half-lives. As such, the observed composite decay curve gives the contribution as sum of both the states. The cross-section obtained from the composite decay curve was divided equally between the two states.

Table 4.3 Experimentally measured cross-sections for the residues populated via xn (x=3, 4 & 5) channels in the fusion of ^{16}O with ^{181}Ta.

Lab Energy (MeV)	σ ($^{194}Tl^{g}$) (mb)	σ ($^{194}Tl^{m}$) (mb)	σ ($^{193}Tl^{g}$) (mb)	σ($^{193}Tl^{m}$)* (mb)	σ ($^{192}Tl^{g}$) (mb)	σ ($^{192}Tl^{m}$) (mb)
76 ± 1.1	2±0.2	2±0.2	26±3.8	0.1±0.01	–	–
80 ± 1.5	6±0.8	6±0.8	45±6.8	0.2±0.02	22±3.0	22±3.0
85 ± 1.2	4±0.5	4±0.5	68±10.2	0.3±0.03	61±9.1	61±9.1
87 ± 1.0	3±0.4	3±0.4	46±6.9	0.2±0.02	44±6.5	44±6.5
88 ± 1.6	2±0.2	2±0.2	44±6.5	0.2±0.02	91±13.7	91±13.7
93 ± 1.1	2±0.3	2.5±0.3	35±5.2	0.1±0.01	184±27.6	184±27.6
97 ± 1.0	1.5±0.2	2±0.3	15±2.3	0.1±0.01	171±25.5	171±25.5
99 ± 0.9	1±0.1	1±0.1	17±2.5	0.1±0.01	222±33.3	222±33.3

*Cross-section values give an upper limit.

(^{16}O,pxn) Channels

Like the xn channels, in the case of pxn channels also, there is no likelyhood of ICF and, therefore, these channels are also populated by CF process only. The individual reaction channels are described here.

^{181}Ta(O, p3n) channel [Residue=$^{193}Hg^{g}$, $T_{1/2}$=3.8 h, $J^{\pi}=3/2^{-}$] [Residue=$^{193}Hg^{m}$, $T_{1/2}$=11.8 h, $J^{\pi}=13/2^{+}$]

The evaporation residue ^{193}Hg may be formed by the evaporation of a proton and three neutrons from the excited composite system ^{197}Tl formed in the interaction of ^{16}O with ^{181}Ta. The residual nucleus ^{193}Hg is populated in ground as well as meta-stable state. The meta-stable and ground states of the residues ^{193}Hg decay with different half-lives. Cross-sections for the production of $^{193}Hg^{m}$ and $^{193}Hg^{g}$ have been determined separately from the intensities of their characteristic γ-lines and are presented in Table 4.4. Further, the ^{193}Hg residues may also be populated by the β^{+}/EC decay of the higher charge isobar precursor ^{193}Tl formed by the reaction channel $^{181}Ta(^{16}O,4n)$. The production of the residue ^{193}Hg via both the processes may be represented as;

$$^{16}O+^{181}Ta \rightarrow {}^{197}Tl^{*} \rightarrow {}^{193}Hg + p3n; \text{ (Independent decay)}$$

$$^{16}O+^{181}Ta \rightarrow {}^{197}Tl^{*} \rightarrow {}^{193}Tl^{*} + 4n;$$

$$^{193}Tl^{*} \xrightarrow{\beta^{+}/EC} {}^{193}Hg;$$ (Precursor decay)

As such, the measured activity of ^{193}Hg may have the contributions from its independent production via p3n channel and also from the β^{+}/EC decay of its higher charge isobar precursor.

^{181}Ta(O, p4n) channel [Residue=^{192}Hg, $T_{1/2}$=4.85 h, $J^{\pi}=0^{+}$]

The residue ^{192}Hg is likely to be formed by the fusion of ^{16}O with ^{181}Ta forming an excited composite system ^{197}Tl followed by the evaporation of a proton and four neutrons. Further, the residue ^{192}Hg may also be populated by the β^{+}/EC decay of higher charge isobar precursor ^{192}Tl, formed by the reaction channel ^{181}Ta(^{16}O,5n). The measured activity of ^{192}Hg may have the contributions, both from its higher charge isobar precursor decay as well as from its independent production. The production of this residue may be represented as;

$$^{16}O + {}^{181}Ta \rightarrow {}^{197}Tl^{*} \rightarrow {}^{192}Hg + p4n;$$ (Independent decay)

$$^{16}O + {}^{181}Ta \rightarrow {}^{197}Tl^{*} \rightarrow {}^{192}Tl^{*} + 5n;$$

$$^{192}Tl^{*} \xrightarrow{\beta^{+}/EC} {}^{192}Hg;$$ (Precursor decay)

^{181}Ta(O, p5n) channel [Residue=^{191}Hg^{g}, $T_{1/2}$=49 m, $J^{\pi}=3/2^{-}$] [Residue=^{191}Hg^{m}, $T_{1/2}$=50.8 m, $J^{\pi}=13/2^{+}$]

The residue ^{191}Hg may be formed by the emission of a proton and five neutrons from the excited composite system ^{197}Tl formed in the fusion of ^{16}O + ^{181}Ta. The meta-stable and ground states of this residue, emit γ-rays of different energies and intensities. The cross-sections for the production of ^{191}Hg have been determined for both the ground and meta-stable states separately using the intensities of their characteristic γ-rays. The measured cross-sections are presented for both the states in Table 4.4. Further, the residue ^{191}Hg may also be populated by the β^{+}/EC decay of higher charge isobar precursor ^{191}Tl formed by the reaction channel ^{181}Ta(^{16}O,6n). As such, the measured activity of ^{191}Hg may have the contributions from its

independent production via p5n channel as well as from higher charge isobar precursor decay. The formation of this residue via both the above processes may be represented as;

$$^{16}O+^{181}Ta \rightarrow ^{197}Tl^{*} \rightarrow ^{191}Hg + p5n; \text{ (Independent decay)}$$

$$^{16}O+^{181}Ta \rightarrow ^{197}Tl^{*} \rightarrow ^{191}Tl^{*} + 6n;$$

$$^{191}Tl^{*} \xrightarrow{\beta^{+}/EC} ^{191}Hg ; \text{ (Precursor decay)}$$

In the case of p3n and p4n channels, the contributions of precursor decay could not be determined because of either the in-complete decay or the unknown decay characteristics of the precursor. For example, in the case of the p4n channel, the cross-sections for the independent decay of precursor formed by the 5n channel are found to be higher than the cross-sections for residue ^{192}Hg populated by the p4n channel. This may happen, if the precursor does not feed the residue ^{192}Hg formed by p4n channel. As such, the decay schemes of ^{192}Hg and ^{193}Hg need further investigation. The cross-section values quoted in Table 4.4, for these reactions also contain precursor contribution, if any, in the case of p3n and p4n channels. However, in the case of the p5n channel, the precursor ^{191}Tl, which may be produced by a 6n channel, is not likely to be produced in the present experiment on account of its higher threshold (≥100 MeV). As such, the cross-section of $^{191}Hg(p5n)$ may be considered as due to the independent production of this residue.

Table 4.4 Experimentally measured cross-sections for the residues populated via pxn (x=3, 4 & 5) channels in the interaction of ^{16}O with ^{181}Ta.

Lab Energy (MeV)	σ ($^{193}Hg^{g}$) (mb)	σ ($^{193}Hg^{m}$) (mb)	σ (^{192}Hg) (mb)	σ ($^{191}Hg^{g}$) (mb)	σ ($^{191}Hg^{m}$) (mb)
76 ± 1.1	23±3.5	8±0.8	–	–	–
80 ± 1.5	47±7.0	21±2.1	4±0.5	–	–
85 ± 1.2	60±8.9	30±3.0	40±6.0	–	–
87 ± 1.0	49±7.4	22±2.2	36±5.5	–	–
88 ± 1.6	42±6.2	24±2.3	65±9.8	3±0.5	0.3±0.04
93 ± 1.1	29±4.4	13±1.3	121±18.2	5±0.7	3±0.5
97 ± 1.0	12±1.7	8±0.7	131±6.0	7±0.9	8±1.2
99 ± 0.9	10±1.5	6±0.5	154±23.2	14±2.1	18±2.7

(^{16}O, αxn) Channels

In the case of αxn channels, the residues may be formed in two ways; (i) by CF of $^{16}O+^{181}Ta$, followed by the formation of an excited composite nucleus, from which, the evaporation of neutrons and α-particles takes place and/or (ii) on the other hand, the ^{16}O ion breaks-up into fragments (α + ^{12}C, ^{8}Be + ^{8}Be or ^{12}C + α), out of these, one of the fragments fuses with the target nucleus leaving remaining part of the projectile as spectator. The excited nucleus formed by the fusion of one of the fragments, from the projectile, may emit neutrons/light ions while de-exciting. In the present work, three α-emitting channels viz., αn, α2n and α3n have been observed. The measured cross-sections for the population of these residues at different energies are presented in Table 4.5.

$^{181}Ta(O, \alpha n)$ channel [Residue=$^{192}Au^{g}$, $T_{1/2}$=4.94 h, $J^{\pi}=1^{-}$]

The ^{192}Au residues are likely to be produced by i) the CF process in the interaction of ^{16}O with ^{181}Ta followed by the evaporation of an α-particle and a neutron from the composite system $^{197}Tl^{*}$ and also by ii) the ICF process, assuming that the ^{16}O ion breaks-up into $\alpha+^{12}C$ fragments and one of the fragments ^{12}C fuses with the target nucleus ^{181}Ta forming $^{193}Au^{*}$ in the excited state, which decays by emitting a neutron leaving an α-particle as spectator. In this case also the meta-stable state of ^{192}Au (half-life ≈160 m sec) could not be measured because of the experimental limitations. The measured cross-sections for this channel may include contributions from both the CF and ICF processes of the types;

Complete fusion of ^{16}O, i.e.,

$$^{16}O + {}^{181}Ta \rightarrow {}^{197}Tl^{*} \rightarrow {}^{192}Au^{*} + \alpha + n;$$

In-complete fusion of ^{16}O, i.e.,

$$^{16}O\left(^{12}C+\alpha\right)+{}^{181}Ta \rightarrow {}^{193}Au^{*}+\alpha; \text{ (Spectator)}$$
$$^{193}Au^{*} \rightarrow {}^{192}Au^{g*} + n$$

^{181}Ta(O, α2n) channel [Residue=^{191}Au^{g}, $T_{1/2}$=3.18 h, $J^{\pi}=3/2^{+}$]

The residues ^{191}Au may also be produced by the CF and/or ICF processes. In case of CF, the composite system ^{197}Tl decays by the evaporation of an α-particle and two neutrons. While, in case of ICF, the same residual nucleus may also be produced, assuming that the ^{16}O ion breaks-up into α+^{12}C fragments and one of the fragments ^{12}C fuses with the target nucleus ^{181}Ta, forming ^{193}Au* in the excited state which decays by emitting two neutrons leaving an α-particle as spectator. The meta-stable state ^{191}Au^{m} of half-life ≈0.92 sec. could not be measured because of very short half-life. The measured cross-sections for this residue include the contributions from both the CF and ICF processes of the types;

Complete fusion of ^{16}O, i.e.,

$$^{16}O + {}^{181}Ta \rightarrow {}^{197}Tl^{*} \rightarrow {}^{191}Au^{*} + \alpha + 2n$$

In-complete fusion of ^{16}O, i.e.,

$$^{16}O\left({}^{12}C+\alpha\right)+{}^{181}Ta \rightarrow {}^{193}Au^{*}+\alpha; \text{ (Spectator)}$$

$$^{193}Au^{*} \rightarrow {}^{191}Au^{g\,*} + 2n$$

^{181}Ta(O, α3n) channel [Residue=^{190}Au^{g}, $T_{1/2}$=42.8 m, $J^{\pi}=1^{-}$]

Similar to the αn and α2n channels the ^{190}Au residues may be populated both by the CF and/or ICF processes of the types;

Complete fusion of ^{16}O, i.e.,

$$^{16}O + {}^{181}Ta \rightarrow {}^{197}Tl^{*} \rightarrow {}^{190}Au^{*} + \alpha + 3n$$

In-complete fusion of ^{16}O, i.e.,

$$^{16}O\left({}^{12}C+\alpha\right)+{}^{181}Ta \rightarrow {}^{193}Au^{*}+\alpha; \text{ (Spectator)}$$

$$^{193}Au^{*} \rightarrow {}^{190}Au^{g\,*} + 3n;$$

In this case also the meta-stable state (^{190}Au^{m}) could not be observed because the half-life of this residue is only 125 msec.

Table 4.5 Experimentally measured cross-sections for the residues populated via αxn (x=1, 2 & 3) channels in the interaction of ^{16}O with the ^{181}Ta.

Lab Energy (MeV)	σ ($^{192}Au^{g}$) (mb)	σ($^{191}Au^{g}$) (mb)	σ ($^{190}Au^{g}$) (mb)
80 ± 1.5	2±0.2	–	–
85 ± 1.2	10±1.5	–	8±1.3
87 ± 1.0	12±1.8	2±0.3	6±0.8
88 ± 1.6	31±4.6	2±0.3	23±3.5
93 ± 1.1	46±6.9	3±0.5	20±2.9
97 ± 1.0	63±9.5	14±2.1	40±5.9
99 ± 0.9	50±7.5	22±3.2	21±3.2

4.1.2 $^{16}O+^{103}Rh$ System:

In case of $^{16}O+^{103}Rh$ system the excitation functions (EFs) for eight reactions [5], have been measured in the energy range ≈46 to 85 MeV. A list of the reaction residues, their half-lives, characteristic γ-rays used for identification of the residues and their branching ratios etc., are given in Table 4.6.

Table 4.6 List of reaction products alongwith reaction channels and their other spectroscopic properties in the $^{16}O+^{103}Rh$ system.

S. No.	Reaction	Residue	Half-life ($T_{1/2}$)	Spin (J^{π})	Energy of γ-ray (keV)	Branching ratio (%)
1.	$^{103}Rh(O, pn)$	$^{117}Te^{g}$	62 m	$(1/2)^{+}$	719.7 1090.7	64.7 6.9
2.	$^{103}Rh(O, p2n)$	^{116}Te	2.49 h	0^{+}	628.7	1.0
3.	$^{103}Rh(O, p3n)$	$^{115}Te^{g*}$	5.8 m	$(7/2)^{+}$	1326.8 1380.5	22.7 23.0
4.	$^{103}Rh(O, p3n)$	$^{115}Te^{m*}$	6.7 m	$(1/2)^{+}$	770.3	34.2
5.	$^{103}Rh(O, p4n)$	$^{114}Te^{*}$	15.2 m	0^{+}	244.6 726.5	33.0 43.0
6.	$^{103}Rh(O, 2p)$	^{117}Sb	2.8 h	$(5/2)^{+}$	158.6	85.9
7.	$^{103}Rh(O, 2p2n)$	^{115}Sb	32.1 m	$(5/2)^{+}$	497.4 489.1	98.0 1.3
8.	$^{103}Rh(O, 2\alpha)$	$^{111}In^{g}$	2.8 d	$(9/2)^{+}$	171.3	90.2

					245.4	94.0
9.	^{103}Rh(O, 2αn)	^{110}In^{g*}	4.9 h	7^+	641.6 884.6 937.4	25.9 92.9 68.4
10.	^{103}Rh(O, 2αn)	^{110}In^{m*}	1.15 h	2^+	657.7 1235.6	98.0 0.26
11.	^{103}Rh(O, 2α2n)	^{109}In^{g}	4.2 h	$(9/2)^+$	203.2 623.6	73.5 6.0
12.	^{103}Rh(O, 2α3n)	^{108}In^{g*}	58 m	7^+	242.7	38.0
13.	^{103}Rh(O, 2α3n)	^{108}In^{m*}	39.6 m	2^+	311.9 968.0	1.01 4.38
14.	^{103}Rh(O, 3αn)	^{106}Ag^{m}	8.28 d	6^+	451.0 717.4	27.6 29.0
15.	^{103}Rh(O, 3α3n)	^{104}Ag^{g}	69.2 m	5^+	767.8 555.8	65.9 92.8
16.	^{103}Rh(O, 3α4n)	^{103}Ag^{g*}	65.7 m	$(7/2)^+$	146.0	28.3

It may be pointed out that the residues marked with "*" in this table have been studied presently. However, in order to have completeness, other residues studied [6] by our group have also been included in the Table 4.6. The residues presented in this table are likely to be populated both via CF and/or ICF reactions.

(^{16}O,pxn) Channels

^{103}Rh(O, p3n) channel [Residue=^{115}Te^{g}, $T_{1/2}$=5.8 m, $J^{\pi}=7/2^+$] [Residue=^{115}Te^{m}, $T_{1/2}$=6.7 m, $J^{\pi}=1/2^+$]

The residue ^{115}Te may be formed by the CF of ^{16}O with ^{103}Rh forming an excited composite system ^{119}I followed by the emission of a proton and three neutrons. The residual nucleus ^{115}Te is produced in the ground state (^{115}Te^{g}) as well as in the meta-stable state (^{115}Te^{m}). The meta-stable and ground states of the respective residues emit γ-rays of different energies. The activities of both the residues (corresponding to p3n channel) were identified by measuring the half-lives using decay curve analysis and by the characteristic γ-ray energies. Further, the residue ^{115}Te may also be populated by the β^+/EC decay of higher charge isobar precursor ^{115}I formed by the reaction channel ^{103}Rh(O, 4n). As such, the measured activity of ^{115}Te

may have the contributions due to its independent production and also from its higher charge isobar precursor decay. The formation of this residue via CF and from its higher charge isobar precursor may be represented as;

$$^{16}O+^{103}Rh \rightarrow {}^{119}I^{*} \rightarrow {}^{115}Te + p3n; \quad \text{(Independent decay)}$$

$$^{16}O+^{103}Rh \rightarrow {}^{119}I^{*} \rightarrow {}^{115}I^{*} + 4n;$$

$$^{115}I^{*} \xrightarrow{\beta^{+}/EC} {}^{115}Te \quad \text{(Precursor decay)}$$

The residue ^{115}I (populated via 4n channel) of half-life $\approx$1.3 m could not be observed because of short half-life. To separate out the contribution of higher charge isobar precursor from the residue ^{115}Te, the cross-sections of the higher charge isobar precursor ^{115}I, have been taken from theoretical model code PACE4 [7], which is based on the Hauser-Feshbach approach. The contributions due to the decay of precursor isobar ^{115}I to the residues $^{115}Te^{g,m}$ have been separated out by using the standard successive radio-active decay formulations [8]. In this case, the half-life (1.3 m) of precursor is considerably smaller than the daughter nucleus (^{115}Te). As such, the independent production cross-section (σ_{ind}) has been estimated from the cumulative production cross-section (σ_{cum}). The σ_{cum} of a given residue is the sum of σ_{ind} and the cross-section for the independent production of its precursor σ_{pre}, multiplied by a numerical coefficient F_P, i.e.,

$$\sigma_{cum} = \sigma_{ind} + F_P \sigma_{pre} \tag{4.1}$$

The value of F_p depends on the branching ratio P_p for the precursor decay to the residue and is given by [8];

$$F_p = P_p \frac{T_{ind}^{1/2}}{T_{ind}^{1/2} - T_{pre}^{1/2}} \tag{4.2}$$

here, T_{pre} and T_{ind} are the half-lives of the pre-cursor and the residue. In this way the cumulative cross-section is given by;

$$\sigma\left(^{115}_{cum}Te^{g}\right) = \sigma\left(^{115}_{ind}Te^{g}\right) + 1.28 \times \sigma\left(^{115}_{pre}I\right)$$

$$\sigma\left(^{115}_{cum}Te^{m}\right) = \sigma\left(^{115}_{ind}Te^{m}\right) + 1.48 \times \sigma\left(^{115}_{pre}I\right)$$

where, the subscripts 'cum' and 'ind' stand, respectively, for cumulative and independent yields. The experimentally determined independent cross-sections for the formation of ^{115}Te are given in Table 4.7.

^{103}Rh(O, p4n) channel [Residue=^{114}Te, $T_{1/2}$=15.2 m, $J^{\pi}=0^{+}$]

The residue ^{114}Te may be formed by the CF of ^{16}O with ^{103}Rh forming an excited composite system ^{119}I followed by the evaporation of a proton and four neutrons. Further, the residue ^{114}Te may also be populated by the β^{+}/EC decay of its higher charge isobar precursor ^{114}I formed by the reaction channel ^{103}Rh(O,5n). As such, the measured activity of ^{114}Te may have the contributions from its higher charge isobar precursor decay also. The formation of this residue via CF and from its higher charge isobar precursor may be represented as;

$$^{16}O + ^{103}Rh \rightarrow ^{119}I^{*} \rightarrow ^{114}Te + p4n; \quad \text{(Independent decay)}$$

$$^{16}O + ^{103}Rh \rightarrow ^{119}I^{*} \rightarrow ^{114}I^{*} + 5n;$$

$$^{114}I^{*} \xrightarrow{\beta^{+}/EC} ^{114}Te; \quad \text{(Precursor decay)}$$

The higher charge isobar precursor residues $^{114}I^{g,m}$, populated via 5n channel could not be observed because of their short half-lives ≈2.1 sec. and 6.2 sec. respectively. Further, the theoretical calculations for 5n channel gives negligible values of the cross-sections at these energies, as such, the precursor contribution to the population of ^{114}Te may be neglected. Hence, the values of cross-sections quoted for ^{114}Te, in Table 4.7, may be considered as the independent production values.

Table 4.7 Experimentally measured cross-sections for the residues populated via pxn (x=3 & 4) channels in the interaction of ^{16}O with ^{103}Rh.

E_{Lab} (MeV)	σ_{cum} ($^{115}Te^{g}$) (mb)	σ_{ind} ($^{115}Te^{g}$) (mb)	σ_{cum}($^{115}Te^{m}$) (mb)	σ_{ind}($^{115}Te^{m}$) (mb)	σ(^{114}Te) (mb)
57.8 ± 3.5	3.0 ± 0.3	3.0 ± 0.3	1.0 ± 0.1	1.0 ± 0.1	-
65.8 ± 2.3	27.0 ± 3.0	24.0 ± 2.0	23.0 ± 2.0	22.0 ± 2.0	-
70.8 ± 3.1	43.0 ± 4.0	39.0 ± 4.0	57.0 ± 6.0	54.0 ± 5.0	-
77.1 ± 2.6	118.0 ± 12.0	95.0 ± 9.0	43.0 ± 4.0	28.0 ± 3.0	4.0 ± 0.4
82.8 ± 2.6	161.0 ± 16.0	138.0 ± 14.0	37.0 ± 4.0	13.0 ± 1.0	15.0 ±1.0

(^{16}O, 2αxn) Channels

In the case of 2αxn channels also, the residues may be formed in two ways; (i) by CF of ^{16}O+^{103}Rh followed by the formation of excited composite nuclei, from which, the evaporation of neutrons and α-particles may take and/or (ii) on the other hand, the incident ^{16}O ion breaks-up into fragments (α + ^{12}C, ^{8}Be + ^{8}Be and/or ^{12}C + α). One of the fragments fuses with the target nucleus leaving remaining part as the spectator. Brief description of various α-channels studied in the present work is given in the following.

^{103}Rh(O, 2αn) channel [Residue=$^{110}In^{g}$, $T_{1/2}$=4.9 h, $J^{\pi}=7^{+}$] [Residue=$^{110}In^{m}$, $T_{1/2}$=1.15 h, $J^{\pi}=2^{+}$]

The residue ^{110}In(2αn) is likely to be formed by the CF as well ICF processes. In case of CF, it may be formed by the evaporation of 2α-particles and a neutron from the excited composite system ^{119}I formed in the fusion of ^{16}O with ^{103}Rh. On the other hand, the same reaction product may also be produced assuming that the ^{16}O ion breaks-up into ^{8}Be+^{8}Be fragments and one of the fragments, ^{8}Be fuses with the target nucleus ^{103}Rh forming ^{111}In* in the excited state which emits a neutron, leaving ^{8}Be as spectator. Further, the measured cross-sections for this channel may, therefore, include contributions from both the CF and ICF processes. The mode of formation of ^{110}In residues by CF and ICF processes may be represented as;

Complete fusion of ^{16}O, i.e.,

$$^{16}O + ^{103}Rh \rightarrow ^{119}I^* \rightarrow ^{110}In + 2\alpha + n;$$

In-complete fusion of ^{16}O, i.e.,

$$^{16}O\left(^{8}Be + ^{8}Be\right) + ^{103}Rh \rightarrow ^{111}In^* + ^{8}Be\ (2\alpha);\ (Spectator)$$

$$^{111}In^* \rightarrow ^{110}In^{g,m*} + n$$

The residual nuclei ^{110}In are populated in two states, the ground state $^{110}In^g$ ($t_{1/2}$=4.9 hrs) and the meta-stable state $^{110}In^m$ ($t_{1/2}$=1.15 hrs). Since, both the meta-stable and ground states have γ-rays of different energies, as such their production cross-sections have been measured separately.

^{103}Rh(O, 2α3n) channel [Residue=$^{108}In^g$, $T_{1/2}$=58 m, $J^\pi=7^+$] [Residue=$^{108}In^m$, $T_{1/2}$=39.6 m, $J^\pi=2^+$]

Similar to the above, the ^{108}In residues are also likely to be populated by CF and/or the ICF processes. Firstly, it may be formed by the CF of ^{16}O+^{103}Rh forming an excited composite system ^{119}I followed by the evaporation of 2α particles and three neutrons. On the other hand, the same residual nucleus may also be produced assuming that the ^{16}O ion breaks-up into ^{8}Be+^{8}Be fragments and one of the fragments, ^{8}Be fuses with the target nucleus ^{103}Rh forming $^{111}In^*$ in the excited state which decay by emitting three neutrons, leaving one of the fragments ^{8}Be as spectator. The measured cross-sections for this channel may, therefore, include contributions from both the CF and ICF processes. The mode of formation of this residue by two different processes namely CF and ICF may be represented as;

Complete fusion of ^{16}O, i.e.,

$$^{16}O + ^{103}Rh \rightarrow ^{119}I^* \rightarrow ^{108}In + 2\alpha + 3n;$$

In-complete fusion of ^{16}O, i.e.,

$$^{16}O\left(^{8}Be + ^{8}Be\right) + ^{103}Rh \rightarrow ^{111}In^* + ^{8}Be\,(2\alpha);\ (Spectator)$$

$$^{111}In^{*} \rightarrow {}^{108}In^{g,m} + 3n$$

The ground state $^{110}In^{g}$ ($t_{1/2}$=58 m) and the meta-stable state $^{108}In^{m}$ ($t_{1/2}$=39.6 m) were identified separately on the basis of γ-ray energies and half-lives of the residues.

(^{16}O,3αxn) Channels

$^{103}Rh(O,3\alpha 4n)$ channel [Residue=$^{103}Ag^{g}$,$T_{1/2}$=65.7m, $J^{\pi}=7/2^{+}$]

The residues ^{103}Ag (3α4n) are also likely to be formed by CF as well as by the ICF processes. In this case the composite system ^{119}I may emit 3α particles and 4 neutrons via CF process forming ^{103}Ag nuclei. On the other hand the ICF of α particle and ^{12}C moving as spectator may form $^{107}Ag^{*}$ excited nuclei, which may emit 4 neutrons leaving behind the ^{103}Ag nuclei. The residual nucleus ^{103}Ag has two states, the ground state $^{103}Ag^{g}$ and the meta-stable state $^{103}Ag^{m}$. In the present case, the meta-stable state of this residue could not be observed because of its short half-life $\approx$5.7 sec. The measured cross-sections for this channel may, however, include contributions from both the CF and ICF processes. The experimentally determined cross-sections for the formation of $^{103}Ag^{g}$ are given in Table 4.8. The mode of formation of this residue by CF and ICF processes may be represented as;

Complete fusion of ^{16}O, i.e.,

$$^{16}O + {}^{103}Rh \rightarrow {}^{119}I^{*} \rightarrow {}^{103}Ag^{g} + 3\alpha + 4n;$$

In-complete fusion of ^{16}O, i.e.,

$$^{16}O(\alpha + {}^{12}C) + {}^{103}Rh \rightarrow {}^{107}Ag^{*} + {}^{12}C(3\alpha); \text{(Spectator)}$$

$$^{107}Ag^{*} \rightarrow {}^{103}Ag^{g} + 4n$$

Table 4.8 Experimentally measured cross-sections for the residues populated via 2αxn (x=1 & 3) and 3αxn (x=4) channels in the interaction of ^{16}O with ^{103}Rh.

Lab Energy (MeV)	σ ($^{110}In^{g}$) (mb)	σ($^{110}In^{m}$) (mb)	σ($^{108}In^{g}$) (mb)	σ($^{108}In^{m}$) (mb)	σ($^{103}Ag^{g}$) (mb)
57.8 ± 3.5	1.0 ± 0.1	1.0 ± 0.1	-	-	-
65.8 ± 2.3	3.0 ± 0.3	18.0 ± 2.0	-	-	5.0 ± 0.5
70.8 ± 3.1	4.0 ± 0.4	51.0 ± 5.0	0.4 ± 0.04	4.0 ± 0.4	16.0 ± 2.0
77.1 ± 2.6	2.0 ± 0.3	93.0 ± 9.0	2.0 ± 0.2	5.0 ± 0.5	28.0 ±3.0
82.8 ± 2.6	4.0 ± 0.4	132.0 ± 13.0	3.0 ± 0.3	9.0 ±1.0	-

4.1.3 $^{16}O+^{27}Al$ System:

The excitation functions for five reactions in $^{16}O+^{27}Al$ system [9], have been measured in the energy range ≈58 to 94 MeV in order to study the reaction dynamics particularly in the low mass region. Most of the studies in which the occurrence of ICF has been observed were carried out generally with heavier mass target nuclei. One advantage of using a lighter mass system is to avoid the possibility of fission, which is one of the competing modes in HI reactions at these energies. The reaction residues studied for this system, characteristic γ-rays identifying the residues, their branching ratios etc., are given in Table 4.9.

Table 4.9 A list of reaction products alongwith reaction channels and their spectroscopic properties in the $^{16}O+^{27}Al$ system.

S. No.	Reaction	Residue	Half-life ($T_{1/2}$)	Spin (J^{π})	Energy of γ-ray (keV)	Branching ratio (%)
1.	$^{27}Al(O, 2\alpha n)$	$^{34}Cl^{m}$	32.2 m	3^{+}	146.5	40.5
2.	$^{27}Al(O, 3\alpha 3p)$	^{28}Mg	20.9 h	0^{+}	400.5 342.3	36.0 54
3.	$^{27}Al(O, 3\alpha 3pn)$	^{27}Mg	9.4 m	$(1/2)^{+}$	843.7	73.0
4.	$^{27}Al(O, 4\alpha 2pn)$	^{24}Na	14.6 h	4^{+}	1368	100
5.	$^{27}Al(O, 4\alpha 3p)$	^{24}Ne	3.8 m	0^{+}	472.2	100

$^{27}Al(O,2\alpha n)$ channel [Residue=$^{34}Cl^{m}$, $T_{1/2}$=32.2 min., J^{π}= 3^{+}]

The evaporation residue ^{34}Cl is likely to be formed by the CF as well ICF processes. In case of CF, it may be formed by the evaporation of 2α particles and a neutron from the excited composite system $^{43}Sc^{*}$ formed via the fusion of $^{16}O+^{27}Al$. On the other hand, the same residual nucleus may also be produced assuming that the ^{16}O ion breaks-up into $^{8}Be+^{8}Be$ fragments and one of the fragments fuses with the target nucleus ^{27}Al forming $^{35}Cl^{*}$ in the excited state which emits a neutron leaving ^{8}Be as spectator. It may also be pointed out that the residue ^{34}Cl produced via $^{27}Al(O,2\alpha n)$ channel has meta-stable as well as ground states. In the present work, the meta-stable state of the residue $^{34}Cl^{m}$ was observed through the 146.5 keV γ-ray of intensity 40.5%. Since, the intensity of the ground state of the residue $^{34}Cl^{g}$ is very low, it could not be observed. The production cross-sections of the residue $^{34}Cl^{m}$ were converted into the total cross-section of the residue ^{34}Cl by using the standard radioactive decay method. The measured cross-sections for this channel may, however, include contributions from both the CF as well as ICF processes. The production cross-sections for residues ^{34}Cl are given in Table 4.10. The CF and ICF processes leading to the formation of ^{34}Cl are;

Complete fusion of ^{16}O, i.e.,

$$^{16}O + ^{27}Al \rightarrow {}^{43}Sc^{*} \rightarrow {}^{34}Cl + 2\alpha + n;$$

In-complete fusion of ^{16}O, i.e.,

$$^{16}O\left(^{8}Be + {}^{8}Be\right) + ^{27}Al \rightarrow {}^{35}Cl^{*} + {}^{8}Be\,(2\alpha);\ \text{(Spectator)}$$

$$^{35}Cl^{*} \rightarrow {}^{34}Cl^{m} + n$$

$^{27}Al(O, 3\alpha 3p)$ channel [Residue=^{28}Mg, $T_{1/2}$=20.9 h, $J^{\pi}=0^{+}$]

The reaction product ^{28}Mg populated through $3\alpha 3p$ channel may be produced assuming that the ^{16}O ion breaks into $\alpha+^{12}C$ fragments and one of the fragments, α fuses with the target nucleus ^{27}Al forming $^{31}P^{*}$ in the excited state which decays by emitting three protons forming ^{28}Mg nuclei. The experimentally determined production cross-sections for this residue are given in Table 4.10. The mode of formation of this residue may be represented as;

Complete fusion of ^{16}O, i.e.,

$$^{16}O + ^{27}Al \rightarrow ^{43}Sc^* \rightarrow ^{31}P + 3\alpha + 3p;$$

In-complete fusion of ^{16}O, i.e.,

$$^{16}O(\alpha + ^{12}C) + ^{27}Al \rightarrow ^{31}P^* + ^{12}C(3\alpha);\ \text{(Spectator)}$$
$$^{31}P^* \rightarrow ^{28}Mg + 3p$$

$^{27}Al(O, 3\alpha 3pn)$ channel [Residue=^{27}Mg, $T_{1/2}$=9.4 m, $J^{\pi}=1/2^+$]

In case of the reaction product ^{27}Mg populated through $3\alpha 3pn$ channel, available theoretical models give negligible cross-sections, so this reaction cannot be explained by CF processes. Further, the same residual nucleus may be produced assuming that the ^{16}O ion breaks into $\alpha+^{12}C$ fragments and one of the fragments, α-particle fuses with the target nucleus ^{27}Al forming $^{31}P^*$ in the excited state which decays by emitting three protons and a neutron leaving ^{12}C particle as spectator. Activities of ^{27}Mg corresponding to $3\alpha 3pn$ channel were identified by the characteristic γ-ray energies and measured half-life. The experimentally determined cross-sections for this residue are given in Table 4.10. The mode of formation of this residue may be represented as;

In-complete fusion of ^{16}O, i.e.,

$$^{16}O(\alpha + ^{12}C) + ^{27}Al \rightarrow ^{31}P^* + ^{12}C(3\alpha);\ \text{(Spectator)}$$
$$^{31}P^* \rightarrow ^{27}Mg + 3p + n$$

$^{27}Al(O, 4\alpha 2pn)$ channel [Residue=^{24}Na, $T_{1/2}$=14.6 h, $J^{\pi}=4^+$]
$^{27}Al(O, 4\alpha 3p)$ channel [Residue=^{24}Ne, $T_{1/2}$=3.8 min., $J^{\pi}=0^+$]

The reaction products ^{24}Na and ^{24}Ne are produced through $4\alpha 2pn$ and $4\alpha 3p$ channels. The experimentally determined cross-sections for the formation of ^{24}Na and ^{24}Ne are given in Table 4.10. The detailed analysis regarding the population of these residues is presented in Chapter V.

Table 4.10 Experimentally measured cross-sections for the residues populated via 2αn, 3α3p, 3α3pn, 4α2pn and 4α3p channels in the interaction of $^{16}O + ^{27}Al$.

Lab Energy (MeV)	σ (^{34}Cl) (mb)	σ (^{28}Mg) (mb)	σ(^{27}Mg) (mb)	σ(^{24}Ne) (mb)	σ(^{24}Na) (mb)
58.0±1.3	9.40±1.69	-	-	-	0.46±0.08
58.7±1.3	1 4.57±2.62	-	-	-	1±0.18
66.5±1.2	57.72±10.39	-	-	-	0.94±0.17
68.0±1.2	62.70±11.29	-	-	-	0.96±0.17
68.2±1.2	154.09±27.74	-	-	-	0.275±0.05
71.6±1.1	115.49±20.79	-	-	-	0.63±0.11
75.4±1.1	169.53±30.52	-	-	-	0.89±0.16
76.2±1.1	100.98±18.18	0.08±0.01	-	-	1.35±0.24
77.1±1.0	126.40±22.75	0.09±0.01	-	-	1.17±0.21
78.8±1.0	95.32±17.16	-	-	-	1.2±0.22
81.8±1.0	81.96±14.75	2.48±0.44	-	-	2.35±0.42
82.0±0.9	120.91±21.76	-	-	-	1.37±0.25
85.5±0.6	84.79±15.26	2.21±0.4	-	0.12±0.03	7.88±1.41
85.9±0.9	140.79±28.26	3.11±0.5	-	0.11±0.02	5.15±0.9
88.2±0.6	15.53±2.80	1.53±0.26	0.22±0.05	0.36±0.09	1.03±0.18
88.5±0.8	-	0.42±0.05	0.2±0.05	-	1.58±0.28
91.4±0.6	5.43±0.98	-	0.08±0.02	0.22±0.05	1.15±0.20
93.4±0.8	8.26±1.48	0.4±0.08	0.11±0.02	0.12±0.05	1.5±0.27
94.4±0.6	4.75±0.85	0.2±0.06	0.1±0.03	0.1±0.03	1.33±0.24

4.2 THE FORWARD RECOIL RANGE DISTRIBUTIONS

$^{16}O+^{181}Ta$ System

The degree of the linear momentum transfer from the projectile to the target nucleus is the basis of recoil velocity of the reaction products, which may be used to differentiate the CF and ICF processes. In order to understand the CF and ICF reaction dynamics, on the basis of linear momentum transfer, the yield as a function of absorber thickness for $^{194}Tl(3n)$, $^{193}Tl^{g}(4n)$, $^{192}Tl(5n)$, $^{193}Hg^{g}(p3n)$, $^{193}Hg^{m}(p3n)$, $^{192}Hg(p4n)$, $^{191}Hg^{g}(p5n)$, $^{191}Hg^{m}(p5n)$, $^{192}Au^{g}(\alpha n)$, $^{191}Au^{g}(\alpha 2n)$, $^{190}Au^{g}(\alpha 3n)$ and $^{186}Ir^{g}(2\alpha 3n)$ nuclides produced in the $^{16}O+^{181}Ta$ system have been measured at three different projectile energies ≈81, 90 and 96 MeV. The experimental yield data has been analyzed to determine the forward recoil

ranges in each case. Details of reactions, residues, identified γ-rays and their branching ratios are listed in Table 4.2. For these reactions EFs have also been measured [1] and the details have already been given in section 4.1.1.

Table 4.11 Experimentally measured forward recoil range distributions (FRRDs) for the reaction products populated via xn (x=3, 4 & 5) and pxn (x= 3, 4 & 5) channels at ≈81 MeV beam energy.

Cumulative Thickness ($\mu g/cm^2$)	Recoil range distributions (Yield) in the unit of [mb/(mg/cm²)] for the residues							
	^{194}Tl	$^{193}Tl^{g}$	^{192}Tl	$^{193}Hg^{g}$	$^{193}Hg^{m}$	^{192}Hg	$^{191}Hg^{g}$	$^{191}Hg^{m}$
9.96	-	-	-	-	61.2	5.0	-	-
25.15	-	-	-	27.0	11.9	5.2	-	-
56.01	4.5	28.0	15.0	28.0	17.8	5.2	8.1	11.3
86.95	5.8	42.1	15.2	35.0	97.4	5.7	8.4	11.3
118.00	6.8	60.0	15.8	45.0	89.5	-	8.4	12.8
149.15	11.0	75.5	16.1	65.0	123.0	9.1	9.1	15.0
181.12	16.2	120.0	20.0	107.6	474.0	11.3	10.6	19.2
213.25	25.3	175.0	22.5	130.4	724.2	15.8	13.7	23.3
245.34	29.9	233.0	23.7	175.0	1260.0	18.7	20.8	24.1
277.61	30.5	238.0	22.8	180.7	1376.5	16.6	27.0	20.4
309.92	28.0	215.0	20.2	163.1	1198.0	12.4	22.7	15.2
343.13	22.0	174.0	17.3	145.7	1037.6	10.0	17.1	13.0
376.63	15.0	100.0	16.2	95.8	700.7	6.6	11.2	11.1
410.16	11.0	65.0	15.2	60.0	400.8	5.4	8.6	11.0
443.69	7.0	45.0	14.9	45.7	200.3	4.7	8.5	10.8
477.24	5.4	25.0	15.0	36.7	90.4	4.8	8.2	10.8
510.83	-	-	-	24.4	18.8	5.0	-	-

In the experiment performed to measure the FRRDs [10], samples of ^{181}Ta (≈150 $\mu g/cm^2$) deposited on Al-backing (≈1.0-1.2 mg/cm^2) were bombarded by ^{16}O beam, with Al-backing facing the beam, at three different projectile energies i.e., at 85, 94 and 100 MeV. After some energy loss in the Al-backing the incident energies in three separate irradiations are estimated to be ≈81, 90 and 96 MeV respectively. The samples were followed by a stack of thin Al-catcher foils of thickness ranging from ≈10-65 $\mu g/cm^2$. The recoiling residues get trapped in the catcher foils at different thicknesses in Al-catchers. The activities induced in individual

catcher foils were followed off-line. The residues embedded in different catcher foils were identified by their characteristic γ-radiations as well as by the measured half-lives. The cross-sections corresponding to various radioactive residues in each catcher were obtained from the intensity of identified γ-rays. In this way, the cross-section for a particular evaporation residue in each catcher foil was determined. In order to obtain the FRRDs, the measured cross-section for each evaporation residue in individual catcher was divided by the respective thickness of that catcher foil. The results of FRRD measurements for $^{16}O+^{181}Ta$ system at ≈81, 90 and 96 MeV, are tabulated in Tables 4.11-4.16.

Table 4.12 Experimentally measured forward recoil range distributions (FRRDs) for the reaction products populated via αxn (x=1, 2 & 3) and 2α3n channels at ≈81 MeV beam energy.

Cumulative Thickness ($\mu g/cm^2$)	Recoil range distributions (Yield) in the unit of [mb/(mg/cm²)] for the residues			
	$^{192}Au^g$	$^{191}Au^g$	$^{190}Au^g$	$^{186}Ir^g$
9.96	1.3	9.0	-	7.0
25.15	1.2	9.0	-	7.1
56.01	1.8	9.0	49.7	7.5
86.95	4.9	9.7	49.6	9.9
118.00	10.6	13.6	43.5	11.4
149.15	14.1	30.1	78.4	10.1
181.12	14.3	43.3	160.8	16.1
213.25	17.5	49.7	151.1	10.7
245.34	22.7	55.0	247.7	15.8
277.61	26.3	47.4	329.7	14.0
309.92	22.6	29.8	339.5	10.8
343.13	16.6	15.2	239.3	8.3
376.63	8.2	9.7	128.6	7.2
410.16	3.7	8.4	67.8	6.9
443.69	1.8	9.0	50.4	6.8
477.24	1.2	7.5	46.5	6.6
510.83	1.2	9.0	-	7.1

Table 4.13 Experimentally measured forward recoil range distributions (FRRDs) for the reaction products populated via xn (x=3, 4 & 5) and pxn (x= 3, 4 & 5) channels at ≈90 MeV beam energy.

Cumulative Thickness ($\mu g/cm^2$)	Recoil range distributions (Yield) in the unit of [mb/(mg/cm²)] for the residues							
	^{194}Tl	$^{193}Tl^{g}$	^{192}Tl	$^{193}Hg^{g}$	$^{193}Hg^{m}$	^{192}Hg	$^{191}Hg^{g}$	$^{191}Hg^{m}$
23.33	28.3	52.3	-	-	1.7	-	-	-
46.85	8.9	85.0	-	23.4	3.4	7.7	20.0	16.0
70.63	15.1	96.3	-	30.0	3.8	8.8	22.0	17.0
94.52	8.8	50.0	-	40.0	3.4	5.9	21.0	18.4
118.87	9.9	51.8	198.0	55.0	4.9	10.7	18.0	22.0
143.93	12.0	55.0	175.0	110.0	8.8	31.1	24.0	30.7
169.28	-	-	180.0	125.0	24.5	77.7	-	-
195.84	22.0	122.4	200.0	170.6	41.4	113.0	50.0	39.0
224.92	48.8	175.0	353.2	200.0	55.0	196.0	70.0	45.4
254.00	64.0	254.8	760.3	230.4	71.5	280.0	91.5	42.0
283.40	73.5	195.2	452.4	220.0	71.8	379.3	77.0	34.4
318.85	55.0	125.0	194.9	175.0	42.6	310.3	50.0	27.9
354.92	23.8	61.8	190.0	120.0	25.7	145.6	30.0	20.2
391.27	16.0	50.0	185.0	55.9	12.4	88.0	24.0	18.0
445.31	12.0	43.0	-	18.7	5.9	22.4	20.5	17.0
500.05	11.0	41.0	-	17.4	2.9	13.3	21.0	16.5
554.99	11.0	46.0	-	8.4	1.0	1.8	19.0	16.0

Table 4.14 Experimentally measured forward recoil range distributions (FRRDs) for the reaction products populated via αxn (x=1, 2 & 3) and 2α3n channels at ≈90 MeV beam energy.

Cumulative Thickness ($\mu g/cm^2$)	Recoil range distributions (Yield) in the unit of [mb/(mg/cm²)] for the residues			
	$^{192}Au^{g}$	$^{191}Au^{g}$	$^{190}Au^{g}$	$^{186}Ir^{g}$
23.33	-	-	14.0	-
46.85	4.2	25.0	16.6	2.6
70.63	5.9	28.0	16.0	12.6
94.52	5.1	48.0	13.8	6.0
118.87	19.3	76.0	23.0	6.5

143.93	85.0	128.0	42.7	10.0
169.28	321.5	150.0	120.0	14.0
195.84	555.0	45.0	165.0	8.0
224.92	831.2	165.0	144.0	17.0
254.00	1244.0	220.0	210.1	20.3
283.40	1050.0	303.4	245.2	19.1
318.85	450.0	230.0	150.6	10.0
354.92	170.0	86.8	49.6	5.0
391.27	30.0	30.0	28.1	3.0
445.31	35.0	20.0	20.0	3.0
500.05	29.0	20.0	22.0	2.7
554.99	2.9.0	12.0	21.0	3.0

Table 4.15 Experimentally measured forward recoil range distributions (FRRDs) for the reaction products populated via xn (x=3, 4 & 5) and pxn (x= 3, 4 & 5) channels at ≈96 MeV beam energy.

Cumulative Thickness ($\mu g/cm^2$)	Recoil range distributions (Yield) in the unit of [mb/(mg/cm²)] for the residues							
	^{194}Tl	$^{193}Tl^{g}$	^{192}Tl	$^{193}Hg^{g}$	$^{193}Hg^{m}$	^{192}Hg	$^{191}Hg^{g}$	$^{191}Hg^{m}$
10.01	9.90	9.9	15.9	5.0	-	2.0	9.0	3.0
26.18	20.00	-	-	4.9	-	1.9	14.8	4.3
44.35	10.40	-	-	5.0	0.6	3.9	7.7	3.3
62.67	8.10	-	-	4.9	0.6	4.4	8.2	3.3
81.67	2.50	9.5	278.4	5.3	0.5	3.5	6.8	3.7
100.96	2.60	10.3	34.0	-	0.5	5.0	7.3	4.7
120.86	2.00	10.5	49.8	6.0	0.5	8.0	7.0	4.1
142.45	2.30	11.5	95.0	6.1	0.6	17.1	8.3	5.6
165.78	3.50	14.1	130.0	7.0	0.6	25.7	13.3	9.0
205.94	7.00	20.4	201.4	12.5	1.0	38.8	30.0	15.0
246.11	17.50	27.0	230.0	25.0	1.7	60.0	63.5	22.0
286.67	21.70	32.3	226.0	38.0	2.5	72.7	67.3	26.9
337.37	13.60	27.0	135.0	27.2	2.0	64.1	35.0	21.7
388.10	4.33	18.0	60.0	12.0	0.9	35.5	12.0	13.0
438.99	3.20	12.5	25.0	5.3	0.6	17.0	7.0	6.0
490.67	2.10	10.3	23.0	4.8	0.5	7.0	8.0	4.1
547.44	1.80	9.7	20.0	4.6	0.5	3.2	7.0	3.8

Table 4.16 Experimentally measured forward recoil range distributions (FRRDs) for the reaction products populated via αxn (x=1, 2 & 3) and 2α3n channels at ≈96 MeV beam energy.

Cumulative Thickness ($\mu g/cm^2$)	Recoil range distributions (Yield) in the unit of [mb/(mg/cm²)] for the residues			
	$^{192}Au^g$	$^{191}Au^g$	$^{190}Au^g$	$^{186}Ir^g$
10.01	11.0	7.0	11.0	-
26.18	6.2	-	-	-
44.35	9.9	7.2	-	0.8
62.67	12.0	7.0	12.6	1.1
81.67	12.1	7.4	10.0	1.3
100.96	16.1	8.3	10.0	1.8
120.86	18.0	9.1	10.1	2.5
142.45	39.4	11.1	23.0	1.8
165.78	45.0	14.0	32.0	1.4
205.94	91.6	17.9	49.1	2.2
246.11	95.0	11.5	48.5	1.0
286.67	144.7	16.5	42.4	1.7
337.37	92.0	13.6	26.0	0.8
388.10	25.0	7.5	12.0	0.8
438.99	13.0	6.8	11.0	0.8
490.67	13.0	7.0	10.0	-
547.44	12.0	7.1	9.0	-

In order to obtain the relative contributions of CF and ICF processes in various reactions in $^{16}O+^{181}Ta$ system. The measured FRRDs have been analyzed within the frame work of linear momentum transfer based on break-up fusion model. The analysis of these FRRDs is discussed in the Chapter V.

4.3 ANGULAR DISTRIBUTIONS

$^{16}O+^{27}Al$ System

In the present work, angular distribution of the recoiling residues produced in the ^{16}O $+^{27}Al$ system have been measured at ≈85 MeV incident projectile energy. The details of the experimental setup are already given in section 2.4.3, of Chapter II of the thesis. The outgoing residues were trapped in the annular catcher foils. The activities induced in the individual annular catcher foils were followed off-line. It may be pointed out that, out of the five reactions identified in the EF measurements, only the γ-ray of 146.5 keV corresponding to the reaction $^{27}Al(^{16}O,2\alpha n)^{34}Cl$ could be identified from its energy as well as by the half-life of residue ^{34}Cl in the angular distribution measurements. The likely reasons for not observing γ-rays corresponding to other residues have been discussed in Chapter V, section 5.5. Further, the measured cross-sections for the reaction $^{27}Al(^{16}O,2\alpha n)^{34}Cl$ corresponding to various angular ranges are given in Table 4.17.

Table 4.17 Experimentally measured angular distribution for the reaction $^{27}Al(^{16}O,2\alpha n)^{34}Cl$ at ≈85 MeV beam energy.

S. No.	Angular range	σ(mb)
1	0°-13°	142.76 ± 21.4
2	13°-21°	9.05 ± 1.4
3	21°-30°	10.23 ± 1.5
4	30°-39°	1.39 ± 0.2
5	39°-45°	0.17 ± 0.03
6	45°-60°	0.46 ± 0.07

References

[1] Devendra P. Singh, Unnati, Abhishek Yadav, Pushpendra P. Singh, Manoj Kumar Sharma, B.P. Singh, K. S. Golda, R. Kumar, A. K. Sinha and R. Prasad; Physical Review C 80, 014601(2009).

[2] S. F. Mughabghab, M. Divadeenam, and N. E. Holden, Neutron Cross Sections (Academic Press, New York, 1981), Vol. 1, Part A, page 89

[3] E. Browne and R. B. Firestone; Table of Radioactive Isotopes (Wiley, New York, 1986).

[4] U. Reus and W.Westmeirer; At. Data Nucl. Data Tables 29, 338(1983).

[5] Unnati Gupta, Pushpendra P. Singh, Devendra P. Singh, Manoj Kumar Sharma, Abhishek Yadav, R. Kumar, B. P. Singh and R. Prasad; Nuclear Physics A 811, 77(2008).

[6] Unnati; Ph. D. Thesis, Aligarh Muslim University, Aligarh (2006) Unpublished.

[7] A. Gavron; Phys. Rev. C 21, 230(1980).

[8] M. Cavinato, E. Fabrici, E. Gadioli Ebra, P. Vergani, M. Crippa, G. Colombo, I. Redaelli and M. Riapamonti; Phys. Rev. C52, 2577(1995).

[9] Manoj Kumar Sharma, Unnati, Devendra P. Singh, Pushpendra P. Singh, B. P. Singh, H. D. Bhardwaj and R. Prasad; Phys. Rev. C75, 064608(2007).

[10] Devendra P. Singh, Unnati, Abhishek Yadav, Pushpendra P. Singh, Manoj Kumar Sharma, B. P. Singh, K. S. Golda, R. Kumar, A. K. Sinha and R. Prasad; Physical Review C, Communicated (2009).

Chapter V

RESULTS AND DISCUSSION

In order to understand the reaction dynamics of heavy ion interaction at about 7 MeV/nucleon energy, several experiments have been performed by our group. Results on ^{16}O + ^{181}Ta, ^{16}O + ^{103}Rh and ^{16}O + ^{27}Al systems are discussed here. In the present work, excitation functions (EFs) for twenty seven reactions have been measured at energies < 7 MeV/nucleon. A list of these reactions is given below;

$^{181}Ta(O, 3n)^{194}Tl^{g}$, $^{181}Ta(O, 3n)^{194}Tl^{m}$, $^{181}Ta(O, 4n)^{193}Tl^{g}$,

$^{181}Ta(O,4n)^{193}Tl^{m}$, $^{181}Ta(O,5n)^{192}Tl^{g}$, $^{181}Ta(O, 5n)^{192}Tl^{m}$,

$^{181}Ta(O, p3n)^{193}Hg^{g}$, $^{181}Ta(O, p3n)^{193}Hg^{m}$, $^{181}Ta(O, p4n)^{192}Hg$,

$^{181}Ta(O, p5n)^{191}Hg^{g}$, $^{181}Ta(O, p5n)^{191}Hg^{m}$, $^{181}Ta(O, \alpha n)^{192}Au^{g}$,

$^{181}Ta(O, \alpha 2n)^{191}Au^{g}$, $^{181}Ta(O, \alpha 3n)^{190}Au^{g}$, $^{103}Rh(O, p3n)^{115}Te^{g}$,

$^{103}Rh(O, p3n)^{115}Te^{m}$, $^{103}Rh(O, p4n)^{114}Te$, $^{103}Rh(O, 2\alpha n)^{110}In^{g}$,

$^{103}Rh(O, 2\alpha n)^{110}In^{m}$, $^{103}Rh(O, 2\alpha 3n)^{108}In^{g}$, $^{103}Rh(O,2\alpha 3n)^{108}In^{m}$,

$^{103}Rh(O, 3\alpha 4n)^{103}Ag^{g}$, $^{27}Al(O, 2\alpha n)^{34}Cl$, $^{27}Al(O, 3\alpha 3p)^{28}Mg$,

$^{27}Al(O, 3\alpha 3pn)^{27}Mg$, $^{27}Al(O, 4\alpha 2pn)^{24}Na$ and $^{27}Al(O, 4\alpha 3p)^{24}Ne$.

The presently measured EFs have been analyzed within the framework of theoretical model code PACE4 [1]. Further, in the complementary experiments to investigate fusion in-completeness due to fractional linear momentum transfer from the projectile to the target nucleus and to separate out the relative percentage contributions of complete fusion (CF) and/or in-complete fusion (ICF), forward recoil range distributions (FRRDs) of various radio-nuclides produced via CF and/or ICF in $^{16}O+^{181}Ta$ system have been measured at ≈81, 90 & 96 MeV beam energies. A list of the reactions for which the RRDs have been measured is given below;

$^{181}Ta(O, 3n)^{194}Tl$, $^{181}Ta(O, 4n)^{193}Tl$, $^{181}Ta(O,5n)^{192}Tl$,

$^{181}Ta(O, p3n)^{193}Hg^{g}$, $^{181}Ta(O, p3n)^{193}Hg^{m}$, $^{181}Ta(O, p4n)^{192}Hg$,

^{181}Ta(O, p5n)^{191}Hg^{g}, ^{181}Ta(O, p5n)^{191}Hg^{m}, ^{181}Ta(O, αn)^{192}Au^{g},

^{181}Ta(O, α2n)^{191}Au^{g}, ^{181}Ta(O, α3n)^{190}Au^{g} and ^{181}Ta(O, 2α3n)^{186}Ir^{g}

Further, the angular distribution (AD) for residues populated in the system ^{16}O + ^{27}Al have also been measured with a view to separate the CF and ICF components.

Analysis of Excitation Functions

In the present work, analysis of measured EFs has been done using the code PACE4 [1]. However, in case of the system ^{16}O + ^{27}Al, the codes CASCADE and ALICE-91 have also been used. The code PACE4 [1] is based on statistical approach. In this code the de-excitation of the compound nucleus (CN) is followed by Monte-Carlo procedure. In code PACE4 the level density parameter (LDP) 'a' (a = A/K) is an important parameter which mainly governs the equilibrium state. Here, 'A' is the atomic mass number of the compound nucleus and 'K' is a free parameter. The value of 'K' may be varied to match the experimental data. In the present work, the experimental data has been tested using different values of level density parameters. Although, it is possible to explain all the EFs for a given system with different values of LDPs for individual channels, however, from the physics point of view, it is quite unreasonable. As such, in the present work all the calculations have been performed consistently using same set of parameters for all the channels of a given system. The theoretical calculations done by adopting a given set of parameters are found to agree well with the experimentally measured EFs for CF channels.

5.1 ^{16}O +^{181}Ta System

In order to study the effect of 'K' on the EFs, calculations have been performed for different values of 'K' (=8, 9 and 10). The effect of variation of K on calculated EFs is shown in the Figs. 5.1.1 (a-c) and Figs. 5.1.2 (a-c), for CF channels. As can be seen from these figures, in the present work, a value of K =10 is found to give a satisfactory representation of the experimental data for these channels, in general. Obviously these channels are populated only by CF. As can be seen from Fig. 5.1.1 (a) that, the measured EF for the reaction ^{181}Ta(^{16}O, 3n)^{194}Tl is qualitatively in good

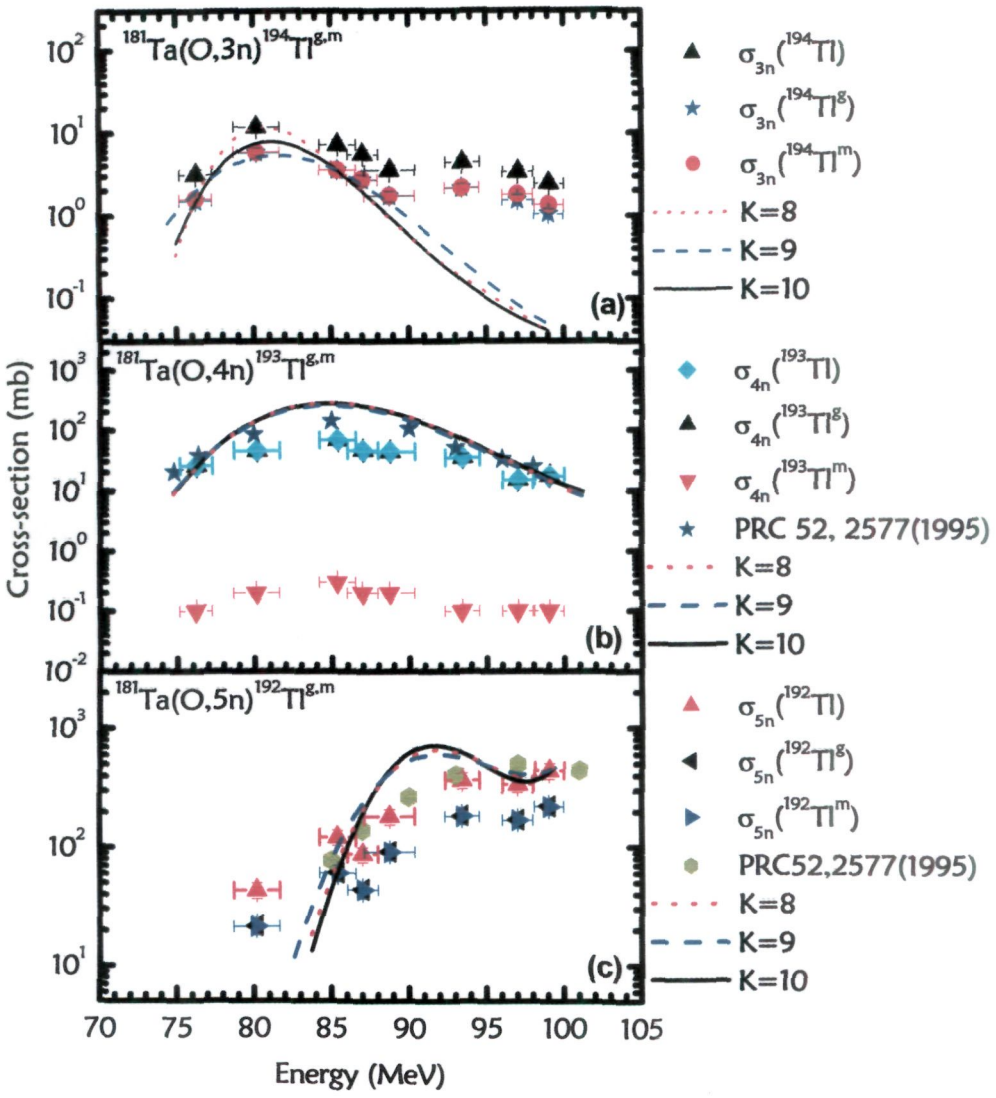

Figure 5.1.1: Experimentally measured and theoretically calculated EFs for ^{194}Tl, ^{193}Tl and ^{192}Tl residues populated via xn (x=3, 4 & 5) channels respectively in the interaction of ^{16}O+^{181}Ta. The filled symbols represent the experimental data and various curves correspond to the theoretical predictions of the code PACE4 for different values of K.

agreement with the predictions based on the theoretical model code PACE4 at energies from near the threshold to well above the peak region. However, in the tail portion of the EF, the theoretical calculation of code PACE4 underestimates the experimental data. As has already been mentioned, the code PACE4 does not take into account the pre-equilibrium (PE) emission. As such, the discrepancy in the tail part between the measured and calculated EFs for 3n-channel may be attributed to the PE emission, which is likely to be a dominant mode of reaction mechanism at relatively higher energies [2]. Blann [3, 4], in his study on the role of pre-compound decay in HI reactions has indicated that the significant contribution to the PE-emission may come from the multiple pre-compound emissions at higher energies and also from equilibration collisions, if they take place in the low density region. It has also been pointed out that in HI reactions, all partial waves do not contribute to the fusion and the assumed spherical shape for corresponding HI may not be appropriate. As such, the difference of measured cross-sections as compared to statistical model CN calculations may be attributed to the PE-emission, which in case of ^{181}Ta(^{16}O, 3n)^{194}Tl reaction is more than an order of magnitude higher at $\approx$ 100 MeV. Since, code PACE4 does not taken into account the PE-emission and since, ICF can not be considered for 3n-channel, the enhancement in the measured EF as compared to PACE4 calculations in the higher energy region may be due to PE-emission. Further, as can be seen from Figs. 5.1.1 (b & c), where EFs for ^{193}Tl(4n) and ^{192}Tl(5n) are compared with statistical model calculations, that the shapes of the EFs are satisfactorily reproduced for the entire energy region of interest. It is because the probability of pre-equilibrium emission in these cases is much lower on account of low excitation energy.

In the case of pxn (x =3, 4 & 5) channels, there is no likelihood of ICF and, therefore, these channels are also populated by CF only, like xn channels. The measured EFs for the residues corresponding to p3n, p4n, and p5n channels are shown in Figs. 5.1.2 (a-c). It may, be pointed out that in the present work, the population cross-sections for ^{193}Hg(p3n) and ^{191}Hg(p5n) residues of ground as well as meta-stable states have been measured and are shown by respective symbols alongwith the sum of ground and meta-stable state contributions. It may, however, be mentioned that the general trends and shape of the measured EFs for the CF residues populated via pxn (x =3, 4 & 5) channels are satisfactorily reproduced by PACE4 calculations. Further, as can be seen from these figures that the measured

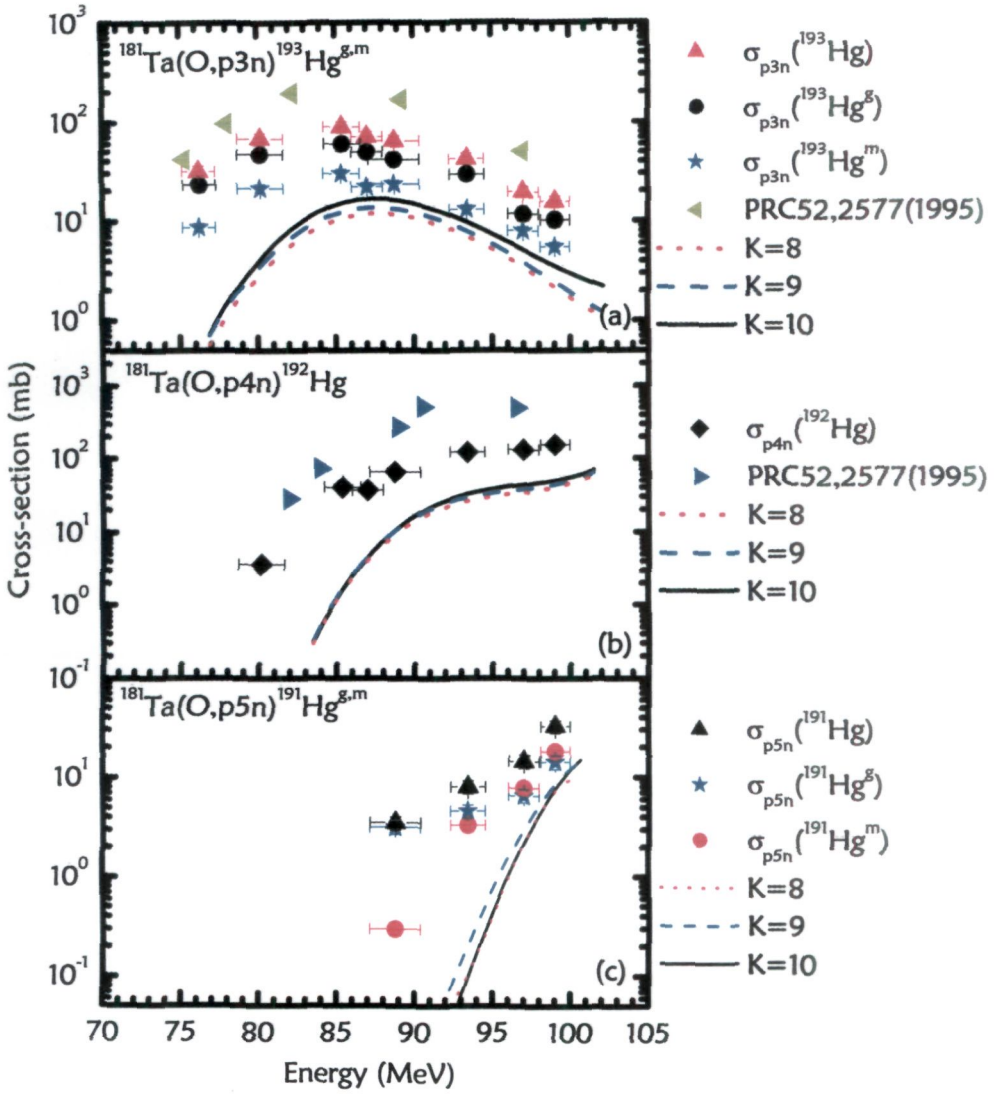

Figure 5.1.2: Experimentally measured and theoretically calculated EFs for ^{193}Hg, ^{192}Hg and ^{191}Hg residues populated via pxn (x=3, 4 & 5) channels in the interaction of ^{16}O+^{181}Ta. The filled symbols represent the experimental data and various curves correspond to the theoretical predictions of the code PACE4 for different values of parameter K.

cross-sections are somewhat enhanced as compared to the theoretical model predictions. The enhancement in the measured cross-sections over their theoretical predictions based on code PACE4 may be explained considering some contribution to these residues coming from the decay of higher charge isobar precursor (Tl) isotopes. In the case of p3n and p4n channels, the contribution of precursor decay could not be determined because of either the in-complete decay scheme or the unknown decay characteristics of the precursor. For example, in the case of p4n channel, the cross-sections for the independent decay of precursor formed by the 5n channel are found to be higher than the cross-sections for residue ^{192}Hg populated by the p4n channel. This may happen, if the precursor does not feed the residue ^{192}Hg formed by the p4n channel. As such, the decay schemes of ^{192}Hg and ^{193}Hg need further investigation. The cross-section values shown in the respective figures for these reactions also contain precursor contribution, if any. However, in the case of the p5n channel, the precursor ^{191}Tl, which may be produced by 6n channel, is not likely to be produced in the present experiment on account of its higher threshold (≥100 MeV).

In Fig. 5.1.3, to determine the total measured fusion cross-section $\Sigma\sigma_{CF}$ (expt), the sum of cross-sections due to xn channels, i.e., $\Sigma\sigma_{xn}$, and the sum of cross-sections due to all measured pxn channels, i.e., $\Sigma\sigma_{pxn}$, have been added. The $\Sigma\sigma_{CF}$ (expt) shown in Fig. 5.1.3, has been compared with $\Sigma\sigma_{CF}$ (Th) obtained using the code PACE4 [1] with different values of level density parameter constant 'K'. As can be seen from Fig. 5.1.3, the $\Sigma\sigma_{CF}$ (expt) is in good agreement with theoretical $\Sigma\sigma_{CF}$ values. The fact that the measured fusion cross-section $\Sigma\sigma_{CF}$ (expt) could be reproduced satisfactorily by PACE4 predictions strengthens the confidence in the choice of input parameters. Also, a value of LDP (a = A/8 MeV^{-1}) has also been suggested by Cavinato et al. [5] for nuclei far from the magic region. The same set of parameters has been retained and used to fit the EFs of all the α-emitting channels as well. As has already been pointed out, ICF is not taken into consideration in the theoretical model code PACE4, hence, if there is any enhancement in the experimentally measured production cross-section as compared to PACE4 calculations, it may be attributed to the ICF processes [6, 7]. In Figs. 5.1.4(a-c), the measured cross-sections for the population of $^{193-x}$Au (x = 1, 2 & 3) isotopes via αxn channels are shown alongwith the

theoretical predictions of code PACE4 using consistently the same set of parameters as used for reproducing the CF channels. Note that in the case of αxn channels, the residues may be formed in two ways; (i) by CF of ^{16}O followed by the formation of an excited CN from which evaporation of neutrons and α-particles takes place, and/or (ii) the ^{16}O ion breaks into α + ^{12}C and ^{12}C fuses with the target nucleus leaving an α-particle as spectator. In this case the excited nucleus formed by the fusion of ^{12}C may emit neutrons while de-exciting. As can be perceived from these figures, the experimentally measured EFs are relatively higher, by several orders of magnitude, as compared to that of theoretical predictions. Since, the code PACE4 does not take ICF processes into account, the enhancement in the experimentally measured production cross-sections may be attributed to

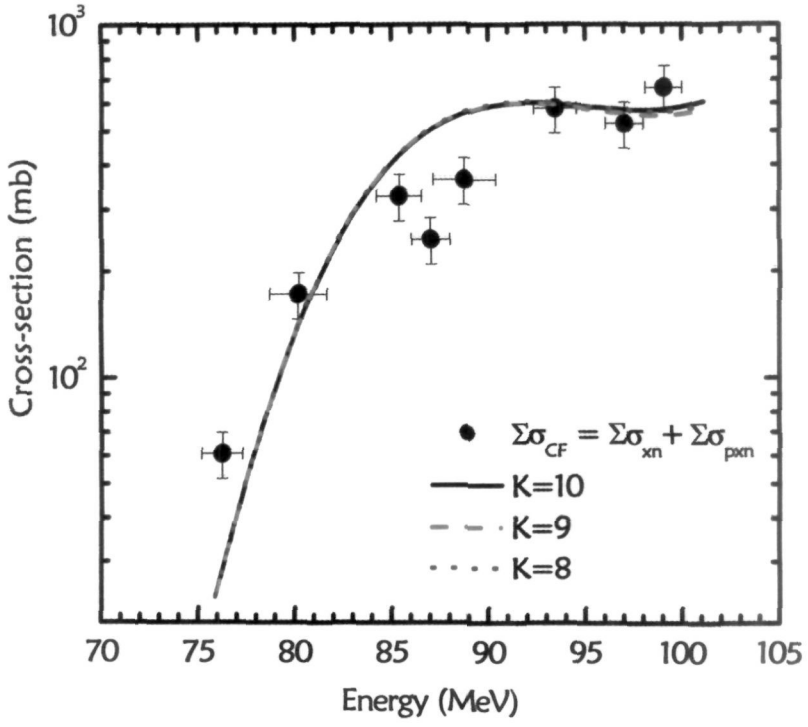

Figure 5.1.3: The sum of cross-sections for the xn and pxn channels. The effect of the variation of the level density parameter K (=8, 9 & 10) on calculated $\Sigma\sigma_{CF}$ is also shown.

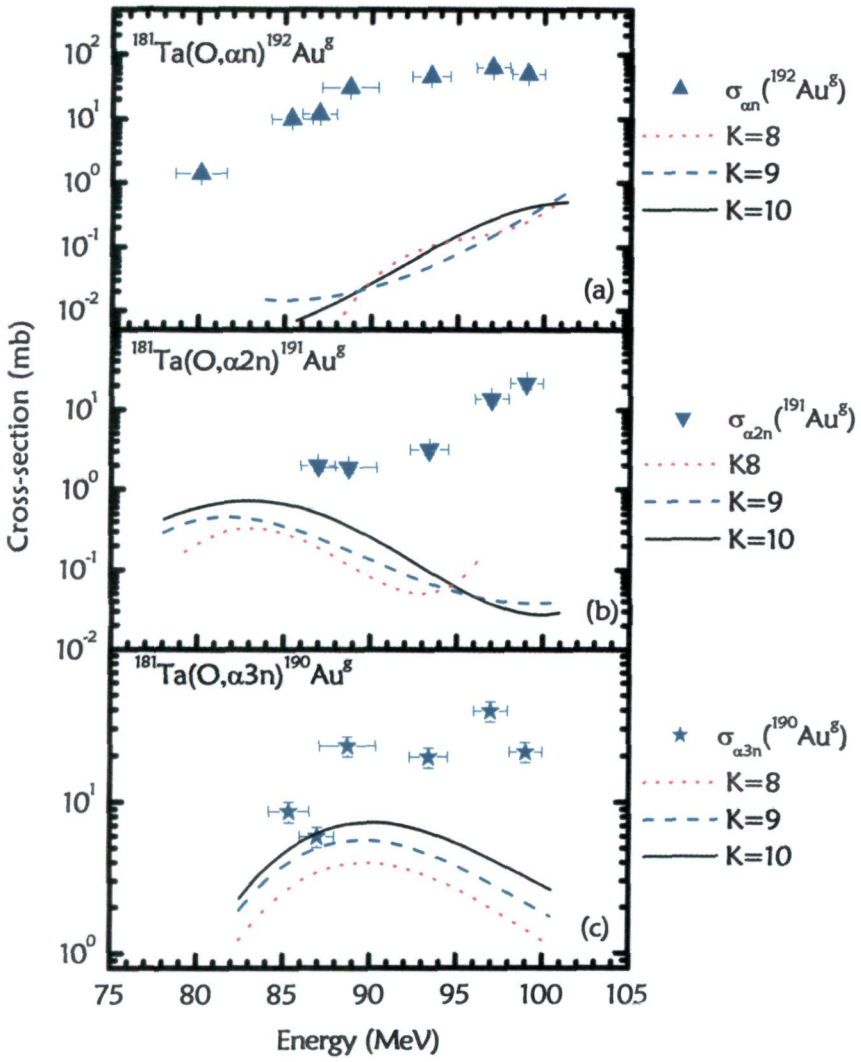

Figure 5.1.4: Experimentally measured and theoretically calculated EFs for ^{192}Au^{g}, ^{191}Au^{g} and ^{190}Au^{g} residues populated respectively via αxn (x=1, 2 & 3) channels produced in the interaction of ^{16}O+^{181}Ta. The filled symbols represent the experimental data and various curves correspond to the *theoretical predictions of the code* PACE4 *for different values of parameter* K.

the contribution coming from ICF of ^{16}O with the target nucleus. As such, these residues are supposed to be populated both via CF and/or ICF processes. The production of these residues may take place via the decay of CN followed by entire projectile fusion in CF process, and/or via fusion of ^{12}C from ^{16}O projectile in ICF process leading to the formation of $^{193}Au^*$, an in-completely fused composite system. In this case, it has been assumed that ^{16}O projectile may breakup into $^{12}C+\alpha$, and out of these a part of the projectile i.e., ^{12}C fuses with the target ^{181}Ta, while remaining part moves in the forward direction with almost the same velocity as that of the projectile.

The residue $^{192}Au^g$ populated via αn channel needs special mention. The *residue $^{192}Au^g$ may also be populated through the decay of ^{192}Hg via β^+/EC* decay. Both, $^{192}Au^g$ ($T_{1/2}$ = 4.94 h) and ^{192}Hg ($T_{1/2}$ = 4.85 h) have nearly the same half-lives. In this case, it has been possible to separate out the contribution from the decay of ^{192}Hg populated via the p4n channel using decay curve analysis. It is known from the successive radio-active decay that, if the daughter nucleus half-life (T_A) and the parent nucleus half-life (T_B) are nearly equal, as in the present case, such that $T_A = T_B(1 + \delta)$, where $\delta << 1$, *then the activity ratio increases approximately linearly with time, so* long as $t << 2\tau_B/\delta$ [8], where τ_B is the mean-life time of the parent nucleus. To obtain the cross-section of $^{192}Au^g$, a curve between the lapse time and its production cross-section was plotted at different times and also at different energies. To obtain the independent production cross-sections at each energy, plots for different lapse times were extrapolated at t = 0 time using a least-square linear fitting method. The cross-section at time t = 0 is the independent cross-section for the production of $^{192}Au^g$. In Figs. 5.1.4(a) and 5.1.5(a), the cross-sections deduced as mentioned above for the independent production of $^{192}Au^g$ have been plotted. Here [Fig. 5.1.5 (a)], the sum of cross-sections for all measured αxn channels, i.e., $\Sigma\sigma_{\alpha xn}$(expt), is also shown alongwith measured αxn channels, and is found to increase with energy.

It has already been mentioned that all the α-emission channels identified in the present work are expected to have significant contributions from ICF processes. To determine the contribution from ICF processes to the αxn channels, the measured $\Sigma\sigma_{\alpha xn}$(expt) has been compared with the corresponding values calculated using the theoretical model code PACE4,

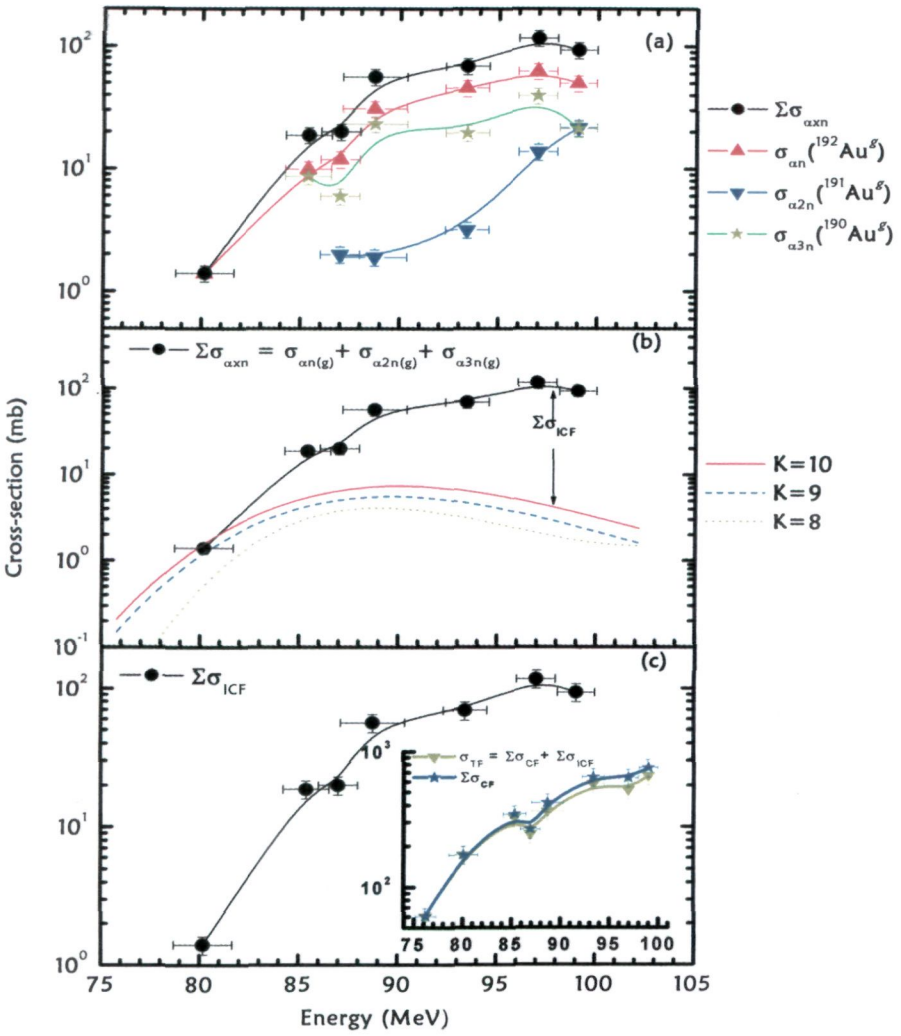

Figure 5.1.5: (a) Measured EFs for αxn (x = 1, 2 & 3) channels and $\Sigma\sigma_{\alpha xn}$, (b) sum of the αxn channels, measured as well as calculated using PACE4 for K (= 8, 9 & 10) and (c) sum of σ_{ICF} (all αxn) channels. In panels (a), (b) & (c) the spline like lines joining the experimental data points are just to guide the eyes. The inset shows cross-sections for the sum of both CF and ICF channels and for CF channels separately. The increasing difference, between the two curves in the inset, with energy indicates the dominance of ICF processes with energy.

which is based on statistical CN theory. Because the code does not take ICF into consideration, the calculated cross-sections for $\Sigma\sigma_{\alpha xn}$ with code PACE4 have predictions based on the CF model only. In Fig. 5.1.5 (b), a comparison of $\Sigma\sigma_{\alpha xn}$(expt) has been made with $\Sigma\sigma_{\alpha xn}$(Th) calculated using the CF model for three different values of physically acceptable [9] level density parameters (K = 8, 9 & 10). As can be seen from this figure, the $\Sigma\sigma_{\alpha xn}$(Th), with any of the reasonable parameters could not reproduce $\Sigma\sigma_{\alpha xn}$(expt) above 85 MeV. The measured $\Sigma\sigma_{\alpha xn}$(expt) agree very well with $\Sigma\sigma_{\alpha xn}$(Th) at 80 MeV. However, above this data point all the measured cross-sections are found to be much higher as compared to the theoretical predictions based on the PACE4 model. The difference between the experimental and the theoretical values of $\Sigma\sigma_{\alpha xn}$ may be assigned to the ICF processes and has been denoted by $\Sigma\sigma_{ICF}$ (expt). Further, the difference between $\Sigma\sigma_{\alpha xn}$(expt) and $\Sigma\sigma_{\alpha xn}$(Th) is found to increase with energy above 80 MeV, indicating the dominance of ICF processes at relatively higher energies, with maximum ICF contribution at the highest studied energy i.e., 100 MeV. In Fig. 5.1.5 (c), the $\Sigma\sigma_{ICF}$ values obtained by subtracting $\Sigma\sigma_{ICF}$(Th) (K =10) from measured $\Sigma\sigma_{\alpha xn}$ have been plotted as a function of beam energy. As can be seen from this figure, ICF production increases very rapidly with energy. In the inset of Fig. 5.1.5 (c), σ_{TF} (total sum of cross-sections for all measured channels) and $\Sigma\sigma_{CF}$ are compared. As can be seen from this figure (inset), with the increase in energy the difference between σ_{TF} and $\Sigma\sigma_{CF}$ continues to increase, indicating the dominance of ICF at relatively higher energies.

At energies above the CB, where $E >> V_0$, the classical formula of Weisskopf [10] for capture of charge particle by a nucleus is given by;

$$\sigma_{CF}(E) = \pi r_0^2 \, (1 - V_0 / E) \qquad (1)$$

where, V_0 is the value of CB and E is the energy in center of mass system. As such, if σ_{CF} (expt) is plotted against $1/E_{c.m.}$, it should be a linear curve. The deduced $\Sigma\sigma_{CF}$ values from $\Sigma\sigma_{xn} + \Sigma\sigma_{pxn} + \Sigma\sigma_{\alpha xn}$(Th) have been plotted as a function of $1/E_{c.m.}$ in Fig. 5.1.6. A fit to the $\Sigma\sigma_{CF}$ data points indicates a linear curve that cuts the x-axis at the beam energy equal to CB. It may, however, be pointed out that a departure from linearity above CB may indicate the approach to and beginning of a quantal regime giving rise to sub-barrier fusion.

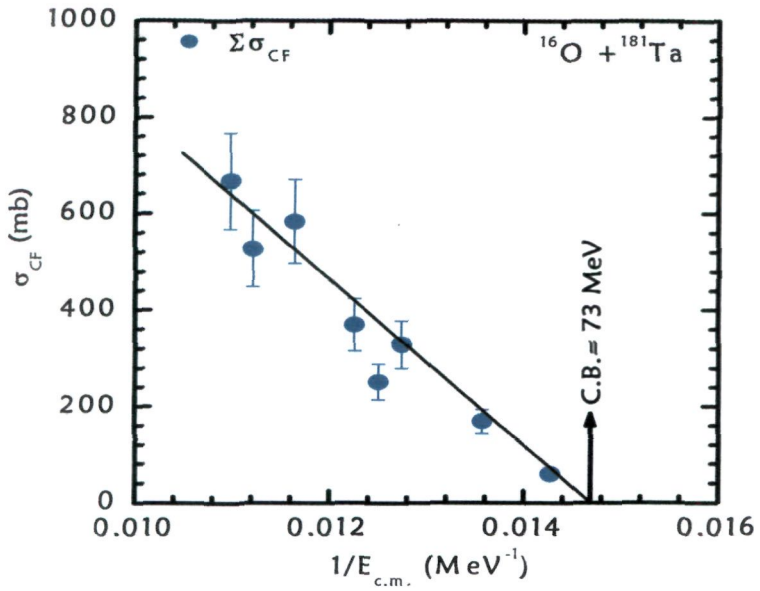

Figure 5.1.6: Experimentally measured production cross-sections found to reproduce the Coulomb barrier of $^{16}O+^{181}Ta$ system.

5.2 $^{16}O + ^{103}Rh$ System

In the present work, EFs for the reactions produced in $^{16}O+^{103}Rh$ system have also been analyzed employing the theoretical model code PACE4. Since, in these calculations 'K' is an important parameter, effect of variation of K(=8, 9 & 10) have been tested and are shown in Figs. 5.2.1-5.2.2, alongwith the experimentally measured cross-sections for the reactions $^{103}Rh(^{16}O, p3n)$, $^{103}Rh(^{16}O, p4n)$, $^{103}Rh(^{16}O, 2\alpha n)$, $^{103}Rh(^{16}O, 2\alpha 3n)$ and $^{103}Rh(^{16}O, 3\alpha 4n)$. In the present work a value of K =8 is found to give a satisfactory reproduction of experimental data for CF channels. The calculations with same value of K(=8) have been found to give a satisfactory reproduction of experimental data in case of $^{16}O+^{181}Ta$ system as well. As mentioned earlier also, it might be possible to reproduce all the EFs with different values of parameters of the code for individual channels, however, it is not reasonable from the physics point of view. Further, a value of K > 10 may give rise to the anomalous effect in the particle

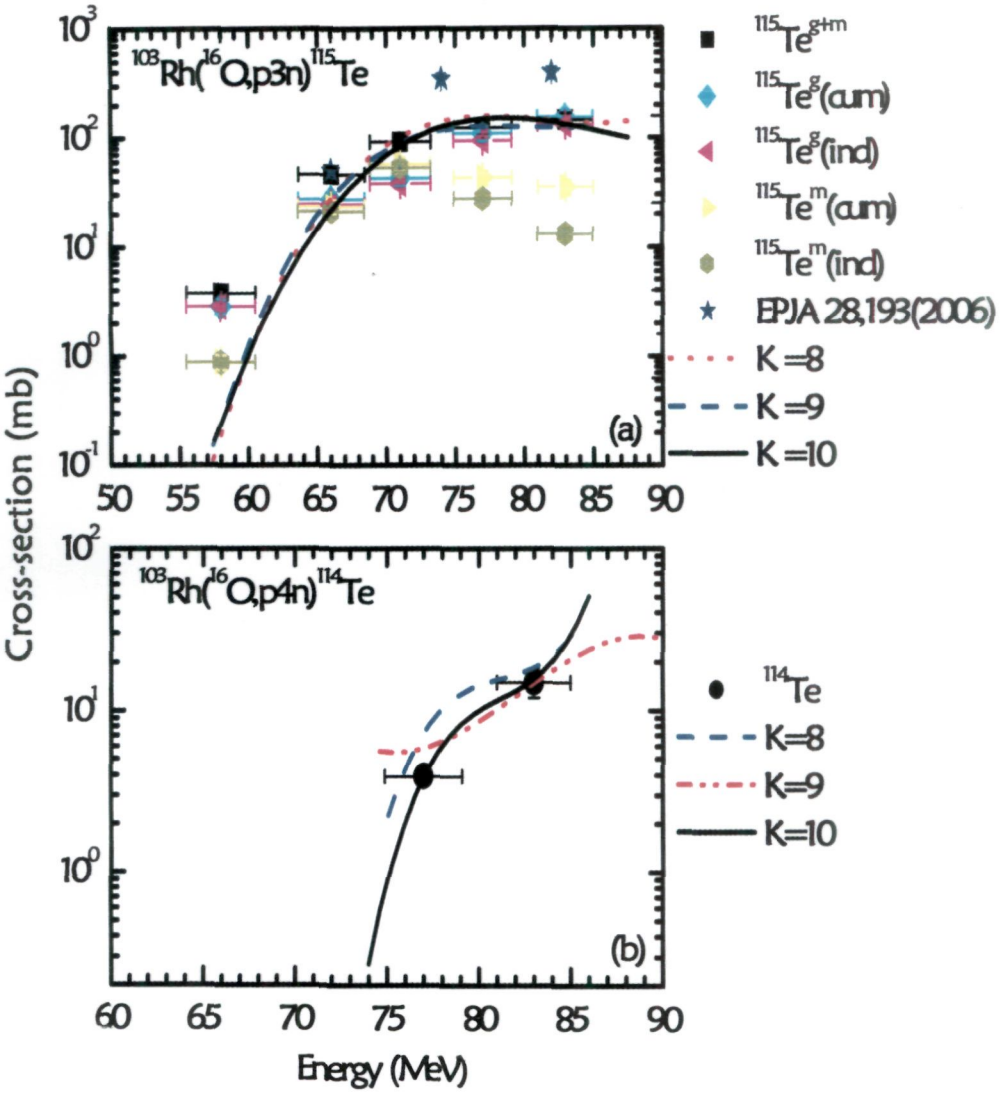

Figure 5.2.1: Experimentally measured and theoretically calculated EFs for (a) ^{115}Te and (b) ^{114}Te residues, populated via p3n and p4n channels in ^{16}O + ^{103}Rh system. The filled symbols represent the experimental data and various curves correspond to the theoretical predictions of the code PACE4 for different values of parameter K.

multiplicity [5].

As has already been mentioned, in some cases the same residue may be populated via two different modes of decay, viz., (i) directly from the decay of CN (independent production), and (ii) through the β^+/EC decay of higher charge isobar pre-cursors. As such, the experimentally measured production cross-section (σ_{cum}) is the sum of two cross-sections due to different decay modes. The independent production cross-section (σ_{ind}) has been separated out from the cumulative cross-sections (σ_{cum}) using standard successive radio-active decay analysis [5] as discussed in section 4.1.2, in Chapter IV. Experimentally measured cross-sections for the ground and meta-stable state population of residue ^{115}Te are shown in Fig. 5.2.1(a). Both the measured cumulative cross-sections as well independent cross-sections deduced as discussed above are shown for both ^{115}Te^{g} as well as ^{115}Te^{m} residues, alongwith the literature values. As can be seen from this figure, there is a reasonable agreement between theoretical and experimental EFs after subtracting the contribution of precursor decay. Further, the experimentally measured EF for radio-nuclide ^{114}Te populated via p4n channel is also satisfactorily reproduced by theoretical model calculations within the experimental uncertainties as shown in Fig. 5.2.1 (b). Both of these radio-nuclides are populated via CF process only (as there is no α-particle in exit-channels). The fact that the measured EFs for almost all the channels (pre-dominantly populated by CF) could be reproduced by PACE4 predictions, gives confidence to the choice of input parameters of theoretical model code. Therefore, same set of input parameters has been used to fit the EFs for all the α-emitting channels as well, measured in the present work.

It may be observed from Figs. 5.2.2 (a-b), the experimentally measured EFs for 2αn and 2α3n channels are relatively higher as compared to the theoretical predictions of code PACE4. Since, the theoretical model code PACE4 does not take ICF into account, therefore the enhancement in the experimentally measured production cross-sections may be attributed to the contribution coming from ICF of ^{16}O with the target nucleus. As such, these residues are expected to be populated both via CF and/or ICF of the projectile. The production of these residues may, therefore, take place (i) by the CF of ^{16}O with the target nucleus ^{103}Rh giving rise to the compound nucleus ^{119}I* which then decays by emitting 2α particles and three neutrons,

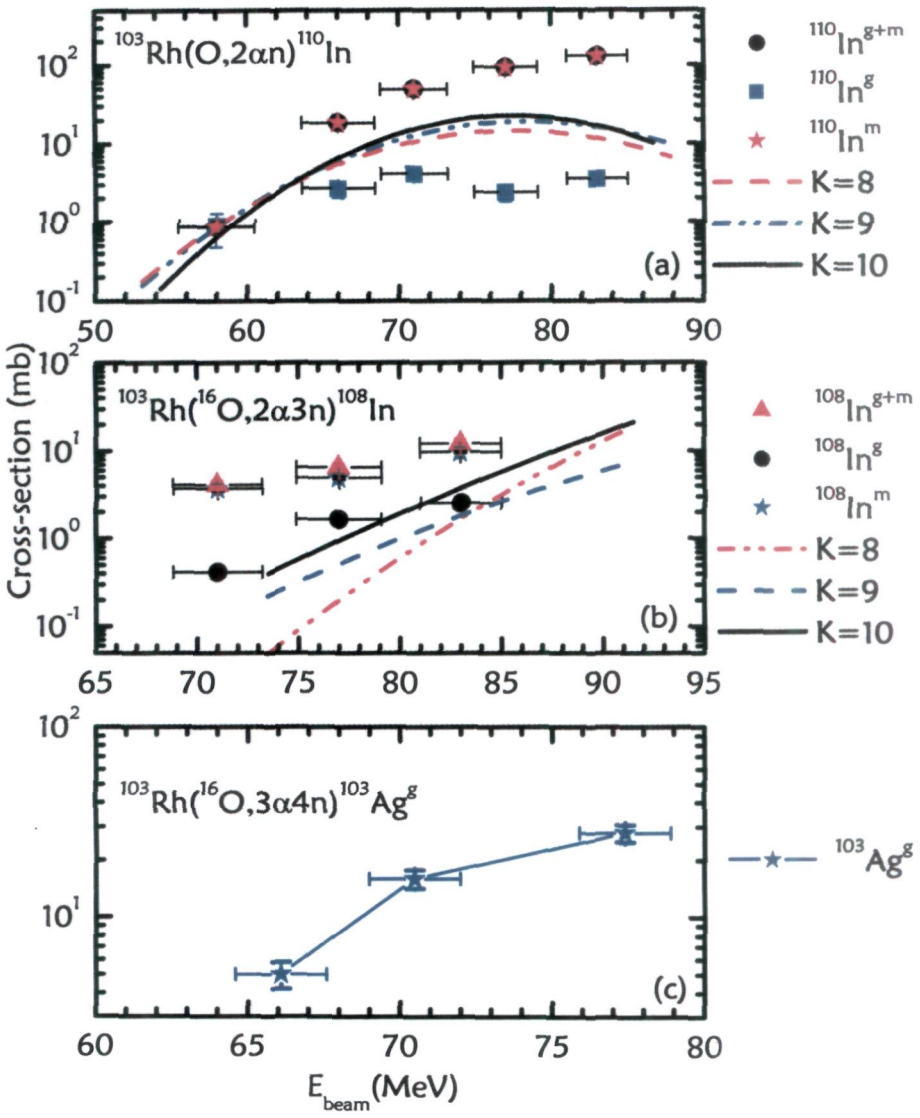

Figure 5.2.2: Experimentally measured and theoretically calculated EFs for different residues (a) populated via 2αn, (b) 2α3n and (c) 3α4n channels in ^{16}O + ^{103}Rh system. The symbols represent the experimental data and various curves correspond to the theoretical predictions of the code PACE4 for different values of parameter K.

and/or (ii) through the ICF of ^{16}O (only ^{8}Be fuses) forming the compound nucleus $^{111}In^*$ which emits three neutrons. In this case (ii) it has been assumed that ^{16}O projectile breaks-up into its clusters, viz., $^{8}Be + {}^{8}Be$, a part of projectile fuses with ^{103}Rh, while remnant moves in forward cone with a velocity almost that of projectile velocity. Further, the experimentally measured EF for $^{103}Ag^{g}(3\alpha 4n)$ channel is shown in Fig. 5.2.2 (c). The theoretical calculations with code PACE4 give negligible cross-sections for this residue and hence are not shown in Fig. 5.2.2 (c), meaning thereby, this residue is likely to be populated predominantly via ICF. It may also be pointed out that no choice of physically reasonable parameters in theoretical calculations could reproduce the measured EF for this residue. Similarly, the theoretical calculations for $3\alpha n$ and $3\alpha 3n$ channels were also found to have negligible values [6].

It may be observed from Figs. 5.2.2(a-c), ICF is expected to contribute a significant amount to the evaporation residue cross-sections. As such, an attempt has been made to deduce the ICF contribution from experimentally measured and theoretically predicted EFs. Although, it is not possible to directly obtain the relative contribution of CF and ICF from the measurement of EFs, therefore the enhancement in the experimentally measured production cross-sections over theoretical model predictions based on CF calculations has been attributed to the contribution from ICF. As such, the ICF contribution for individual channels has been deduced by subtracting CF cross-sections (σ_{CF}) (predicted by theoretical model code) from the experimentally measured cross-sections (σ_{expt}) at respective projectile energies. The ICF contributions (σ_{ICF}) deduced for presently measured evaporation residues are plotted in Fig. 5.2.3(a) along with the sum of cross-section for all ICF channels ($\Sigma\sigma_{ICF}$) [6], as a function of projectile energy. It may be noted that $\Sigma\sigma_{ICF}$ contains cross-sections for all measured ICF channels as indicated in Ref. [6]. The lines drawn in these figures are just to guide the eyes. As can be seen from these curves, in general, the ICF contribution increases with projectile energy. It may be because the break-up probability of incident ion in the field of the target nucleus increases significantly with incident energy. As mentioned, the sum of cross-sections for all measured ICF-channels ($\Sigma\sigma_{ICF}$) [6] and the sum of cross-sections for all CF-channels ($\Sigma\sigma_{CF}$) [6] obtained from theoretical model predictions are plotted along with the total fusion cross-section ($\sigma_{TF} = \Sigma\sigma_{CF}$

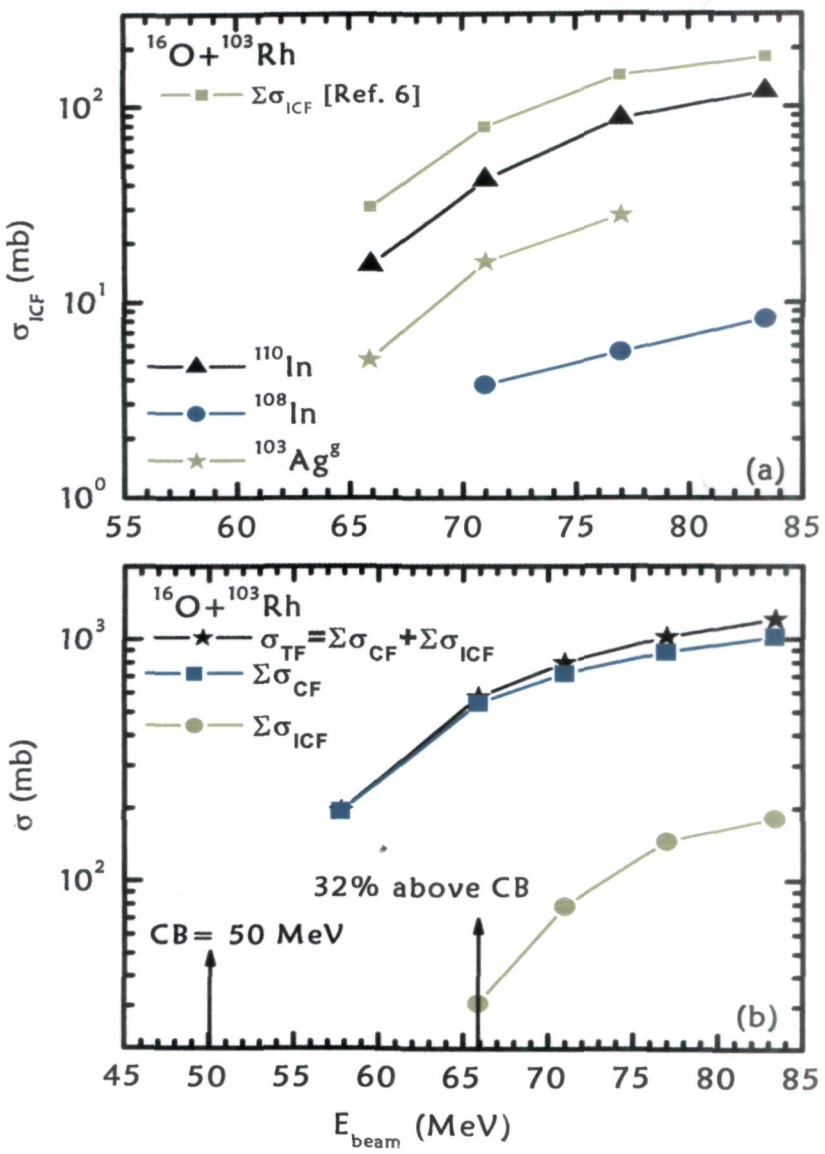

Figure 5.2.3: (a) Deduced EFs for residues populated via 2αn, 2α3n and 3α4n channels. $\Sigma\sigma_{ICF}$ values have also been plotted for all ICF channels measured as given in Ref. [6]. (b) total fusion probability (σ_{TF}) alongwith the sum of complete fusion ($\Sigma\sigma_{CF}$) and in-complete fusion ($\Sigma\sigma_{ICF}$).

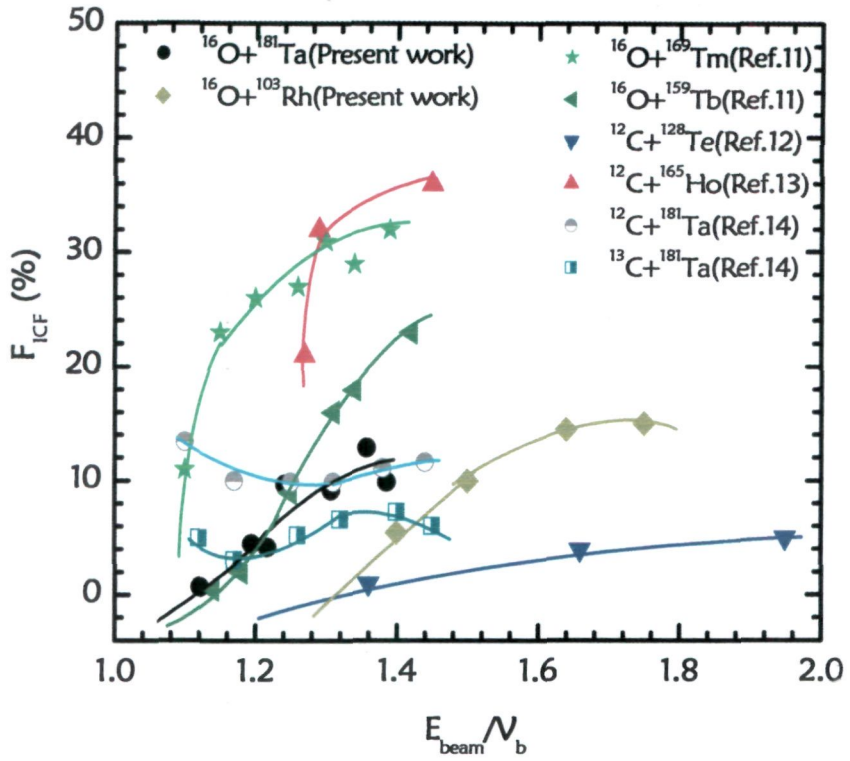

Figure 5.2.4: Deduced percentage ICF fraction (F_{ICF}) as a function of normalized projectile energy for the $^{16}O+^{181}Ta$ and $^{16}O+^{103}Rh$ systems and F_{ICF} values for some systems available in literature. The spline-like lines joining the experimental data points are just to guide the eyes.

$+ \Sigma\sigma_{ICF}$) in Fig. 5.2.3(b). It can be observed from this figure that the CF component has measurable contribution even at ≈58 MeV, while ICF contribution seems to start from ≈ 66 MeV, in the present case. Further, it may be noted from Fig. 5.2.3(b), that the separation between the plots for σ_{TF} and σ_{CF} increases with projectile energy, which indicates larger contribution from ICF at relatively high projectile energies.

In the present work a significant ICF contribution in almost all the α-emitting channels have been observed. The relative contribution of CF and

ICF cross-sections is expected to depend on the energy of the projectile. As such, to study the dependence of ICF contribution on energy, for the presently studied systems, the percentage fraction of ICF cross-section (F_{ICF}) has been plotted in Fig. 5.2.4, as a function of beam energy normalized to CB, along with several other literature values [6, 11, 12, 13, 14].

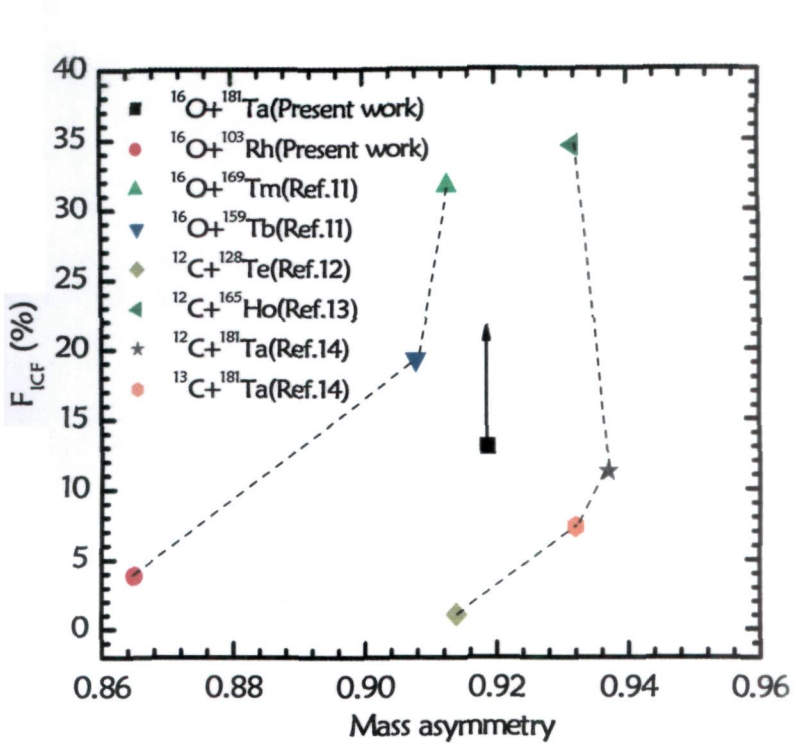

Figure 5.2.5: The percentage ICF fraction as a function of mass asymmetry at a constant normalized projectile energy. The arrow indicates that the present value of F_{ICF} for $^{16}O+^{181}Ta$ is expected to go up, if all other remaining α-emission channels are also included.

As can be seen from this figure, percentage F_{ICF} increases with the increase in normalized beam energy for all the systems, indicating the dominance of ICF processes on relatively higher energies. To study the dependence of F_{ICF} on mass asymmetry, the percent F_{ICF} has been plotted in Fig. 5.2.5, as a function of mass asymmetry at a constant value (E_{beam}/V_b = 1.38) of

normalized beam energy. As can be seen from this figure, the F_{ICF} for the presently studied $^{16}O+^{181}Ta$ system is not following the expected trend shown for other systems involving ^{16}O beam. The present F_{ICF} value for ^{16}O + ^{181}Ta is found to be significantly small and is expected to go up. It may be because of the fact that in the present measurements several other α-emission channels, e.g., 2αxn and 3αxn channels, could not be observed as the residues populated via these channels were either stable or short lived and/or had very low γ-ray intensity. We propose to measure the contribution of these α-emission channels in an in-beam experiment using particle γ-coincidence technique, so that the present data may be supplemented. Further, as can be seen from Fig. 5.2.4, the value of F_{ICF} is found to be ≈4% for ^{16}O + ^{103}Rh system, ≈19% for ^{16}O + ^{159}Tb while for $^{16}O+^{169}Tm$ system it is found to be around ≈32% at the same normalized projectile energy (i.e. E_{beam}/V_b =1.38). This striking observation clearly reveals the sensitiveness of F_{ICF} on the target mass. As can be seen from Fig. 5.2.5, the systematics presented [15] do not explain the experimental data as a whole. The value of F_{ICF} is found to increase with the mass asymmetry, individually for ^{16}O and ^{12}C projectiles. Therefore, it can be inferred that, not only mass asymmetry of interacting partners but also the projectile structure effect needs to be taken into account. The analysis of the data for ^{12}C + ^{181}Ta and ^{13}C + ^{181}Ta presented [14] also indicates that the ICF depends on the projectile structure in the beam energy range ≈5-6 MeV/nucleon. The lower value of binding energy in case of ^{12}C as compared to that in ^{13}C results in higher break-up probability of ^{12}C into $^{8}Be+\alpha$, near the field of the target nucleus resulting into higher ICF cross-sections. The above description indicates that the break-up fusion model of ICF appears to be somewhat more appropriate for explaining the observations of the present work.

5.3 ^{16}O +^{27}Al System

The experimentally measured EFs for the reactions $^{27}Al(^{16}O,2\alpha n)^{34}Cl$, $^{27}Al(^{16}O,3\alpha 3p)^{28}Mg$, $^{27}Al(^{16}O,3\alpha 3pn)^{27}Mg$, $^{27}Al(^{16}O,4\alpha 2pn)^{24}Na$ and $^{27}Al(^{16}O,4\alpha 3p)^{24}Ne$ are shown in Figs. 5.3.1(a-c) and Figs. 5.3.2(a-b). In the (a) panel of Fig. 5.3.1, the experimentally measured and theoretically calculated EFs for the production of ^{34}Cl residues are shown. In Figs. 5.3.1(b) and 5.3.2(b) the solid lines are drawn just to guide the eyes to the experimental data. In Figs. 5.3.1(a) and 5.3.2(a), the literature [16] values

of the cross-sections are also shown. Earlier measurements on $^{16}O+^{27}Al$ system were done [16] employing activation technique using low resolution NaI(Tl) detector and gas flow end-window β-counter. The energy spread of the data points in these measurements is substantially large [16], because of relatively large thickness of the Al-foils used. It may, however, be pointed out that no theoretical interpretation of data was made [16]. More recently, McKenna et. al., [17] tried to reproduce the experimental data [16] using a high intensity LASER produced plasma beam. They also performed theoretical calculations [17] using the Monte Carlo code PACE4. Since, in the present work, theoretical calculations for these reactions give considerably small values of cross-sections and hence are not shown in Figs. 5.3.1(b & c) and Fig. 5.3.2. As such, the observed enhancement by several orders of magnitude over their negligible theoretical predictions for these channels may be attributed to the fact that these residues are populated by some processes other than CF process. McKenna et. al., [17] reported that the residue ^{34}Cl is produced by the evaporation of two α-particles and one neutron from the compound nucleus formed by $^{16}O+^{27}Al$ system. Furthermore, the production of other radio-isotopes viz., ^{27}Mg, ^{24}Na and ^{24}Ne, was attributed to the compound nucleus as well as to direct reactions. It is not out of place to mention here that in-complete fusion and deep in-elastic collisions are also dominant mechanisms in HI reactions at these energies, and hence the contribution of these reaction channels are also required to be taken into account. Furthermore, to confirm whether these reactions are formed by CF and/or ICF processes and to obtain the complementary information about the processes involved in lighter mass system, the angular distributions of the residues produced in $^{16}O+^{27}Al$ system have also been measured at 85 MeV beam energy and are discussed in section 5.6 of the thesis.

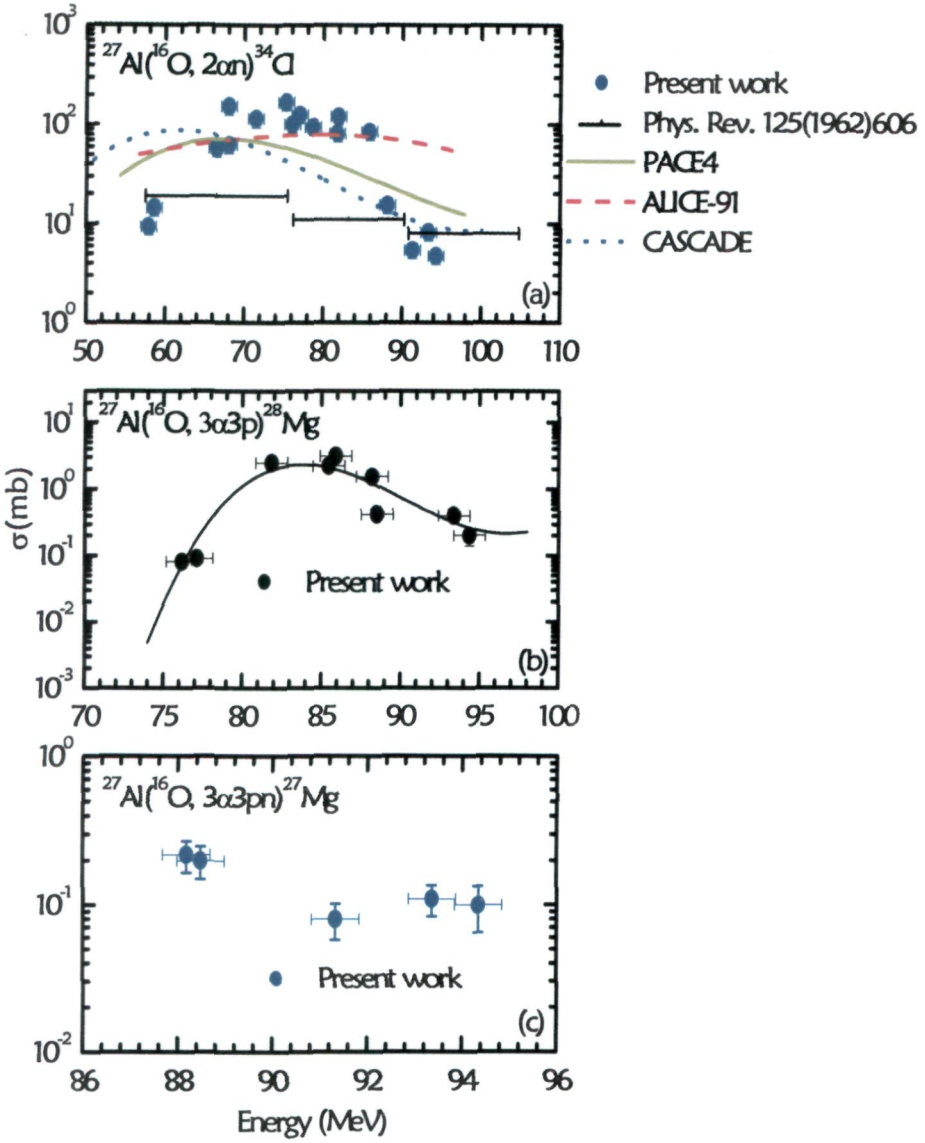

Figure 5.3.1: Experimentally measured EFs for (a) the production of ^{34}Cl, (b) ^{28}Mg and (c) ^{27}Mg in the system $^{16}O+^{27}Al$. The dark symbols represent the experimental data and in panel (a) various curves correspond to the theoretical predictions of the code PACE4. In (b) the line drawn is just to guide the eyes to the data points.

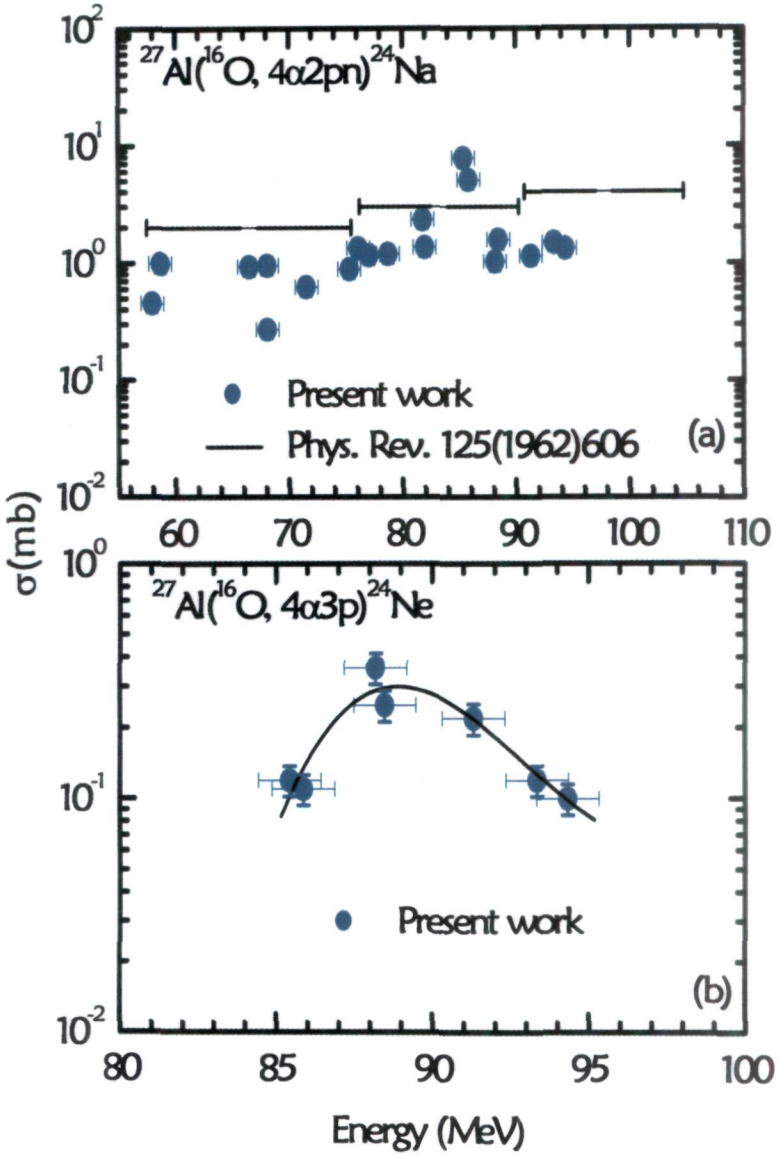

Figure 5.3.2: Experimentally measured EFs for residues (a) ^{24}Na and (b) ^{24}Ne. Dark circles represent the experimental data. The line drawn in panel (b) is just to guide the eyes to the data points.

5.4 FORWARD RECOIL RANGE DISTRIBUTIONS

$^{16}O+^{181}Ta$ System

The degree of the linear momentum transfer (p_{LMT}) from the projectile to the target nucleus decides the recoil velocity of the reaction products. This may be used to differentiate the CF and ICF processes. As already mentioned, p_{LMT} is proportional to the fused mass of the projectile, i.e., maximum LMT gives rise to maximum recoil velocity to the reaction product. In the CF process, the maximum p_{LMT} from the projectile to the target nucleus is expected. For a given entrance channel the CN has pre-determined mass, energy and linear momentum. In case of ICF, partial p_{LMT} leads to the formation of an in-completely fused composite system in the excited state. For an in-completely fused composite system, the mass, energy and momenta of CN may not have unique values. This may be because of the fluctuations in the fused mass from the projectile to the target nucleus. The experimentally measured forward recoil ranges of final reaction products in the stopping medium may give an indication of the p_{LMT} involved. As such, the radio-nuclides populated via lower degree of LMT, will show relatively smaller depth (momentum transfer component) in the stopping medium as compared to the entire LMT populations. Therefore, the forward recoil range distributions may be used as a probe to investigate the partial fusion of the projectile in the ICF processes.

In the present work, the production probabilities of $^{194}Tl(3n)$, $^{193}Tl^{g}(4n)$, $^{192}Tl(5n)$, $^{193}Hg^{g}(p3n)$, $^{193}Hg^{m}(p3n)$, $^{192}Hg(p4n)$, $^{191}Hg^{g}(p5n)$, $^{191}Hg^{m}(p5n)$, $^{192}Au^{g}(\alpha n)$, $^{191}Au^{g}(\alpha 2n)$, $^{190}Au^{g}(\alpha 3n)$ and $^{186}Ir^{g}(2\alpha 3n)$ nuclides produced in the $^{16}O+^{181}Ta$ system have been measured at different catcher foil thicknesses to obtain the FRRDs. The FRRDs for these residues have been measured at ≈81, 90 and 96 MeV beam energies. The details of the measurements of these FRRDs have already been presented in section 4.2, of Chapter IV. The production yields of different reaction products have been deduced by normalizing the experimentally measured production cross-sections with the respective catcher foil-thicknesses. In order to generate RRDs, the normalized yields of a individual reaction product have been plotted as a function of cumulative catcher foil thickness. For the better description of the FRRDs, the measured yields of each residue have

been presented (Figs. 5.4.1-5.4.12) at three different projectile energies in a single figure at three different panels.

In heavy ion reactions, it is difficult to exactly measure the degree of LMT from the projectile to the target nucleus. It is because of the recoil velocity distribution of evaporation residues due to straggling effects. In addition to this, the effects due to particle(s) emission may also contribute extra broadening in the recoil range distributions (RRDs). As such, in order to get a reliable form for the degree of LMT from the experimental data, a careful de-convolution is required. The relative contributions and precise form of RRDs in case of CF and ICF processes in the production of particular reaction products may be obtained by fitting the experimentally measured RRD data with Gaussian peaks using the ORIGIN software. The yield curves of evaporation residues obtained from RRDs assumed to be Gaussian, may be given as [18];

$$Y = Y_0 + \frac{A}{\sqrt{2\pi\omega_A^2}} e^{-(R-R_P)^2/2\omega_A^2} \qquad (5.1)$$

where, R_p is most probable mean range, ω_A is the width parameter (FWHM) of the RRD, and 'A' is the area under the peak. Further, the normalized yield 'Y' may be estimated by chi-square (χ^2) fit, from the experimentally determined production yield at different catcher-foil thicknesses. The value of χ^2 was minimized in this analysis using a non-linear least square fit routine. As indicated in the Figs. 5.4.9–5.4.12, most of the residues show more than one LMT components. In such cases, the experimentally measured normalized yields have been fitted by assuming multi-peaks in the similar way as mentioned above.

xn-Channels

The measured FRRDs for the residues populated via xn(x =3, 4 & 5) channels at three different projectile energies ≈81, 90 and 96 MeV are shown in Figs. 5.4.1(a-c) to 5.4.3(a-c). As can be seen from these figures, there is only a single peak in RRDs, indicating only single LMT component involved in the production of these reaction products. As such, it may be concluded that these reactions are populated by CF processes only. In case of CF, the incoming ion completely fuses with the target nucleus and

transfers its total linear momentum to the fused system, which recoils in order to conserve the input linear momentum.

As has already been mentioned, these residues viz., ^{194}Tl, ^{193}Tl^{g}, ^{192}Tl, produced from the reactions ^{181}Ta(^{16}O,3n), ^{181}Ta(^{16}O,4n) and ^{181}Ta(^{16}O,5n) respectively, are populated via CF processes. The experimental data for the FRRDs at three different energies ≈81, 90 and 96 MeV can be well fitted by Gaussian distributions. In case of the residue ^{194}Tl(3n), the peaks are found at the cumulative thickness ≈265±76, 275±47 and 286±48 μg/cm^2 respectively, for incident energies ≈81, 90 and 96 MeV [Figs. 5.4.1.(a, b & c)]. In case of the residue ^{193}Tl^{g}(4n), the peaks are at the cumulative thickness ≈260±77, 254±39 and 286±67 μg/cm^2, respectively [Figs. 5.4.2.(a, b & (c)], while for the residue ^{192}Tl(5n), the peaks are at the cumulative thickness ≈244±58, 255±21 and 264±75 μg/cm^2, respectively [Figs. 5.4.3.(a, b & c)]. The recoil ranges for the above mentioned residues have also been calculated theoretically using stopping power tables of Northcliffe and Schilling [19]. The calculated values of ranges R_p(Th) agree well with the measured R_p(expt) data and are presented in Table 5.1. It may, therefore, be taken as a conclusive evidence that these residues are produced only by the CF process. On the basis of above description, it may be mentioned that the reaction products ^{194,193g,192}Tl populated via xn(x=3,4&5) channels are associated with the entire LMT.

pxn-Channels

In case of pxn channels, there is no likelyhood of ICF therefore, these residues are also populated by CF like xn channels. The Gaussian fits of the RRD data for the residues ^{193}Hg^{g} and ^{193}Hg^{m} (populated through the reaction ^{181}Ta(^{16}O, p3n)) at three different projectile energies ≈81, 90 & 96 MeV are shown respectively in Figs. 5.4.4(a-c) and Figs. 5.4.5(a-c). As can be seen from these figures, the experimental RRD data, at three different incident energies may be fitted by a single peak, at the cumulative thickness ≈261±82, 257±75 and 290±52 μg/cm^2 for the residue ^{193}Hg^{g} and at ≈275±75, 270±60 and 292±51 μg/cm^2 for the residue ^{193}Hg^{m} respectively. The residue ^{192}Hg may also be populated by CF through the reaction ^{181}Ta(^{16}O, p4n). The Gaussian fits of the RRD data for ^{192}Hg at three different energies are shown in Figs. 5.4.6(a-c). It may be observed from the figures, that the experimental RRD peaks are found at the cumulative

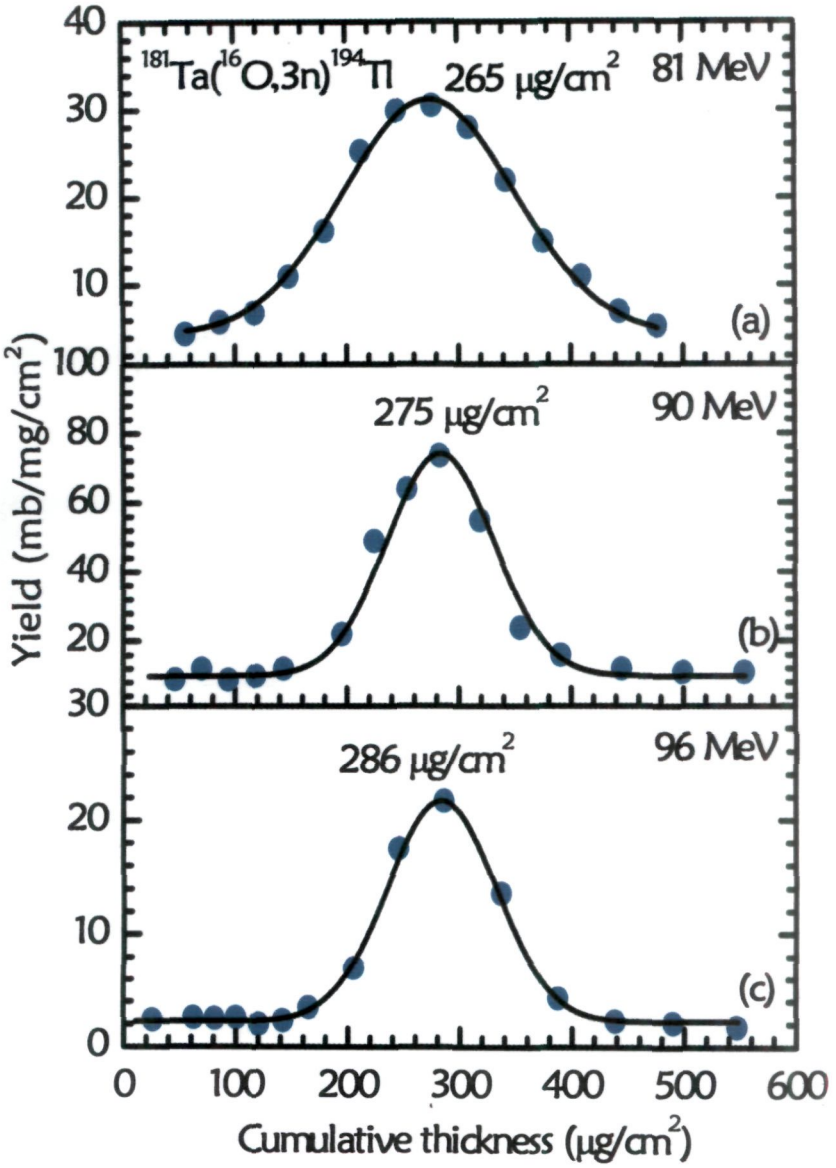

Figure 5.4.1: Experimentally measured forward recoil range distributions for ^{194}Tl(3n) at projectile energies ≈81, 90 and 96 MeV. The lines joining data points are the result of best fit to the experimental data points.

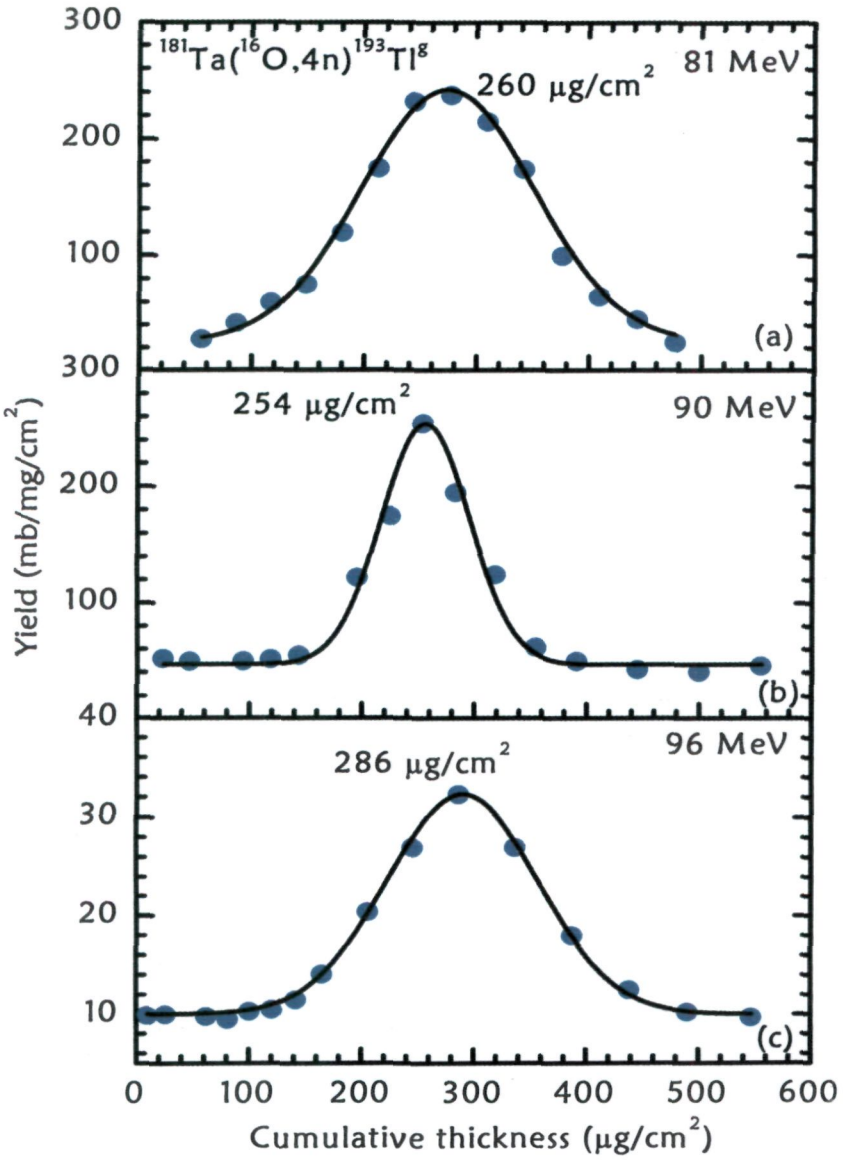

Figure 5.4.2: Experimentally measured forward recoil range distributions for $^{193}Tl^{g}$(4n) at projectile energies ≈81, 90 and 96 MeV. The lines joining data points are the result of best fit to the experimental data points.

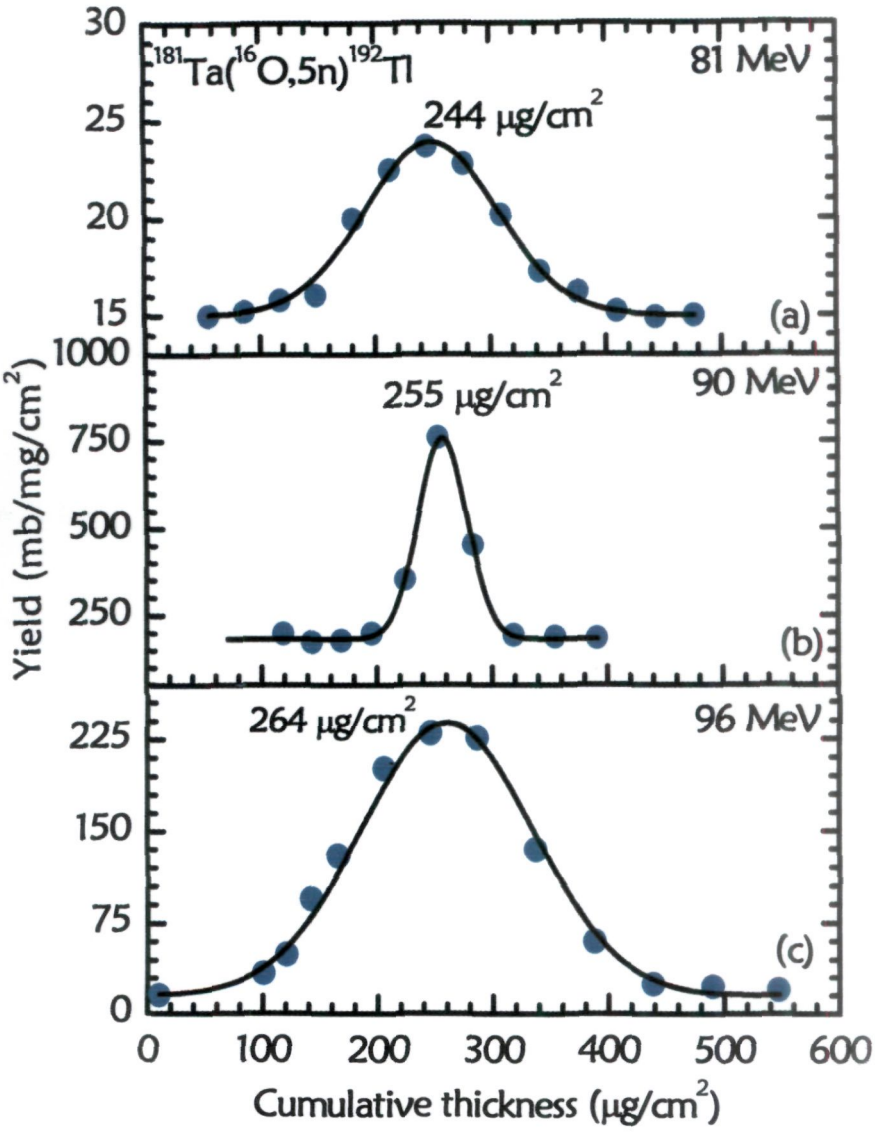

Figure 5.4.3: Experimentally measured forward recoil range distributions for ^{192}Tl(5n) at projectile energies ≈81, 90 and 96 MeV. The lines joining data points are the result of best fit to the experimental data points.

thicknesses ≈252±61, 282±57 and 291±80 μg/cm^2 respectively at three energies. While, in case of the residues ^{191}Hg^{g,m}, the measured RRD data at ≈81, 90 & 96 MeV incident energies may be fitted by a single peak, at ≈276±47, 256±47 and 277±50 μg/cm^2 and at ≈249±53, 230±65 and 287±68 μg/cm^2 cumulative thicknesses, respectively as shown in Figs. 5.4.7 (a-c) & 5.4.8 (a-c). The origin of these peaks may be well understood, if it is assumed that the residue is produced by CF process in the reaction ^{181}Ta(^{16}O, p5n). Since, only one peak appears at each incident energy for all the above mentioned residues, it may be concluded that these residues are populated only by CF process. Experimentally measured R_P(expt) and theoretically calculated R_P(Th) for various CF residues are given in Table 5.1. In general, the experimental values of the absorber thickness at peak position agree well with the calculations done using stopping power values within the quoted uncertainties.

αxn and 2αxn-Channels

The experimentally measured FRRDs for the residues ^{192,191,190}Au^g and ^{186}Ir^g populated via CF and/or ICF in ^{16}O+^{181}Ta system at three different energies ≈81, 90 & 96 MeV are shown in Figs. 5.4.9(a-c) to Figs. 5.4.12(a-c). As can be seen from the Figs. 5.4.9(a-c) to Figs. 5.4.11(a-c), for the residues ^{192,191,190}Au^g, the FRRDs in each case may be resolved into two Gaussian peaks (in case of αxn channels), indicating the presence of more than one linear momentum transfer components associated with the fusion of ^{16}O and/or ^{12}C. In case of CF, the composite system ^{197}Tl* is formed, which may decay by the statistical emission of an α-particle and 1, 2 and 3 neutrons, respectively leaving behind ^{192,191,190}Au^g residues. The above residues may also be populated, if it is assumed that, the incident ^{16}O ion breaks-up into fragments (e.g., ^{12}C & α), as it enters in the nuclear field of the target nucleus. One of the fragments ^{12}C, fuses with the target nucleus forming an in-completely fused composite system ^{193}Au*, which recoils in the forward direction to conserve the input linear momentum and decay by the emission of respectively one neutron forming ^{192}Au^g, two neutrons forming ^{191}Au^g and three neutrons forming the residue ^{190}Au^g. As can be observed from Figs. 5.4.9(a-c), that the RRD for the residue ^{192}Au^g show both ICF and CF components having peaks at the cumulative catcher thicknesses at ≈ 145±37, 168±20 and 200±35 μg/cm^2 (due to ^{12}C-fusion) and at ≈ 275±60, 256±37 and 290±47 μg/cm^2 (due to ^{16}O-fusion) at three different

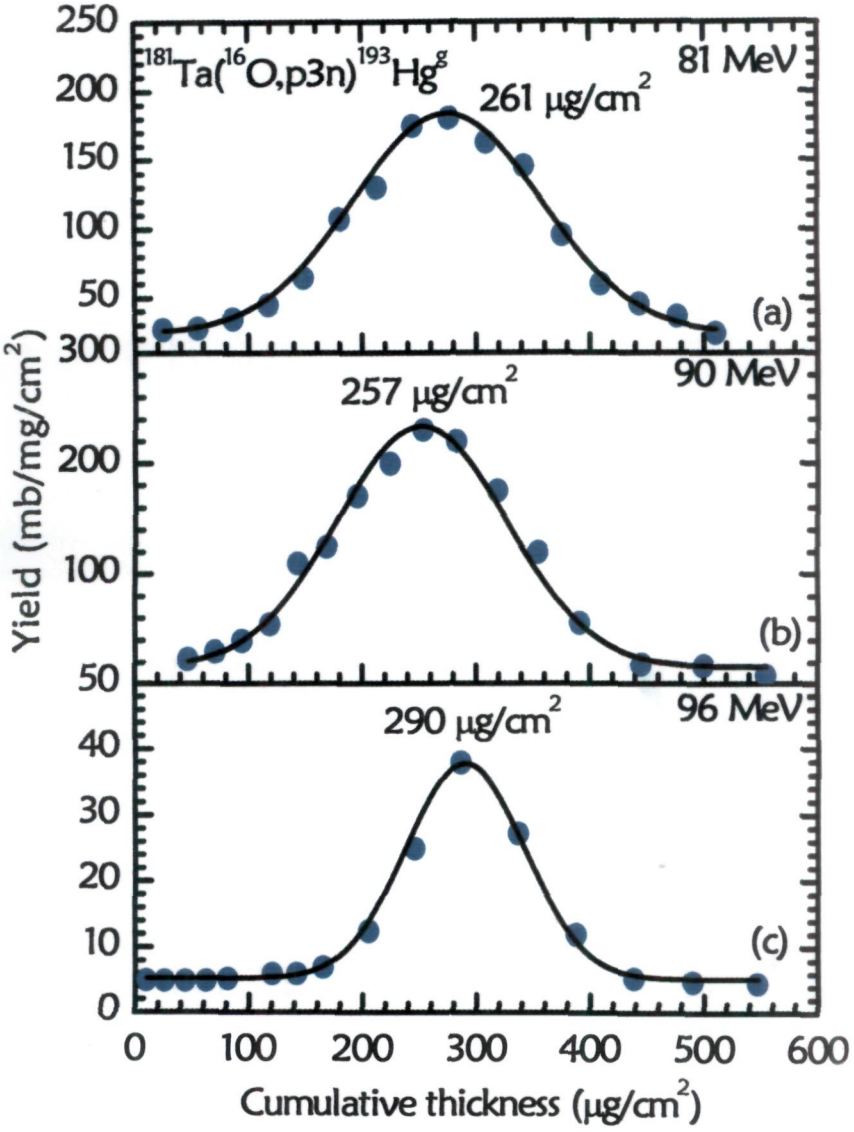

Figure 5.4.4: Experimentally measured forward recoil range distributions for $^{193}Hg^{g}$(p3n) at projectile energies ≈81, 90 and 96 MeV. The lines joining data points are the result of best fit to the experimental data points.

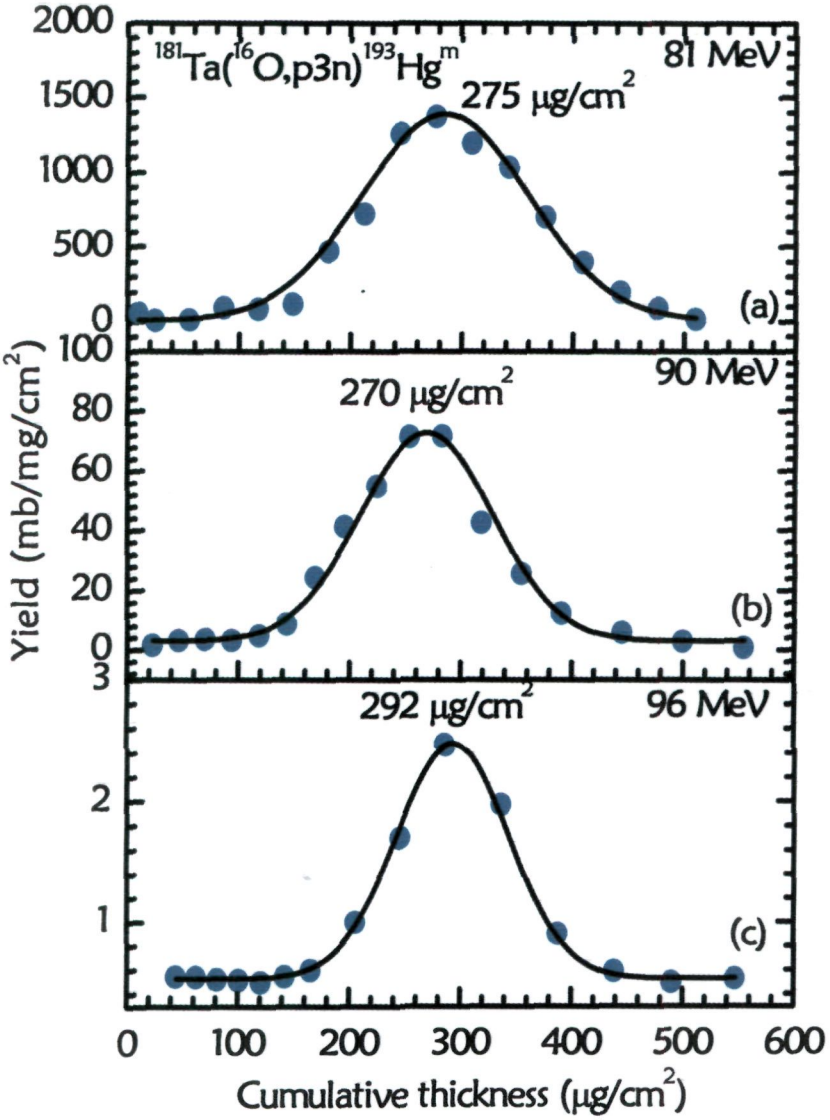

Figure 5.4.5: Experimentally measured forward recoil range distributions for $^{193}Hg^{m}$(p3n) at projectile energies ≈81, 90 and 96 MeV. The lines joining data points are the result of best fit to the experimental data points.

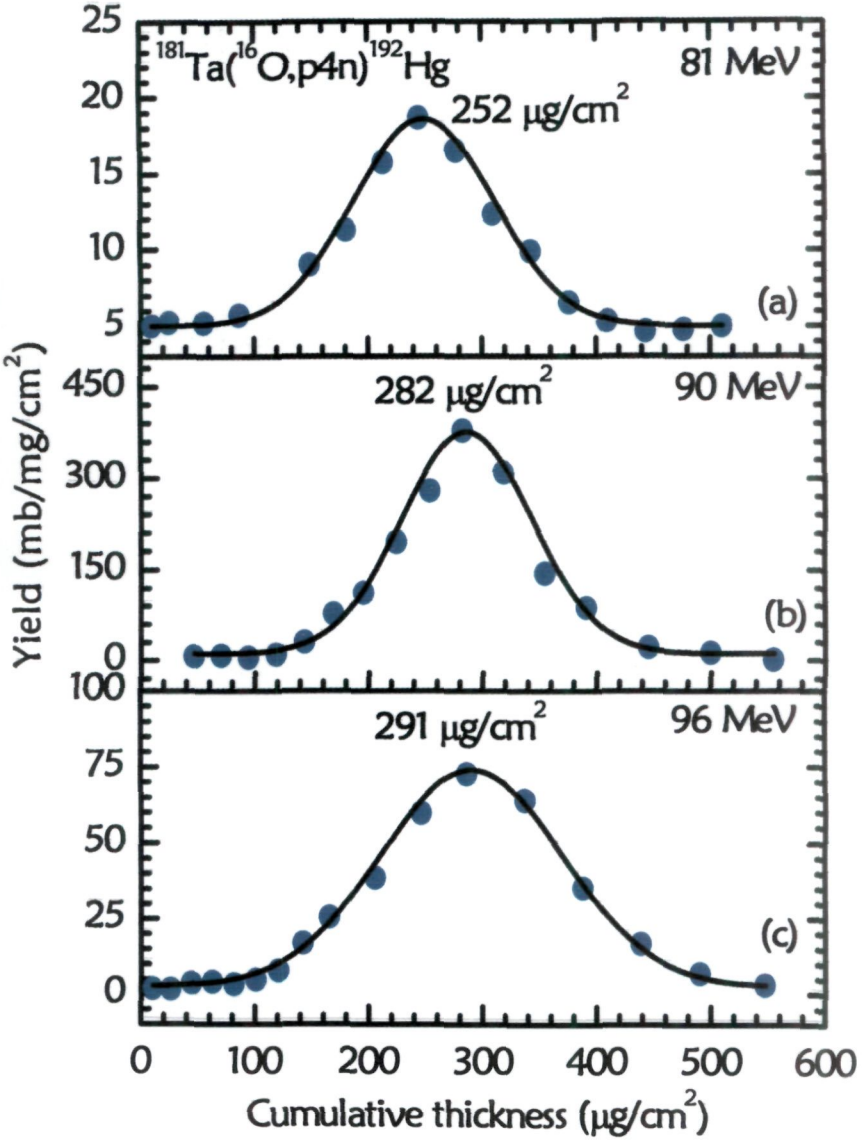

Figure 5.4.6: Experimentally measured forward recoil range distributions for ^{192}Hg(p4n) at projectile energies ≈81, 90 and 96 MeV. The lines joining data points are the result of best fit to the experimental data points.

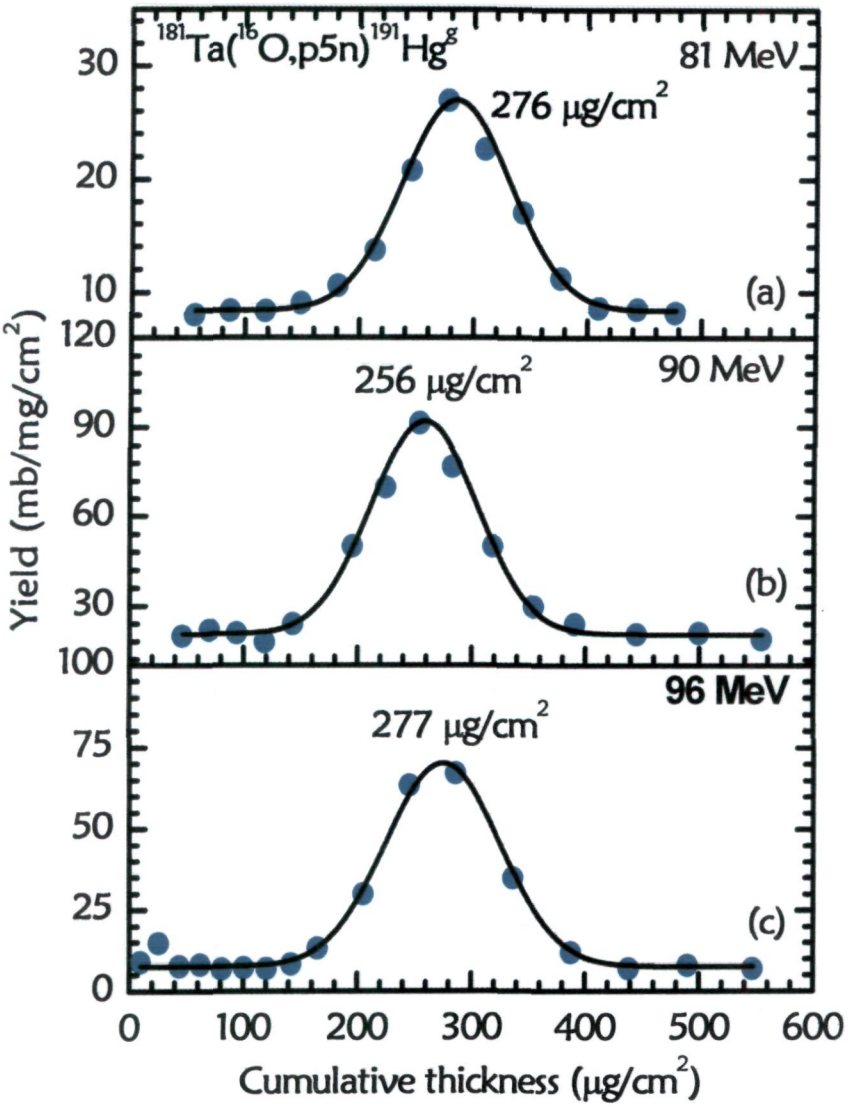

Figure 5.4.7: Experimentally measured forward recoil range distributions for $^{191}Hg^{g}$(p5n) at projectile energies ≈81, 90 and 96 MeV. The lines joining data points are the result of best fit to the experimental data points.

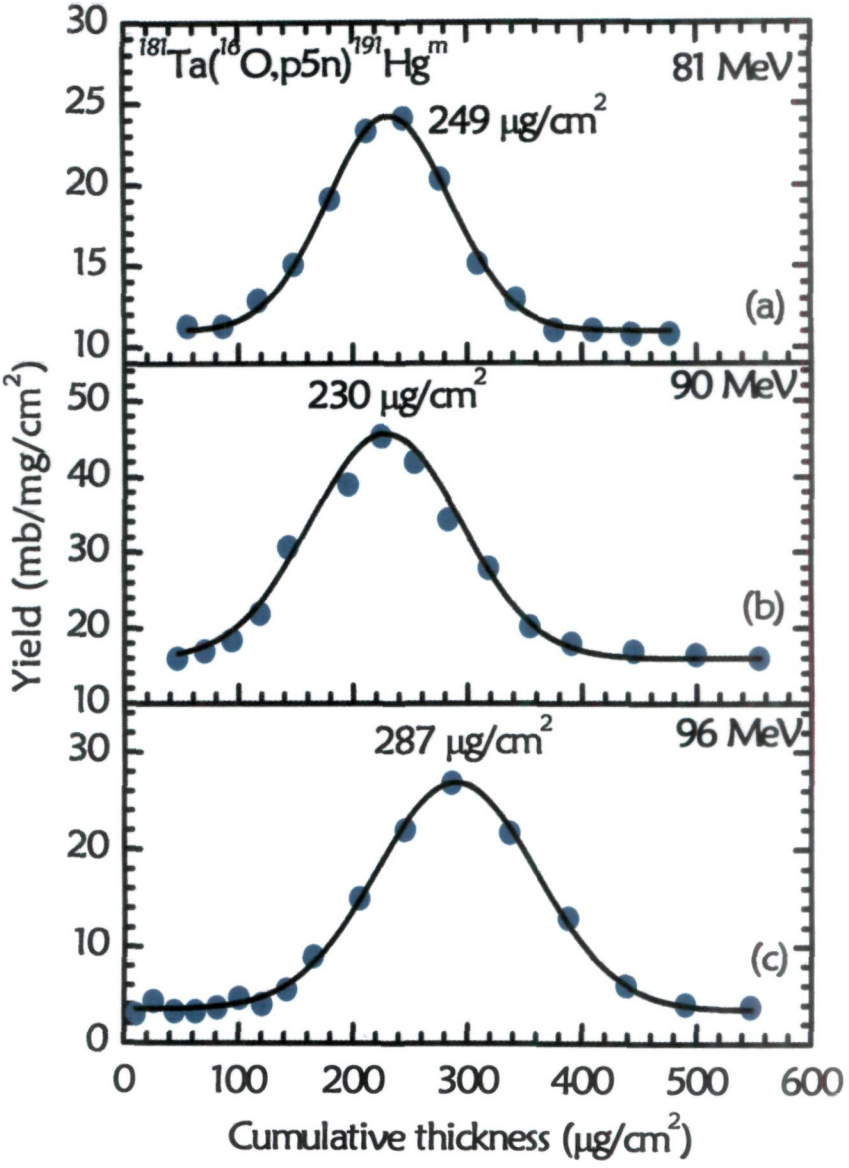

Figure 5.4.8: Experimentally measured forward recoil range distributions for $^{191}Hg^{m}$(p5n) at projectile energies ≈81, 90 and 96 MeV. The lines joining data points are the result of best fit to the experimental data points.

Table 5.1: Experimentally measured forward recoil ranges R_P(expt) deduced from RRD curves, and theoretically calculated most probable mean ranges R_P (Th) for CF components at ≈ 81, 90 & 96 MeV, in the interaction of ^{16}O with ^{181}Ta.

Residue	Energy (E) ≈ 81 MeV		Energy (E) ≈90 MeV		Energy (E) ≈96 MeV	
	R_P(expt) (μg/cm^2)	R_P(Th) (μg/cm^2)	R_P(expt) (μg/cm^2)	R_P(Th) (μg/cm^2)	R_P(expt) (μg/cm^2)	R_P(Th) (μg/cm^2)
^{194}Tl(3n)	265±76	267	275±47	287	286±48	298
$^{193}Tl^g$(4n)	260±77	267	254±39	287	286±67	298
^{192}Tl(5n)	244±58	267	255±21	287	264±75	298
$^{193}Hg^g$(p3n)	261±82	267	257±75	287	290±52	298
$^{193}Hg^m$(p3n)	275±75	267	270±60	287	292±51	298
^{192}Hg(p4n)	252±61	267	282±57	287	291±80	298
$^{191}Hg^g$(p5n)	276±47	267	256±47	287	277±50	298
$^{191}Hg^m$(p5n)	249±53	267	230±65	287	287±69	298

projectile energies i.e., ≈81, 90 & 96 MeV respectively. The contribution of different fusion components (^{16}O and/or ^{12}C) may be obtained by dividing the area under the peak of the corresponding fusion component by the total area associated with the distribution. It may, however, be pointed out that, the relative contribution of ^{12}C-fusion for the reaction $^{181}Ta(^{16}O,\alpha n)^{192}Au^g$, [Figs. 5.4.9(a-c)], is found to be ≈20.8%, 11.5% and 23.8% while the contribution from ^{16}O-fusion is found to be ≈79.2%, 88.5% and 76.2% at three different projectile energies (≈81, 90 & 96 MeV) respectively.

Similar to the $^{192}Au^g$ residues, in case of the radio-isotopes $^{191}Au^g$ and $^{190}Au^g$ populated through the reactions $^{181}Ta(^{16}O,\alpha 2n)$ and $^{181}Ta(^{16}O,\alpha 3n)$ also show two LMT components in RRD data. In case of the residue $^{191}Au^g$, peaks at the cumulative catcher thicknesses are found at ≈ 165±27, 170±37 and 204±43 μg/cm^2 (due to ^{12}C-fusion) and ≈ 256±48, 281±43 and 294±45 μg/cm^2 (due to ^{16}O-fusion) respectively, at three different projectile energies. Further, the relative contribution of ^{12}C- fusion for the reaction $^{181}Ta(^{16}O,\alpha 2n)^{191}Au^g$, [Figs. 5.4.10(a-c)], is found to be ≈20.5%, 28.6% and 52.5% while the contribution from ^{16}O-fusion is found to be ≈79.5%,

71.4% and 47.5% at three different projectile energies (81, 90 & 96 MeV) respectively. While, in case of the residues $^{190}Au^{g}$, peaks at the cumulative catcher thicknesses are found at ≈ 181±22, 196±25 and 213±35 μg/cm^2 (due to ^{12}C-fusion) and at ≈ 290±50, 282±35 and 286±51 μg/cm^2 (due to ^{16}O-fusion) at three studied energies ≈81, 90 & 96 MeV. The relative contribution of ^{12}C-fusion for the reaction $^{181}Ta(^{16}O,\alpha 3n)^{190}Au^{g}$, [Figs. 5.4.11(a-c)], is found to be ≈11.6%, 29.8% and 35.8% while the contribution from ^{16}O-fusion is found to be ≈88.4%, 70.2% and 64.2% respectively at 81, 90 & 96 MeV beam energies. The observation of peaks at relatively smaller cumulative depths clearly indicates relatively less degrees of LMT involved in the process. The percentage relative contributions for different CF and/or ICF components for the residues populated via α-emission channels deduced from RRD data are also indicated in Table 5.2.

The FRRDs for $^{186}Ir^{g}$ residues populated via 2α3n channel, are shown in Figs. 5.4.12(a-c). As can be seen from these figures, the FRRDs may be resolved into three Gaussian peaks, indicating the presence of three different linear momentum transfer components associated with the fusion of ^{16}O, ^{12}C and ^{8}Be. The reaction products $^{186}Ir^{g}$ may be formed via CF and /or ICF of ^{16}O with ^{181}Ta. In case of CF, the composite system $^{197}Tl^{*}$ is formed, which may decay via the statistical emission of two α-particles and 3 neutrons leaving behind the above mentioned residue. On the other hand, the residue $^{186}Ir^{g}$ may also be populated, if it is assumed that, the incident ^{16}O ion breaks-up into its fragments (e.g., ^{12}C & α and ^{8}Be & ^{8}Be), one of the fragments (^{12}C) fuses with the target nucleus forming an in-completely fused composite system $^{193}Au^{*}$, which decay by the emission of an α-particle and three neutrons forming $^{186}Ir^{g}$. Moreover, if ^{8}Be fuses with the target, in-completely fused $^{189}Ir^{*}$ will be formed which may emit three neutrons to leave the residue ^{186}Ir. The Fig. 5.4.12 show three LMT components for $^{186}Ir^{g}$ arising out of the three modes of formation. The peaks for these distributions are at ≈100±27, 70±21 and 121±21 μg/cm^2 (fusion of ^{8}Be), at ≈183±13, 166±27 and 213±23 μg/cm^2 (fusion of ^{12}C) and ≈258±38, 262±40 and 290±50 μg/cm^2 (fusion of ^{16}O) at the three respective energies. From the above, it can be inferred that the residues $^{186}Ir^{g}$ produced through $^{181}Ta(^{16}O, 2\alpha 3n)$ channel has the contribution from both the processes namely, CF and ICF. Further, the relative contribution of ^{8}Be - fusion for the reaction $^{181}Ta(^{16}O,2\alpha 3n)^{186}Ir^{g}$, [Figs. 5.4.12(a-c)], is

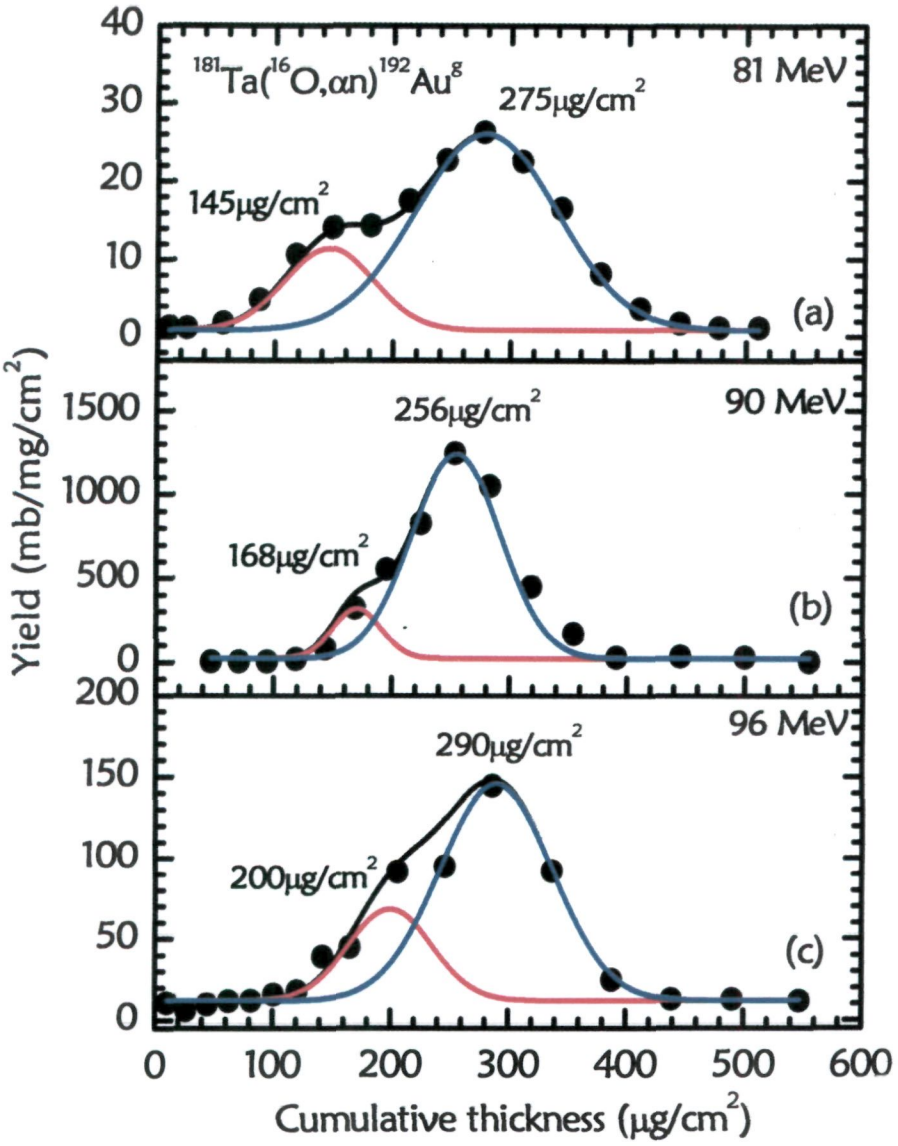

Figure 5.4.9: Experimentally measured forward recoil range distributions for $^{192}Au^{g}(\alpha n)$ at projectile energies ≈81, 90 and 96 MeV. The lines joining data points are the result of best fit to the experimental data points.

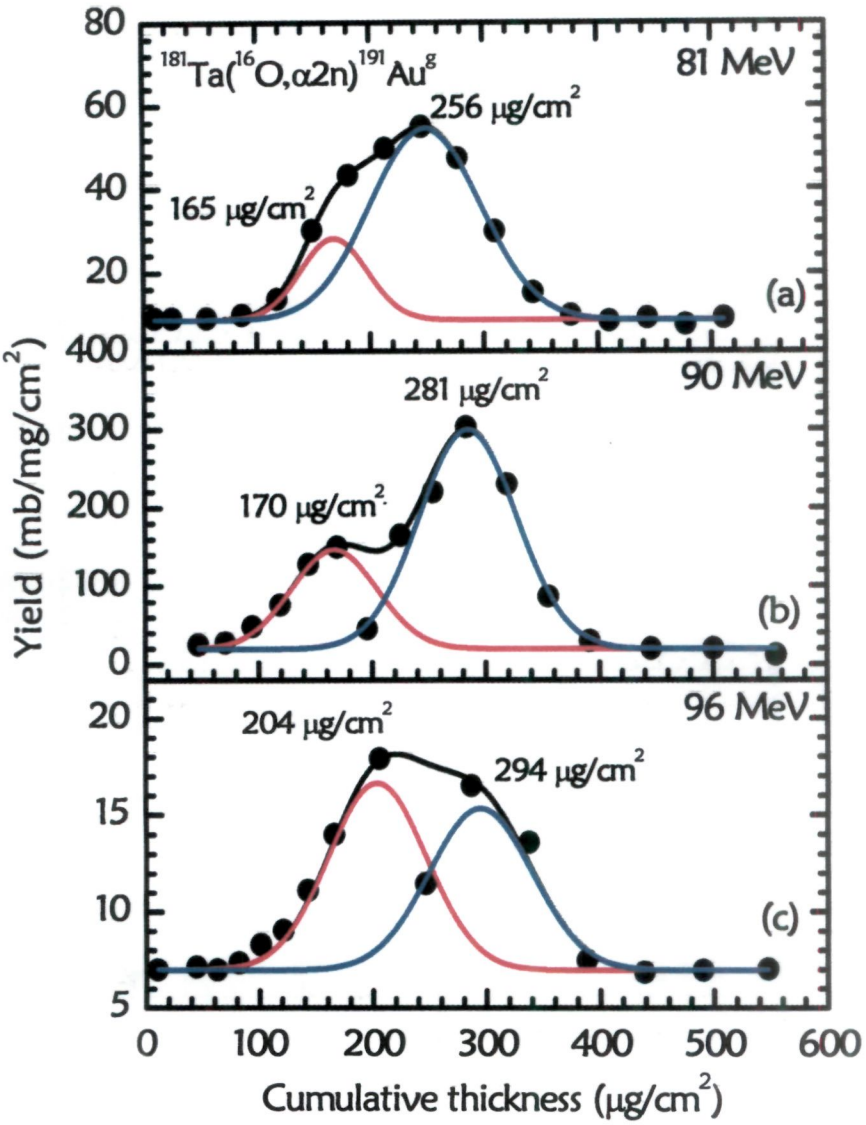

Figure 5.4.10: Experimentally measured forward recoil range distributions for $^{191}Au^{g}(\alpha 2n)$ at projectile energies ≈81, 90 and 96 MeV. The lines joining data points are the result of best fit to the experimental data points.

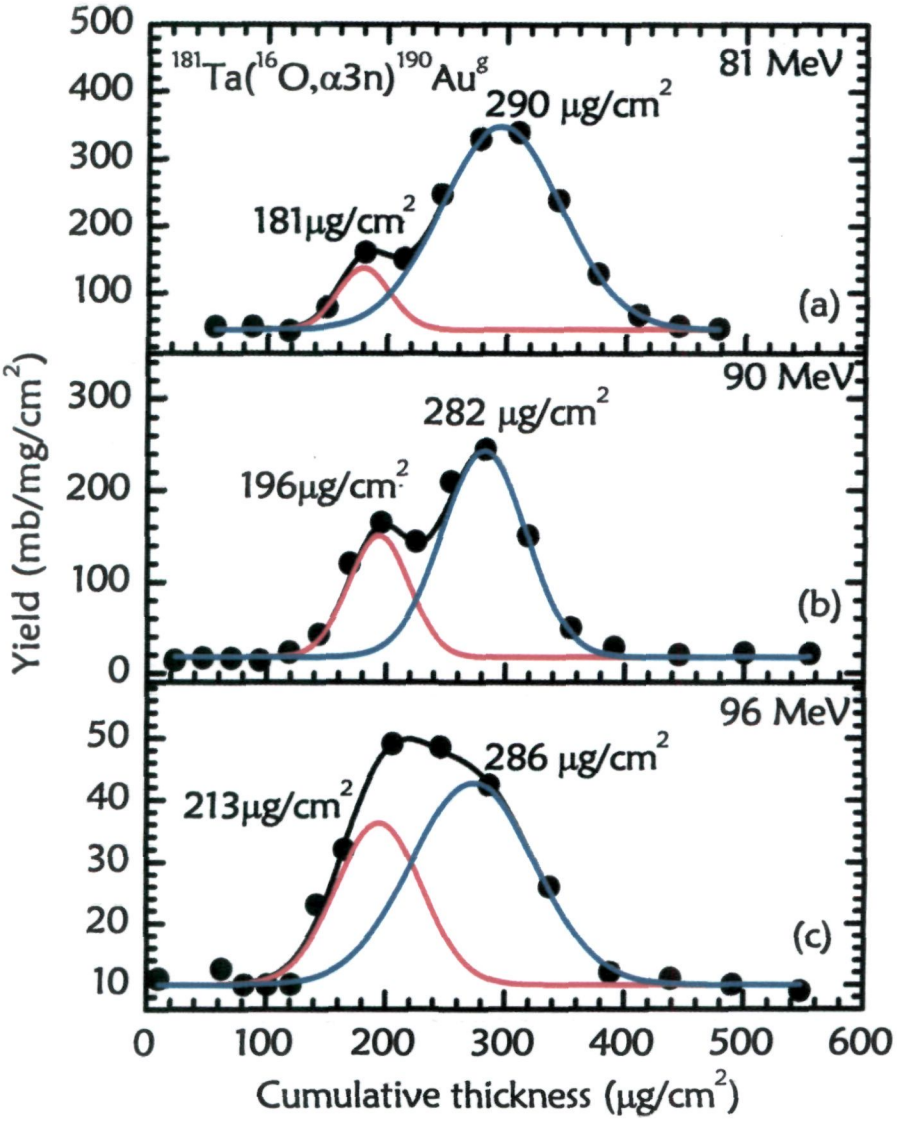

Figure 5.4.11: Experimentally measured forward recoil range distributions for ^{190}Au^{g}(α3n) at projectile energies ≈81, 90 and 96 MeV. The lines joining data points are the result of best fit to the experimental data points.

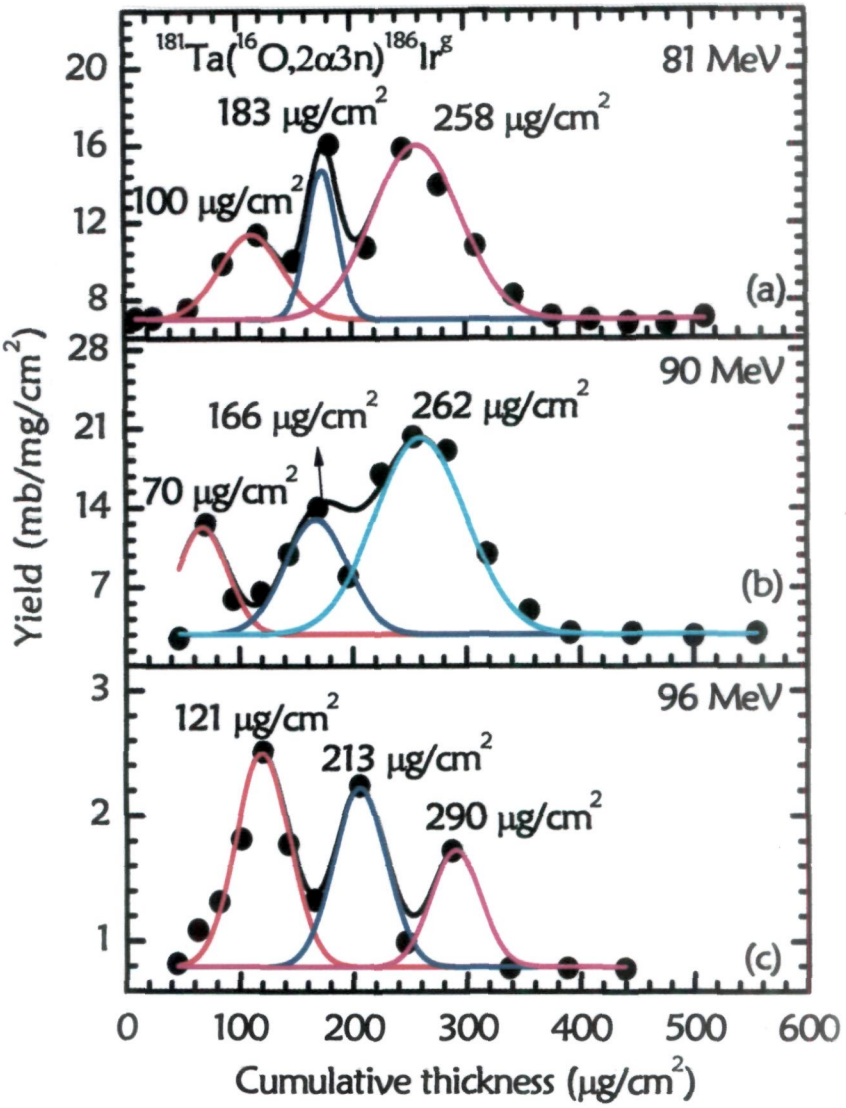

Figure 5.4.12: Experimentally measured forward recoil range distributions for $^{186}Ir^{g}(2\alpha3n)$ at projectile energies ≈81, 90 and 96 MeV. The lines joining data points are the result of best fit to the experimental data points.

found to be ≈21.2%, 17.0% and 42.7%, relative contribution for ^{12}C-fusion in the same reaction, is found to be ≈18.0%, 23.7% and 35.5% while the contribution from ^{16}O-fusion is found to be ≈60.8%, 59.3% and 21.8% at 81, 90 and 96 MeV projectile energies respectively.

In order to get the confidence in the experimentally measured FRRDs, an attempt has been made to theoretically estimate the most probable mean ranges, R_p(Th), using range-energy relation. The experimentally measured most probable mean ranges R_p(expt) for both CF and/or ICF components, in case of α-emitting channels are shown in Table 5.3, and are found to agree well, in general, with the theoretically calculated range values within the experimental uncertainties. In Table 5.3, the errors shown in R_p(expt) indicates the FWHM of the Gaussian distribution of the experimental data. It may be observed from the RRD data that in some cases, the peak corresponding to a particular fusion component at higher incident energy is observed at slightly lower thicknesses than the peak at lower beam energy. This may be due to the finite resolution in RRD data and the fact that the catcher foils may also have uncertainty in their thicknesses.

Table 5.2: Relative contributions of CF and ICF processes, at ≈81, 90 and 96 MeV energies, deduced from RRD data.

Residue	E_{lab} (MeV)	CF of ^{16}O(%)	ICF of ^{12}C(%)	ICF of ^{8}Be(%)
$^{192}Au^{g}$(αn)	81	79.2	20.8	-
	90	88.5	11.5	-
	96	76.2	23.8	-
$^{191}Au^{g}$(α2n)	81	79.5	20.5	-
	90	71.4	28.6	-
	96	47.5	52.5	-
$^{190}Au^{g}$(α3n)	81	88.4	11.6	-
	90	70.2	29.8	-
	96	64.2	35.8	-
$^{186}Ir^{g}$(2α3n)	81	60.8	18.0	21.2
	90	59.3	23.7	17.0
	96	21.8	35.5	42.7

Table 5.3: Experimentally measured R_P(expt) deduced from RRD curves and theoretically calculated R_P(Th) for ICF components at ≈81, 90 and 96 MeV energies.

Residue	R_P(expt) (μg/cm²) (CF of ^{16}O)	R_P(Th) (μg/cm²) (CF of ^{16}O)	R_P(expt) (μg/cm²) (ICF of ^{12}C)	R_P(Th) (μg/cm²) (ICF of ^{12}C)	R_P(expt) (μg/cm²) (ICF of ^{8}Be)	R_P(Th) (μg/cm²) (ICF of ^{8}Be)
Energy (E) ≈81 MeV						
^{192}Au^{g}(αn)	275±60	267	145±37	198	-	-
^{191}Au^{g}(α2n)	256±48	267	165±27	198	-	-
^{190}Au^{g}(α3n)	290±50	267	181±22	198	-	-
^{186}Ir^{g}(2α3n)	258±38	267	183±13	198	100±27	108
Energy (E) ≈90MeV						
^{192}Au^{g}(αn)	256±37	287	168±20	215	-	-
^{191}Au^{g}(α2n)	281±43	287	170±37	215	-	-
^{190}Au^{g}(α3n)	282±35	287	196±25	215	-	-
^{186}Ir^{g}(2α3n)	262±40	287	166±27	215	70±21	117
Energy (E) ≈96 MeV						
^{192}Au^{g}(αn)	290±47	298	200±35	227	-	-
^{191}Au^{g}(α2n)	294±45	298	204±43	227	-	-
^{190}Au^{g}(α3n)	286±51	298	213±35	227	-	-
^{186}Ir^{g}(2α3n)	290±50	298	213±23	227	121±21	122

In order to study the energy dependence of CF (full LMT) and ICF (partial LMT) components, percentage relative contributions of the CF and ICF components are plotted against the projectile energy in Figs. 5.4.13(a-b) and Figs. 5.4.14(a-b) for all the four α-emitting channels. The overall errors in relative contributions are expected to be less than ≈10%. As can be seen from the Fig. 5.4.13 (a) that in case of αn channel the relative percentage contribution of CF and ICF remains almost constant. However, it may be observed from Figs. 5.4.13(b) and Figs. 5.4.14(a), in case of α2n and α3n reaction channels (which are expected to be populated via both CF and/or ICF process), the CF contribution decreases with projectile energy, while the ICF contribution (fusion of ^{12}C) is found to increase with projectile energy. Further, from Fig. 5.4.14 (b), in case of 2α3n reaction channel, the relative contribution for the CF of ^{16}O decreases and the contributions of ICF of ^{16}O (fusion of ^{12}C and ^{8}Be) increases with incident energy. It may, however, be inferred that, in general, ICF starts dominating for individual reaction channels as the projectile energy increases. While deriving the relative contributions from the fitting of RRD data, the value of χ^2 was minimized in the present analysis using a non-linear least-square fit routine.

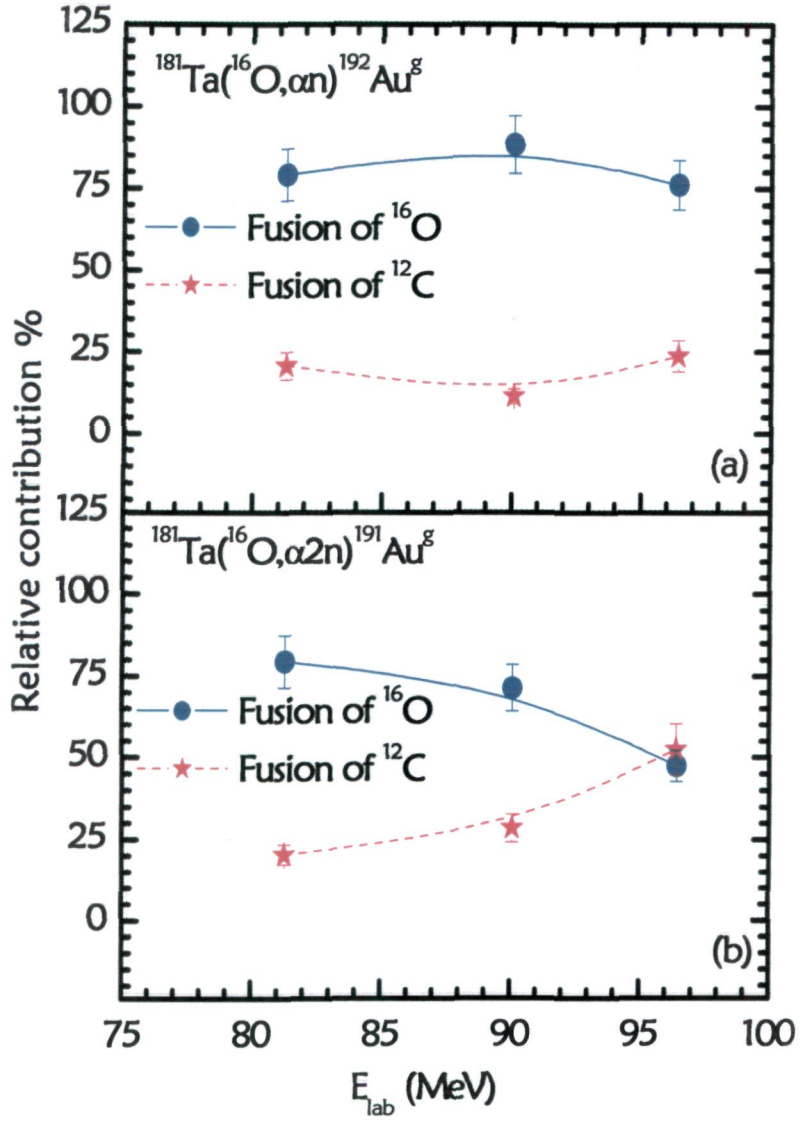

Figure 5.4.13: Relative strengths of the contribution coming from CF and ICF of ^{16}O with ^{181}Ta at projectile energies ≈81, 90 & 96 MeV for $^{192}Au^{g}$ (αn) & $^{191}Au^{g}$ (α2n) reaction products. The lines joining data points are just to guide the eyes.

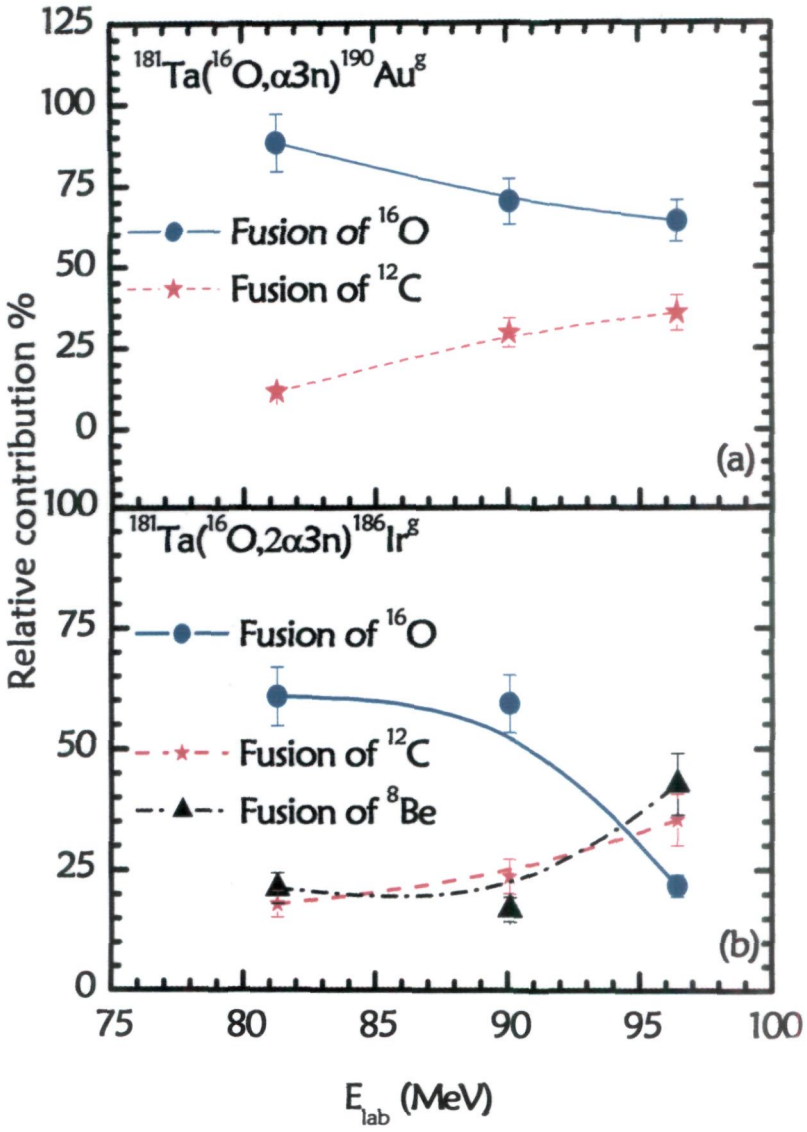

Figure 5.4.14: Relative strengths of the contribution coming from CF and ICF of ^{16}O with ^{181}Ta at projectile energies ≈81, 90 & 96 MeV for $^{190}Au^{g}$ ($\alpha 3n$) & $^{186}Ir^{g}$ ($2\alpha 3n$) reaction products. The lines joining data points are just to guide the eyes.

keeping the width (ω_A) of the distribution as a free parameter and most probable mean range (R_P) has been kept at the peak position. As such, only the width remains as a free parameter. Moreover, as indicated in Figs. 5.4.9 to 5.4.12, the RRD for the corresponding residues show more than one LMT components (RRD peaks). In such cases, the experimentally measured normalized yields have been fitted using the multi-peak option. It may, however, be pointed out that choosing the width of Gaussian peak as a free parameter may influence the relative contributions derived from the RRD data. In the present work the minimization of χ^2 and selected values of FWHM for the peak in the complex RRD data were found to fit the experimental data satisfactorily. In the present work an attempt has been made to disentangle the CF and ICF contributions by fitting the FRRDs with Gaussian constrained at a range expected for full momentum transfer to estimate their relative contributions. The values of F_{ICF} deduced from ICF data are plotted as a function of normalized beam energy (E_{beam}/CB) in Fig. 5.4.15. As can be seen from this figure that the ICF fraction increases with energy rapidly at lower energies, however, at relatively higher energies the F_{ICF} seems to move towards saturation for $^{16}O+^{181}Ta$ system. Further, extrapolation of this curve in the lower energy region clearly indicates the onset of ICF processes even at energies very close to CB i.e., from ≈5% above CB. It may be pointed out here that the F_{ICF} given in Fig. 5.2.4, presents the lower limit of in-complete fusion contributions as several other ICF channels could not be measured due to their short half-lives, and/or low intensity γ-lines of the residues. It may not be out of place to mention that similar observations of ICF contributions increasing with energy and mass asymmetry have been reported by Morgenstern et. al [15]. However, their work involved measuring the velocity spectra employing time of flight method in the lighter systems and also at relatively higher energies ≈10-25 MeV/n.

Further, Fig. 5.4.16 shows the ICF contributions of different Au isotopes at three different projectile energies. It may be observed from this figure that the production of $^{190}Au^g$ via ICF channel is nearly same at 81, 90 & 96 MeV. However, the production probability of $^{191}Au^g$ is largest at 90 MeV and smallest at 96 MeV with some intermediate value at 81 MeV. Further, a comparison of production probability of $^{190,191,192}Au^g$ at 81, 90 and 96 MeV indicates that maximum production of $^{192}Au^g$ is at 90 MeV and smallest at 81 MeV. However, at 96 MeV it has some intermediate value.

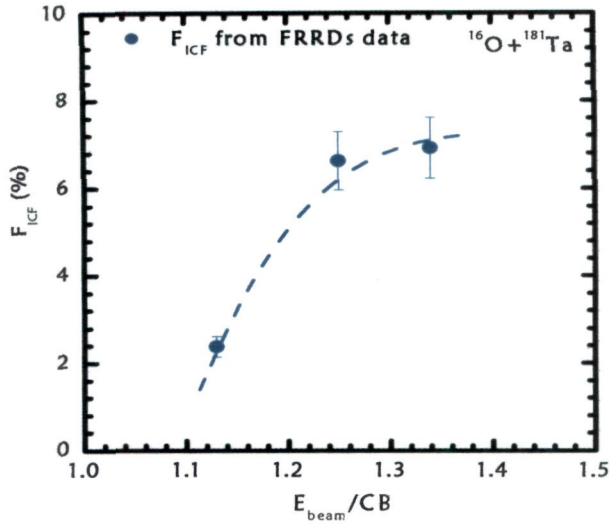

Figure 5.4.15: Deduced percentage ICF fraction (F_{ICF}) as a function of normalized projectile energy for the system $^{16}O+^{181}Ta$. The lines joining data points are just to guide the eyes.

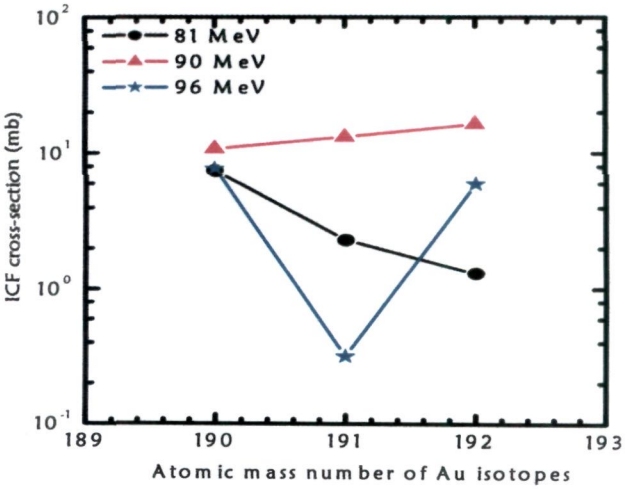

Figure 5.4.16: ICF contribution of different Au isotopes produced in $^{16}O+^{181}Ta$ system at projectile energies ≈81, 90 & 96 MeV. The lines joining data points are just to guide the eyes.

The present data seems to be explained on the basis of BUF model assuming that as the incident ion comes near the field of target nucleus, it may break-up into its fragments and one of the fragments may fuse with the target nucleus resulting finally into partial linear momentum transfer. The presently measured FRRD data clearly indicates that the momentum (mass) lost in case of ICF processes at the time of interaction preferentially originates from the incident beam nuclei. A more detailed particle γ-coincidence experiment for this system ($^{16}O+^{181}Ta$) is proposed, to have better insight in the reaction mechanism and the associated ℓ-values in case of CF and ICF processes.

5.5 Analysis using SUMRULE model

As has already been mentioned, it is possible to calculate cross-sections for CF and ICF channels using the SUMRULE model [20]. The underlying assumption in the SUMRULE model is that the ICF channels open only for those partial waves which have ℓ values greater than $\ell_{critical}$ i.e., ($\ell \geq \ell_{critical}$). On the other hand, partial waves with $\ell < \ell_{critical}$ values contribute to CF. There are three important parameters in the model viz., the temperature T of the contact zone, the diffuseness Δ of the T_ℓ distribution and the Coulomb interaction radius R_C. The values; T=3.5 MeV, Δ=1.7 $\hbar$ and R_C=1.5 fm have been suggested [21] for these parameters. The reaction residues, experimentally measured range integrated cross-sections obtained from the recoil range distribution data and cross-sections calculated by SUMRULE model for presently measured ICF channels populated in the system ^{16}O +^{181}Ta at ≈81, 90 and 96 MeV incident projectile energies are given in Table 5.4. As may be seen from this table, that there is a large discrepancy between the measured and calculated cross-section values for these channels. Wilczynski et. al. [20], tested the SUMRULE model for some reactions at ≈10 MeV/nucleon energy and found satisfactory agreement in the calculated and experimental cross-sections. The SUMRULE model calculations, carried out for the present system, which allow the ICF processes only for $\ell > \ell_{crit}$, underestimates the presently measured ICF cross-section data by a few orders of magnitude. As a typical example the experimentally measured cross-sections σ(expt) for (α3n) and (2α3n) channels are ≈ 64.0 ± 9.6 mb and 5.0 ± 0.7 mb, however, the theoretically calculated SUMRULE values σ(Th), are found to be 1.32 $\times10^{-2}$ mb and 3.02 $\times10^{-3}$ mb at 81 MeV beam energy. These discrepancies may

indicate deviations in the assumptions of the model. Similar deviations have also been found by Parker et. al.,[22] in their study on $^{12}C+^{51}V$ system up to 100 MeV (≈8 MeV/nucleon). The SUMRULE model assumes sharp cut-off ℓ-values for CF and ICF processes. The possible reason for the disagreement between the presently measured and SUMRULE model calculations for ICF channels may be the non-validity of the concept of critical angular momentum at these low energies. The present findings indicate a diffused boundary in ℓ-space which may penetrate close to the barrier. The cluster structure of the incident ion may also play an important role in ICF reactions.

Table 5.4: Experimentally measured and theoretically calculated cross-sections using SUMRULE model for the residues populated via αxn (x = 1, 2 & 3) and 2αxn (x =3) channels in $^{16}O+^{181}Ta$ system.

Residue(s)	RRD @ 81 MeV		RRD @ 90 MeV		RRD @ 96 MeV	
	σ(expt) (mb)	σ (Th) (mb)	σ(expt) (mb)	σ (Th) (mb)	σ(expt) (mb)	σ (Th) (mb)
$^{192}Au^{g}$ (αn)	6.0±0.9	0.87	144.0±21.6	1.85	25.0±3.75	2.49
$^{191}Au^{g}$ (α2n)	11.0±1.65	0.20	46.0±6.9	0.43	0.6±0.09	0.57
$^{190}Au^{g}$ (α3n)	64.0±9.6	1.32×10^{-2}	36.0±5.4	0.03	12.0±1.80	3.79×10^{-2}
$^{186}Ir^{g}$ (2α3n)	5.0±0.75	3.02×10^{-3}	4.2±0.63	6.44×10^{-3}	0.54±0.08	8.69×10^{-3}

5.6 Angular distributions

The analysis of EFs for the presently studied system $^{16}O+^{27}Al$, as mentioned in Section 4.3, clearly indicates that these reactions have significant contributions from the processes other than that of CF. To confirm the reaction mechanism involved, a specially designed experimental setup was used, as shown in Fig. 2.5 of Chapter II. In this experiment, an Al-target supported by a natural thulium material of thickness ≈0.48 mg/cm^2 followed by a stack of thick annular concentric Al-catcher foils was used. Depending on the momentum transfer from the projectile to the composite system, the residues formed by CF and ICF processes get trapped in the concentric annular aluminum catchers at different angles. The residues that are expected to be populated by a mechanism such as a direct reaction may be stopped within the thulium layer. The measured angular distributions for the reaction $^{27}Al(^{16}O,2\alpha n)^{34}Cl$ is shown in Fig. 5.6.1. Two peaks are observed, one around 0^0–13^0 may be assigned to the residues populated by

complete fusion, and the other peak in the angular range 45°–60° may be assigned to the residues populated by ICF processes. Note that, out of the five reactions identified in the EF measurements, only the γ-ray of 146.5 keV corresponding to the reaction $^{27}Al(^{16}O,2\alpha n)$ could be identified from its energy as well as the half-life of ^{34}Cl residues in the angular distribution measurements. The residues formed by CF are likely to recoil in the forward cone, as such peaking of angular distribution around 0° indicates the population of residue ^{34}Cl via CF. However, the same residue ^{34}Cl when populated by ICF of ^{16}O will show peak at much higher angles. Therefore, it may be concluded that the basic mechanism of population of ^{34}Cl may be based on both CF and ICF processes.

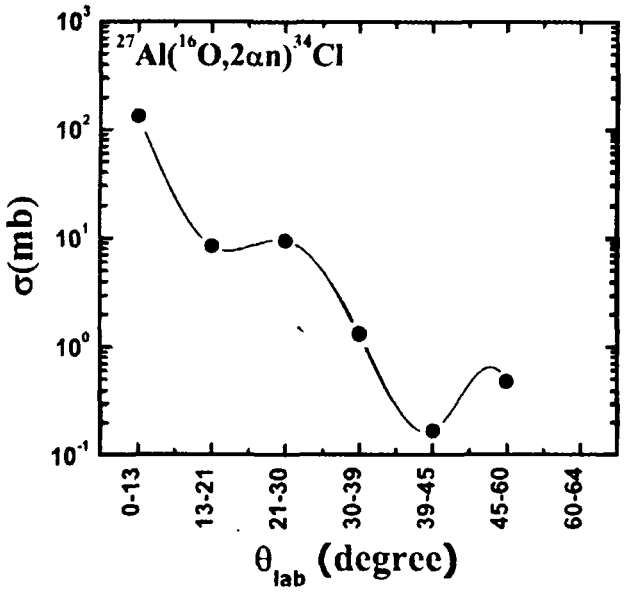

Figure 5.6.1: Measured angular distribution for reaction $^{27}Al(^{16}O,2\alpha n)^{34}Cl$. The lines joining data points are just to guide the eyes.

However, in case of reactions $^{27}Al(^{16}O,3\alpha 3p)^{28}Mg$, $^{27}Al(^{16}O,3\alpha 3pn)^{27}Mg$, $^{27}Al(^{16}O,4\alpha 2pn)^{24}Na$ and $^{27}Al(^{16}O,4\alpha 3p)^{24}Ne$, the EF analysis clearly indicated that these residues are not likely to be populated by the CF process as the theoretical calculations based on statistical model give negligible contribution for these reactions. This is further confirmed from the angular distribution measurements, since no γ-peak corresponding to

these residues has been observed in any of the angular zones. Thus, these residues are not likely to be populated either via complete or in-complete fusion processes. However, these residues may be formed by direct reaction process, where the ejectile takes away a large fraction of the energy and hence, the residues formed may have ranges much smaller than those of residues formed by CF and/or ICF processes and may be trapped in the thulium layer.

5.7 A note on spin distributions and feeding intensity profile studies

Apart from obtaining the relative contributions of CF and/or ICF processes in heavy ion reactions and their energy and mass asymmetry dependence, other most debated and still out-standing issues about the ICF reaction dynamics at energies ≈4-7 MeV/nucleon are i) the estimation of the localization of ℓ-window and ii) to examine the possibility to populate high spin states via ICF. As such, in order to understand above issues two particle γ-co-incidence experiments have been performed [23-25], to draw some co-relations between driving angular momenta and successively opened ICF channels. Details of these experiments, carried out at the IUAC, New Delhi, Pelletron Accelerator Facility, are given elsewhere [23-25]. However, for the sake of completeness a brief description of how the particle γ-co-incidence experiments may give useful information in this regard is given here. The experimental arrangement consists of a Gamma Detector Array (GDA) along with a Charged Particle Detector Array (CPDA). The GDA is an assembly of 12 Compton suppressed high resolution HPGe γ-spectrometers at 45°, 99° and 153° with respect to the beam axis and there are four detectors at each of these angles. However, CPDA is a set of 14 Phoswich detectors housed in a 14-cm diameter scattering chamber, covering nearly 90% of the solid angle. The division of these detectors into forward (F), backward (B) and sideways (S) zones was used to differentiate between forward and backward going α-particles. The fast α-particles (due to ICF process) were detected in the forward cone. The in-beam prompt γ-ray spectra have been recorded in multi-parameter mode, which includes different co-incidences like; α and 2α detected in backward, forward and 90° angles. Finally, several CF and ICF channels have been identified in co-incidence with forward and backward emitted α-particles. As a typical example, the experimentally measured spin

distributions for the residues ^{180}Ir(5n), ^{177}Re(α4n) and ^{174}Ta(2α3n), in the ^{16}O+^{169}Tm system, are shown in Figs. 5.7.1 (a) [23]. As can be seen from this figure that the patterns of spin distributions of the residues populated via CF and ICF processes are entirely different. A comparison of the spin distribution of the same residue ^{177}Re identified in co-incidence with backward (B) and forward (F) going α-particles clearly indicates the entirely different spin distribution patterns, a characteristic of such processes. As can be seen from this figure that the intensity of yrast line transitions decreases gradually with high spin for CF, while in case of ICF, the intensity remains almost constant upto a certain limiting spin value and then decreases rapidly for higher spins, indicating the entirely different de-excitation patterns for CF and ICF from entry state to the yrast line. This implies a rather smooth and broad feeding distribution for "yrast states" in case of CF. However, for ICF channels this distribution must have a 'narrow window' meaning thereby a well localized angular momentum region where a given projectile like fragment is emitted in contrast to the large window for fusion reactions. The same is reflected from the feeding intensity profiles shown in Figs. 5.7.1 (b) [23].

The complementary and useful information that can be obtained from the above results is that the value of mean input angular momentum increases with direct α-multiplicity in the forward cone, which indicates the competition from successively opened ICF channels for each ℓ-value above ℓ_{crit} for normal fusion (CF), even at projectile energies $\approx$5-6 MeV/nucleon. This confirms that the ICF reactions predominantly occur due to the influence of centrifugal potential at higher values of input angular momenta where CF is expected to be dominant. As such, it may not be out of place to mention that the ICF is a natural extension of the fusion processes for those interaction trajectories for which the limit of input angular momenta do not allow the CF to occur. From the analysis of some of our recent experiments [23-25] it has been concluded that ICF can populate a given residue via ICF channel with a relatively large angular momentum compared to that populated via CF process. As such, the study of ICF reactions also opens an opportunity to populate and study the residues with higher spins, even at lower projectile energies. An extension to this work is in progress to obtain better insight into the reaction dynamics and associated ℓ-values.

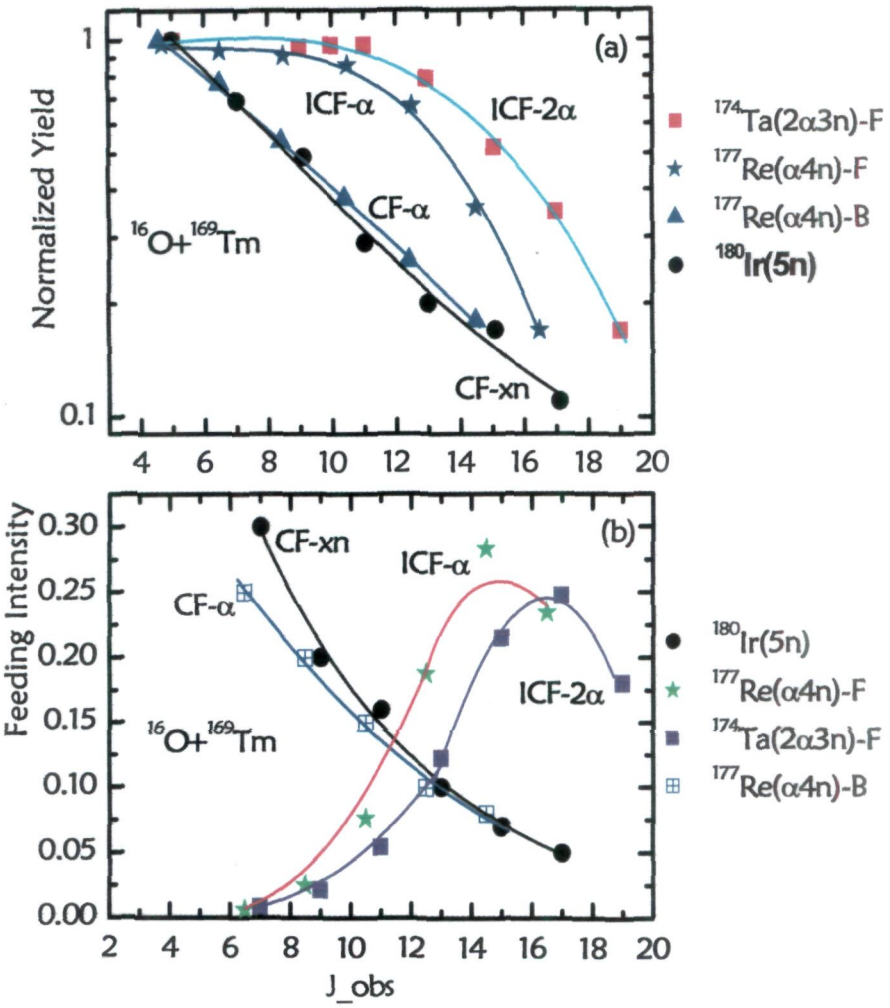

Figure 5.7.1 (a) Experimentally measured spin distributions for different residues populated via xn (CF product) and αxn/2αxn (both CF and/or ICF products), (b) Deduced feeding intensities of gamma cascades of different ER's expected to be produced via; xn, αxn and/or 2αxn channels in $^{16}O+^{169}Tm$ system at ≈5.6 MeV/nucleon. The lines and curves through data points are drawn to just guide the eyes.

Conclusions and Future Perspectives

In the present work, experiments have been carried out to study the heavy ion reaction dynamics at energies from near the Coulomb barrier to well above it. An attempt has been made to study the CF and ICF of ^{16}O with ^{181}Ta, ^{103}Rh and ^{27}Al targets. Analysis of data has provided significant information about CF and ICF reactions. To be more specific, in order to study the influence of ICF on CF, the EFs of fourteen radio-nuclides; $^{194}Tl^{g}$, $^{194}Tl^{m}$, $^{193}Tl^{g}$, $^{193}Tl^{m}$, $^{192}Tl^{g}$, $^{192}Tl^{m}$, $^{193}Hg^{g}$, $^{193}Hg^{m}$, ^{192}Hg, $^{191}Hg^{g}$, $^{191}Hg^{m}$, $^{192}Au^{g}$, $^{191}Au^{g}$ and $^{190}Au^{g}$ produced in $^{16}O+^{181}Ta$ system, eight radio-nuclides; $^{115}Te^{g}$, $^{115}Te^{m}$, ^{114}Te, $^{110}In^{g}$, $^{110}In^{m}$, $^{108}In^{g}$, $^{108}In^{m}$ and $^{103}Ag^{g}$ produced in $^{16}O+^{103}Rh$ system and five radio-nuclides; ^{34}Cl, ^{28}Mg, ^{27}Mg, ^{24}Na and ^{24}Ne produced in $^{16}O+^{27}Al$ system have been measured. The experimentally measured EFs have been compared with the predictions of the theoretical model code PACE4. The measured EFs for xn and pxn channels, likely to be populated by CF process are, in general, well reproduced by the theoretical calculations. However, the enhancement of the experimentally measured production cross-sections over the theoretical model predictions have been observed for most of the α-emission channels. The enhancement may not be due to the experimental uncertainties as they have been estimated to be $\leq$15 %. As such, this enhancement has been attributed to the contribution coming from ICF reaction dynamics. Further, in order to understand the influence of ICF on CF, the percentage fraction of in-complete fusion (F_{ICF}) has been deduced as a function of beam energy and mass asymmetry of the interacting ions. The F_{ICF} has been found to be very sensitive to the projectile energy, and also to the mass asymmetry of interacting partners. Further, the value of F_{ICF} is found to be $\approx$4.0% for ^{16}O + ^{103}Rh system while for ^{16}O + ^{181}Ta system it is found to be around $\approx$12.0% at the same normalized projectile energy (i.e. E_{beam}/V_b =1.38). This indicates the sensitiveness of F_{ICF} on the atomic mass number of the target. In order to have a better insight into mass asymmetry dependence the values of F_{ICF} for several projectile-target systems (including some literature results) are compared. In general, the value of F_{ICF} is found to increase with the mass asymmetry, separately for ^{16}O and ^{12}C projectiles. From the above, it may be inferred that, not only mass asymmetry of interacting partners but the projectile structure also affects the ICF population. Further, the observation of large percentage F_{ICF} may be attributed to the prompt break-up of projectile ^{16}O into its α-clusters ($^{12}C+^{4}He$ and/or $^{8}Be+^{8}Be$). The break-up

probability increases with the incident projectile energy, and hence the percentage F_{ICF} may increase with projectile energy. It may also be pointed out that the present observations are in agreement with the systematics presented by Morgenstern et al. [15]. The observation of large percentage F_{ICF} in case of ^{16}O-projectile as compared to ^{12}C induced reactions may be because of the fact that the ^{16}O is assumed to be a group of 4α-clusters, while ^{12}C consists only of 3α-clusters. The above mentioned description/discussion on ICF based on the measurement and analysis of EFs strongly reveals that apart from CF, the ICF is also a process of greater importance at these energies.

In order to study the energy dependence and fusion in-completeness in these processes, the forward recoil range distributions (FRRDs) for the following twelve radio-nuclides; ^{194}Tl, ^{193}Tl, ^{192}Tl, $^{193}Hg^{g}$, $^{193}Hg^{m}$, ^{192}Hg, $^{191}Hg^{g}$, $^{191}Hg^{m}$, $^{192}Au^{g}$, $^{191}Au^{g}$, $^{190}Au^{g}$ and $^{186}Ir^{g}$ produced in $^{16}O+^{181}Ta$ system, at three different projectile energies ≈81, 90 and 96 MeV have also been measured. Different linear momentum transfer components attributed to the fusion of ^{16}O and/or of ^{12}C and/or ^{8}Be from ^{16}O projectile to the target nucleus have been observed. The results presented on the measurement and analysis of forward recoil ranges of heavy reaction products, strongly reveal a significant contribution coming from partial linear momentum transfer of projectile associated with in-complete fusion. An attempt has also been made to obtain the percentage relative contributions of complete and/or in-complete fusion components, which show ICF as a competing mode of reaction at these energies. The break-up fusion model of ICF has been found to explain the measured FRRDs at the energies of interest. Based on RRDs analysis, it may be concluded irrefutably that the residues are not only populated via CF but ICF is also found to play an important role in the production of different reaction products involving direct α-cluster emission. The experimentally measured most probable recoil ranges R_P(expt) have been compared with those estimated by using range energy formulations, and are found to be generally in good agreement. The results obtained clearly indicate the partial fusion of projectile with target nucleus associated with ICF at these energies. Calculations for cross-sections have also been performed using SUMRULE model. The cross-sections for in-complete fusion channels calculated with SUMRULE model are found to be significantly small as compared to the measured values. The large discrepancy for ICF channels may be due to the cluster structure of the

projectile and/or due to the non-validity of the concept of critical angular momentum at these energies. Further, the present findings indicate a defused boundary for ℓ-values which may penetrate close to the barrier.

Further, angular distributions in the system $^{16}O+^{27}Al$ have also been measured. From the study of the angular distributions of the residue, it may be inferred that in the case of complete fusion, the residues are emitted in the forward cone along the beam direction, while for in-complete fusion the recoiling residues emerge at relatively large angles with respect to the beam direction, as expected. As such, angular distributions of residues with respect to the beam direction may also provide complementary information about the complete and in-complete fusion processes. The analysis of angular distribution data confirms the presence of significant contribution from the ICF process in the $^{27}Al(^{16}O, 2\alpha n)^{34}Cl$ reaction.

As an extension of the present work, it is proposed to carry out some experiments to measure the energy spectra of projectile-like fragments, which is supposed to be an extra degree of freedom to explain the findings of the present work. The extension of the present work at relatively higher energies would also be interesting, and will be helpful for the refinement of the present findings. The data of present measurements may be of use in developing a model for in-complete fusion and also for developing the systematics employing several projectile-target parameters and energies of incident ions.

References

[1] A. Gavron, Phys. Rev. C21, 230 (1980).

[2] P. Vergani, E. Gadioli, E. Vaciago, E. Fabrici, E. Gadioli Erba, M.Galmarini, G.Ciavola, andC.Marchetta, Phys. Rev. C 48, 1815 (1993).

[3] M. Blann; Nucl. Phys. A235, 211 (1974).

[4] M. Blann; Annu. Rev. Nucl. Sci. 25, 123 (1975).

[5] M. Cavinato, E. Fabrici, E. Gadioli Erba, P. Vergani, M. Crippa, G. Colombc I. Redaeli and M. Ripamonti, Phys. Rev. C 52, 2577 (1995).

[6] Unnati Gupta, Pushpendra P. Singh, Devendra P. Singh, Manoj Kumar Sharma, Abhishek Yadav, Rakesh Kumar, B.P. Singh, R. Prasad; Nuclear Physics A 811, 77(2008).

[7] Devendra P. Singh, Unnati, Pushpendra P. Singh, Abhishek Yadav, Manoj Kumar Sharma, Rakesh Kumar, K. S. Golda, B. P. Singh, A. K. Sinha and R Prasad; Phys. Rev. C80, 014601(2009).

[8] R. D. Evans, The Atomic Nucleus (McGraw–Hill, New York, 1982), p. 481.

[9] M. Blann, G. Reffo, and F. Fabbri; Nucl. Instrum. Methods A 265, 490 (1988).

[10] V. F. Weisskopf; Phys. Rev. 52, 295 (1937).

[11] Pushpendra P. Singh, B. P. Singh, Manoj K. Sharma, Unnati, Devendra P. Singh, R. Prasad, R. Kumar, and K. S. Golda, Phys. Rev. C 77, 014607 (2008).

[12] Manoj Kumar Sharma, B. P. Singh, Sunita Gupta, M. M. Muthafa, H. D. Bhardwaj, and R. Prasad, J. Phys. Soc. Jpn. 72, 1917 (2003).

[13] S. Gupta, B. P. Singh, M. M. Musthafa, H. D. Bhardwaj, and R. Prasad, Phys. Rev. C 61, 064613 (2000).

[14] K. Surendra Babu, R. Tripathi, K. Sudarshan, B. D. Shrivastava, A. Goswami and B. S. Tomar; J. Phys. G; Nucl. Part. Phys. 29, 1011(2003).

[15] Morgenstern et. al., Phys. Rev. Lett. 113B, 463 (1982); Phys. Rev. Lett. 52 No. 13, 1104 (1984).

[16] Inge-Maria Ladenbaurer-Bellis, Ivor L. Preiss, and C. E. Anderson, Phys. Rev. 125, 606 (1962).

[17] P. Mckenna et. al., Phys. Rev. Lett. 91, 075006(2003)

[18] Pushpendra P. Singh, Manoj Kumar Sharma, Unnati, Devendra P. Singh, B. P. Singh, Rakesh Kumar and R. Prasad; Eur. Phys. J. A34, 29 (2007).

[19] L.C. Northcliffe and R.F. Schilling, At. Data Nucl. Data Tables A7, (1970) 264.

[20] J. Wilczynski, K. Siwek-Wilczynska, J.Van Driel, S. Gonggrijp, D. C. J. M.

Hageman, R. V. F. Janssens, J. Lukasiak and R. H. Siemssen; Phys. Rev. Lett. 45, No. 8, 606(1980).

[21] J. Wilczynski, K. Siwek-Wilczynska, J.Van Driel, S. Gonggrijp, D. C. J. M. Hagman, R. V. F. Janssens, J. Lukasiak, R. H. Siemssen and S. Y. Van Der Werf; Nucl. Phys. A 373, 109(1982).

[22] D. J. Parker, J. Asher, T. W. Conlon, N. Naquib; Phys. Rev. C 30, 143 (1984).

[23] Pushpendra P. Singh, B. P. Singh, M. K. Sharma, Unnati Gupta, Rakesh Kumar, D. P. Singh, R. P. Singh, S. Murlithar, M. A. Ansari, R. Prasad and R. K. Bhowmik; Physics Letters B 671, 20 (2009).

[24] Pushpendra P. Singh, B. P. Singh, M. K. Sharma, Unnati Gupta, Rakesh Kumar, K. S. Golda, D. P. Singh, R. P. Singh, S. Murlithar, M. A. Ansari, R. Prasad and R. K. Bhowmik; Phys. Rev. C 78, 017602 (2008).

[25] Pushpendra P. Singh, Abhishek Yadav, Devendra P. Singh, Unnati Gupta, M. K. Sharma, R. Kumar, D. Singh, R. P. Singh, S. Murlithar, M. A. Ansari, B. P. Singh, R. Prasad and R. K. Bhowmik; Phys. Rev. C 80, 064603 (2009).

PHYSICAL REVIEW C 80, 014601 (2009)

Investigation of the role of break-up processes on the fusion of ^{16}O induced reactions

Devendra P. Singh,[1,*] Unnati,[1] Pushpendra P. Singh,[1] Abhishek Yadav,[1] Manoj Kumar Sharma,[2]
B. P. Singh,[1,†] K. S. Golda,[3] Rakesh Kumar,[3] A. K. Sinha,[4] and R. Prasad[1]
[1]*Department of Physics, Aligarh Muslim University, Aligarh (UP) 202 002, India*
[2]*Department of Physics, S. V. College, Aligarh (UP) 202 001, India*
[3]*Inter-University Accelerator Center, Aruna Asaf Ali Marg, New Delhi 110 067, India*
[4]*UGC-DAE-CSR, Bidhan Nagar, Kolkata 700 098, India*
(Received 27 March 2009; published 7 July 2009)

An experiment was carried out to explore heavy ion incomplete fusion reaction dynamics, within the framework of the break-up fusion model, at energies near and above the Coulomb barrier. Excitation functions for several radionuclides produced via xn, pxn, and αxn channels were measured in the $^{16}O + {}^{181}Ta$ system at energies of ≈76–100 MeV. The experimental excitation functions were compared with those calculated using the theoretical model code PACE4. It was observed that excitation functions of xn/pxn channels are in good agreement with theoretical predictions. However, a significant enhancement in the measured excitation functions of α-emitting channels was observed and attributed to the incomplete fusion processes. The incomplete fusion fraction (F_{ICF}) that gives the relative importance of complete and incomplete fusion processes was found to increase with energy. The results are discussed in terms of α-cluster structure of the projectile on various fusion reactions.

DOI: 10.1103/PhysRevC.80.014601 PACS number(s): 25.70.Jj, 25.70.Gh

I. INTRODUCTION

For many years, the study of heavy ion (HI) induced reactions has been used as an important tool to understand the reaction dynamics and the decay characteristics of excited compound nuclei at energies near and above the Coulomb barrier (CB) [1–4]. It is now experimentally established that complete (CF) and incomplete fusion (ICF) are the most dominating modes of reaction processes at these energies [5–10]. In the case of CF, all the nucleons of the projectile and target nuclei lose their identity and form a single, excited complex system, which may eventually lead to a fully equilibrated compound nucleus (CN). The equilibrium state occurs as the composite system produces an intense mean field that prevents the escape of nucleons from the excited complex system and leads to complete thermalization. At later stages, the CN de-excites via emission of light nuclear particle(s) and/or the characteristic γ rays. However, in case of ICF, as the projectile comes within the field of the target nucleus, it is assumed to break up into its fragments (predominantly into α clusters, in the case of the projectiles having an α-cluster structure), where one of the fragments may get fused with the target nucleus leading to the formation of an excited incompletely fused composite (IFC) system with a mass and/or charge less than the CN formed via CF [7]. The unfused fragment flows in forward cone with almost projectile velocity. Further, it has also been observed that, apart from CF and ICF, pre-equilibrium (PE) emission of light nuclear particles may also take place at these energies before the thermalization of the composite system [11–15]. Recently, it has been observed that ICF becomes more and more dominant as the projectile energy increases [16–21]. The different modes of reactions can also be understood on the basis of driving input angular momenta imparted into the system. The CF occurs for the input angular momenta values $\leqslant l_{crit}$, as per the sharp cutoff approximation. However, at relatively higher projectile energies and/or at larger impact parameters, ICF starts influencing the CF. It may, further, be pointed out that the multitude of driving input angular momenta may vary with the projectile energy and/or with the impact parameter. However, there is no sharp boundary for the CF and ICF processes; both the processes have been observed below and/or above the limiting value of input angular momenta [22]. A few reports have indicated that ICF can selectively populate high spin states in the final reaction products at low bombarding energies and can be used as a spectroscopic tool as well [23,24]. The ICF reactions have been demonstrated to populate neutron-rich nuclei compared to conventional fusion-evaporation reactions, opening possibilities for the study of nuclei along the neutron-rich side of the line of stability [25].

A variety of dynamical models/theories, like the Break-up Fusion (BUF) model [26], the SUMRULE model [27], the Promptly Emitted Particles (PEPs) model [28], the EXCITON model [29], the Hot Spot model [30], the Multistep Direct Reaction theory [31], and the Overlap model [32–34], have been proposed to explain ICF dynamics. Apart from the aforementioned dynamical models, Mogenstern *et al.* [35,36] investigated the mass asymmetry dependence of the ICF contribution. The details of the above models are given in Ref. [20]. It may, however, be pointed out that these models correctly predict the magnitude of ICF, to some extent, in some cases at energies $\geqslant$10 MeV/nucleon, but none of these models/theories is able to successfully explain the ICF data at energies of ≈4–7 MeV/nucleon. As such, the study of ICF is still an active area of investigation. Despite the existence of so many models, a clear picture of the mechanism of ICF is yet to emerge, particularly at relatively low bombarding energies, i.e., ≈4–7 MeV/nucleon, where the systematic study

*dpsingh19@gmail.com
†bpsinghamu@gmail.com

is available only for a few projectile-target combinations [5,20].

As such, for better understanding of ICF dynamics at low energies, excitation functions (EFs) for several radionuclides produced in the $^{16}O+^{181}Ta$ system ($Z_1.Z_2 \approx 584$) have been measured in the projectile energy range ≈76–100 MeV. It may be pointed out that, the charge multiplication $Z_1.Z_2$ for the system is much less than 1600 and, therefore, the fission probability in this case is quite low [37]. Cavinato *et al.* [1] have also studied the same projectile-target combination and measured the EFs for the production of some isotopes of Tl, Hg, Au, Pt, Ir, Os, and Re at energies of ≈69–126 MeV. However, they have limited themselves to discussing the data concerning fusion reactions only and have not made any comment about ICF even for those reaction channels where α particles are emitted. In the present work, cross sections have been measured for those residues that may be populated via ICF processes as well. In the work of Cavinato *et al.* [1], a part of the data is obtained using the thick target-catcher technique and a part from the angular distribution. In the present work, up to 100 MeV, the cross sections have been measured at eight different energies using the thick target-catcher technique. Further, as already mentioned, the cross sections for several reactions expected to be populated via CF and/or ICF processes have been measured. The data set from Ref. [1], in general, agree with the present work in the overlapping energy range. In the present work, the ^{189,191}Pt isotopes studied by Cavinato *et al.* [1] could not be detected because of long half-lives and low intensities of γ radiations. Also, the cross sections for ^{190}Hg could not be measured because the threshold for this reaction is above 100 MeV. Cavinato *et al.* [1] have not measured the cross sections for the individual reaction channels and have measured the cumulative cross sections for Hg and Pt isotopes. In addition to the work presented in Ref. [1], the cross sections for several Tl isotopes populated by xn channels ($^{194}Tl^{g}$, $^{194}Tl^{m}$, $^{193}Tl^{g}$, $^{193}Tl^{m}$, $^{192}Tl^{g}$, and $^{192}Tl^{m}$) have been measured in the present work, which could not be measured by Cavinato *et al.* [1]. In view of the above, the present work not only supplements the data of earlier work [1] but also provides a new cross-section database for several residues. Further, in the present work, an attempt has also been made to estimate the relative contribution of CF and ICF to study the influence of ICF on CF processes. This article is organized as follows: a brief description of the experimental procedure is given in Sec. II, comparison and analysis of the experimental data with the theoretical model predictions is presented in Sec. III along with the results and their interpretation. The conclusions drawn from the present study are given in the last section.

II. EXPERIMENTAL PROCEDURE

The experiment was performed using an $^{16}O^{7+}$ beam delivered from the 15UD-Pelletron Accelerator at the Inter-University Accelerator Centre (IUAC), New Delhi, India. Targets of spectroscopically pure ^{181}Ta (≈99.99%) of thickness ≈1.5 mg/cm^2 were prepared at the target laboratory of IUAC, using the rolling technique. To trap the recoiling products produced via different reaction processes, Al catchers of appropriate thickness were placed after each target. The thickness of each target and catcher foil was separately measured by weighing and also by the α-transmission method. The α-transmission method is based on the measurement of the energy lost by 5.487 MeV α particles (obtained from standard ^{241}Am source) while passing through the target material. Irradiations were carried out in the General Purpose Scattering Chamber (GPSC), which has an in-vacuum transfer facility (ITF). The targets along with the Al catchers in the form of a stack were placed normal to the beam direction, so that the recoiling products could be trapped in the catcher foils and there would be no loss of activity. The experimental setup (target-catcher foil arrangement) was similar to that given in Ref. [20]. Three stacks, each of four foils, three foils, and one foil, respectively, were irradiated at energies of ≈100, 98, and 88 MeV to cover a wide energy range. Keeping in view the half-lives of interest, irradiations were carried out for ≈8–10 h for each stack. The Pelletron crew provided a constant beam current ≈50 nA throughout the irradiations. The beam flux was calculated using the total charge collected in the Faraday cup, which was placed behind the target-catcher foil assembly. The activities produced after irradiation were recorded using a precalibrated, High Purity Germanium (HPGe) detector of

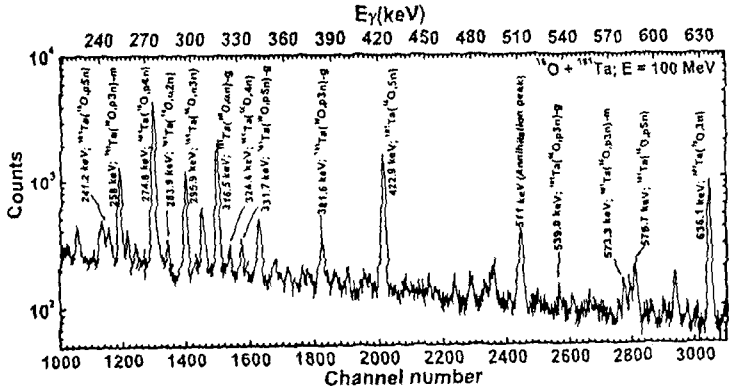

FIG. 1. An observed γ-ray spectrum of a ^{181}Ta sample irradiated by an ≈100 MeV $^{16}O^{7+}$ beam.

TABLE I. List of final reaction products along with populated channels and their spectroscopic properties.

Residue	$T_{1/2}$	J^{π}	E_γ (keV)	I_γ (%)
$^{194}Tl^{m}(3n)$	32.8 min	7^+	636.1	99
$^{194}Tl^{g}(3n)$	33 min	2^-	636.1	15.3
$^{193}Tl^{m}(4n)$	2.1min	$9/2^-$	365.0	90.1
$^{193}Tl^{g}(4n)$	21.6 min	$1/2^+$	324.4, 1044.7	15.2, 8.99
$^{192}Tl^{m}(5n)$	10.6 min	7^+	422.9	31.1
$^{192}Tl^{g}(5n)$	9.6 min	2^-	422.9	31.1
$^{193}Hg^{g}(p3n)$	3.8 h	$3/2^-$	381.6, 539.0	11.0, 1.2
			827.8, 861.1	4, 13.0
			1118.8	8.3
$^{193}Hg^{m}(p3n)$	11.8 h	$3/2^-$	258.1	60.0
$^{192}Hg(p4n)$	4.85 h	0^+	274.8	50.4
$^{191}Hg^{g}(p5n)$	49 min	$3/2^-$	224.6, 241.2	17.4, 8.9
			331.7	11.24
$^{191}Hg^{m}(p5n)$	50.8 min	$13/2^+$	420.3, 578.7	17.9, 17.0
$^{192}Au^{g}(\alpha n)$	4.94 h	1^-	295.5, 316.5	22.7, 58.0
$^{191}Au^{g}(\alpha 2n)$	3.18 h	$3/2^+$	283.9, 399.8	6.3, 4.5
$^{190}Au^{g}(\alpha 3n)$	42.8 min	1^-	295.9, 301.9	71.0, 25.1

100 c.c. active volume coupled to a PC through CAMAC based FREEDOM software [38]. The detector was calibrated using various standard γ sources, such as ^{60}Co, ^{133}Ba, and ^{152}Eu, of known strengths. The efficiency of the detector was determined at various source-detector separations. The detail of efficiency determination is given elsewhere [20].

A typical γ-ray spectrum for the $^{16}O + ^{181}Ta$ system at $\approx$100 MeV is shown in Fig. 1, where various γ peaks corresponding to different reaction products populated via CF and/or ICF channels are indicated. Further confirmation of the identification of reaction products has been made by the decay curve analysis. Identified evaporation residues along with their important spectroscopic properties are given in Table I. A FORTRAN programme based on standard formulation given in Ref. [20] has been used to determine the production cross sections of the reaction products. The experimentally measured cross sections for the population of residues via CF and/or ICF processes are given in Tables II and III. The errors in these measurements may arise mostly because of (a) nonuniformity of the target foil, (b) uncertainty in the determination of the efficiency of the detector, (c) fluctuations in the beam current, (d) the solid angle effect, etc. Details of errors due to above-mentioned factors are given in Ref. [20]. Attempts were made to minimize the uncertainties due to all the above factors. The overall error in the present work is estimated to be $\leqslant$15%, including the statistical errors.

III. RESULTS AND ANALYSIS OF DATA

To study the ICF reaction dynamics in the $^{16}O + ^{181}Ta$ system, the EFs for $^{194}Tl^{g}$, $^{194}Tl^{m}$, $^{193}Tl^{g}$, $^{193}Tl^{m}$, $^{192}Tl^{g}$, $^{192}Tl^{m}$, $^{193}Hg^{g}$, $^{193}Hg^{m}$, ^{192}Hg, $^{191}Hg^{g}$, $^{191}Hg^{m}$, $^{192}Au^{g}$, $^{191}Au^{g}$, and $^{190}Au^{g}$ radionuclides expected to be populated via CF and/or ICF were measured. A list of reactions populating various residues, their half-lives, characteristic γ lines, etc., is given in Table I. In general, a residue populated via a specific channel often emits several γ rays of different energies. The cross section for the channel was determined from the measured intensities of several characteristic γ rays and the value quoted is the weighted average of cross sections obtained for these γ rays [39].

A. (^{16}O, xn) channels

The measured EFs for residues populated via xn channels are shown in Fig. 2(a). Obviously these channels are populated only by CF. From the analysis of experimental data, activities corresponding to $3n$, $4n$, and $5n$ channels were identified. The identification was done on the basis of measured half-lives and γ-ray energies of the residues. It may be pointed out that in the case of $3n$ and $5n$ channels metastable and ground states of ^{194}Tl and ^{192}Tl are plotted. In both these cases, the metastable and ground states of the respective residues decay with γ rays of nearly the same energy and half-life. As such, the observed composite decay curves give the sum of both the states in each case. Individual cross sections were obtained by dividing the measured composite cross sections in the ratio of their γ-ray intensities [40,41]. $^{193}Tl^{g,m}$ are populated by a $4n$ channel. The metastable state of a half-life of $\approx$2 min decays to the ground state, which has a half-life of $\approx$22 min. Because counting of the irradiated samples was done after

TABLE II. Experimentally measured cross sections for the residues populated in the interaction of ^{16}O with the ^{181}Ta system.

Lab energy (MeV)	$\sigma(^{194}Tl^{m})$ (mb)	$\sigma(^{194}Tl^{g})$ (mb)	$\sigma(^{193}Tl^{m})^a$ (mb)	$\sigma(^{193}Tl^{g})$ (mb)	$\sigma(^{192}Tl^{m})$ (mb)	$\sigma(^{192}Tl^{g})$ (mb)	$\sigma(^{193}Hg^{g})$ (mb)	$\sigma(^{193}Hg^{m})$ (mb)
76 ± 1.1	2 ± 0.2	2 ± 0.2	0.1 ± 0.01	26 ± 3.8	–	–	23 ± 3.5	8 ± 0.8
80 ± 1.5	6 ± 0.8	6 ± 0.8	0.2 ± 0.02	45 ± 6.8	22 ± 3.2	22 ± 3.2	47 ± 7.0	21 ± 2.1
85 ± 1.2	4 ± 0.5	4 ± 0.5	0.3 ± 0.03	68 ± 10.2	61 ± 9.1	61 ± 9.1	60 ± 8.9	30 ± 3.0
87 ± 1.0	3 ± 0.4	3 ± 0.4	0.2 ± 0.02	46 ± 6.9	44 ± 6.5	44 ± 6.5	49 ± 7.4	22 ± 2.2
88 ± 1.6	2 ± 0.2	2 ± 0.2	0.2 ± 0.02	44 ± 6.5	91 ± 13.7	91 ± 13.7	42 ± 6.2	24 ± 2.3
93 ± 1.1	2.5 ± 0.3	2 ± 0.3	0.1 ± 0.01	35 ± 5.2	184 ± 27.6	184 ± 27.6	29 ± 4.4	13 ± 1.3
97 ± 1.0	2 ± 0.3	1.5 ± 0.2	0.1 ± 0.01	15 ± 2.3	171 ± 25.5	171 ± 25.5	12 ± 1.7	8 ± 0.7
99 ± 0.9	1 ± 0.1	1 ± 0.1	0.1 ± 0.01	17 ± 2.5	222 ± 33.3	222 ± 33.3	10 ± 1.5	6 ± 0.5

[a]Cross-section values give an upper limit.

TABLE III. Experimentally measured cross sections for the residues populated in the interaction of ^{16}O with the ^{181}Ta system.

Lab energy (MeV)	$\sigma(^{192}\text{Hg})$ (mb)	$\sigma(^{191}\text{Hg}^{g})$ (mb)	$\sigma(^{191}\text{Hg}^{m})$ (mb)	$\sigma(^{192}\text{Au}^{g})$ (mb)	$\sigma(^{191}\text{Au}^{g})$ (mb)	$\sigma(^{190}\text{Au}^{g})$ (mb)
80 ± 1.5	4 ± 0.5	–	–	2 ± 0.2	–	–
85 ± 1.2	40 ± 6.0	–	–	10 ± 1.5	–	8 ± 1.3
87 ± 1.0	36 ± 5.5	–	–	12 ± 1.8	2 ± 0.3	6 ± 0.8
88 ± 1.6	65 ± 9.8	3 ± 0.5	0.3 ± 0.04	31 ± 4.6	2 ± 0.3	23 ± 3.5
93 ± 1.1	121 ± 18.2	5 ± 0.7	3 ± 0.5	46 ± 6.9	3 ± 0.5	20 ± 2.9
97 ± 1.0	131 ± 6	7 ± .9	8 ± 1.2	63 ± 9.5	14 ± 2.1	40 ± 5.9
99 ± 0.9	154 ± 23.2	14 ± 2.1	18 ± 2.7	50 ± 7.5	22 ± 3.2	21 ± 3.2

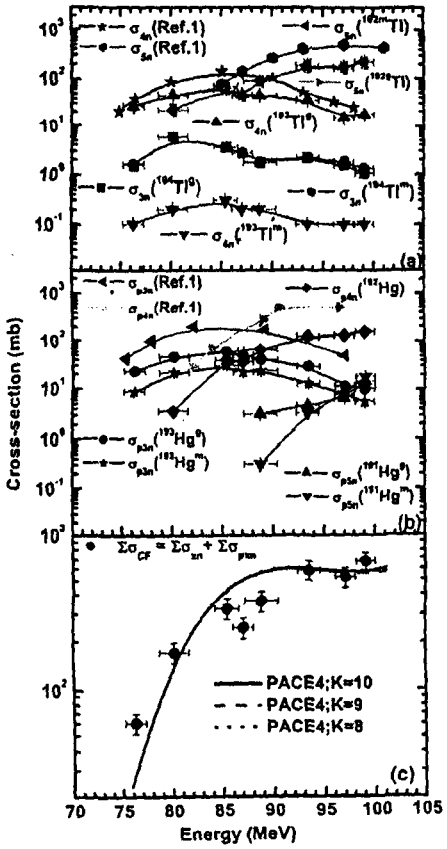

FIG. 2. (Color online) Measured EFs for (a) xn ($x = 3, 4$, and 5) channels and (b) pxn ($x = 3, 4$, and 5) channels. In panels (a) and (b), the spline-like lines joining the experimental data points are just to guide the eyes. Panel (c) shows the sum of cross sections for the xn and pxn channels. The effect of the variation of the choice of the level density parameter $K = 8, 9$, and 10 (dotted, dashed, and solid lines, respectively) on calculated $\Sigma\sigma_{CF}$ is also shown.

about 10 min from the cessation of irradiation, the measured cross sections for the ground state also contain contributions ($\lesssim$0.38%) from the metastable state. As such, an upper limit for the cross section for the independent production of the metastable state has been determined and is given in Table II. The sum of cross sections ($\Sigma\sigma_{xn}$) for all the populated residues produced via xn ($x = 3, 4$, and 5) channels is also shown in Fig. 2(a), indicating the initial rise in $\Sigma\sigma_{xn}$ values and then nearly saturating at higher energies.

B. (^{16}O, pxn) channels

In the case of pxn channels, there is no likelihood of ICF and, therefore, these channels are also populated by CF only like xn channels. Residues corresponding to $p3n$, $p4n$, and $p5n$ channels have been identified through their characteristic γ rays and also by the respective half-lives. In the case of the $p3n$ and $p5n$ channels metastable and ground states of the residues are populated while in the case of the $p4n$ channel only one state is formed. All the residues in the pxn cases decay independently with their respective half-lives and γ rays of known energies. The cross sections for these channels are plotted in Fig. 2(b) and are tabulated in Tables II and III. Note that in the case of pxn channels the residues may be populated both by independent formation and also by the decay of the higher charge isobar precursor as shown below:

$$^{16}\text{O} + ^{181}\text{Ta} \Longrightarrow {}^{197}\text{Tl}^{*} \Longrightarrow {}^{193}\text{Tl}^{*} + 4n;$$
$$^{193}\text{Tl}^{*} \Longrightarrow {}^{193}\text{Hg} + \beta^{+}/EC;$$
(precursor decay)
$$^{16}\text{O} + ^{181}\text{Ta} \Longrightarrow {}^{197}\text{Tl}^{*} \Longrightarrow {}^{193}\text{Hg} + p3n.$$
(independent decay)

Similarly, the population of residues ^{192}Hg and ^{191}Hg may also be expected via the independent decay as well as the precursor decay of the type:

$$^{16}\text{O} + ^{181}\text{Ta} \Longrightarrow {}^{197}\text{Tl}^{*} \Longrightarrow {}^{192}\text{Tl}^{*} + 5n;$$
$$^{192}\text{Tl}^{*} \Longrightarrow {}^{192}\text{Hg} + \beta^{+}/EC;$$
(precursor decay)
$$^{16}\text{O} + ^{181}\text{Ta} \Longrightarrow {}^{197}\text{Tl}^{*} \Longrightarrow {}^{192}\text{Hg} + p4n;$$
(independent decay)

and

$$^{16}O + ^{181}Ta \Longrightarrow ^{197}Tl^* \Longrightarrow ^{191}Tl^* + 6n;$$
$$^{191}Tl^* \Longrightarrow ^{191}Hg + \beta^+/EC;$$
(precursor decay)
$$^{16}O + ^{181}Ta \Longrightarrow ^{197}Tl^* \Longrightarrow ^{191}Hg + p5n.$$
(independent decay)

However, in the case of the $p5n$ channel, the precursor ^{191}Tl, which may be produced by a $6n$ channel, is not likely to be produced in the present experiment on account of its higher threshold ($\geq$100 MeV). In the case of $p3n$ and $p4n$ channels, the contribution of precursor decay could not be determined because of either the incomplete decay or the unknown decay characteristics of the precursor. For example, in the case of the $p4n$ channel, the cross sections for the independent decay of precursor formed by the $5n$ channel determined from its characteristic γ rays are found to be higher than the cross sections for residue ^{192}Hg populated by the $p4n$ channel. This may happen, if the precursor does not feed the residue ^{192}Hg formed by the $p4n$ channel. As such, the decay scheme of ^{192}Hg and ^{193}Hg needs further investigation. The cross-section values quoted in Tables II and III for these reactions also contain precursor contribution, if any, in the case of $p3n$ and $p4n$ channels.

In Fig. 2(b), the sum of cross sections for all measured pxn channels, denoted by $\Sigma\sigma_{pxn}$, has been obtained by adding the measured cross sections for $p3n$, $p4n$, and $p5n$ channels. To determine the total measured fusion cross section $\Sigma\sigma_{CF}$ (expt), the sum of cross sections due to xn channels, i.e., $\Sigma\sigma_{xn}$, and the sum of cross sections due to all measured pxn channels, i.e., $\Sigma\sigma_{pxn}$, have been added. The total $\Sigma\sigma_{CF}$ (expt) shown in Fig. 2(c) has been compared with $\Sigma\sigma_{CF}$ (Th) obtained using the code PACE4 [42] with different values of level density parameters a ($a = A/K$). This code is based on statistical Hausher Fashback formalism followed by Monte Carlo simulations to determine the decay sequence of an excited compound nucleus. The code calculates the cross sections for a particular reaction using Bass formulation [43]. A detailed discussion of this code is given in one of our recent works [20]. However, for the sake of completeness, it must be pointed out that nuclear level density plays a central role in any statistical analysis of nuclear reactions. In this code the most sensitive parameter is the level density parameter (LDP) a ($a = A/K$), which mainly governs the equilibrium state. Here, A is the atomic mass number of the compound nucleus and K is a free parameter. The value of K may be varied to match the experimental data. As can be seen from Fig. 2(c), the $\Sigma\sigma_{CF}$ (expt) is in good agreement with theoretical $\Sigma\sigma_{CF}$ values. The fact that the measured fusion cross section $\Sigma\sigma_{CF}$ (expt) could be reproduced satisfactorily by PACE4 predictions strengthens the confidence in the choice of input parameters. Also, a value of LDP ($a = A/8$ MeV^{-1}) has also been suggested by Cavinato *et al.* [1] for nuclei far from the magic region. Further, the literature values [1] for fusion cross sections are found to agree well with the present measurements and are shown in Fig. 2(c).

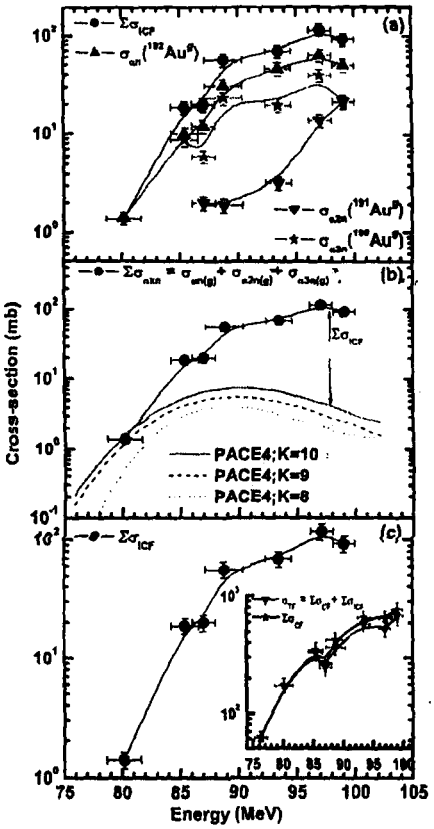

FIG. 3. (Color online) (a) Measured EFs for αxn ($x = 1, 2$, and 3) channels, (b) sum of the αxn channels, measured as well as calculated using PACE4 for $K = 8, 9, 10$ (dotted, dashed, and solid lines, respectively), and (c) sum of σ_{ICF} (all αxn) channels. In panels (a), (b), and (c), the spline-like lines joining the experimental data points are just to guide the eyes. The inset shows cross sections for the sum of both CF and ICF channels and for CF channels separately. The increasing difference, between the two curves in the inset, with energy indicates the dominance of ICF processes with energy.

C. (^{16}O, αxn) channels

In Fig. 3(a), the measured cross sections for the population of $^{193-x}$Au ($x = 1, 2$, and 3) isotopes via αxn channels are shown. Note that in the case of αxn channels, the residue may be formed in two ways: (i) by CF of ^{16}O followed by the formation of an excited CN from which evaporation of neutrons and α particles takes place, or (ii) the ^{16}O ion breaks into $\alpha + ^{12}$C and ^{12}C fuses with the target leaving an α particle as a spectator. In this case the excited nucleus formed by the fusion of ^{12}C may emit neutrons while de-exciting. Option (i) refers to CF and option (ii) to ICF. These modes may be

represented by the following equations.

$$^{16}O(^{12}C+\alpha) \Longrightarrow {}^{12}C + {}^{181}Ta \Longrightarrow {}^{193}Au^{*} + \alpha.$$

(α as spectator)

The residue $^{192}Au^{g}$ may be populated via CF and/or ICF channels as

(i) complete fusion of ^{16}O, i.e.,

$$^{16}O + {}^{181}Ta \Longrightarrow {}^{197}Tl^{*} \Longrightarrow {}^{192}Au^{g*} + \alpha + n,$$

(ii) incomplete fusion of ^{16}O, i.e.,

$$^{16}O(^{12}C+\alpha) + {}^{181}Ta \Longrightarrow {}^{193}Au^{*} + \alpha,$$

(spectator)

$$^{193}Au^{*} \Longrightarrow {}^{192}Au^{g*} + n.$$

The residue $^{191}Au^{g}$ may be populated via CF and/or ICF channels as

(i) complete fusion of ^{16}O, i.e.,

$$^{16}O + {}^{181}Ta \Longrightarrow {}^{197}Tl^{*} \Longrightarrow {}^{191}Au^{g*} + \alpha + 2n,$$

(ii) incomplete fusion of ^{16}O, i.e.,

$$^{16}O(^{12}C+\alpha) + {}^{181}Ta \Longrightarrow {}^{193}Au^{*} + \alpha,$$

(spectator)

$$^{193}Au^{*} \Longrightarrow {}^{191}Au^{g*} + 2n.$$

Similarly, the residue $^{190}Au^{g}$ may be populated via CF and/or ICF channels as

(i) complete fusion of ^{16}O, i.e.,

$$^{16}O + {}^{181}Ta \Longrightarrow {}^{197}Tl^{*} \Longrightarrow {}^{190}Au^{g*} + \alpha + 3n,$$

(ii) incomplete fusion of ^{16}O, i.e.,

$$^{16}O(^{12}C+\alpha) + {}^{181}Ta \Longrightarrow {}^{193}Au^{*} + \alpha,$$

(spectator)

$$^{193}Au^{*} \Longrightarrow {}^{190}Au^{g*} + 3n.$$

The residue $^{192}Au^{g}$ may also be populated via the decay of ^{192}Hg via β^{+}/EC decay. Both, $^{192}Au^{g}$ ($T_{1/2} = 4.94$ h) and ^{192}Hg ($T_{1/2} = 4.85$ h) have nearly the same half-lives. In this case, it has been possible to separate out the contribution from the decay of ^{192}Hg populated via the $p4n$ channel using decay analysis. It is known from the successive radioactive decay, if the daughter nucleus half-life (T_A) and the parent nucleus half-life (T_B) are nearly equal, as in the present case, such that $T_A = T_B(1+\delta)$, where $\delta \ll 1$, then the activity ratio increases approximately linearly with time, so long as $t \ll 2\tau_B/\delta$ [44], where τ_B is the mean lifetime of the parent nucleus. To obtain the cross section of $^{192}Au^{g}$, a curve between the lapse time and its production cross section was plotted at different times and also at different energies. To obtain the independent cross sections at each energy, plots for different lapse times were extrapolated at $t = 0$ time using a least-square linear fitting method. The cross section at time $t = 0$ is the independent cross section for the production of $^{192}Au^{g}$. In Fig. 3(a), the cross sections deduced as mentioned above for the independent production of $^{192}Au^{g}$ have been plotted. Here [Fig. 3(a)] the sum of cross sections for all measured αxn channels, i.e., $\Sigma\sigma_{\alpha xn}$(expt), is also shown and is found to increase with energy. It has already been mentioned that all the α-emission channels identified in the present work are expected to have significant contributions from ICF processes. To determine the contribution from ICF processes to the αxn channels, the measured $\Sigma\sigma_{\alpha xn}$(expt) has been compared with the corresponding values calculated using the theoretical model code PACE4, which is based on statistical CN theory. Because the code does not take ICF into consideration, the calculated cross sections for $\Sigma\sigma_{\alpha xn}$ with code PACE4 have predictions based on the CF model only. In Fig. 3(b) a comparison of $\Sigma\sigma_{\alpha xn}$(expt) has been made with $\Sigma\sigma_{\alpha xn}$(Th) calculated theoretically using the CF model for three different values of physically acceptable [45] level density parameters ($K = 8, 9$, and 10). As can be seen from this figure, the $\Sigma\sigma_{\alpha xn}$(Th), with any of the reasonable parameters could not reproduce $\Sigma\sigma_{\alpha xn}$(expt) above 85 MeV. The measured $\Sigma\sigma_{\alpha xn}$(expt) agree very well with $\Sigma\sigma_{\alpha xn}$(Th) at 80 MeV. However, above this data point all the measured cross sections are found to be much higher as compared to those of theoretical predictions based on the PACE4 model. The difference between the experimental and the theoretical values of $\Sigma\sigma_{\alpha xn}$ may be assigned to ICF and has been denoted by $\Sigma\sigma_{\rm ICF}$(expt). Further, the difference between $\Sigma\sigma_{\alpha xn}$(expt) and $\Sigma\sigma_{\alpha xn}$(Th) is found to increase with energy above 80 MeV, indicating the dominance of ICF processes at relatively higher energies, with maximum ICF contribution at the highest studied energy i.e., 100 MeV. Further, in Fig. 3(c) $\Sigma\sigma_{\rm ICF}$ obtained by subtracting $\Sigma\sigma_{\rm ICF}$(Th) ($K = 10$) from measured $\Sigma\sigma_{\alpha xn}$ is been plotted as a function of energy. As can be seen from this figure, ICF production increases very rapidly with energy. In the inset of Fig. 3(c) $\Sigma\sigma_{\rm TF}$ (total sum of cross sections for all measured channels) and $\Sigma\sigma_{\rm CF}$ are compared. As can be seen from Fig. 3(c) (inset), with the increase in energy the difference between $\sigma_{\rm TF}$ and $\Sigma\sigma_{\rm CF}$ continues to increase, indicating the dominance of ICF at relatively higher energies. In a complementary experiment [46], recoil ranges for the same residues have been determined to get information about the degree of linear momentum transfer and the relative contribution of CF and ICF channels. The relative contribution of CF and ICF channels obtained from the complementary experiment agree with the present data within the experimental uncertainties.

At energies above the CB, where $E \gg V_0$, the classical formula of Weisskopf [47] for capture of charge particle by a nucleus is given by

$$\sigma_{\rm CF}(E) = \pi r_0^2(1 - V_0/E).$$

where, V_0 is the value of CB and E is the energy in center of mass system. As such, if $\sigma_{\rm CF}$ (Exp) is plotted against $1/E_{\rm c.m.}$, it should be a linear curve. The deduced $\Sigma\sigma_{\rm CF}$ values from $\Sigma\sigma_{xn} + \Sigma\sigma_{pxn} + \Sigma\sigma_{\alpha xn}$(Th) have been plotted as a function of $1/E_{\rm c.m.}$ in Fig. 4. A fit to the $\Sigma\sigma_{\rm CF}$ data points indicates a linear curve that cuts the x axis at the beam energy equal to CB. It may, however, be pointed out that a departure from linearity above CB may indicate the approach to and beginning of a quantal regime giving rise to subbarrier fusion. Further,

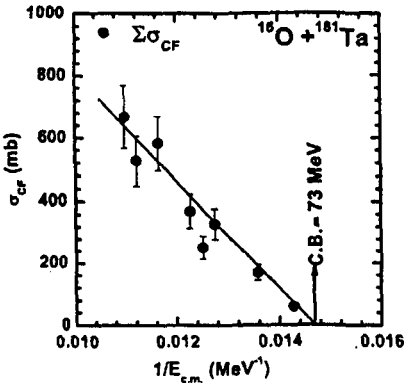

FIG. 4. (Color online) Experimentally measured production cross sections found to reproduce the Coulomb barrier of the system.

to study the dependence of ICF contribution on energy, for the presently studied system, the percentage fraction of ICF fusion cross section (F_{ICF}) has been plotted in Fig. 5 as a function of beam energy normalized to CB, along with several other literature values [5,16,19,20]. As can be seen from this figure, F_{ICF} increases with the increase in normalized beam energy for all the systems. To study the dependence of F_{ICF} on mass asymmetry, the percent F_{ICF} has also been plotted in Fig. 6 as a function of mass asymmetry at a constant value ($E_{beam}/V_b = 1.38$) of normalized beam energy. As can be seen from this figure, the F_{ICF} for the presently studied system is not following the expected trend shown for other systems involving ^{16}O beam. The present F_{ICF} for $^{16}O + ^{181}Ta$ is found to be significantly small. It may be because of the fact that in the present measurements several other α-emission channels, e.g., $2\alpha xn$ and $3\alpha xn$ channels, could not be observed as the

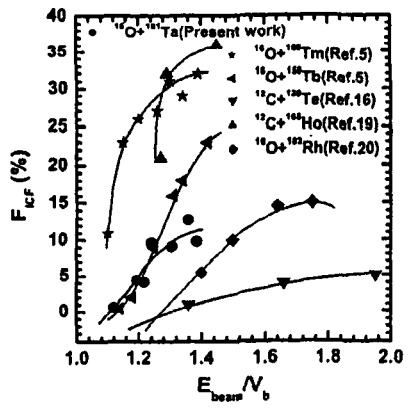

FIG. 5. (Color online) Deduced percentage ICF fraction (F_{ICF}) as a function of normalized projectile energy for the $^{16}O + ^{181}Ta$ system along with literature values. The spline-like lines joining the experimental data points are just to guide the eyes.

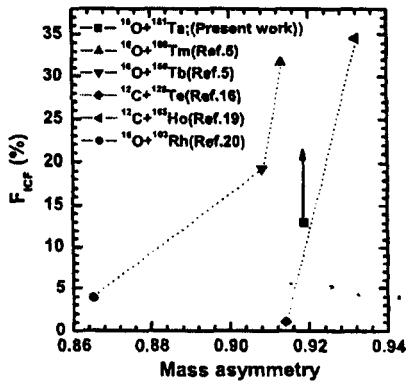

FIG. 6. (Color online) The percentage ICF fraction as a function of mass asymmetry at a constant normalized projectile energy. The arrow indicates that the present value of F_{ICF} for $^{16}O + ^{181}Ta$ is expected to go up, if all other remaining α-emission channels are also measured.

residues populated via these channels were either stable or short lived and/or had very low γ-ray intensity. We propose to measure the contribution of these α-emission channels in an in-beam experiment using particle-γ coincidence technique, so that the present data may be supplemented.

IV. CONCLUSIONS

In the present work, EFs for the production of 14 radionuclides, $^{194}Tl^{g}(3n)$, $^{194}Tl^{m}(3n)$, $^{193}Tl^{g}(4n)$, $^{193}Tl^{m}(4n)$, $^{192}Tl^{g}(5n)$, $^{192}Tl^{m}(5n)$, $^{193}Hg^{g}(p3n)$, $^{193}Hg^{m}(p3n)$, $^{192}Hg(p4n)$, $^{191}Hg^{g}(p5n)$, $^{191}Hg^{m}(p5n)$, $^{192}Au^{g}(\alpha n)$, $^{191}Au^{g}(\alpha 2n)$, and $^{190}Au^{g}(\alpha 3n)$, were measured. The experimental data were compared with the predictions of the theoretical code PACE4 based on a statistical model. The CF cross sections were found agree with PACE4 calculations over the entire energy range. A significant enhancement in the cross sections was observed, for α-emitting channels, as compared to the theoretical PACE4 model predictions. The observed enhancement was attributed to the prompt break up of the projectile into α clusters, with ^{16}O into $^{12}C + ^{4}He$ leading to the ICF process. As such, it may be concluded that apart from CF, ICF is also a process of greater importance even at these low energies and, hence, when predicting the total reaction cross sections, the ICF contribution should also be taken into consideration. Further, as expected $\Sigma\sigma_{ICF}$ was found to increase with energy.

ACKNOWLEDGMENTS

The authors are thankful to Professor Amit Roy, Director, Inter-University Accelerator Centre (IUAC), New Delhi, India, for extending all the necessary facilities for performing the experiments and for extending hospitality. We are also thankful to Dr. R. K. Bhaumik for scientific discussions and support during the experiments. The authors also thank the Chairman,

Department of Physics, Aligarh Muslim University, Aligarh, for providing all the necessary facilities One of the authors (DPS) thanks the UGC-DAE, Consortium for Scientific Research Calcutta Centre, India, for providing financial support under Project CRS-076/AMU/P/RP/7409, MKS thanks the DST, and RP thanks the DST and UGC

[1] M Cavinato, E Fabrici, E Gadioli, E Gadioli Erba, P Vergani, M Crippa G Colombo, I Redaelli, and M Ripamonti Phys Rev C **52**, 2577 (1995)
[2] P Vergani, E Gadioli, E Vaciago, E Fabrici, E Gadioli Erba, M Galmarini, G Ciavola, and C Marchetta, Phys Rev C **48**, 1815 (1993)
[3] F Schussler, H Nifenecker, B Jakobsson, V Kopljar, K Soderstrom, S Leray, C Ngo, S Souza, J P Bondrof, and K Sneppen, Nucl Phys **A584**, 704 (1995)
[4] E Gadioli, C Brattari, M Cavinato, E Fabrici, E Gadioli Erba, V Allori, A Di Filippo, S Vailati, T G Stevens, S H Connell, J P F Sellschop, F M Nortier, G F Steyn, and C Marchetta, Nucl Phys **A641** 271 (1998)
[5] P P Singh, B P Singh, M K. Sharma, Unnati D P Singh, R Prasad, R Kumar, and K S Golda, Phys Rev C **77**, 014607 (2008)
[6] P P Singh, M K Sharma Unnati D P Singh, R Kumar, K S Golda, B P Singh, and R Prasad, Eur Phys J A **34**, 29 (2007)
[7] R H Siemsen *et al*, Nucl Phys **A400**, 245c (1983)
[8] D J Parker, J Asher, T W Conlon, and I Naqib, Phys Rev C **30**, 143 (1984)
[9] Ch Ngo Prog Part Nucl Phys **16**, 139 (1985)
[10] D R Zolnowski H Yamada S E Cala, A C Kahler, and T T Sugihara, Phys Rev Lett **41**, 92 (1978)
[11] A Yoshida *et al*, Phys Lett. **B44**, 1528 (1991)
[12] C Signorini *et al*, Nucl Phys **A735**, 329 (2004)
[13] M Blann, Nucl Phys **A235**, 211 (1974)
[14] M Blann, Annu Rev Nucl Sci **25**, 123 (1975)
[15] F Amorini, M Cabibbo, G Cardella, A Di Pietro, A Musumarra, M Papa, G Pappalardo, F Rizzo, and S Tudisco, Phys Rev C **58**, 987 (1998)
[16] Manoj Kumar Sharma, B P Singh, Sunita Gupta, M M Muthafa, H D Bhardwaj and R Prasad J Phys Soc Jpn **72** 1917 (2003)
[17] M K Sharma, Unnati, B K Sharma, B P Singh H D Bhardwaj, R Kumar, K S Golda and R Prasad Phys Rev C **70**, 044606 (2004)
[18] M K Sharma, Unnati, B P Singh, R Kumar, K S Golda, H D Bhardwaj, and R Prasad, Nucl Phys **A776**, 83 (2006)
[19] S Gupta, B P Singh, M M Musthafa, H D Bhardwaj, and R Prasad, Phys Rev C **61**, 064613 (2000)
[20] Unnati, P P Singh, D P Singh, M K Sharma, A Yadav, R Kumar B P Singh and R Prasad Nucl Phys **A811**, 77 (2008)
[21] P P Singh, B P Singh M K Sharma, Unnati, R Kumar, K S Golda, D Singh, R P Singh, S Muralithar, M A Ansari, R Prasad, and R K Bhowmik, Phys Rev C **78**, 017602 (2008)
[22] I Tserruya, Y Steiner, Z Fraenkel, and P Jacobs, Phys Rev Lett **60** 14 (1988)
[23] S M Mullins, A P Byrne, G D Dracoulis, T R McGoram, and W A Seale, Phys Rev C **58**, 831 (1998)
[24] S M Mullins, G D Dracoulis, A P Byrne, T R McGoram, S Bayer, R A Bark, R T Newman, W A Seale, and P G Kondev, Phys Rev C **61**, 044315 (2000)
[25] G J Lane, G D Dracoulis, A P Byrne, A R Poletti, and T R McGoram, Phys Rev C **60**, 067301 (1999)
[26] T Udagawa and T Tamura, Phys Rev Lett **45**, 1311 (1980)
[27] J Wilczynski *et al.* Phys Rev Lett **45**, 606 (1980)
[28] J P Bondrof *et al*, Nucl Phys **A333**, 285 (1980)
[29] M Blann, Phys Rev Lett **27** 337 (1971)
[30] R Weiner *et al*, Nucl Phys **A286**, 282 (1977)
[31] V I Zagrebaev, Ann Phys (NY) **197**, 33 (1990)
[32] B G Harvey, Nucl Phys **A444**, 498 (1985)
[33] M H Simbel and A Y Abdul Magd, Z. Phys A **294**, 277 (1980)
[34] A Y Abdul Magd, Z. Phys A **298**, 143 (1980)
[35] H Morgenstern, W Bohne, W Galster, D G Kovar, and H Lehr, Phys Lett **B113**, 463 (1982)
[36] H Morgenstern, W Bohne, W Galster, and K Grabisch, Z. Phys A **324**, 443 (1986)
[37] P E Hodgson, E Gadioli, and E Gadioli Erba, *Introductory Nuclear Physics* (Oxford University Press, London, 1997), Chap 18
[38] FREEDOM, data acquisition and analysis system designed to support the accelerator based experiments at the Nuclear Science Centre, New Delhi, India
[39] S F Mughabghab, M Divadeenam, and N E Holden, *Neutron Cross-Sections* (Academic Press, New York, 1981), Vol 1, Part A p 89
[40] E Browne and R B Firestone, *Table of Radioactive Isotopes* (Wiley, New York, 1986)
[41] U Reus and W Westmeirer, At Data Nucl Data Tables **29**, 338 (1983)
[42] A Gavron, Phys Rev C **21**, 230 (1980)
[43] R Bass, Nucl Phys **A231**, 45 (1974)
[44] R D Evans, *The Atomic Nucleus* (McGraw–Hill, New York, 1982), p 481
[45] M Blann, G Reffo, and F Fabbri, Nucl Instrum Methods A **265** 490 (1988)
[46] Devendra P Singh *et al.*, Ph D thesis, Aligarh Muslim University, Aligarh 202002, India (to be submitted, 2009)
[47] V Weisskopf, Phys Rev **52**, 295 (1937)

Available online at www.sciencedirect.com
ScienceDirect
Nuclear Physics A 811 (2008) 77–92
NUCLEAR PHYSICS A
www.elsevier.com/locate/nuclphysa

Observation of large incomplete fusion in $^{16}O + ^{103}Rh$ system at $\approx$ 3–5 MeV/nucleon

Unnati Gupta [a], Pushpendra P. Singh [a], Devendra P. Singh [a], Manoj Kumar Sharma [a], Abhishek Yadav [a], Rakesh Kumar [b], B.P. Singh [a,*], R. Prasad [a]

[a] *Accelerator Laboratory, Department of Physics, A.M. University, Aligarh-202002, India*
[b] *NP-Group, Inter-University Accelerator Center, PO Box No. 10502, Aruna Asaf Ali Marg, New Delhi-110067, India*

Received 26 April 2008; received in revised form 4 July 2008; accepted 7 July 2008

Available online 24 July 2008

Abstract

Incomplete fusion of $^{16}O(\approx 3–5$ MeV/nucleon) with ^{103}Rh has been investigated using measurement and analysis of excitation functions. Some $pxn/\alpha pxn$-channels are found to have contribution from pre-cursor decay, which has been separated out from cumulative cross-section of evaporation residues. The xn/pxn-channels are found to be satisfactorily reproduced with the predictions of PACE4 after subtraction of pre-cursor decay contribution, in general. Sizable enhancement in the experimental cross-sections has been observed for α-emitting channels over the theoretical once, which may be attributed to the incomplete fusion. The percentage fraction of incomplete fusion has also been deduced, which seems to be sensitive for projectile energy, entrance channel mass-asymmetry and/or projectile structure. The present work deals with the competition of incomplete fusion with complete fusion even at $\approx$ 3–5 MeV/nucleon for $^{16}O + ^{103}Rh$ system.

PACS: 25.70.Jj; 27.70.Gh

Keywords: Heavy ion induced reactions; Activation technique; Measurement of excitation functions; Comparisons with PACE4; Influence of incomplete fusion on complete fusion; Fraction of incomplete fusion as a function of projectile energy; Fraction of incomplete fusion as a function of mass-asymmetry

* Corresponding author. Tel.: +91 941 2133929; fax: +91 571 2701001.
E-mail address: bpsinghamu@gmail.com (B.P. Singh).

0375-9474/$ – see front matter
doi:10.1016/j.nuclphysa.2008.07.013

1. Introduction

In recent years, the study of reaction dynamics in heavy ion (HI) interactions has acquired central place in nuclear physics research [1–7]. The HI-induced reactions are widely different from light ion induced reactions due to large fusion barrier ($B_{\rm fus}$) and availability of different ℓ-bins. In favorable conditions (only if the projectile energy is comparable to the $B_{\rm fus}$), associated input angular momentum (ℓ) is supposed to be large enough to produce nuclei in extreme conditions (high excitation energy and spin). Since, the de-Broglie wavelength in HI-induced reactions is of the order of nuclear dimensions, therefore, the interaction may be explained by adopting semi-classical approach [8]. Classically, the interaction trajectories depending on different ℓ-bins and/or impact parameters lying within the target dimensions may lead prominently to reaction processes like (i) complete fusion (CF), and (ii) incomplete fusion (ICF). In case of CF, with the collision trajectories $0 \leqslant \ell \leqslant \ell_{\rm crit}$, the interacting partners may be trapped in the pocket of entrance channel potential involving all nucleonic degrees of freedom [9–11]. Consequently, the entire kinetic energy and linear momentum of the projectile are ultimately equally shared among all the constituents of the composite system leading to the fully equilibrated compound nucleus (CN). However, at relatively higher values of impact parameters for the collision trajectories (input angular momentum range) with $\ell \geqslant \ell_{\rm crit}$, the pocket in the entrance channel potential vanishes [12–14]. Therefore, the nuclear field of target nucleus is no longer strong enough to trap all the nucleons, consequently, the fractional momentum transfer takes place leading to the ICF process. As a result of ICF of projectile, (i) the CN is formed with less mass and charge as compared to the total mass and charge of interacting partners; (ii) the recoil velocity of the reaction products should be less than the complete fusion population and (iii) the angular distribution of ejectiles is expected to show maxima at forward angles. In case of ICF processes, the mass transfer occurs mostly from lighter to heavier partner, the feature observed more prominently for mass asymmetric systems as compared to mass symmetric systems [15–18].

With a view to explain various ICF processes, several dynamical models like; Break-Up Fusion (BUF) model [19], SUMRULE model [20], Promptly Emitted Particles (PEPs) model [21], EXCITON model [22], etc., have been proposed. In SUMRULE model, Wilczyński et al. [20] suggested that ICF is mainly confined to the ℓ-space above ($\ell_{\rm crit}$) for CF, and originate from peripheral interactions or non-central collisions. The non-central nature of ICF dynamics has also been emphasized by Trautmann et al. [14], and Inamura et al. [23,24]. The BUF-model [19] of Udagawa and Tamura is based on the Distorted Wave Born Approximation (*DWBA*), in which the projectile is assumed to break-up into constituent *alpha*-clusters (e.g., ^{16}O may break-up into $^{12}\mathrm{C} + \alpha$ and/or $^{8}\mathrm{Be} + {}^{8}\mathrm{Be}$) within the nuclear field range of target nucleus. One of the fragments may get fused with target nucleus (depending on the available ℓ-value) [19], while the remnant behaves like a spectator dominantly ejected in the forward cone. According to PEP model [21], the nucleons transferred from projectile to the target nucleus may get accelerated in the nuclear field of target nucleus and consequently acquire extra velocity to escape before equilibration. The EXCITON model assumes that the projectile nucleons undergo a series of collisions with the target nucleus creating particle-hole excitations, which de-excite by emitting fast nuclear particles [22]. Apart from these, Overlap model [25–27] and Multistep Direct Reaction theory [28] have also been proposed, and Morgenstern et al. [17,29], correlated the probability of ICF reactions to the entrance channel mass asymmetry. It may, further, be pointed out that the aforementioned models/theories, generally, have been used to fit the experimental data obtained at energies $E/A \geqslant 10.5$ MeV or so, but no satisfactory comparison has been made at relatively low bombarding energies (i.e., 5–7 MeV/nucleon). As such, due to the unavailability of any re-

liable theoretical model to fit the experimental data obtained at energies $\approx$ 5–7 MeV/nucleon, the study of ICF is still an active area of investigations. Furthermore, there is a renewed interest in the study of ICF dynamics after observation of these reactions at relatively low bombarding energies [30–33]. Moreover, the ICF reactions are considered to be a promising route to produce high spin states even at low bombarding energies [34,35]. Furthermore, some important issues associated with ICF dynamics at energies $\leqslant$ 7 MeV/nucleon are (i) the onset of ICF at energies slightly above the B_{fus}, and (ii) the relative contributions of CF and ICF processes, which have not yet been fully explored or limited up to a few projectile–target combinations only. Therefore, in order to have better understanding of ICF processes, a comprehensive study of excitation functions (EFs), forward recoil range distributions (RRDs) and angular distributions (ADs) of recoils in HI induced reactions have been undertaken by our group [30,36–38]. In the present work, the measurement of EFs for several radio-active isotopes produced in $^{16}O + {}^{103}Rh$ system have been performed in the energy range $\approx$ 50–85 MeV. Similar measurements for the same system have also been performed by Z. Buthelezi et al. [39], at energies $\approx$ 40–400 MeV. However, in the present work, precursor decay contributions (if any) in the production of several reaction products have also been estimated from cumulative cross-sections of residues, which has not been considered in Ref. [39]. As such, the present work may serve as the complement and/or as, at some places, supplement to the above measurements at energies $\approx$ 50–85 MeV. The present paper is organized as follows: the experimental details and methodology are given in Section 2. However, the production cross-section measurement and estimation of independent cross-section from cumulative cross-section are described in Section 3. The analysis of experimentally measured EFs with the predictions of statistical model code PACE4 are given in Section 4. The influence of ICF on CF and its dependence on projectile energy and mass-asymmetry of interacting partners are presented in Section 4.1, while, Section 5 deals with the summary and conclusions of the present work.

2. Experimental details and methodology

Experiments have been performed at the Inter-University Accelerator Centre (IUAC), New Delhi, India. The targets of ^{103}Rh of thickness $\approx$ 2.0 mg/cm^2 were prepared from the spectroscopically pure foils of natural Rhodium (^{103}Rh) employing rolling technique. The thickness of each target was determined by α-transmission method. The targets were fixed on Al-holders of 1.2 $\times$ 1.2 cm^2 size and concentric hole of $\approx$ 10 mm diameter. In order to cover a wide energy region in a single irradiation, energy degradation technique has been used. Two stacks, each containing three ^{103}Rh-target foils were irradiated by $^{16}O^{7+}$ beam at energies $\approx$ 80 and 85 MeV, separately. Typical stacked foil arrangement used for EF measurements is shown in Fig. 1. The successive targets in the stack are backed by Al-catchers of appropriate thicknesses, so that the recoiling nuclei may be trapped in the catcher foil thickness itself. The incident energy on each target-catcher foil assembly in a stack has been estimated using code SRIM, based on stopping power formulation. The errors in the incident energies on each foil have been calculated as the energy loss at half thickness of the target/catcher foils. The first foil of the first stack at highest beam energy (i.e. $\approx$ 85 MeV) has an energy uncertainty of $\pm$2.06 MeV, however, the last foil of the second stack has the uncertainty of $\pm$2.77 MeV, calculated as discussed above. Irradiations have been carried out in the General Purpose Scattering Chamber (GPSC), with a beam current $\approx$ 10 pnA. Keeping in view, the half-lives of interest irradiations have been carried out for $\approx$ 8 hours. After the irradiation, the target-catcher foil assembly has been taken out from the scattering chamber with the help of invacuum transfer system. The activities produced in the

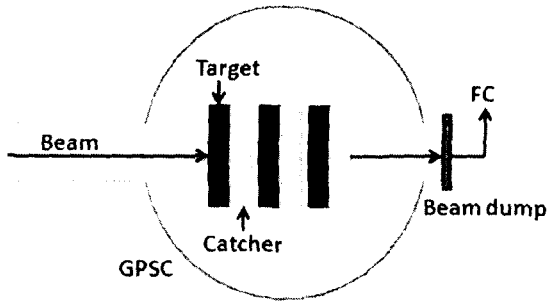

Fig. 1. Typical experimental setup for EF measurement using energy degradation technique.

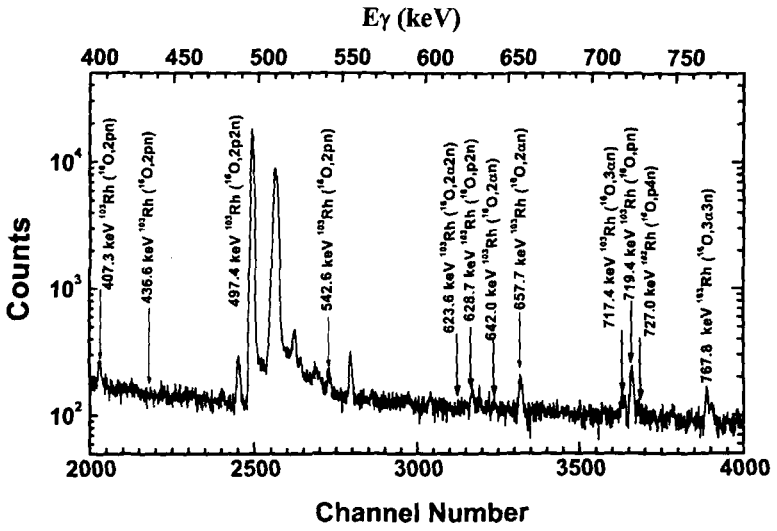

Fig. 2. Typical γ-ray spectrum of $^{16}O + {}^{103}Rh$ at $\approx$ 85 MeV, peaks are assigned to the different reaction products expected to be populated via complete and/or incomplete fusion.

samples were recorded by a pre-calibrated HPGe detector of 100 c.c. active volume coupled to a CAMAC based software FREEDOM.[1] The detector used in this experiment was pre-calibrated for energy and efficiency using various standard γ-sources, viz., ^{60}Co, ^{133}Ba and ^{152}Eu at different source-detector separations. The target-detector separation was suitably adjusted so as to keep the dead time $< 10\%$. In order to detect and follow the longer lived residues, the counting of irradiated samples has been done for a week or so. A relevant portion of a typical γ-ray spectra of the $^{16}O + {}^{103}Rh$ system at $\approx 82.94 \pm 2.06$ MeV is shown in Fig. 2. The residues were identified by their characteristic γ-rays as well as by decay curve analysis. A list of residues, γ-ray energies, abundances, etc., used in the present work are tabulated in Table 1. The spectroscopic data has been taken from the "Table of Radioactive Isotopes" by Browne and Firestone [40].

[1] FREEDOM, Data acquisition and analysis system designed to support the accelerator based experiments at the Nuclear Science Centre, New Delhi, India (2000).

Table 1
Spectroscopic properties of identified residues

Channel	Residue	Half-life	J^{π}	E_{γ} (keV)	γ (%)
(pn)	^{117g}Te	62 m	$(1/2)^{+}$	719.7	64.7
				1090.7	6.9
(p2n)	^{116}Te	2.49 h	0^{+}	628.7	1.0
(p3n)	^{115g}Te	5.8 m	$(7/2)^{+}$	1326.8	22.7
				1380.5	23.0
(p3n)	^{115m}Te	6.7 m	$(1/2)^{+}$	770.3	34.2
(p4n)	^{114}Te	15.2 m	0^{+}	244.6	33
				726.5	43
(2p)	^{117}Sb	2.8 h	$(5/2)^{+}$	158.6	85.9
(2p2n)	^{115}Sb	32.1 m	$(5/2)^{+}$	497.4	98
				489.1	1.3
(2α)	^{111g}In	2.8 d	$(9/2)^{+}$	171.3	90.2
				245.4	94.0
(2αn)	^{110g}In	4.9 h	7^{+}	641.6	25.9
				884.6	92.9
				937.4	68.4
(2αn)	^{110m}In	1.152 h	2^{+}	657.7	98.0
				1235.6	0.26
(2α2n)	^{109g}In	4.2 h	$(9/2)^{+}$	203.2	73.5
				623.6	6.0
(2α3n)	^{108g}In	58 m	7^{+}	242.7	38.0
(2α3n)	^{108m}In	39.6 m	2^{+}	311.9	1.01
				968.0	4.38
(3αn)	^{106m}Ag	8.28 d	6^{+}	451.0	27.6
				717.4	29.0
(3α3n)	^{104g}Ag	69.2 m	5^{+}	767.8	65.9
				555.8	92.8
(3α4n)	^{103g}Ag	65.7 m	$(7/2)^{+}$	146.0	28.3

3. Measurement of production cross-sections

The projectile energy dependent reaction cross-sections $\sigma_r(E)$, for different radio-nuclides have been determined using the following expression [48]:

$$\sigma_r = \frac{C_{t=0}}{N_0\theta\phi G_{\varepsilon}K[1-\exp(-\lambda t_1)]} \tag{1}$$

where

$C_{t=0}$ = The count rate just after the irradiation, i.e., at zero time,
N_0 = Initial number of nuclei in the target sample,
θ = Branching ratio of the characteristic γ-rays assigned to different reaction products,
ϕ = The incident beam flux,
G_{ε} = Geometry dependent efficiency of the HPGe detector,
$K = [1-\exp(-\mu d)]/\mu d$ = The self absorption correction factor for the γ-rays in the material of the sample of thickness d(gm/cm^2) and the absorption coefficient μ(cm^2/gm),
λ = Decay constant of the radio-nuclides, and
t_1 = Time of irradiation.

Further, the errors in the measured production cross-sections of different radio-nuclides may arise due to various factors like: (i) Non-uniform thickness of the samples, i.e., the inaccurate estimate of foil thickness may lead to the uncertainty in the determination of the number of target nuclei in the sample. However, in order to check the uniformity of the sample, thickness of each sample was measured at different positions by α-transmission method. The error in the thickness of the sample is estimated to be $\approx 1\%$. (ii) Fluctuations in the beam current may result in the variation of incident flux, as such proper care has been taken to maintain the beam current constant so that the error due to beam current fluctuations may be minimized. (iii) Uncertainty in the determination of geometry dependent spectrometer efficiency. The error in the efficiency determination due to the statistical fluctuations in counts is estimated to be less than 2%. (iv) The loss of product nuclei recoiling out of the target may introduce large errors in the measured cross-sections. The thickness of the catcher foils used in the present work were sufficient to stop even the most energetic residues. However, in the present measurements both the sample and the catcher foils were counted together and hence, the losses due to the recoiling of nuclei is avoided. (v) Dead time of the spectrometer was kept less than 10% by suitably adjusting sample-detector distance. The overall errors including statistical errors are estimated to be $\leqslant 15\%$, excluding the uncertainty in branching ratio, decay constant, etc., which have been taken from the "Table of Radioactive Isotopes" [40].

3.1. Estimation of independent cross-section from cumulative cross-sections

In the present work, the EFs for several radio-nuclides ^{117g}Te(pn), ^{116}Te(p2n), ^{115g,m}Te(p3n), ^{114}Te(p4n), ^{117}Sb(2p), ^{116g,m}Sb(2pn), ^{115}Sb(2p2n), ^{110}Sn(αp4n), ^{111g}In(2α), ^{110g,m}In(2αn), ^{109g}In(2α2n), ^{108g,m}In(2α3n), ^{106m}Ag(3αn), ^{104g}Ag(3α3n) and ^{103g}Ag(3α4n) expected to be populated via CF and/or ICF have been measured. Some of the pxn/αpxn-channels are found to have contribution from higher charge isobar pre-cursor through β^+-emission and/or electron capture (EC), where the cumulative cross-sections have been measured. For such cases, if the half-life of the pre-cursor is considerably smaller than that of the daughter residue, the independent production cross-sections (σ_{ind}) have been estimated from the cumulative production cross-sections (σ_{cum}). The σ_{cum} of a given residue is the sum of σ_{ind} and the cross-section for the independent production of its pre-cursor σ_{pre} multiplied by a numerical coefficient F_p, i.e.,

$$\sigma_{\text{cum}} = \sigma_{\text{ind}} + F_p \sigma_{\text{pre}}. \tag{2}$$

The value of F_p depends on the branching ratio P_p for pre-cursor decay to the residue and is given by

$$F_p = P_p \frac{T_{\text{ind}}^{1/2}}{T_{\text{ind}}^{1/2} - T_{\text{pre}}^{1/2}}, \tag{3}$$

here T_{pre} and T_{ind} are the half-lives of the pre-cursor and the residue. In this way the cumulative cross-section is given by

$$\sigma_{\text{cum}} = \sigma_{\text{ind}} + P_p \frac{T_{\text{ind}}^{1/2}}{T_{\text{ind}}^{1/2} - T_{\text{pre}}^{1/2}} \sigma_{\text{pre}}. \tag{4}$$

As a representative case, the evaporation residue ^{117g}Te (Fig. 3(a)) is likely to be populated via CF of ^{16}O with the ^{103}Rh nucleus forming the composite system ^{119}I* followed by the evap-

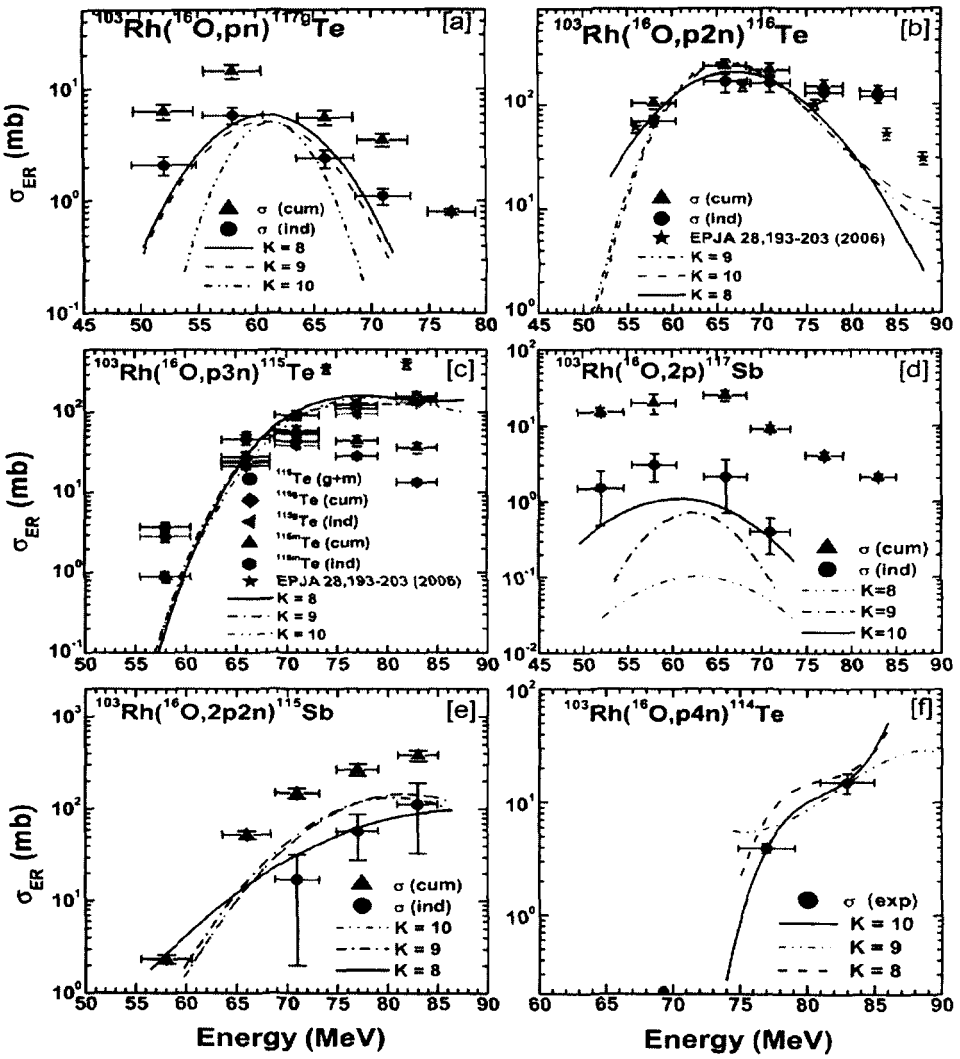

Fig. 3. Experimentally measured and theoretically calculated EFs for different residues populated via CF (xn/pxn-channels) in $^{16}O + {}^{103}Rh$ system at $\approx$ 46–85 MeV. The lines represent the theoretical calculations done using code PACE4 for different values of K, where a value of $K = 8$ is found to be the best choice for the studied system. The solid (black) triangle and solid (red) circles, respectively, represent cumulative (σ_{cum}) and independent (σ_{ind}) production cross-section of residues. Measured EFs have been compared with Ref. [39], the experimental data points taken from Ref. [39], are given by solid star. Ground and metastable states (if any) are given in self explanatory manner in the figures. (For interpretation of the references to colour in this figure legend, the reader is referred to the web version of this paper.)

oration of a proton and a neutron. The same residue ^{117g}Te may also be populated by the β^+ emission and/or electron capture (EC) of higher charge pre-cursor isobar ^{117}I. As such, the measured activity of residues ^{117g}Te may have contribution from the decay of its pre-cursor isobar also. The values of branching ratios required for obtaining the coefficient F_p are taken from

Ref. [41]. Using the above formulation, the cumulative yield ($\sigma_{\rm cum}$) and independent yield ($\sigma_{\rm ind}$) for ^{117g}Te are related by the equation

$$\sigma_{\rm cum}(^{117g}{\rm Te}) = \sigma_{\rm ind}(^{117g}{\rm Te}) + 1.03\sigma_{\rm pre}(^{117g}{\rm I}). \tag{5}$$

Here $\sigma_{\rm pre}(^{117g}{\rm I})$ is the independent yield of the pre-cursor.

In the similar way, the independent production cross-sections for other residues have also been deduced from the $\sigma_{\rm cum}$ and $\sigma_{\rm pre}$ contributions. The independent production cross-sections have been compared with statistical model code PACE4 [43], and are found to agree reasonably well with the theoretical calculations. The optimization of input parameters has been done by achieving best fitting for CF products (xn/pxn-channels), details of the code PACE4 (which is the modified version of PACE2) and data analysis are discussed in the following section.

4. Analysis of EFs with PACE4

The calculation of theoretical production cross-sections for the evaporation residues populated via CF channels have been obtained using code PACE4. The code PACE4 (which is a revised version of PACE2) is based on Hauser–Feshbach approach. It may be pointed out that the ICF and PE-emission are not taken into consideration in this code. The cross-sections for evaporation residues are calculated using Bass formula [42]. The de-excitation of the compound nucleus is followed by Monte Carlo procedure. The projections of angular momentum are calculated at each stage of de-excitation, which enables the determination of angular distribution of the emitted particles. The optical model parameters for neutrons, protons and α-particles are used as default in the code [43]. The γ-ray strength functions for E_1, E_2 and M_1 transition were taken from tables of Endt [44]. This code has been modified to take into account the excitation energy dependence of level density parameter using the prescription of Kataria et al. [45].

The partial cross-section (σ_ℓ) for the formation of CN at angular momentum ℓ and specific bombarding energy E, is given by

$$\sigma_\ell = \frac{\lambda^2}{4\pi}(2\ell+1)T_\ell. \tag{6}$$

Here λ is the reduced wavelength. The transmission coefficients T_ℓ may be given by the expression

$$T_\ell = \left[1 + \exp\left(\frac{\ell - \ell_{\rm max}}{\Delta}\right)\right]^{-1} \tag{7}$$

where Δ is the diffuseness parameter and $\ell_{\rm max}$ the maximum value of ℓ detained by total fusion cross-section,

$$\sigma_F = \sum_{\ell=0}^{\infty}\sigma_\ell. \tag{8}$$

The transmission coefficients for the evaporation of light particles (n, p and α) during the de-excitation are obtained by optical model calculations [46,47]. The fission decay mode may be considered using a rotating liquid fission barrier routine [43]. As a typical example, at 85 MeV incident beam energy the values of $\ell_{\rm max}$ and Δ are $\approx 63\hbar$ and $\approx 2\hbar$. The level density in this code is calculated using the expression $a = A/K$, where A is the atomic mass number and K is a parameter called level density parameter. In these calculations K is an important parameter and affects the equilibrium component. As such, in order to show the effect of variation of K on

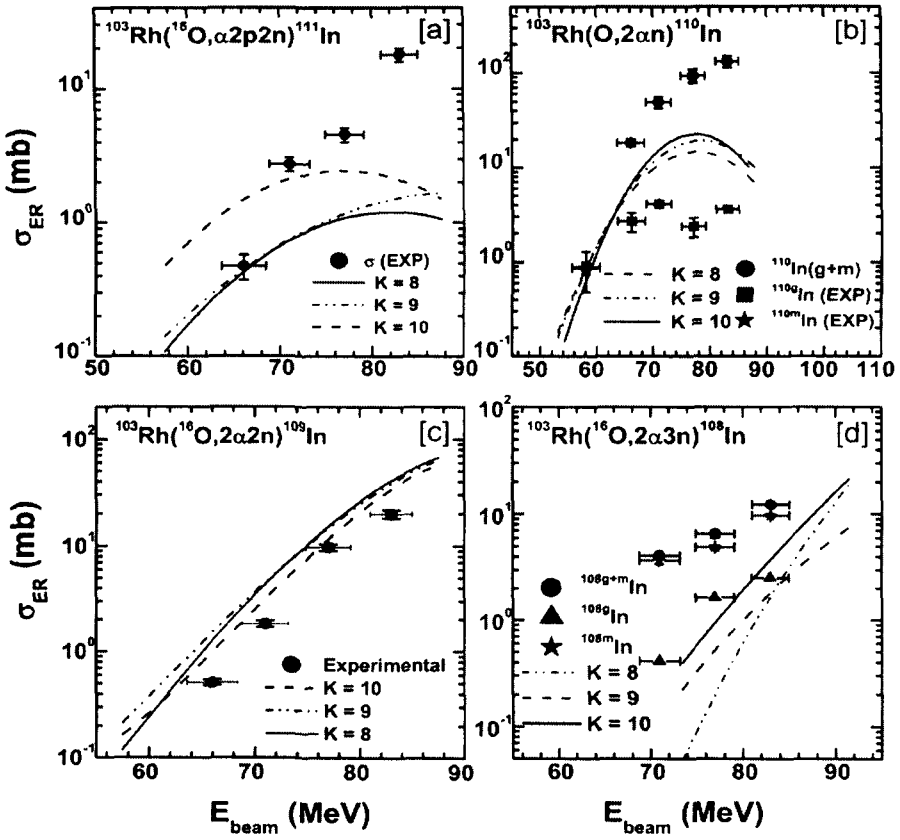

Fig. 4. Experimentally measured and theoretically calculated EFs for different residues populated via CF and/or ICF ($\alpha xn/2\alpha xn$-channels) in $^{16}O + ^{103}Rh$ system at $\approx$ 46–85 MeV. Dark circles represent the experimental cross-sections. The enhancement over the theoretical model predictions may be attributed to ICF processes.

calculated EFs, different values of K (8, 9 and 10) have been tested, and are shown in Figs. 3(a)–(f) and 4(a)–(d). It may be pointed out that, it might be possible to predict all the EFs with different values of parameters of the code for individual channels. However, it is not reasonable from the physics point of view. Further, a value of $K \geqslant 10$ may give rise to the anomalous effect in the particle multiplicity. In the present work, a value of $K = 8$ is found to give a satisfactory reproduction of experimental data for CF-channels within the experimental uncertainties.

The metastable state of ^{117}Te could not be observed due to its very short half-life ($\approx$ 103 ms). As can be seen from the Figs. 3(a)–(f), the experimentally measured EFs for radio-nuclides ^{117g}Te(pn), ^{116}Te(p2n), ^{115g,m}Te(p3n), ^{115}Sb(2p2n), ^{117}Sb(2p) and ^{114}Te(p4n) are satisfactorily reproduced by theoretical model predictions within the experimental uncertainties, and may be assumed to be populated via CF (as there is no alpha-particle in exit-channels). Further, in some cases (Fig. 3) experimental data is somewhat enhanced as compared to the theoretical model predictions. In such cases the same residues may be populated via two different modes of decay, viz., (i) directly from the decay of CN (independent production), and (ii) through the β^+/EC decay of higher charge isobar pre-cursors. As such, the experimentally measured production cross-section

is expected to be the admixture of two different decay modes as mentioned above. The independent cross-section ($\sigma_{\rm ind}$) has been separated out from cumulative cross-section ($\sigma_{\rm cum}$) using prescription of Cavinato et al. [31], discussed in Section 3.1 of this paper. As can be seen from the figures, there is a reasonable agreement between theoretical and experimental EFs after subtracting the contribution coming from pre-cursor decay. However, in Fig. 3(b) the higher values of cross-sections in the tail portion of the EFs may be an indication of pre-equilibrium-emission at higher energies [49–52], which is not taken into account in these calculations.

4.1. Interpretation of experimental results

The fact that the measured EFs for almost all predominantly populated CF-channels could be reproduced by PACE4 predictions, gives confidence to the choice of input parameters of theoretical model code. Therefore, same set of input parameters has also been used to fit the EFs of all α-emitting channels. As can be observed from Figs. 4(a)–(d), the experimentally measured EFs are relatively higher as compared to the theoretical predictions. Since the theoretical model code PACE4 does not take ICF into account, therefore the enhancement in the experimentally measured production cross-sections may be attributed to the contribution coming from ICF of ^{16}O with target nucleus. As such, these residues are expected to be populated both via CF and/or ICF of projectile. The production of these residues is assumed to be originated from the successive decay of CN followed by entire projectile fusion in CF process, and/or via fusion of ^{12}C/^{8}Be from ^{16}O-projectile in ICF processes leading to ^{115}Sb*/^{111}In*, respectively. The final reaction products appear after emission of a few nucleons from ^{115}Sb*/^{111}In* (incompletely fused composites). In this case it has been assumed that ^{16}O projectile breaks-up into its α-clusters, viz., ^{12}C + α and/or ^{8}Be + ^{8}Be, a part of projectile fuses with ^{103}Rh, while remnant moves in forward cone with almost projectile velocity. As can be seen from Fig. 4(c), the theoretically calculated EFs for ^{103}Rh(^{16}O, 2α2n)^{109g}In reaction is almost matching/slightly higher than the experimental data for all values of K, revealing very less/negligible contribution from ICF. It may, however, be pointed out that recoil range distribution measurement for this channel may give some clue about its population via CF only. Further, experimentally measured EFs for 3αxn-channels ($x = 1, 3, 4$) are shown in Fig. 5. The theoretical calculations give negligible cross-sections for these residues and hence are not shown in Fig. 5, meaning thereby, these residues are likely to be populated only via ICF. It may also be pointed out that no choice of physically reasonable parameters in theoretical calculations could reproduce the population of these residues.

Moreover, the reaction ^{103}Rh(^{16}O, 3αn)^{106m}Ag may be explained assuming that only α-particle fuses with the target-nucleus leading to ^{107}Ag*, which emits a neutron leaving behind the residue ^{106m}Ag. Similarly, the reactions ^{103}Rh(^{16}O, 3α3n)^{104g}Ag and ^{103}Rh(^{16}O, 3α4n)^{103g}Ag, may be explained, if 3 and 4 neutrons are emitted, respectively from ^{107}Ag*. In these cases, ^{12}C may be assumed to be a spectator. Further, in order to understand the ICF contributions in all α-emitting channels, an attempt has also been made to estimate ICF fraction from the comparison of experimentally measured EFs and theoretically calculated ones [48]. In the present work, the contribution of ICF has been separated out for ^{111}In(α2p2n), ^{110}In(2αn), ^{108}In(2α3n), ^{106m}Ag(3αn), ^{104g}Ag(3α3n) and ^{103g}Ag(3α4n) reaction products which are expected to have contribution from both CF and/or ICF processes. The deduced ICF cross-sections for the residues ^{111,110,108}In and ^{103g,104g,106m}Ag have been plotted in Fig. 6(a). From these figure, it may be observed that the ICF contribution in all α-emitting channels increases with projectile energy, as expected.

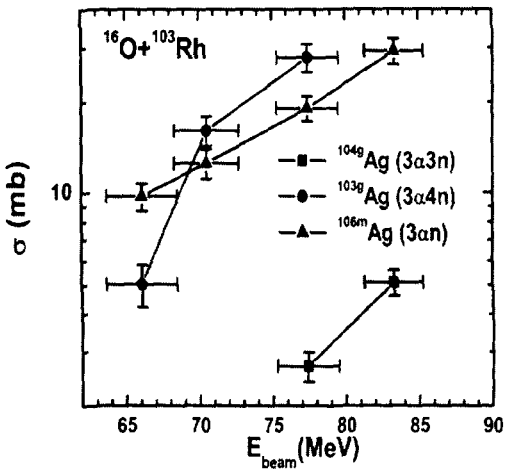

Fig. 5. Experimentally measured and theoretically calculated EFs for different residues expected to be populated via only incomplete fusion ($\alpha xn/2\alpha xn$-channels) of ^{16}O with ^{103}Rh.

Further, as indicated in Figs. 4(a), (b) and (d), ICF is expected to contribute significant amount to the evaporation residue cross-sections. As such, an attempt has been made to deduce the ICF contribution from experimentally measured and theoretically predicted EFs. Although, it is not possible to directly obtain the relative contribution of CF and ICF from the measurement of EFs, therefore some systematics has been followed. As already mentioned, the enhancement in the experimentally measured production cross-sections over theoretical model predictions based on CF calculations may be attributed to the contribution from ICF. As such, the ICF contribution for individual channels has been deduced by subtracting CF cross-sections (σ_{CF}) (predicted by theoretical model code) from the experimentally measured cross-sections (σ_{EXP}) at respective projectile energies, as suggested by Gomes et al. [3]. The ICF contributions (σ_{ICF}) deduced as mentioned in Ref. [3], for presently measured evaporation residues are plotted in Fig. 6(a) along with the sum of cross-section for all ICF channels ($\sum\sigma_{ICF}$) as a function of projectile energy. The lines drawn in these figures are just to guide the eyes. As can be seen from these curves, in general, the ICF contribution increases with projectile energy. It may be because of the fact that the projectile break-up probability of incident ion in the field of the target nucleus significantly increases with incident energy.

As mentioned, the sum of cross-sections for all measured ICF-channels ($\sum\sigma_{ICF}$) and the sum of cross-sections for all CF-channels ($\sum\sigma_{CF}$) obtained from theoretical model predictions are plotted along with the total fusion cross-section ($\sigma_{TF} = \sum\sigma_{CF} + \sum\sigma_{ICF}$) in Fig. 6(b). It can be observed from this figure that the CF component has measurable contribution even at $\approx$ 58 MeV, while ICF contribution seems to start from $\approx$ 66 MeV, in the present work. Further, it may be noted from Fig. 6(b), that the separation between the plots for $\sum\sigma_{TF}$ and σ_{CF} increases with projectile energy, which indicates larger contribution from ICF at relatively high projectile energies. This may be because of the fact that the break-up of projectile may be favored as the projectile energy increases. As such, in order to have better representation of projectile energy dependence on ICF contribution, the percentage ICF-fraction (F_{ICF}) has been estimated from the experimentally measured and theoretically calculated EFs similar to as in Ref. [48]. The

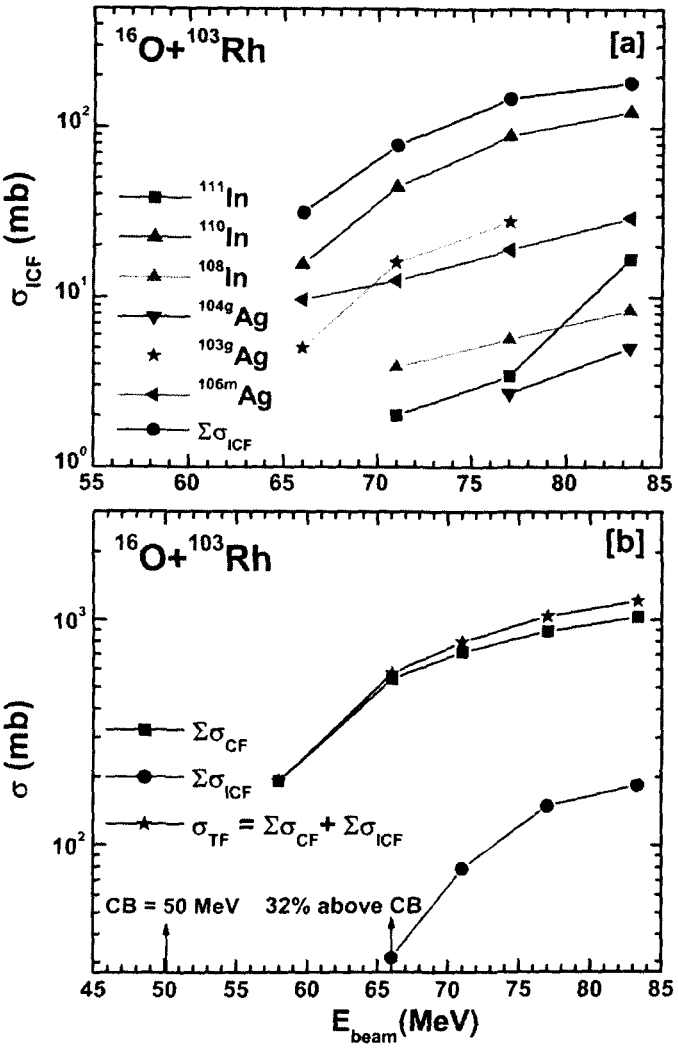

Fig. 6. (a) Deduced EFs for different ICF ($\alpha xn/2\alpha xn$-channels) residues, and (b) total fusion probability (σ_{TF}) along with the sum of complete fusion (σ_{CF}) and incomplete fusion (σ_{ICF}).

F_{ICF} for $^{16}O + ^{103}Rh$ system has been deduced at different energies and is plotted as a function of projectile energy normalized with Coulomb barrier (E_{beam}/V_b) in Fig. 7. The normalized projectile energy (E_{beam}/V_b) has been used to incorporate the effect of Coulomb barrier while comparing different projectile-target combinations in a plot, which is reported as best data reduction procedure for different systems [53]. As can be seen from Fig. 7, the relative percentage F_{ICF} is found to be $\approx 5.5\%$ of the total fusion cross-section (σ_{TF}) at $E_{beam}/V_b = 1.4$, which increases with normalized projectile energy. However, at ≈ 83 MeV (i.e. $E_{beam}/V_b = 1.77$) the relative percentage of F_{ICF} approaches to $\approx 16\%$ of σ_{TF}. Further, in order to support these measurements, similar energy dependence of F_{ICF} for $^{16}O + ^{159}Tb$ and $^{16}O + ^{169}Tm$ systems taken

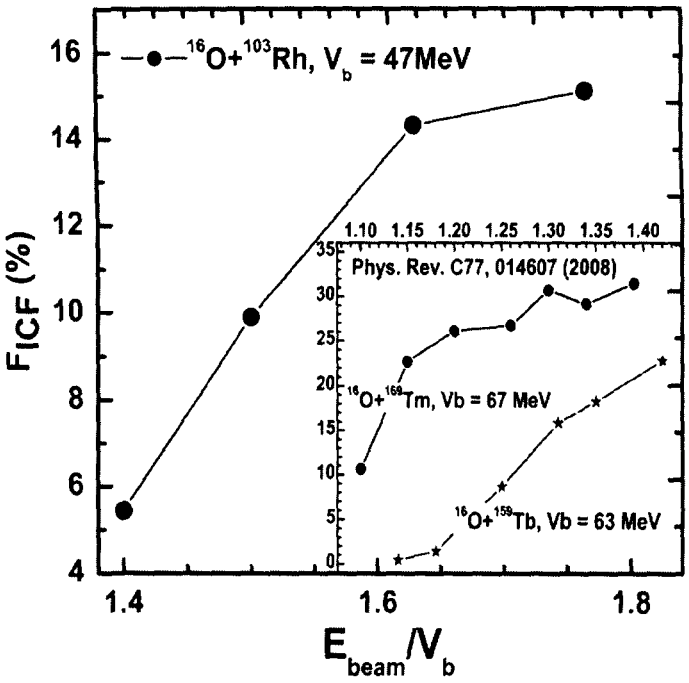

Fig. 7. The percentage ICF fraction (F_{ICF}) as a function of normalized projectile energy (E_{beam}/V_b) for $^{16}O + ^{103}Rh$ system, and also two different systems, viz., $^{16}O + ^{159}Tb$ and $^{16}O + ^{169}Tm$ shown from literature [48].

from our recent publications are also shown in the inset of this figure [48]. As can be noticed from the comparison of F_{ICF} for different projectile target combinations, the F_{ICF} is found to be $\approx 5.5\%$, $\approx 20\%$ and $\approx 30\%$ at the same $E_{beam}/V_b(= 1.4)$ value for $^{16}O + ^{103}Rh$, $^{16}O + ^{159}Tb$ and $^{16}O + ^{169}Tm$ systems, respectively. This striking observation clearly reveals the sensitiveness of F_{ICF} to the mass-asymmetry of interacting partners, which supports the systematics presented by Morgenstern et al. [15–18].

Moreover, similar mass-asymmetry dependence for ICF has been reported in one of our recent publications [48], wherein, it was emphasized that the F_{ICF} depends not only on the mass-asymmetry of interacting partners but also on projectile structure, which plays an important role in the underlying reaction mechanism. In the present work for $^{16}O + ^{103}Rh$ system, the similar systematics for ICF processes has been studied at given energies and presented in Fig. 8, at a constant value of $E_{beam}/V_b = 1.4$, as a representative case. As can be seen from this figure, the F_{ICF} is found to increase with mass-asymmetry, individually for both ^{16}O and ^{12}C as a projectile. It may, further, be pointed out that if one considers only the mass-asymmetry of interacting partners as presented by Morgenstern et al. [15–18], the F_{ICF} do not explain the observed systematics. As such, on the basis of systematics presented in this work and in our earlier publication [48], it may be inferred that not only mass-asymmetry of interacting partners but also the projectile structure effects should also be taken into account, while predicting the F_{ICF}. Further, the systematics can be supported and strengthened by some more experimental data for various projectile–target combinations.

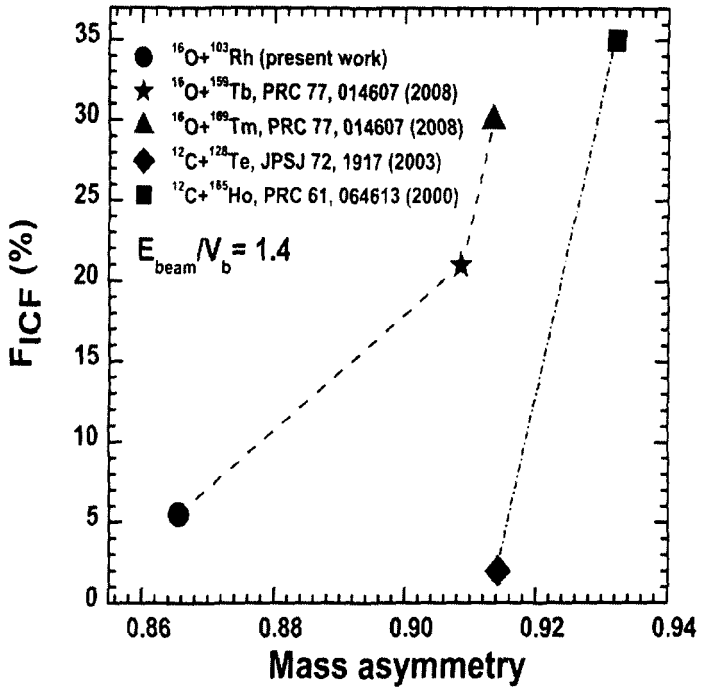

Fig. 8. The percentage ICF fraction (F_{ICF}) as a function of mass asymmetry at a constant normalized projectile energy.

5. Summary and conclusions

Measurement and analysis of EFs for several radio-nuclides produced via CF and/or ICF in $^{16}O + ^{103}Rh$ system at energies $\approx$ 3–5 MeV/nucleon have been presented in this paper. Some pxn and αxn-channels are found to have contribution from both direct and pre-cursor decay of higher charge isobar. As such, an attempt has been made to deduce the independent production cross-section from cumulative and pre-cursor decay contribution of different radio-nuclides. The experimentally measured EFs have been compared with PACE4 predictions after correcting the pre-cursor decay contribution (if any), which have been found to agree reasonably well for xn/pxn-channels (CF-products). However, in case of α-emitting channels, significant enhancement in the production cross-sections has been observed as compared to theoretical model predictions. The observed enhancement in experimentally measured cross-sections may be assumed to come from the prompt break-up of projectile into α-clusters ($^{16}O \Rightarrow {}^{12}C + {}^{4}He$ and/or $^{8}Be + {}^{8}Be$) leading to the various ICF processes. It has also been observed that the probability of break-up increases with the projectile energy, which reveals the dependence of ICF processes sensitively on projectile energy. Moreover, in order to further confirm the findings of Morgenstern et al. [15–18], and of our recent publication [48], the dependence of F_{ICF} on mass-asymmetry and/or the projectile structure effect, experimental data for five experiments have been compared, wherein, the F_{ICF} is found to increase with mass-asymmetry, individually for both ^{16}O and ^{12}C as a projectile. Therefore, it can be inferred that mass-asymmetry of interacting partners along with projectile structure effects should also be taken into consideration to explain the F_{ICF} for different projectile–target combinations. As such, it may be concluded that apart from CF, the ICF is

also found to contribute significantly to the total reaction cross-section even at projectile energies as low as $\approx$ 3–5 MeV/nucleon. Therefore, while predicting the total reaction cross-section for a projectile–target combination, the contribution coming from ICF should also be taken into consideration. Further, the additional information of underlying processes can also be obtained by comparing a rich set of experimental data for various projectile–target combinations. However, the measurement of recoil range distribution and spin-distribution of residues populated by CF as well as ICF using particle-γ coincidence technique both at relatively low and higher bombarding energies may provide a more clear understanding of the incomplete fusion processes.

Acknowledgements

Authors are thankful to the Director, Inter-University Accelerator Center (IUAC), New Delhi, INDIA for extending all the facilities for carrying out the experiments. We are also thankful to Ms. K.S. Golda for her help during target preparation. One of the authors (Unnati) thanks to the CSIR, M.K.S. to the DST, and R.P. thanks to the DST and the UGC for financial support.

References

[1] M. Lunardona, C. Meriglianoa, G. Viestia, D. Fabrisa, G. Nebbiaa, M. Cinauserob, G. de Angelisb, E. Farneab, E. Fiorettob, G. Preteb, A. Brondic, G. La Ranac, R. Moroc, A. Principec, E. Vardacic, N. Gellid, F. Lucarellid, P. Pavana, D.R. Napolib, G. Vedovatob, Nucl. Phys. A 652 (1999) 3–16.
[2] E.Z. Buthelezi, E. Gadioli, G.F. Steyn, F. Albertini, C. Birattari, M. Cavinato, F. Cerutti, E. Fabrici, Nucl. Phys. A 734 (2004) 553–556.
[3] P.R.S. Gomes, I. Padron, E. Crema, O.A. Capurro, J.O. Fernandez Niello, A. Arazi, G.V. Mart, J. Lubian, M. Trotta, A.J. Pacheco, J.E. Testoni, M.D. Rodriguez, M.E. Ortega, L.C. Chamon, R.M. Anjos, R. Veiga, M. Dasgupta, D.J. Hinde, K. Hagino, Phys. Rev. C 73 (2006) 064606.
[4] P. Vergani, E. Gadioli, E. Vaciago, E. Fabrici, E. Gadioli Erba, M. Galmarini, G. Ciavola, C. Marchetta, Phys. Rev. C 48 (1993) 1815.
[5] A. Diaz-Torres, I.J. Thompson, Phys. Rev. C 65 (2002) 024606.
[6] F. Amorini, M. Cabibbo, G. Cardella, A. Di Pietro, P. Figuera, A. Musumarra, M. Papa, G. Pappalardo, F. Rizzo, S. Tudisco, Phys. Rev. C 58 (1998) 987.
[7] M. Dasgupta, P.R.S. Gomes, D.J. Hinde, S.B. Moraes, R.M. Anjos, A.C. Berriman, R.D. Butt, N. Carlin, J. Lubian, C.R. Morton, J.O. Newton, A. Szanto de Toledo, Phys. Rev. C 70 (2004) 024606.
[8] P.E. Hodgson, E. Gadioli, E. Gadioli Erba, Introductory Nuclear Physics, Clarendon Press, Oxford, 1997, Chapter 23.
[9] J. Pochodzallab, R. Butscha, B. Hecka, G. Rosnera, Phys. Lett. B 181 (1986) 33–37.
[10] H. Oeschler, M. Kollatz, W. Bohne, K. Grabisch, H. Lehr, H. Freiesleben, K.D. Hildenbrand, Phys. Lett. B (1983) 177–180.
[11] H.W. Wilschut, G.J. Balster, P.B. Goldhoorn, R.H. Siemssen, Z. Sujkowski, Phys. Lett. B 138 (1984) 43–46.
[12] J.B. Natowitz, E.T. Chulick, M.N. Namboodiri, Phys. Rev. C 6 (1972) 2133.
[13] K. Siwek-Wilczyńska, E.H. du Marchi van Voorthuysen, J. van Popta, R.H. Siemssen, J. Wilczyński, Phys. Rev. Lett. 42 (1979) 1599.
[14] W. Trautmann, O. Hansen, H. Tricoire, W. Hering, R. Ritzka, W. Trombik, Phys. Rev. Lett. 53 (1984) 1630.
[15] H.M. Morgenstern, W. Bohne, W. Galster, K. Grabisch, Phys. Rev. Lett. 52 (1984) 1104.
[16] H. Morgenstern, W. Bohne, K. Grabisch, H. Lehr, W. Stoffler, Z. Phys. A 313 (1983) 39.
[17] H. Morgenstern, W. Bohne, W. Galster, K. Grabisch, Phys. Rev. Lett. 52 (1984) 1104.
[18] H. Morgenstern, W. Bohne, K. Grabisch, D.G. Kovar, H. Lehr, Phys. Lett. 113B (1982) 463.
[19] T. Udagawa, T. Tamura, Phys. Rev. Lett. 45 (1980) 1311.
[20] J. Wilczyński, K. Siwek-Wilczyńska, J. van Driel, S. Gonggrijp, D.C.J.M. Hageman, R.V.F. Janssens, J. Lukasiak, R.H. Siemssen, S.Y. van der Werf, Phys. Rev. Lett. 45 (1980) 606.
[21] J.P. Bondrof, J.N. De, G. Fai, A.O.T. Karvinen, J. Randrup, Nucl. Phys. A 333 (1980) 285.
[22] M. Blann, Phys. Rev. Lett. 27 (1971) 337.
[23] T. Inamura, T. Kjima, T. Nomura, T. Sugitate, H. Utsunomiya, Phys. Lett. 84B (1982) 71.

[24] T. Inamura, A.C. Kahler, D.R. Zolnowski, U. Garg, T.T. Sugihara, M. Wakai, Phys. Rev. C 32 (1985) 1539.
[25] B.G. Harvey, Nucl. Phys. A 444 (1985) 498.
[26] M.H. Simbel, A.Y. Abdul Magd, Z. Phys. A 294 (1980) 277.
[27] A.Y. Abdul Magd, Z. Phys. A 298 (1980) 143.
[28] V.I. Zagrebaev, Ann. Phys. (N.Y.) 197 (1990) 33.
[29] H. Morgenstern, W. Bohne, W. Galster, K. Grabisch, Z. Phys. A 324 (1986) 443.
[30] M.K. Sharma, Unnati, B.K. Sharma, B.P. Singh, H.D. Bhardwaj, R. Kumar, K.S. Golda, R. Prasad, Phys. Rev. C 70 (2004) 044606.
[31] M. Cavinato, E. Fabrici, E. Gadioli Erba, P. Vergani, M. Crippa, G. Colombo, I. Redaeli, M. Ripamonti, Phys. Rev. C 52 (1995) 2577.
[32] M. Crippa, E. Gadioli, P. Vergani, G. Ciavola, C. Marchetta, M. Bonardi, Z. Phys. A 350 (1994) 121.
[33] D.J. Parker, J. Asher, T.W. Conlon, I. Naqib, Phys. Rev. C 30 (1984) 143;
D.J. Parker, J. Asher, T.W. Conlon, I. Naqib, Phys. Rev. C 35 (1987) 161.
[34] P. Walker, G.D. Dracoulis, Nature (London) 399 (1999) 35.
[35] G.D. Dracoulis, A.P. Byrne, T. Kibedi, T.R. McGoram, S.M. Mullins, J. Phys. G: Nucl. Part. Phys. 23 (1997) 1191, and references therein.
[36] M.K. Sharma, Unnati, B.P. Singh, R. Kumar, K.S. Golda, H.D. Bhardwaj, R. Prasad, Nucl. Phys. A 776 (2006) 83.
[37] S. Gupta, B.P. Singh, M.M. Muthafa, H.D. Bhardwaj, R. Prasad, Phys. Rev. C 61 (2000) 0064613.
[38] P.P. Singh, M.K. Sharma, Unnati, D.P. Singh, R. Kumar, K.S. Golda, B.P. Singh, R. Prasad, Eur. Phys. J. A 34 (2007) 29–39.
[39] E.Z. Buthelezi, F. Ceutti, E. Gadioli, G.F. Steyn, A. Pepe, S.H. Connell, A.A. Cowley, Eur. Phys. J. A 28 (2006) 193–203.
[40] E. Browne, R.B. Firestone, Table of Radioactive Isotopes, Wiley, New York, 1986.
[41] U. Reus, W. Westmeirer, At. Data Nucl. Data Tables 29 (1983) 338.
[42] R. Bass, Nucl. Phys. A 231 (1974) 45.
[43] A. Gavron, Phys. Rev. C 21 (1980) 230.
[44] P.M. Endt, At. Data Nucl. Data Tables 26 (1981) 47.
[45] S.K. Kataria, V.S. Ramamurthy, S.K. Kapoor, Phys. Rev. C 18 (1978) 549.
[46] F.D. Becchetti, G.W. Greenlees, Phys. Rev. 182 (1969) 1190.
[47] G.R. Satchler, Nucl. Phys. 70 (1965) 177.
[48] P.P. Singh, B.P. Singh, M.K. Sharma, Unnati, D.P. Singh, R. Prasad, R. Kumar, K.S. Golda, Phys. Rev. C 77 (2008) 014607, and the references therein.
[49] N. Patronis, C.T. Papadopoulos, S. Galanopoulos, M. Kokkoris, G. Perdikakis, R. Vlastou, A. Lagoyannis, S. Harissopulos, Phys. Rev. C 75 (2007) 034607.
[50] T.E. Rodrigues, M.N. Martins, C. Garcia, J.D.T. Arruda-Neto, J. Mesa, K. Shtejer, F. Garcia, Phys. Rev. C 75 (2007) 014605.
[51] J. Pal, S. Saha, C.C. Dey, P. Banerjee, S. Bose, B.K. Sinha, M.B. Chatterjee, S.K. Basu, Phys. Rev. C 71 (2005) 034605.
[52] W. Bauer, A. Botvina, Phys. Rev. C 52 (1995) R1760.
[53] P.R.S. Gomes, J. Lubian, I. Padron, R.M. Anjos, Phys. Rev. C 71 (2005) 017601.

PHYSICAL REVIEW C 75, 064608 (2007)

Reaction mechanism in the $^{16}O+^{27}Al$ system: Measurements and analysis of excitation functions and angular distributions

Manoj Kumar Sharma,[1,*] Unnati,[1] Devendra P. Singh,[1] Pushpendra P. Singh,[1] B. P. Singh,[1,†] H. D. Bhardwaj,[2] and R. Prasad[1]
[1]*Department of Physics, Aligarh Muslim University, Aligarh-202002, India*
[2]*Department of Physics, DSN, College, Unnao, India*
(Received 26 January 2007; published 12 June 2007)

To study the dynamics of heavy ion fusion reactions in the lower mass region, experiments were carried out to measure the cross sections of radioactive residues produced in the interaction of the ^{16}O ion with ^{27}Al target nucleus at 19 different energies in very close intervals covering the energy range from $\approx$58 to 94 MeV, using the well-known recoil catcher off-line γ-ray spectroscopy technique. The simulation of experimental-data was performed using statistical-model-based computer codes, viz., CASCADE, PACE2, and ALICE-91. The analysis of measured excitation functions indicates that these residues are likely to be produced by complete fusion, incomplete fusion, and direct reaction processes. Furthermore, to confirm the contribution of different reaction channels, a complementary experiment was performed that measured the angular distributions of the residues produced in the $^{16}O+^{27}Al$ system at 85 MeV beam energy. The analysis of the results of both experiments indicates that at these energies, the direct reactions compete with complete fusion and incomplete fusion reaction processes.

DOI: 10.1103/PhysRevC.75.064608 PACS number(s): 25.70.Gh

I. INTRODUCTION

During the last couple of decades, efforts have been made to understand the dynamics of nuclear interaction in light and heavy particle induced reactions. In light particle induced reactions, two apparently different mechanisms such as the compound nucleus (CN) and the direct reactions appear to be dominant. In the CN mechanism, the interaction between projectile and target nucleus takes place in such a way that the excitation energy is shared statistically among all the constituent nucleons of the composite system so that memory of its formation is lost. The time scales involved in these reactions are typically $\approx 10^{-16}$ s. The CN reactions are important at relatively low energies and remain a fruitful source of information about nuclear structure. On the other hand, in a direct reaction (DR), the projectile interacts with a single or a few nucleons of the target nucleus. The time taken by the projectile to traverse the target nucleus is very short ($\approx 10^{-22}$ s), thus the energy required for the DR process is relatively high, suggesting only a few degrees of freedom are involved.

Furthermore, at energies between those of the compound nucleus and direct reactions, the preequilibrium (PE) emission of nucleons has been observed, reflecting the dynamics of an excited composite system formation leading to the equilibrated CN [1,2]. In PE emission, the particle emission is assumed to take place after the first projectile target interaction but prior to the establishment of the equilibrated compound nucleus. Some of the important features of PE emission are (1) slowly descending tails of excitation function, (2) forward peaked angular distribution of emitted particles, and (3) relatively large number of high energy particles than predicated by the CN mechanism.

To explain the mechanism of such reactions, several models have been proposed. At present, model-based computer codes are available that include preequilibrium emission to explain the complete features of the experimental data. It is now possible to theoretically describe the sequence of processes, which has led to the comprehensive description of a large set of cross section data for different projectile-nucleus interactions.

In recent years, with the availability of medium energy heavy ion (HI) accelerators, it has become possible to study the nuclei at higher excitation energies and angular momenta, where, along with complete fusion (CF) processes, such processes as incomplete fusion (ICF) or breakup fusion, deep-inelastic collision (DIC), quasielastic collision (QEC), direct reaction (DR), transfer reaction (TR), PE emission, etc., are also likely to occur [3]. Thus, in HI reactions, the cross section is shared predominantly among the following processes: those leading to complete fusion, deep-inelastic collision, and quasielastic collision.

As the energy increases, one observes, in addition to light particles, beam like particle also, evidently emitted at an early stage of the reaction known as ICF particles. This emission is referred to as breakup fusion or ICF. The interplay between fusion and breakup fusion processes takes place at beam energies as low as just above the Coulomb barrier [4–9]. This observation led to a renewed interest to the study of the dynamics of HI reactions. Furthermore, the different behaviors of HI interactions, which depend on the energy regime, entrance channel mass asymmetry, etc., are still some of the unanswered and important open questions.

There are several ways to classify HI interactions. One of them is in terms of the impact parameter [3]. At higher values of impact parameter, the DR may take place, leading to few nucleon transfer processes. However, at smaller impact parameter values, the CF, ICF, and DIC processes may be dominant. In complete fusion reactions, the incident ion is

*mks_amu@rediffmail.com
†bpsinghamu@gmail.com

completely absorbed by the target nucleus, forming an excited composite system from which particles and/or γ rays may be emitted after the formation of the equilibrated compound nucleus.

However, in the case of ICF, the projectile is assumed to break up in the vicinity of the nuclear field of the target nucleus into the fragments called projectile-like fragments (PLFs), and only one of the PLFs fuses with the target nucleus, while the remaining PLFs continue to move in the forward direction with approximately the same velocity as that of the incident ion. The ICF reactions have been reported to have the following characteristics: (1) a forward peaked angular distribution of PLFs, which are predominantly emitted at the beam velocity and are generally viewed as fast breakup of the projectile, (2) a linear momentum transfer less than that of complete fusion, resulting in a smaller range of the evaporation residues, (3) a relatively higher measured cross section than that predicted by statistical models, and (4) a higher energy of the direct α particles than that of the evaporation α particles from the equilibrated compound nucleus. Various models have been proposed to describe the dynamics of ICF reactions, but none of them is able to explain the experimental data over a large energy range and mass region as well. It may not be out of place to mention that there is no satisfactory theoretical support so far for ICF reactions that can be used to simultaneously explain complete and incomplete fusion processes.

Furthermore, DICs may also be likely at these energies, in which the mass of the resulting nuclei are close to the mass of the projectile and target nuclei. The deep-inelastic collision may be characterized by substantial dissipation of initial kinetic energy and angular momentum. The time scale at which DICs are expected to occur is less than the CN lifetime, but long enough for the exchange of a significant number of nucleons between the target and the projectile. One may get the information about the mechanism through the measurement and analysis of cross section data, recoil range, and angular distributions of the residues produced in the interaction of two heavy nuclei. The cross section data obtained for such channels have a wide range of applications. Therefore, the above study is not only an important subject in its own right, but also significant for its impact on related fields of investigation and for its rich variety of applications. In this context, a program of measurement and analysis of the cross sections of nuclear reactions induced by HI has been undertaken [10].

In the present work, the excitation functions (EFs) for radioactive residues produced in the interaction of ^{16}O ion with ^{27}Al have been measured in order to study the reaction dynamics, particularly in the low mass region. Most of the studies in which the occurrence of ICF was observed were carried out generally with heavier mass target nuclei. Though initial studies on incomplete fusion have been carried out at energies $\approx$10 MeV/nucleon using rare-earth targets [11], there are very few studies with lower mass target nuclei. One advantage of using a lighter mass system is to avoid the possibility of fission, which is one of the competing modes in HI reactions on heavier target nuclei at these energies. Furthermore, if heavier targets are used, the emission of α particles from the fused excited system is likely to be substantially reduced [12] because of the high Coulomb barrier. As a result, the emission of α particles in incomplete fusion channels may give rise to residues which may have very little contribution from complete fusion channels. Measurement and analysis of EFs [4,5] in HI reactions for heavier target nuclei have indicated that ICF is an important component of the reaction mechanism at these energies.

With the motivation to determine the contribution of incomplete fusion processes in light mass target nuclei, the measurement and analysis of the cross sections for the reaction channels ($2\alpha n$), ($3\alpha 3p$), ($3\alpha 3pn$), ($4\alpha 2pn$), and ($4\alpha 3p$) produced in the ^{16}O+^{27}Al system have been carried out at 19 different energies at very close intervals covering the energy range from $\approx$58 to 94 MeV. There are mainly two experimental methods which are widely used to study the dynamics of HI reactions: (1) off-beam γ-ray spectrometry by the measurement and analysis of the excitation functions (EFs), recoil range distributions, and angular distributions of the residues produced in the projectile-target interaction using the activation technique and (2) in-beam γ-ray spectrometry by detecting the breakup α particles of the projectile, i.e, projectile-like fragments, in coincidence with the prompt γ rays of the populated residues using the particle-γ coincidence technique. The former is based on the measurement of the activity produced in radioactive residues using off-line γ-ray spectroscopy.

In the literature [13], the measurement of cross section data exists for the ^{16}O+^{27}Al system using the activation technique. Landenbaurer-Bellis *et al.* [13] measured the cross section for the reactions in the above system employing the activation technique in the energy range 10.5–1 MeV/nucleon, using a NaI (Tl) detector to identify γ rays of interest and an end-window gas flow proportional counter to resolve β decay. The energy spread of the data points are substantially large. It may, however, be pointed out that no theoretical interpretation of the data was made [13]. Furthermore, it has been mentioned that observed trend of the data indicates a CN mechanism. However, more recently, McKenna *et al.* [14] tried to reproduce the experimental data [13] in an experiment using a high intensity laser produced plasma beam. They also performed theoretical calculations [14] using the Monte Carlo code PACE2 [15]. They reported that residue ^{34}Cl is produced by the evaporation of two α particles and one neutron from the compound nucleus. Furthermore, the production of other radioisotopes, viz., ^{27}Mg, ^{24}Na, and ^{24}Ne, was attributed to the compound nucleus as well as to direct reactions. It is not out of place to mention here that incomplete fusion and deep-inelastic collision are also dominant mechanisms in HI reactions at these energies, and hence the contributions of these reaction channels are also required to be taken in to account.

In the present work, an attempt has been made to explain the experimentally measured cross sections using statistical-model-based computer codes, viz., CASCADE [16], PACE2 [15], and ALICE-91 [17]. To obtain complementary information about the processes involved in lighter mass symmetric systems, angular distributions of the residues produced in the ^{16}O+^{27}Al system have also been measured at 85 MeV beam energy. Experimental details are discussed in Sec. II of the paper; the analyses of the excitation functions and angular distributions are presented in Secs. III and IV, respectively. Conclusions are given at the end of the paper.

II. EXPERIMENTAL DETAILS

The experiments were performed at the Inter University Accelerator Centre (IUAC) formerly known as Nuclear Science Center (NSC), New Delhi, India, using the 15 UD Pelletron accelerator facility. The experiments for excitation functions and angular distribution measurements were carried out in the general-purpose scattering chamber (GPSC) of 1.5 m diameter dedicated for such studies, having an in-vacuum transfer facility. The time interval between the end of irradiation and the beginning of counting was minimized using in-vacuum transfer of samples from the scattering chamber to the counting system. Details of the measurements of excitations functions and annular distributions are given in the following subsections.

A. Excitation functions

The spectroscopically pure self-supporting foils of ^{27}Al (purity ≈99.999%) were rolled to obtain samples of the desired thickness. Target thickness plays a crucial role in each measurement. Therefore, measurement of target thickness must be as accurate as possible to obtain accuracy in the measured cross section data. In the present case, the thicknesses of the target as well as the catcher foils were determined using the α-transmission method. This method is based on the measurement of the energy lost by 5.485 MeV α particles obtained from a ^{241}Am source while passing through the target thickness. For thickness determination, the stopping power values were calculated using the program SRIM-2006. The measured thickness of ^{27}Al foils were ≈1.8 mg/cm^2. The Al samples and the degrader/catcher foils were cut into 1.2 × 1.2 cm^2 squares and pasted onto rectangular target holders having concentric holes of 1.0 cm diameter. In the present work, two stacks containing five alternating samples of natural Tm and Al and another two stacks containing five and four alternating samples of natural Tb and Al, respectively, were used for the EF studies. The samples of Tm and Tb served as energy degraders and catchers. In separate communications [18,19], the activations of the Tb and Tm samples were studied for the measurement of cross sections for a large number of channels. The calculations of energy loss in the stack were done using the energy range program SRIM-2006. Four stacks containing in all 19 ^{27}Al samples and an equal number of energy degraders were irradiated by the $^{16}O^{7+}$ beam at four different energies, i.e., 86, 88, 92, and 95 MeV. The irradiation of these four stacks covered the desired energy range ≈58 to 95 MeV. As the beam traverses the samples of the stack, the energy spread goes on increasing toward the last sample. As a typical example, the energy spread at ≈58 MeV is ≈2%. Keeping in mind the half-lives of interest, the irradiation of each stack was carried out for ≈8 h duration. The beam currents were ≈50 nA. The total charge collected in the Faraday cup was used to calculate the flux of the incident beam. Furthermore, to monitor the flux of the incident beam, in an auxiliary experiment, two Rutherford monitor detectors kept at ±30° with respect to the beam direction were used. The two readings of the flux agreed with each other within an uncertainty of about 5%. It may, however, be pointed out that the unreacted beam is dumped in the Faraday cup about 1 m away from the samples.

In the present work, the analysis of the $^{16}O+^{27}Al$ system is being presented which provides a data set of 19 points at very close energy intervals. The stacked foil activation technique followed by off-line γ-ray spectroscopy was employed to determine the cross sections for various reaction residues. In the stacked foil technique, the energetic beam traverses through all the samples with degrading beam energies; as such, it is possible to bombard different samples of the stack at different energies. The activities induced in the various samples were recorded by counting the Al samples as well as the degrader/catcher foils using a high-purity Ge γ-ray spectrometer coupled to a personal-computer-based multichannel analyzer setup employing the FREEDOM software [20]. The counts under photo peaks of interest were taken for the determination of cross section after proper background correction. The HPGe γ-ray spectrometer (resolution ≈2 keV for 1.33 MeV γ ray of ^{60}Co) was precalibrated for both energy and efficiency employing various standard γ sources such as ^{22}Na, ^{54}Mn, $^{57,60}Co$, ^{133}Ba, ^{137}Cs, and ^{152}Eu. To determine the geometry-dependent efficiency G_ε for γ rays of different energies, a standard source of ^{152}Eu of known strength was used. A typical plot of G_ε at 2 cm distance from the sample to the detector system is shown in Fig. 1. Relevant portions of the observed γ-ray spectrum of the irradiated ^{27}Al sample at 82 MeV ^{16}O beam are shown in Fig. 2.

The peaks in the observed γ-ray spectrum were assigned to different reaction residues on the basis of their characteristic energy of γ lines as well as measured half-lives. A typical curve used to determine the half-life of the residue ^{34m}Cl is shown in Fig. 3. A list of reactions, energies of the identified γ rays, and their branching ratios [21] are given in Table I.

The measured intensities of the characteristic γ rays were used to compute the reaction cross sections using the formula [22]

$$\sigma_r(E) = \frac{C_a \lambda \exp(\lambda t_l)}{N_a \phi P K(G_\varepsilon)[1-\exp(-\lambda t_i)][1-\exp(-\lambda t_a)]}, \quad (1)$$

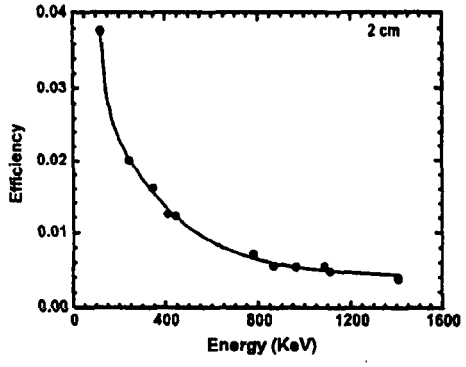

FIG. 1. Typical plot of photo peak efficiency of HPGe detector as a function of γ-ray energies of the ^{152}Eu source.

TABLE I. Reactions, measured half-lives, identified γ rays, and their branching ratios.

Sample no.	Reaction	Half-life	E_γ (keV)	Branching ratio (%)
1	^{27}Al(^{16}O, $2\alpha n$)^{34}Cl	32.2 min	146.5	40.5
2	^{27}Al(^{16}O, $3\alpha 3p$)^{28}Mg	20.9 h	400.5, 1342.3	36.0, 54
3	^{27}Al(^{16}O, $3\alpha 3pn$)^{27}Mg	9.4 min	843.7	73.0
4	^{27}Al(^{16}O, $4\alpha 2pn$)^{24}Na	14.6 h	1368	100
5	^{27}Al(^{16}O, $4\alpha 3p$)^{24}Ne	3.8 min	472.2	100

where C_a is the observed counts under the photo peak during the accumulation time t_a of the induced activity of decay constant λ, N_o the number of target nuclei irradiated for time t_i with a particle beam of flux ϕ, t_l the time lapse between the stop of irradiation and the start of counting, P the branching ratio of the characteristic γ ray, and G_ϵ the geometry-dependent efficiency of the detector for the γ ray of a given energy. Proper correction for the geometry-dependent efficiency was taken into account for each case. The factor $[1 - \exp(-\lambda t_i)]$, known as the saturation correction, takes care of the decay of evaporation residues during the irradiation. The corrections for the decay of the induced activity due to the delay between the stop of irradiation and the start of counting and during the data accumulation are taken into account via the factors $\exp(\lambda t_l)$ and $[1 - \exp(-\lambda t_a)]$, respectively. $K = [1 - \exp(-\mu x)/\mu x]$ is the correction for the self-absorption of the γ radiation in the sample thickness itself, where x is the thickness of the sample and μ is the energy-dependent γ-ray absorption coefficient.

The experimentally measured values of cross sections at different energies for the reactions ^{27}Al(^{16}O, $2\alpha n$)^{34}Cl, ^{27}Al(^{16}O, $3\alpha 3p$)^{28}Mg, ^{27}Al(^{16}O, $3\alpha 3pn$)^{27}Mg, ^{27}Al(^{16}O, $4\alpha 2pn$)^{24}Na, and ^{27}Al(^{16}O, $4\alpha 3p$)^{24}Ne are given in Table II.

B. Angular distributions

A separate experiment has also been carried out to measure the angular distribution of recoiling residues produced in the ^{16}O+^{27}Al system at 85 MeV beam energy. In this experiment, an Al target supported by Tm material of thickness $\approx$0.48 mg/cm^2 followed by a stack of thick annular concentric Al catcher foils was mounted in the irradiation chamber normal to the beam direction. Concentric annular aluminum catchers of thickness $\approx$0.3 mm with diameters 0.81, 1.29, 1.95, 2.64, 3.27, 5.46, and 6.4 cm were used to trap the recoiling nuclei emitted at different angles. A typical arrangement of the target and catcher assembly used for the angular distribution measurements is shown in Fig. 4. The arrangement of annular catchers was placed 1.8 cm behind the target for collecting the residues emitted in seven different angular ranges, viz., 0°–13° (most forward cone), 13°–21°, 21°–30°, 30°–39°, 39°–45°, 45°–60°, and 60°–64°. The irradiation was carried out for about 11 h with a beam current of $\approx$7 pnA. The activities induced in each catcher were followed off line for a couple of days. Typical γ spectra indicating the region of interest for different annular Al catcher rings covering the angular range from 0°–13° to 45°–60° is shown in Fig. 5. For identification of the reaction residues, the similar procedure is adopted, as discussed in Sec. II A. Further,

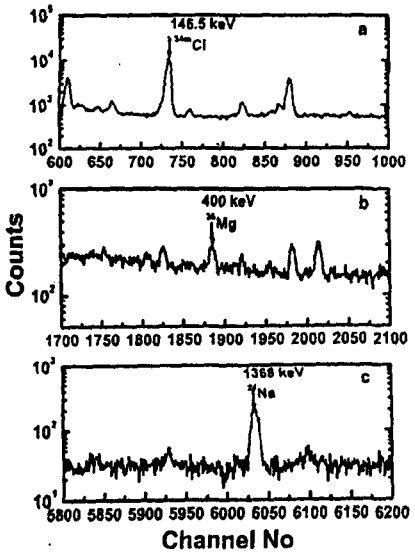

FIG. 2. Observed γ-ray spectrum of irradiated ^{27}Al sample at 82 MeV.

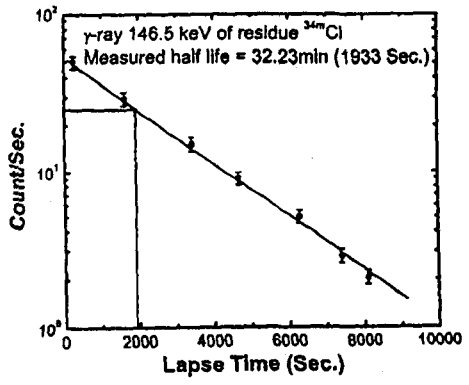

FIG. 3. Typical curve used to determine the half-live of the residue ^{34m}Cl.

TABLE II. Experimentally measured cross sections.

Lab energy (MeV)	$\sigma(^{34}Cl)$ (mb)	$\sigma(^{28}Mg)$ (mb)	$\sigma(^{27}Mg)$ (mb)	$\sigma(^{24}Ne)$ (mb)	$\sigma(^{24}Na)$ (mb)
58.0 ± 1.3	9.40 ± 1.69	–	–	–	0.46 ± 0.08
58.7 ± 1.3	14.57 ± 2.62	–	–	–	1 ± 0.18
66.5 ± 1.2	57.72 ± 10.39	–	–	–	0.94 ± 0.17
68.0 ± 1.2	62.70 ± 11.29	–	–	–	0.96 ± 0.17
68.2 ± 1.2	154.09 ± 27.74	–	–	–	0.275 ± 0.05
71.6 ± 1.1	115.49 ± 20.79	–	–	–	0.63 ± 0.11
75.4 ± 1.1	169.53 ± 30.52	–	–	–	0.89 ± 0.16
76.2 ± 1.1	100.98 ± 18.18	0.08 ± 0.01	–	–	1.35 ± 0.243
77.1 ± 1.0	126.40 ± 22.75	0.09 ± 0.01	–	–	1.17 ± 0.21
78.8 ± 1.0	95.32 ± 17.16	–	–	–	1.2 ± 0.22
81.8 ± 1.0	81.96 ± 14.75	2.48 ± 0.44	–	–	2.35 ± 0.42
82.0 ± 0.9	120.91 ± 21.76	–	–	–	1.37 ± 0.25
85.5 ± 0.6	84.79 ± 15.26	2.21 ± 0.4	–	0.12 ± 0.03	7.88 ± 1.41
85.9 ± 0.9	140.79 ± 28.26	3.11 ± 0.5	–	0.11 ± 0.02	5.15 ± 0.9
88.2 ± 0.6	15.53 ± 2.80	1.53 ± 0.26	0.22 ± 0.05	0.36 ± 0.09	1.03 ± 0.18
88.5 ± 0.8	–	0.42 ± 0.05	0.2 ± 0.05	–	1.58 ± 0.28
91.4 ± 0.6	5.43 ± 0.98	–	0.08 ± 0.02	0.22 ± 0.05	1.15 ± 0.20
93.4 ± 0.8	8.26 ± 1.48	0.4 ± 0.08	0.11 ± 0.02	0.12 ± 0.05	1.5 ± 0.27
94.4 ± 0.6	4.74 ± 0.85	0.2 ± 0.06	0.1 ± 0.03	0.1 ± 0.03	1.33 ± 0.24

the intensities of the characteristic γ rays were used to compute the reaction cross sections at different angular ranges, using Eq. (1), given in Sec. II A of this paper. The efficiency of the detector was obtained for a point source. However, the annular catchers used for trapping the reaction residues had a finite area; therefore, a proper correction [23] was applied to deduce the cross sections for the residues of interest.

III. ANALYSIS

To obtain information regarding the mechanism involved in these reactions, the comparison of measured excitation functions was performed using three computer codes: CASCADE [16], PACE2 [15], and ALICE-91 [17]. Brief details of these codes along with their important parameters, etc., are discussed in the following sections.

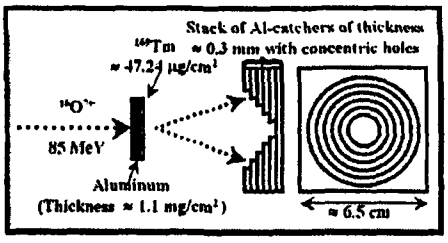

FIG. 4. Typical arrangement of target-catcher assembly used for the angular distribution measurements covering the annular range from 0–13° to 45–60°.

A. Calculations with CASCADE

The code CASCADE [16] is based on Hauser-Feshbach theory [24] and is generally used to obtain the theoretical estimates of cross sections using the CN mechanism. It does not consider the possibility of incomplete fusion (ICF) and PE emission. The main advantage of this code is that it provides the option of scaling the default parameters (i.e., fission barrier, rigid-body momentum of inertia) to obtain cross section values in the mass region of interest. The decay probabilities are

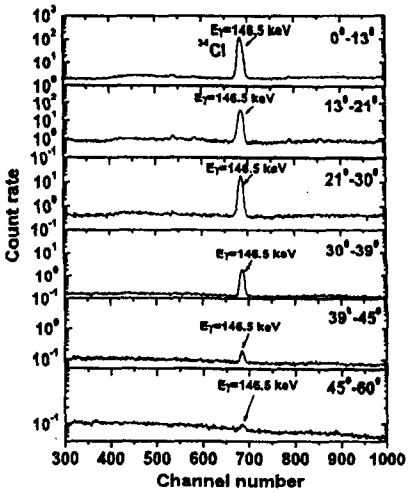

FIG. 5. Typical γ-spectra Al-catcher rings covering the annular range from 0°–13° to 45°–60°.

determined by the level densities of the daughter nuclei and the barrier penetrabilities for the various channels. The optical model potentials of Becchetti and Greenlees [25] are used for calculating the transmission coefficients for protons and neutrons, and the optical model potential of Satchler [26] is used for α particles. The Fermi gas model is used for calculating the level densities for the product nuclei.

The partial cross section for the formation of the compound nucleus of spin J and parity π from a projectile and a target nucleus of spins J_P and J_T, respectively, at center-of-mass energy E is given by [27]

$$\sigma(J,\pi) = \frac{\pi\lambda^2}{4\pi^2}\frac{(2J+1)}{(2J_P+1)(2J_T+1)}\sum_{S=|J_P-J_T|}^{J_P+J_T}\sum_{L=|J-S|}^{J+S} T_L(E), \tag{2}$$

where T_L are the transmission coefficients, which depend on the energy and the orbital angular momentum L, and $S(=J_P+J_T)$ is the channel spin.

The total fusion cross section for the maximum angular momentum L_c of the compound nucleus is given by

$$\sigma_L = \frac{\pi\lambda^2}{4\pi^2}\sum_{L=0}^{L_c}(2L+1)T_L(E). \tag{3}$$

In statistical model calculations, the critical angular momentum L_c for compound nucleus fusion may be sharp, or it may have some overlap from L_c to higher L. The effective moment of inertia I may be obtained from the low-lying states of the isotope using the relation

$$I = \frac{2}{5}mr^2, \tag{4}$$

where r is the radius of spherical nucleus given by $r_oA^{1/3}$.

The level density formula implies a yrast line,

$$E_{rot}(J) = \frac{J(J+1)\hbar^2}{2I} + \Delta, \tag{5}$$

where Δ is the pairing energy which determines the zero point of the effective excitation energy. In this code, the level density parameter constant K and the ratio of actual moment of inertia to the rigid-body moment of inertia of the excited system F_0 are the two important parameters which may be varied to match the experimental data. In HI induced reactions, the high angular momentum and excitation energy are expected to have considerable influence on the deexcitation cascade. Because in HI reactions, the increasing excitation energy also increases the angular momentum; therefore, the deformation of the nucleus due to the angular momentum effect may also be quite substantial. In calculations, the deformation effects may be included by using an angular momentum dependent moment of inertia, which results in the deviation of the yrast line from that calculated assuming the nucleus to be a rigid sphere. The level density parameter a_f at the saddle point, which may be obtained from the relation $a_f = A/D_{AF}$, where A is the mass number of the compound nucleus and D_{AF} is a free parameter, may be varied to match the experimental data. It has been observed that the parameter D_{AF} has considerable influence on calculated EFs in the higher energy region.

It may, however, be pointed out that a value of $K > 10$ may give rise to the anomalous effects in particle multiplicity [28]. In the present work, the calculations were performed consistently using the set of parameters which are widely accepted and were used in our recent publication [19]. Here, calculations have been performed taking a value of $K \approx 8$.

It may also be pointed out that the residue ^{34}Cl produced via the ^{27}Al(^{16}O, $2\alpha n$) channel has metastable as well as ground states. In the present work, the metastable state of the residue ^{34m}Cl was observed through the 146.3 keV γ ray of intensity 40.5%. Since the intensity of the ground state of the residue ^{34g}Cl is very low, the ground state of ^{34g}Cl could not be observed. The production cross sections of the residue ^{34m}Cl were converted into the total cross section of the residue ^{34}Cl by using the standard radioactive decay method. Since the code CASCADE gives the total production cross section of the residue, it is reasonable from a physics point of view to compare the total cross section of the residue ^{34}Cl with the calculations.

The experimentally measured and theoretically calculated EF for the reaction ^{27}Al(^{16}O, $2\alpha n$)^{34}Cl is shown in Fig. 6. The measured values of the cross sections for the residue ^{34}Cl by Landenbaurer-Bellis *et al.* [13], which has some contribution from the residue ^{38}Cl, are also shown. As can be seen from this figure, the measured values [13] of the cross sections of the residue ^{34}Cl have large uncertainties in the energy scale. In the present work, the energy uncertainty resulting from the finite thickness of the sample is much smaller. Furthermore, in the energy range of interest, Landenbaurer-Bellis *et al.* [13] have effectively three data points, whereas in the present work, the measurements were carried out giving 19 data points, indicating a precise measurement at a very close energy interval, as indicated in Fig. 6. As has already been mentioned, the code CASCADE does not take into account the possibility of incomplete fusion processes; therefore, the enhancement of measured cross sections as compared with the calculated EFs for the reaction ^{27}Al(^{16}O, $2\alpha n$)^{34}Cl may be attributed to the ICF process.

The experimentally measured EFs for the reactions ^{27}Al(^{16}O, $3\alpha 3p$)^{28}Mg, ^{27}Al(^{16}O, $3\alpha 3pn$)^{27}Mg, ^{27}Al(^{16}O, $4\alpha 2pn$)^{24}Na, and ^{27}Al(^{16}O, $4\alpha 3p$)^{24}Ne are shown in Figs. 7–10, where the solid curves guide the eye to

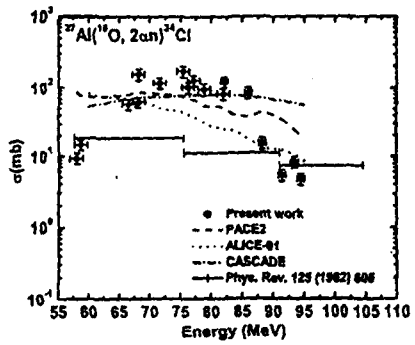

FIG. 6. Experimentally measured and theoretically calculated EFs. Literature values [13] are also shown.

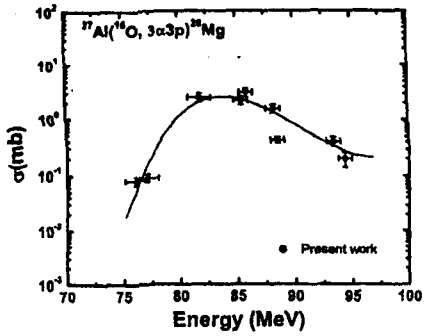

FIG. 7. Experimentally measured EFs. Solid curve guides the eye to the experimental data by curve fitting.

the experimental data by curve fitting. In Fig. 9, the literature values [13] of the cross sections of the residue ^{24}Na are also shown. On the basis of the trends of these curves, Landenbaurer-Bellis *et al.* [13] concluded that these reactions are formed by evaporation processes referred to as the compound nucleus mechanism. Landenbaurer-Bellis *et al.* [13] in their study of the $^{16}O+^{27}Al$ system did not compare the data with theoretical simulations. Since the calculated values of EFs using code CASCADE for these reactions are negligibly small, they are not shown in Figs. 7–10, thus the observed enhancement by several orders of magnitude over their negligible theoretical predictions for these channels may be attributed to the fact that these reactions are likely to be populated by some processes other than CN processes. Furthermore, to confirm whether these reactions are formed by CF or ICF processes, the angular distributions of these recoiling residues produced in the $^{16}O+^{27}Al$ system have also been measured, as discussed in Sec. IV of the paper.

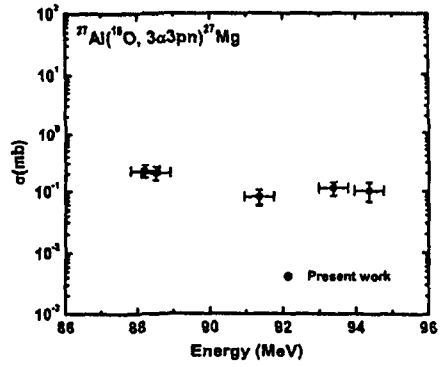

FIG. 8. Experimentally measured EFs.

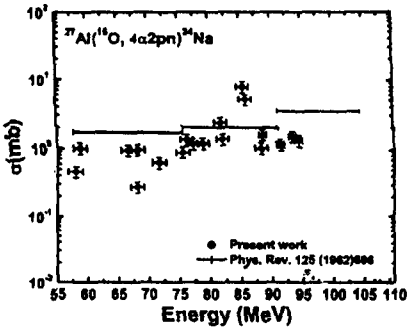

FIG. 9. Experimentally measured EFs. Literature values are also shown.

B. Calculations with PACE2

The theoretical estimate of the cross sections for the evaporation residues has also been obtained using code PACE2 [15], which is based on a statistical approach. It uses a Monte Carlo procedure to determine the decay sequence of an excited nucleus using the Hauser-Fechbach formalism. The angular momentum projections are calculated at each stage of deexcitation, which enables the determination of the angular distribution of the emitted particles. The main advantage of Monte Carlo calculations is that they provide correlations between various quantities, such as particles and γ rays or angular distribution of particles. The evaporation cross sections of the residues are calculated using the Bass formula [29]. The code provides the ability to have an event-by-event traceback of the entire decay sequence from the CN system into any one of the exit channels. The optical model parameters for neutron, proton, and α emission were taken from Perey and Perey [15]. The γ-ray strength functions for $E1$, $E2$, and $M1$ transitions were taken from tables of Endt [30]. This code has been modified to take into account the excitation energy dependence of the level density parameter using the prescription of Kataria *et al.* [31]. In this code, the level density parameter $a = A/K$ is one of the important parameters, where

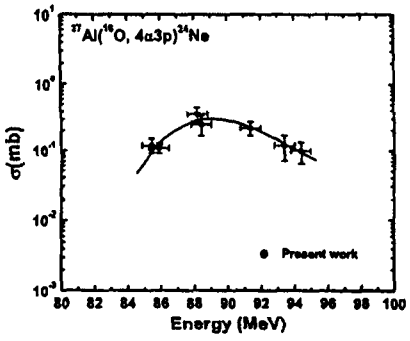

FIG. 10. Experimentally measured EFs. Solid curve guides the eye to the experimental data by curve fitting.

A is the mass number of the compound nucleus and K is a free parameter. The value of K may be varied to match the experimental data. In the present work, a value of $K = 8$ has been taken.

The theoretically calculated EFs using the code PACE2 for the reaction ^{27}Al(^{16}O, $2\alpha n$)^{34}Cl are also shown in Fig. 6 as the dashed curve. The observed enhancement of the measured EFs as compared with the theoretical calculations again indicates that the residue ^{34}Cl may not be produced only by the complete fusion process, but also by some other process such as incomplete fusion. The theoretical calculations for the reactions ^{27}Al(^{16}O, $3\alpha 3p$)^{28}Mg, ^{27}Al(^{16}O, $3\alpha 3pn$)^{27}Mg, ^{27}Al(^{16}O, $4\alpha 2pn$)^{24}Na, and ^{27}Al(^{16}O, $4\alpha 3p$)^{24}Ne give cross sections which are negligibly small, and hence no comparison of the experimental data with the simulations of this code is made in Figs. 7–10. Thus, it may be concluded that the significant contribution to these reaction channels comes from processes other than complete fusion.

C. Calculations with ALICE-91

The code ALICE-91 [17], developed by M. Blann, may be used to calculate the equilibrium as well as preequilibrium (PE) emission cross sections in light and heavy ion induced reactions. The compound nucleus calculations in this code are performed using the Weisskopf-Ewing model [32], while the PE component is simulated using the geometry-dependent hybrid model [33]. In this code, the possibility of incomplete fusion is not taken into account. The particles that could be emitted are neutron, proton, deuteron, and α particles. The code can calculate the reaction cross sections for the residual nuclei up to mass 11 and 9 a.u. away from the compound nucleus. The Myers-Swiatecki/Lysekil mass formula [34] is used for calculating Q values and binding energies of all the nuclei in the evaporation chain. The inverse reaction cross sections used in the code are calculated using the optical model [35] subroutines, although there is also an option of using the classical sharp cutoff model. The transmission coefficients are calculated using the parabolic model of Thomas [36] for heavy ions. Calculations for PE emission in this code are done assuming equipartition of energy among the initial excited particles and holes. The mean free path (MFP) for intranuclear transition rates may be calculated either from the optical model potential parameters of Becchetti and Greenlees [25] or from Pauli-corrected nucleon-nucleon cross sections [37,38]. In the present calculations, the optical potentials of Becchetti and Greenlees [25] were used.

Level densities of the residue in code ALICE-91 may be calculated either from the Fermi gas model or from the constant temperature form. The Fermi gas model gives [39]

$$\rho(U) = (U - \delta)^{-5/4} \exp[2\sqrt{a(U - \delta)}] \tag{6}$$

where δ is the pairing term and U is the excitation energy of the nucleus. The level density parameter a is taken as A/K, A being the mass number of the nucleus and K is an adjustable parameter. The level density $\rho(U)$ in constant temperature form is given as [40]

$$\rho(U) \propto \frac{1}{T}\varepsilon^{U/T}. \tag{7}$$

The differential cross section for emitting a particle with channel energy ε may be written as (cross section per unit energy to emit a particle of type ν)

$$\frac{d\sigma}{d\varepsilon_\nu} = \frac{\pi\lambda^2}{4\pi^2}\sum_{I=|0|}^{\infty}(2I+1)T_I(2S_\nu+1) \times \sum_{l=|0|}^{\infty}T^l{}_\nu(\varepsilon)\sum_{J=|I-l|}^{I+l}\rho(\varepsilon,J)/D, \ldots \tag{8}$$

where λ is the de Broglie wavelength of the incident ion, T_I the transmission coefficient of the Ith partial wave of the incident ion, $\rho(\varepsilon, J)$ the spin-dependent level density for the residual nucleus, D the integral of numerator over all particles and emission energies, and ε the excitation energy of the compound nucleus. S_ν is the intrinsic spin of the particle ν, and $T^l_\nu(\varepsilon)$ is the transmission coefficient for the particle ν with kinetic energy ε and orbital angular momentum l.

In the Weisskopf-Ewing calculations, the nuclear moment of inertia is infinite; hence there is no energy tied to rotation, thus no level density cutoff at high spin. This code does not take into account the angular momentum involved in heavy ion reactions. However, the heavy ion projectile imparts large angular momentum to the composite system having a finite moment of inertia and hence greater rotational energy. Due to nuclear rotation, a nucleus with a given angular momentum J cannot have energy below a minimum value $E_J^{\min}$, that is,

$$E_J^{\min} \approx J(J+1)\frac{\hbar^2}{2I}. \tag{9}$$

Here, I is the moment of inertia of the composite nucleus.

In this code, the level density parameter a, the MFP multiplier COST, and initial exciton number n_0 are some of the important parameters. a largely affects the equilibrium component, while n_0 and COST govern the preequilibrium component. a is calculated from $a = A/K$. In code ALICE-91, the intermediate states of the system are characterized by the excitation energy E and number n_p of excited particles and n_h of excited holes. Particles and holes are defined relative to the ground state of the nucleus and are called excitons. The initial configuration of the compound system defined by the exciton number $n_0 = (n_p + n_h)$ is an important parameter of PE formalism. In the present work, a value of $n_0 = 16$ with configuration $(8p + 8n + 0h)$ has been found to satisfactorily reproduce the experimental data, where p, n and h represent the number of excited protons, neutrons, and holes, respectively. The code ALICE-91 calculates two-body nuclear transition rates using Pauli-corrected free nucleon-nucleon scattering cross section data. The actual MFP inside the nucleus may be quite different from the one calculated using free nucleon-nucleon scattering data. To compensate for this difference, a parameter COST is provided in the code ALICE-91. A value of COST greater than zero means a smaller value of the actual MFP for nucleon-nucleon scattering inside the composite excited nucleus. In the present work, a value

of COST = 2 is found to reproduce the experimental data satisfactorily.

When ALICE-91 calculations with the above-mentioned parameter values were compared with their experimental counterparts, it was observed that the maxima of the measured EFs were at higher energies than those of the calculated EFs. This is to be expected, because in ALICE-91 calculations the angular momentum effects are not taken into account. In HI induced reactions, the incident particle imparts relatively larger angular momentum to the composite system. If, in the last stages of nuclear deexcitation, higher angular momentum inhibits particle emission more than it does γ emission, then the peak of the excitation function corresponding to the particle emission mode will be shifted to higher energies [41]. The effect is more pronounced in heavy ion reactions than in light ion reactions, since the rotational energy is much greater in HI reactions. An estimate of the possible shift due to angular momentum effects may be made from the nuclear rotational energy. For a rigid body, the rotational energy is given by $E_{rot} \approx (m/M)E_{lab}$. Here, m/M is the ratio of the projectile and target nucleus masses and E_{lab} is the incident energy [41]. Since the angular momentum effects have not been considered in the Weisskopf-Ewing calculations of the present version of the ALICE-91 code, it is desirable to shift the calculated EFs by the amount approximately equal to E_{rot} as calculated above. In the present work, the calculated EFs have been shifted by E_{rot} on the energy scale. The experimentally measured and theoretically calculated EFs for the reaction $^{27}Al(^{16}O, 2\alpha n)^{34}Cl$ are shown in Fig. 6, where the dotted curve shows the theoretical calculation done using code ALICE-91. The observed enhancement of the measured EFs compared with the theoretical calculations for the reaction $^{27}Al(^{16}O, 2\alpha n)^{34}Cl$ done by this code indicates that the residue ^{34}Cl may not be produced by complete fusion but by some other processes such as ICF. Furthermore, the measured EFs for the reactions $^{27}Al(^{16}O, 3\alpha 3p)^{28}Mg$, $^{27}Al(^{16}O, 3\alpha 3pn)^{27}Mg$, $^{27}Al(^{16}O, 4\alpha 2pn)^{24}Na$, and $^{27}Al(^{16}O, 4\alpha 3p)^{24}Ne$ are shown in Figs. 7–10. The theoretical calculations for these reactions give cross sections that are negligibly small, similar to the codes CASCADE and PACE2, while the measured EFs for these channels have substantial cross sections. As such, it may be concluded that after including PE emission, which is one of the dominant mode of reaction mechanisms in heavy ion reactions, the experimental data could not be reproduced, indicating the presence of a reaction mechanism other than CF and PE processes.

IV. ANGULAR DISTRIBUTIONS

The analysis of EFs for the presently measured reactions, as mentioned in Secs. III A–III C, clearly indicates that these reactions have significant contributions other than those of CF and ICF processes. To confirm the reaction mechanism involved, a specially designed experimental setup was used as shown in Fig. 4. In this experiment, an Al target supported by a natural thulium material of thickness $\approx$0.48 mg/cm^2 followed by a stack of thick annular concentric Al catcher foils was used. Depending on the momentum transfer from the projectile to the composite system, the residues formed by CF and ICF processes will be trapped in the concentric annular aluminum catchers at different angles. The residues that are expected to be populated by a mechanism such as a direct reaction may be stopped within the thulium layer. The measured angular distributions for the reaction $^{27}Al(^{16}O, 2\alpha n)^{34}Cl$ is shown in Fig. 11. Two peaks are observed: one around 0°–13° can be assigned to the residues populated by complete fusion, and the other peak in the angular range 45°–60° can be assigned to the residues populated by ICF processes.

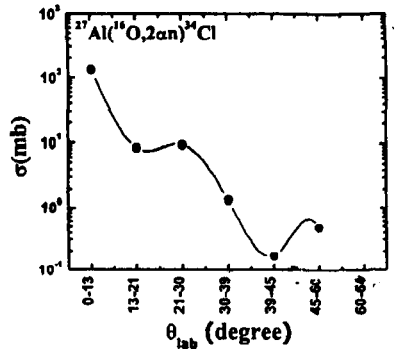

FIG. 11. Measured angular distributions for reaction $^{27}Al(^{16}O, 2\alpha n)^{34}Cl$.

Note that out of the five reactions identified in the EF measurements, only the γ ray of 146.5 keV corresponding to the reaction $^{27}Al(^{16}O, 2\alpha n)^{34}Cl$ could be identified from its energy as well as the half-life of residue ^{34}Cl in the angular distribution measurements. The residues formed by CF are likely to recoil in the forward cone, as such peaking of angular distribution around 0° indicates the population of residue ^{34}Cl via CF. However, the same residue ^{34}Cl when populated by ICF of residue ^{16}O will show peaks at much higher angles. Therefore, it may be concluded that the basic mechanism of population of ^{34}Cl may be based on both CF and ICF processes. However, the EF analysis has clearly indicated that the other reactions, i.e., $^{27}Al(^{16}O, 3\alpha 3p)^{28}Mg$, $^{27}Al(^{16}O, 3\alpha 3pn)^{27}Mg$, $^{27}Al(^{16}O, 4\alpha 2pn)^{24}Na$, and $^{27}Al(^{16}O, 4\alpha 3p)^{24}Ne$, are not likely to be populated via the CF process. The same is reflected from the angular distribution measurements, since no peak corresponding to these residues is identified in the γ-ray spectra of the angular distribution data. Thus, those residues are not likely to be populated via either complete or incomplete fusion processes. In direct reactions, the ejectile takes away a large fraction of the energy; hence, the residues formed may have ranges much smaller than those of residues formed by CF and/or ICF processes and may be trapped in the thulium layer.

V. CONCLUSIONS

Excitation functions for the reactions $^{27}Al(^{16}O, 2\alpha n)^{34}Cl$, $^{27}Al(^{16}O, 3\alpha 3p)^{28}Mg$, $^{27}Al(^{16}O, 3\alpha 3pn)^{27}Mg$, $^{27}Al(^{16}O, 4\alpha 2pn)^{24}Na$, and $^{27}Al(^{16}O, 4\alpha 3p)^{24}Ne$ produced in the $^{16}O+^{27}Al$ system have been measured in the energy range

≈58–94 MeV. Theoretical calculations based on three different computer codes have been carried out using well-accepted parameters. The codes PACE2 and CASCADE used in the present work are based on Hauser-Feshbach theory for compound nucleus calculations; however, the code ALICE-91 is based on the Weisskopf-Ewing model for compound nucleus calculations and the geometry-dependent hybrid model for simulating preequilibrium emission. Though preequilibrium emission may have considerable influence on the measured cross sections at relatively higher energies, even the ALICE-91 calculations which include preequilibrium emission are not found to reproduce the experimental data. The present analysis indicates that the residues ^{27,28}Mg, ^{24}Na, and ^{24}Ne are not populated either via complete or incomplete fusion processes, because theoretical calculations based on all these codes give negligible value of cross sections for their production. At present, we have no satisfactory explanation for the observed high cross sections for these channels; however, Landenbaurer-Bellis *et al.* [13] have attributed their production to a direct reaction mechanism. From the study of the angular distributions of these residues, we have concluded that in the case of complete fusion, the residues are emitted in the forward cone along the beam direction; while for incomplete fusion, the recoiling residues emerge at relatively large angles with respect to the beam direction, as expected. As such, angular distributions of residues with respect to the beam direction may also provide complementary information about the complete and incomplete fusion processes. The analysis of angular distribution data has clearly indicated the significant contribution of the ICF process in the ^{27}Al(^{16}O, $2\alpha n$)^{34}Cl reaction.

ACKNOWLEDGMENTS

The authors are thankful to the Director, NSC, New Delhi, for extending all the facilities for carrying out the experiment. We are also thankful to Dr. R. K. Bhaumik, for all his support during the experiment. We also thank the Chairman, Department of Physics, AMU for providing all the necessary facilities. One of the authors (MKS) thanks the Department of Science and Technology, New Delhi, for providing financial support through Project No. SR/FTP/PS-46/2003.

[1] M. Blann, Nucl. Phys. **A235**, 211 (1974).
[2] M. Blann, Annu. Rev. Nucl. Sci. **25**, 123 (1975).
[3] P. E. Hodgson, *Nuclear Heavy Ion Reactions* (Clarendon, Oxford, 1978).
[4] P. Vergani, E. Gadioli, E. Vaciago, E. Fabrici, E. Gadioli Erba, M Galmarini, G. Ciavola, and C. Marchetta, Phys. Rev. C **48**, 1815 (1993).
[5] M. Crippa, E. Gadioli, P. Vergani, G. Ciavola, C. Marchetta, and M. Bonardi, Z. Phys. A **350**, 121 (1994).
[6] M. Cavinato, E. Fabrici, E. Gadioli, E. Gadioli Erba, P. Vergani, M. Crippa, G. Colombo, I. Redaelli, and M. Ripamonti, Phys. Rev. C **52**, 2577 (1995).
[7] I. Tserruya *et al.*, Phys. Rev. Lett. **60**, 14 (1988).
[8] D. J. Parker, J. Asher, T. W. Conlon, and N. Naqib, Phys. Rev. C **30**, 143 (1984).
[9] D. J. Parker, J. J. Hogan, and J. Asher, Phys. Rev. C **35**, 161 (1987).
[10] Manoj Kumar Sharma, Ph.D. thesis, Aligarh Muslim University, 2002.
[11] J. Wilczynaski, K. Siwek-Wilczynaski, J. VanDriel, S. Gonggrip, D. C. J. M. Hangeman, R. V. F. Janssens, J. Lukasiak, R. H. Siemssen, and S. Y. Van der Werf, Nucl. Phys. **A373**, 109 (1982).
[12] S. Chakrborty, B. S. Tomar, A. Goswami, S. K. G. K. Gubbi, S. B. Manohar, Anil Sharma, B. B. Kumar, and S. Mukherjee, Nucl. Phys. **A678**, 355 (2000).
[13] Inge-Maria Ladenbaurer-Bellis, Ivor L. Preiss, and C. E. Anderson, Phys. Rev. **125**, 606 (1962).
[14] P. McKenna *et al.*, Phys. Rev. Lett. **91**, 075006 (2003).
[15] A. Gavron, Phys. Rev. C **21**, 230 (1980).
[16] F. Puhlhofer, Nucl. Phys. **A280**, 267 (1977).
[17] M. Blann, NEA Data Bank, Gif-sur-Yvette, France, Report PSR-146, 1991 (unpublished).
[18] M. K. Sharma, Unnati, B. K. Sharma, B. P. Singh, H. D. Bhardwaj, R. Kumar, K. S. Golda, and R. Prasad, Phys. Rev. C **70**, 044606 (2004).
[19] M. K. Sharma, Unnati, B. P. Singh, H. D. Bhardwaj, R. Kumar, K. S. Golda, and R. Prasad, Nucl. Phys. **A776**, 83 (2006).
[20] FREEDOM, Data acquisition and analysis system designed to support the accelerator-based experiments at the Nuclear Science Centre, New Delhi, India.
[21] E. Browne and R. B. Firestone, *Table of Radioactive Isotopes* (John Wiley & Sons, New York, 1986).
[22] M. K. Sharma, B. P. Singh, S. Gupta, M. M. Muthafa, H. D. Bhardwaj, and R. Prasad, J. Phys. Soc. Jpn. **72**, 1917 (2003).
[23] R. P. Gardner and K. Verghese, Nucl. Instrum. Methods **93**, 163 (1971).
[24] W. Hauser and H. Feshbach, Phys. Rev. **87**, 336 (1952).
[25] F. D. Becchetti and G. W. Greenlees, Phys. Rev. **182**, 1190 (1969).
[26] G. R. Satchler, Nucl. Phys. **70**, 177 (1965).
[27] J. M. Blatt and V. F. Weisskopf, *Theoretical Nuclear Physics* (John Wiley & Sons, New York, 1952).
[28] J. P. Lestone, Phys. Rev. C **53**, 2014 (1996).
[29] R. Bass, Nucl. Phys. **A231**, 45 (1974).
[30] P. M. Endt, At. Data Nucl. Data Tables **26**, 47 (1981).
[31] S. K. Kataria, V. S. Ramamurthy, and S. K. Kapoor, Phys. Rev. C **18**, 549 (1978).
[32] V. F. Weisskopf and D. H. Ewing, Phys. Rev. **57**, 472 (1940).
[33] M. Blann, Phys. Rev. Lett. **27**, 337 (1971).
[34] W. D. Myers and W. J. Swiatecki, Ark. Fys. **36**, 343 (1967).
[35] M. Blann, Phys. Rev. C **21**, 1770 (1980).
[36] T. D. Thomas, Nucl. Phys. **53**, 577 (1964).
[37] K. Kikuchi and M. Kawai, *Nuclear Matter and Nuclear Reactions* (North-Holland, Amsterdam, 1968).
[38] M. Blann, Nucl. Phys. **A213**, 570 (1973).
[39] M. Blann and H. Vonach, Phys. Rev. C **28**, 1475 (1983).
[40] M. Blann, G. Reffo, and F. Fabbri, Nucl. Instrum. Methods A **265**, 490 (1988).
[41] D. Bodansky, Annu. Rev. Nucl. Sci. **12**, 79 (1962).

Energy dependence of in-complete fusion processes in $^{16}O+^{181}Ta$ system: Measurement and analysis of forward recoil range distributions at $E_{lab} \leq 7$ MeV/A.

Devendra P. Singh[1],* Unnati[1], Pushpendra P. Singh[2], Abhishek Yadav[1], Manoj Kumar Sharma[3], B. P. Singh[1],† K. S. Golda[4], Rakesh Kumar[4], A. K. Sinha[5], and R. Prasad[1]
[1]*Department of Physics, Aligarh Muslim University, Aligarh (UP)-202 002, India*
[2]*INFN-Laboratori Nazionali di Legnaro, I-35020 Legnaro, ITALY*
[3]*Department of Physics, S. V. College, Aligarh (UP)-202 001, India*
[4]*Inter-University Accelerator Center, Aruna Asaf Ali Marg, New Delhi -110 067, India and*
[5]*UGC-DAE-CSR, Bidhan Nagar, Kolkata -700 098, India*
(Dated: January 1, 2010)

In order to study the energy dependence of in-complete fusion processes, the recoil range distributions for the reactions; ^{181}Ta(^{16}O, xn), ^{181}Ta(^{16}O, pxn), ^{181}Ta(^{16}O, αn), ^{181}Ta(^{16}O, α2n), ^{181}Ta(^{16}O, α3n) and ^{181}Ta(^{16}O, 2α3n), have been measured at ≈81, 90 & 96 MeV beam energies. The disentanglement of the complete and in-complete fusion processes have been done in terms of full and partial linear momentum transfer from the projectile to the target nucleus. The measurements have been done using recoil catcher technique. The experimentally measured forward recoil range distributions have been interpreted in terms of break-up fusion model. Detailed analysis of the data indicates that in-complete fusion processes have significant contribution at energies as low as ≈5 MeV/nucleon and their contribution is found to increase with energy.

PACS numbers: 25.70. Jj., 25.70. Gh.

I. INTRODUCTION

The study of the dynamics of heavy ion (HI) collisions involving asymmetric nuclei at energies around the Coulomb barrier (CB) has been a topic of interest in recent years. In recent experiments[1–5] heavy residues populated by complete fusion (CF) with full momentum transfer and due to in-complete fusion (ICF) with partial momentum transfer have been identified. Each of these processes leads to the characteristic velocity distribution of the reaction products. As such, the measured yield of a particular isotope as a function of velocity or rather the range of residues in a stopping medium helps to identify the origin of the observed reaction products. The in-complete momentum transfer events referred to as in-complete fusion (ICF) reactions[6, 7] can be understood on the basis of disappearance of pocket in the one-dimensional inter-nuclear potential energy as the angular momentum increases. In order to reduce the effective angular momentum of the composite nucleus (CN) and to restore a pocket in the inter-nuclear potential energy, as the entrance channel angular momentum is increased, an increasing factor of the projectile may escape and carries away some of the angular momentum. Since, a portion of the projectile is not captured by the target, there is a deficit in the linear momentum of CN, when compared with the projectile momentum. An in-complete linear momentum transfer (LMT) event may be observed directly from the measurement of the velocity/range distribution[8–10] of the residues. The model of Siwek-Wilczynska[6, 11] assumes that the maximum angular momentum (ℓ_{crit}), associated with complete LMT, is given by the disappearance of pocket in the one-dimensional inter-nuclear potential energy and does not take into account angular momentum dissipation in the entrance channel. Due to the localization of this process in ℓ-space, there is a strong co-relation between the captured mass and the angular momentum/excitation energy of the heavy residue. This prediction lay at the root of the angular momentum dependence of the ICF reactions[11].

Though, the ICF reactions have been extensively studied[12–14], nevertheless, no clear picture of the reaction dynamics has followed. With a view to understand various ICF processes, a variety of dynamical models/theories, like the Break-up Fusion (BUF) model[15], Hot-Spot model[16], Promptly Emitted Particle (PEP) model[17–20], the EXCITON model[21], SUMRULE model[22] etc., have been proposed to explain ICF reaction dynamics. It may be pointed out that, though, these models predict the ICF reaction cross-section at E ≥10 MeV/nucleon, but none of these models is suitable to predict the ICF processes at energies ≈5-7 MeV/nucleon. At present, it is well recognized [1, 23–27] that the ICF reactions begin with the CF reactions at moderate energies. Some of the recent studies[28–32] showed the onset of ICF processes just above the CB. Several extensive studies [4, 23, 29–39] based on excitation function (EF) and recoil range distribution (RRD) measurements are available. However, the energy dependence of ICF reactions is still lacking. In the present work, to understand the ICF reaction dynamics and to study its energy dependence, the RRDs of the CF and ICF products in ^{16}O+^{181}Ta system at the beam energies

*Electronic address: dpsingh19@gmail.com
†Electronic address: bpsinghamu@gmail.com

≈ 81, 90 & 96 MeV have been measured. The present work is in continuation to our recent investigation[40] on the same system, where the measurement and analysis of excitation functions has been used to investigate the role of break-up processes. A detailed description of the experimental set-up etc., is already presented[40], however, for the sake of completeness a brief description of the experimental methodology is given in section II. The details of the measurement of RRDs are described in section III and finally the conclusions drawn from this study are presented in section IV.

II. EXPERIMENTAL DETAILS

The experiments have been performed, using energetic $^{16}O^{7+}$ ion beams delivered from the 15UD-Pelletron accelerator of the Inter-University Accelerator Center (IUAC), New Delhi, India. Although, the methodological details are somewhat similar to those already given in our earlier works[32, 40], however, for quick reference, a brief description of sample preparation, irradiations, post-irradiation analysis etc., is given here.

In the present work, the isotopically pure sample of ^{181}Ta (abundance =100%) of thickness ≈150 μg/cm^2 has been deposited by the electro-deposition technique on Al-foils of thickness ≈1.1-1.5 mg/cm^2. The thicknesses of the samples have been determined by the α-transmission method. The samples have been pasted on rectangular Al-holders having concentric holes of 1.0 cm diameter. The irradiations have been performed using an $^{16}O^{7+}$ beam in the General Purpose Scattering Chamber (GPSC) which has an invacuum transfer facility (ITF). In each irradiation, stacks of thin Al-catcher foils (with the total thickness sufficient to stop CN formed via full LMT) have been placed just after the target, so that the heavy (slow) residues populated via CF and/or ICF could be trapped at various catcher foil thicknesses. The target, ^{181}Ta has been mounted in such a way that the Al-backing first faces the beam so that the recoiling nuclei, if any, of very short range, does not stop in the target thickness itself. The beam energies provided by accelerator, in three separate irradiations were 85, 94 & 100 MeV, so that after an energy loss of ≈ 3.7, 3.9 & 3.5 MeV in the target backing, the incident energies on the targets are estimated to be respectively 81.3, 90.1 & 96.5 MeV. The irradiations have been carried out for the duration of ≈12 h, with a beam current ≈7 pnA.

After irradiation, the stacks of the samples as well as Al-catchers were taken out of GPSC using an ITF. The activities produced in each Al-catcher foil of the stacks were counted separately using a high purity germanium (HPGe) spectrometer of 100 c.c. active volume coupled with the CAMAC-based FREEDOM[41] software. The spectrometer was pre-calibrated both for energy and efficiency using standard γ-sources like ^{60}Co and ^{152}Eu. The resolution of the γ-spectrometer was found to be ≈2 keV, for 1.33 MeV γ-ray of ^{60}Co source, during the counting of the samples. A list of the radio-nuclides populated in ^{16}O+^{181}Ta system, the energy of identified γ-rays used for the decay-curve analysis along with their branching ratios are given in our earlier work on the same system[40]. The evaporation residues (ERs) populated via CF and/or ICF are supposed to be trapped at different catcher foil thicknesses, depending on the recoil velocity and/or the degree of LMT of projectile associated with the mode of formation. The γ-ray spectra of each foil have been recorded at increasing times so that the decay curve analysis can be done to verify the half-lives and identification of the residues. The measured half-lives of the residues were found to be in good agreement with the literature values[42]. A FORTRAN program EXPSIGMA based on the standard formulation[43] has been used for the determination of the production yield of evaporation residues in different catcher foils.

In the present work, the production probabilities of ^{194}Tl(3n), ^{193}Tl^g(4n), ^{192}Tl(5n), ^{193}Hg^{g,m}(p3n), ^{192}Hg(p4n), ^{191}Hg^{g,m}(p5n), ^{192}Au^g(αn), ^{191}Au^g(α2n), ^{190}Au^g(α3n) and ^{186}Ir^g(2α3n) nuclides produced in the ^{16}O+^{181}Ta system have been measured at different catcher foil thicknesses to estimate the RRDs. In general, a residue populated via a specific channel, often emits several γ-rays of different energies. The cross-section for a channel has been determined from the measured intensities of several characteristic γ-rays and the final value is taken as the weighted average of cross-sections obtained for these γ-rays[44]. The production yield of different reaction products have been deduced by normalizing the experimentally measured production cross-sections with the respective catcher foil thicknesses. In order to generate RRDs, the normalized yield of a individual reaction product has been plotted as a function of cumulative catcher foil thicknesses. The sources of uncertainty are already described in Ref.[40].

III. ANALYSIS OF FORWARD RECOIL RANGE DISTRIBUTIONS

The degree of the linear momentum transfer (ρ_{LMT}) from the projectile to the target nucleus is the basis of recoil velocity of the reaction products, which may be used to differentiate the CF and ICF processes. As already mentioned, ρ_{LMT} is proportional to the fused mass of the projectile, i.e., maximum LMT gives rise to maximum recoil velocity to the reaction product. In the CF process, the maximum ρ_{LMT} from the projectile to the target nucleus is expected. For a given entrance channel the CN has pre-determined mass, energy and linear momentum. In case of ICF, partial ρ_{LMT} leads

TABLE I: Experimentally measured forward recoil ranges $R_{p(exp)}$ deduced from RRD curves, and theoretically calculated most probable mean ranges $R_{p(the)}$ for CF components at ≈ 81, 90 & 96 MeV, using the range energy relation[45] for the reaction products produced in the interaction of ^{16}O with ^{181}Ta.

Residues	Energy (E)≈ 81 MeV		Energy (E)≈ 90 MeV		Energy (E)≈ 96 MeV	
	$R_{p(exp)}$ ($\mu g/cm^2$)	$R_{p(the)}$ ($\mu g/cm^2$)	$R_{p(exp)}$ ($\mu g/cm^2$)	$R_{p(the)}$ ($\mu g/cm^2$)	$R_{p(exp)}$ ($\mu g/cm^2$)	$R_{p(the)}$ ($\mu g/cm^2$)
^{194}Tl(3n)	265±76	267	275±47	287	286±48	298
^{193}Tl^g(4n)	260±77	267	254±39	287	286±67	298
^{192}Tl(5n)	244±58	267	255±21	287	264±75	298
^{193}Hg^g(p3n)	261±82	267	257±75	287	290±52	298
^{193}Hg^m(p3n)	275±75	267	270±60	287	292±51	298
^{192}Hg(p4n)	252±61	267	282±57	287	291±80	298
^{191}Hg^g(p5n)	276±47	267	256±47	287	277±50	298
^{191}Hg^m(p5n)	249±53	267	230±65	287	287±69	298

TABLE II: Experimentally measured $R_{p(exp)}$ deduced from RRD curves and theoretically calculated $R_{p(the)}$ for ICF components at ≈ 81, 90 & 96 MeV

Residues	$R_{p(exp)}\mu g/cm^2$ (CF of ^{16}O)	$R_{p(the)}\mu g/cm^2$ (CF of ^{16}O)	$R_{p(exp)}\mu g/cm^2$ (ICF of ^{12}C)	$R_{p(the)}\mu g/cm^2$ (ICF of ^{12}C)	$R_{p(exp)}\mu g/cm^2$ (ICF of ^{8}Be)	$R_{p(the)}\mu g/cm^2$ (ICF of ^{8}Be)
Energy (E)≈ 81 MeV						
^{192}Au^g(αn)	275±60	267	145±37	198	-	-
^{191}Au^g(α2n)	256±48	267	165±27	198	-	-
^{190}Au^g(α3n)	282±50	267	181±22	198	-	-
^{186}Ir^g(2α3n)	258±38	267	183±13	198	100±27	108
Energy (E)≈ 90 MeV						
^{192}Au^g(αn)	256±37	287	168±20	215	-	-
^{191}Au^g(α2n)	281±43	287	170±37	215	-	-
^{190}Au^g(α3n)	282±35	287	196±25	215	-	-
^{186}Ir^g(2α3n)	262±40	287	166±27	215	70±21	117
Energy (E)≈ 96 MeV						
^{192}Au^g(αn)	290±47	298	200±35	227	-	-
^{191}Au^g(α2n)	294±45	298	204±43	227	-	-
^{190}Au^g(α3n)	286±51	298	213±35	227	-	-
^{186}Ir^g(2α3n)	290±50	298	213±23	227	121±21	122

to the formation of an in-completely fused composite system in excited state. For an in-completely fused composite system, the following quantities viz., mass, energy and momenta of CN may not have unique values. This may be because of the fluctuations in the fused mass from the projectile to the target nucleus. The experimentally measured forward recoil ranges of final reaction products in the stopping medium may give an indication of the ρ_{LMT} involved. As such, the radionuclides populated via a lower degree of LMT, show relatively smaller depth (momentum transfer component) in the stopping medium as compared to the entire LMT populations. For a different ρ_{LMT}, the residues may have different recoil ranges in the stopping medium. Therefore, the forward recoil range distributions may be used as a probe to investigate the partial fusion of the projectile in ICF processes. The normalized yields of different reaction products have been generated for the residues viz., ^{194}Tl, ^{193}Tl, ^{192}Tl, ^{193}Hg^g, ^{193}Hg^m, ^{192}Hg, ^{191}Hg^g, ^{191}Hg^m, ^{192}Au^g, ^{191}Au^g, ^{190}Au^g and ^{186}Ir^g and plotted as a function of cummulative catcher thickness. However, as representative cases to show different ρ_{LMT} components in various CF and ICF processes the RRDs for ^{192}Hg(p4n), ^{191}Au^g(α2n) and ^{186}Ir^g(2α3n) residues have been presented in Figs. 1-3, at three different beam energies each. The size of the circles, in Figs.1-3, includes the uncertainty in the yield values. As can be seen from these figures, the measured RRDs clearly indicate the different momentum transfer components, depending on the fused mass of the projectile with the target nucleus.

In case of p4n channel (Fig.1), the measured RRDs show only a single peak, at all the three bombarding energies, indicating only single linear momentum transfer component (a characteristic of CF process) involved in the production of ^{192}Hg. A close observation of the range distribution of ^{192}Hg (Fig. 1) reveals that FRRDs peaks at relatively higher cumulative catcher thickness as the beam energy increases. It is simply because the LMT increases with beam energy. Further, it may be pointed out that, the neutron emission from the recoiling

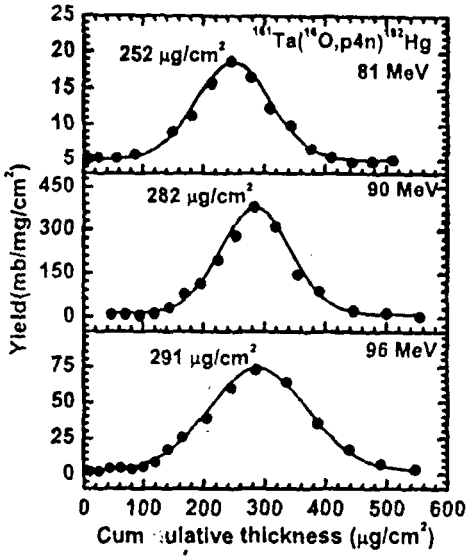

FIG. 1: Experimentally measured forward recoil range distributions for ^{192}Hg(p4n) at projectile energies at ≈ 81, 90 & 96 MeV.

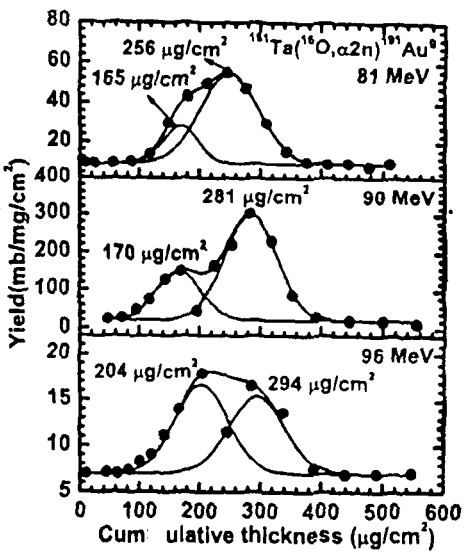

FIG. 2: (Color online) Experimentally measured forward recoil range distributions for ^{191g}Au(α2n) at projectile energies ≈ 81, 90 & 96 MeV.

nuclei may change the energy/momentum of the recoiling nucleus, depending on their direction of emission. This may be reflected in the width (FWHM) of the experimentally measured recoil range distributions. The width may also arise due to the contribution from straggling effects. The identified reaction products and their experimentally measured most probable FRRDs, $R_{p(exp)}$, for all the CF residues along with the theoretically estimated (using the code SRIM[45]) mean ranges $R_{p(the)}$, are given in Table I. The most probable recoil ranges have been theoretically calculated, assuming that; in case of CF, the incoming ion completely fuses with the target nucleus and transfers its total linear momentum to the fused system, which recoils, in order to conserve the input linear momentum. On the basis of above description, it may be mentioned that the population of reaction products ^{192}Hg populated via p4n channel is associated with the entire LMT from projectile to the target nucleus, and may be represented as;

$$^{16}O + ^{181}Ta \longrightarrow ^{197}Tl^* \longrightarrow ^{192}Hg + p4n$$

In the similar fashion, the RRDs for the residues ^{194}Tl, ^{193}Tl, ^{192}Tl, ^{193}Hg^g, ^{193}Hg^m, ^{191}Hg^g and ^{191}Hg^m are found to have single peak associated with complete linear momentum transfer from projectile to the composite nucleus, indicating their production via CF process only.

Further, in case of reaction channels (αn), (α2n) and (α3n) where, the residues ^{192}Au^g, ^{191}Au^g and ^{190}Au^g are populated, each of the FRRDs are found to have two peak structure. The observed FRRDs were resolved into two peaks, with Gaussion peak fitting option of ORIGIN software, one corresponding to the complete momentum transfer events and the other corresponding to the fusion of ^{12}C (if ^{16}O breaks into ^{12}C + α; and ^{12}C fuses) with ^{181}Ta. As a representative case, the FRRDs for the residues, ^{191}Au^g have been plotted at three different energies and are shown in Fig. 2. As can be seen from this figure, the FRRDs in this case may be resolved into two Gaussian peaks (also in case of all other αxn channels), indicating the presence of more than one linear momentum transfer components, one associated with the fusion of ^{16}O and the other due to the fusion of ^{12}C. From Fig.2, it may be observed that for the residues ^{191}Au^g, there are two linear momentum transfer components one having mean ranges at 256±38, 281±43 & 294±45 μg/cm^2 at ≈ 81, 90 & 96 MeV beam energies (indicating fusion of ^{16}O) and at 165±26, 170±25 & 204±30 μg/cm^2 (indicating fusion of ^{12}C) at the respective three energies. It may also be observed from the Fig. 2, that the peak value of the ranges i.e., $R_{p(exp)}$ shifts towards higher cumulative catcher

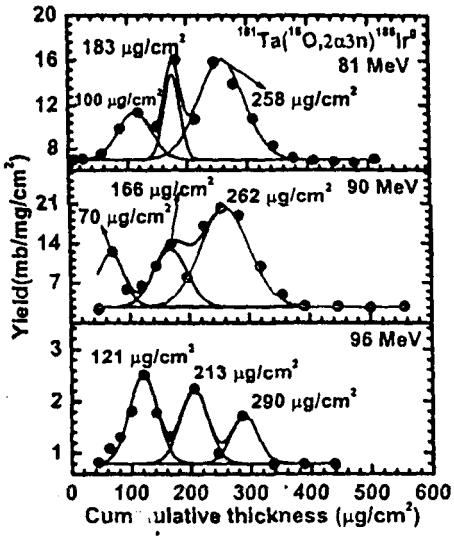

FIG. 3: (Color online) Experimentally measured forward recoil range distributions for ^{186g}Ir(2α3n) at projectile energies ≈ 81, 90 & 96 MeV.

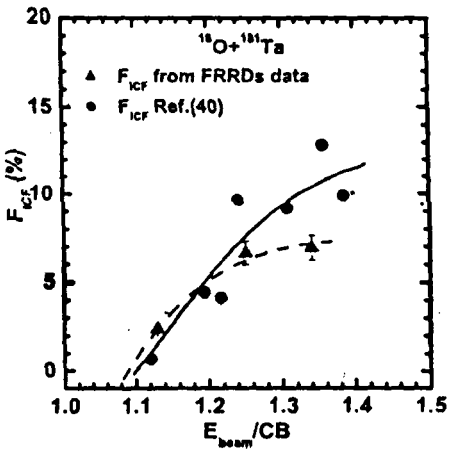

FIG. 4: (Color online) The percentage in-complete fusion fraction (F_{ICF}) deduced from the analysis of forward recoil range distributions as a function of normalized projectile energy. Data shown by triangle is obtained from the analysis of EFs[40].

thickness as the beam energy increases, as expected. It can be inferred that the residues ^{191}Au^g populated through ^{181}Ta(^{16}O, α2n) channel have the contributions from both the processes viz., CF and ICF. The residues ^{191}Au^g may be populated via CF and/or ICF channels i.e., via,

(a) Complete fusion of ^{16}O as;

$$^{16}O + ^{181}Ta \Longrightarrow ^{197}Tl^* \Longrightarrow ^{191}Au^{g*} + \alpha + 2n;$$

(b) In-complete fusion of ^{16}O as;

$$^{16}O(^{12}C+\alpha) + ^{181}Ta \Longrightarrow ^{193}Au^* + \alpha \quad \text{(spectator)}$$
$$^{193}Au^* \Longrightarrow ^{191}Au^g + 2n$$

The measured ranges for the channels (αn), (α2n) and (α3n) via CF and ICF processes as mentioned above are presented in Table II, and are found to agree reasonably well with those calculated using code SRIM, on the basis of break-up fusion model. In these calculations, it is assumed that no energy is lost during the break-up of the incident ion. In these reactions α-particle essentially act as spectator during the reaction, so that linear momentum transfer of the residue is reduced to 3/4 of the CN value. Similarly, it may also be assumed that ^{16}O may break into 4 α fragments, two α-particles may fuse with the target nucleus and the remaining two may escape without any interaction. One such case has been observed in the present work where ^{186}Ir^g($T_{1/2}$ =16.64 hrs), residues are produced via 2α3n channel. The measured FRRDs for residues ^{186}Ir^g is shown in Fig.3. As can be seen from this figure, the FRRDs may be resolved clearly into three Gaussian peaks, indicating the presence of more than one linear momentum transfer components associated with the CF of ^{16}O and ICF of ^{12}C and ^{8}Be. From this figure, it may be resolved that for the population of ^{186}Ir^g residues, at the energies of interest, may take place via all the three linear momentum transfer components. The peaks at ranges 258±38, 262±40 & 290±44 μg/cm^2 at ≈ 81, 90 & 96 MeV energies, respectively, may be attributed to the fusion of ^{16}O. The ranges at 183±27, 166±25 & 213±30 μg/cm^2 (fusion of ^{12}C) and 100±15, 70±10 & 121±18 μg/cm^2 (fusion of ^{8}Be) at the respective energies have also been observed. As such, it can be inferred that the residues ^{186}Ir^g produced through ^{181}Ta(^{16}O, 2α3n) reaction channel have the contribution from both the processes namely, CF as well as ICF, which may be represented as due to;

(a) Complete fusion of ^{16}O i.e.,

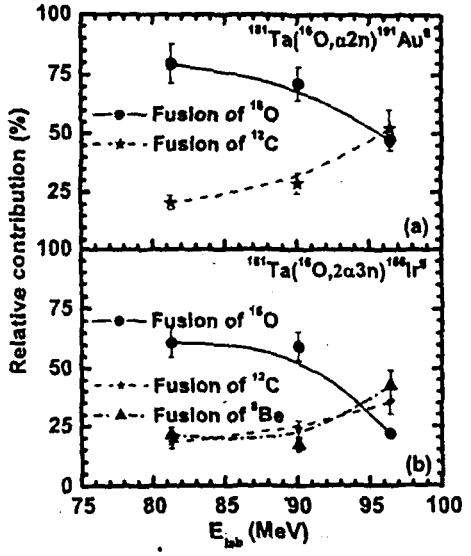

FIG. 5: (Color online) Relative strengths of the contributions coming from CF and ICF of ^{16}O with ^{181}Ta at projectile energies ≈ 81, 90 & 96 MeV for the production of residues ^{191g}Au(α2n) & ^{186g}Ir(2α3n). The lines joining data points are just to guide the eyes.

$$^{16}O + ^{181}Ta \Longrightarrow {}^{197}Tl^* \Longrightarrow {}^{186}Ir^{g*} + 2\alpha + 3n;$$

(b) In-complete fusion of ^{16}O i.e.,

$$^{16}O(^{12}C+\alpha) + {}^{181}Ta \Longrightarrow {}^{193}Au^* + \alpha + 3n \quad \text{(spectator)}$$

(c) In-complete fusion of ^{16}O i.e.,

$$^{16}O(^{8}Be+{}^{8}Be) + {}^{181}Ta \Longrightarrow {}^{189}Ir^* + 2\alpha \quad \text{(spectator)}$$

$$^{189}Ir^* \Longrightarrow {}^{186}Ir^g + 3n$$

In case of ICF, it is assumed that, the incident ^{16}O ion breaks into fragments (e.g., ^{12}C & α or ^{8}Be & ^{8}Be), as it enters in the nuclear field of target nucleus. The fragments so produced are assumed to move with the velocity of the incident ion. One of the fragments (^{12}C or ^{8}Be or α) fuses with the target nucleus forming a composite system, which recoils in the forward direction to conserve the input linear momentum. It may be pointed out that the events due to fusion of single α-particles have not been observed in the present work.

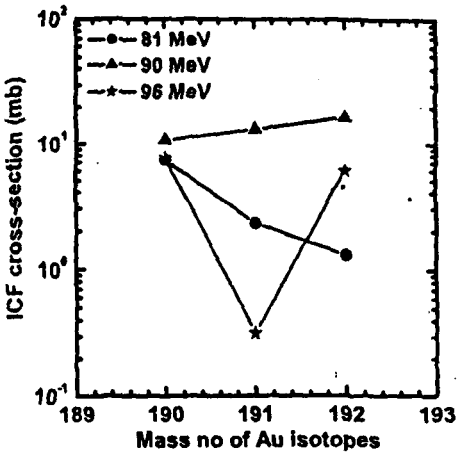

FIG. 6: (Color online) ICF contribution of different Au isotopes produced in ^{16}O+^{181}Ta system at projectile energies ≈ 81, 90 & 96 MeV. The lines joining data points are just to guide the eyes.

In order to study the energy dependence of CF (full LMT) and ICF (partial LMT) components, percentage relative contributions[32] of the CF and ICF components are deduced using the relation,

$$F_{ICF} = \frac{\Sigma\sigma_{ICF}}{\Sigma\sigma_{CF} + \Sigma\sigma_{ICF}} \times 100 \qquad (1)$$

where, $\Sigma\sigma_{CF}$ and $\Sigma\sigma_{ICF}$ are the sum of cross sections (for all the measured xn, pxn, αxn and 2αxn channels obtained from the analysis of FRRDs) of CF and ICF processes, respectively.

The relative contribution of CF and ICF in the production of a particular reaction product may be computed by fitting the experimentally measured RRDs with Gaussian peaks using the ORIGIN software. The yield curves of evaporation residues obtained from RRDs are assumed to be Gaussian in nature and may be given as;

$$Y = Y_0 + \frac{A}{\sqrt{2\pi\omega_A^2}} e^{-(R-R_P)^2/2\pi\omega_A^2} \qquad (2)$$

where, R_P is the most probable mean range, ω_A is the width parameter (FWHM) of the RRD, and A is the area under the peak.

The value of the χ^2 was minimized in the present analysis using a non-linear least-square fit routine,

keeping the width (ω_A) as free parameter and most probable mean range (R_P) has been kept at the peak position from the RRD data. As such, only the width remains as a free parameter. Moreover, as indicated in Figs.2-3, the residues show more than one RRD component. In such cases, the experimentally measured normalized yields have been fitted using the multi-peak option in a similar way as mentioned above. It may, however, be pointed out that choosing the width of Gaussian peak as a free parameter may influence the relative contributions derived from the figures. In the present work the minimization of χ^2 and selected values of FWHM for the peak in complex RRD data were found to fit the experimental data satisfactorily. In the present work an attempt has been made to disentangle the CF and ICF contributions by fitting the FRRD with Gaussian constrained at a range expected for full momentum transfer to estimate their relative contributions. The percentage ICF contributions of different fusion components have been obtained by dividing the area under the ICF peak of the corresponding fusion component by the total area associated with the experimental data employing equation (1). The values of F_{ICF} deduced from ICF data are plotted as a function of normalized beam energy (E_{beam}/CB) in Fig.4. As can be seen from this figure that the ICF fraction increases with energy rapidly at lower energies, however, at relatively higher energies the F_{ICF} seems to move towards saturation. Further, extrapolation of the curve in the lower energy region clearly indicates the onset of ICF processes even at energies very close to CB i.e., from $\approx$ 5 % above CB. It may be pointed out here that the F_{ICF} given in Fig. 4, presents the lower limit of in-complete fusion contributions as several other ICF channels could not be measured due to their short half-lives, and/or low intensity γ-lines of the residues. It may not be out of place to mention that similar observations of ICF contributions increasing with energy and mass asymmetry have been obtained in several papers[9] by Morgenstern et. al. However, their work involved measuring the velocity spectra employing time of flight method in lighter systems and also at relatively higher energies $\approx$10-25 MeV/n.

Further, to understand the variation of CF and ICF contribution with energy in the individual reaction channels, the relative percentage contribution for CF and ICF processes for α2n and 2α3n are plotted as a function of laboratory beam energy as representative sets. As can be seen from Figs. 5(a & b), that as the energy increases, the CF contribution goes on decreasing. However, ICF contribution (fusion of ^{12}C) increases with energy. Further, the contribution due to the fusion of ^{8}Be, observed in case of 2α3n channel also increases having almost similar percentage contribution as that for ^{12}C fusion. From Figs 5(a & b), it may be observed that the relative ICF contribution for an individual channel may be as large as $\approx$50% at 96 MeV, however, the overall ICF contribution at this energy is around 7% only (Fig. 4). Moreover, as already mentioned, the RRDs for the residues ^{192,191,190}Au^g and ^{186}Ir^g also show peaks corresponding to the ICF of ^{12}C and/or ^{8}Be. The experimental ICF contributions for these residues could not be compared with theoretical values as there is no satisfactory model which can give ICF contributions. Following our previous work we relate the R_P(exp) to the degree of LMT or mean evaporation residue velocity, by adopting the allowance for variation of upto $\approx$ 10 % in the FWHM of FRRDs. It may be noted that de-convolution of complex range distribution of heavy residues into various ICF components due to FWHM variation is likely to affect the relative contribution by $\leq$ 10 %. Further, Fig. 6 shows the ICF contributions of different Au isotopes at three different projectile energies. It may be observed from this figure that the production of ^{190}Au^g via ICF channel is nearly same at 81, 90 & 96 MeV. However, The production probability of ^{191}Au^g is largest at 90 MeV and smallest at 96 MeV with some intermediate value at 81 MeV. Further, a comparison of production probability of ^{190,191,192}Au^g at 81, 90 and 96 MeV indicates that maximum production of ^{192}Au^g is at 90 MeV and smallest at 81 MeV. However, at 96 MeV it has some intermediate value. The present data seems to be explained on the basis of BUF model assuming that as the incident ion comes near the field of target nucleus, it may break-up into its fragments and one of the fragments may fuse with the target nucleus resulting finally into partial linear momentum transfer. The presently measured FRRD data clearly indicates that the momentum (mass) lost in case of ICF processes at the time of interaction preferentially originates from the incident beam nuclei. A more detailed particle γ-coincidence experiments for this system (^{16}O+^{181}Ta) is proposed, to have better insight in the reaction mechanism and the associated l-values in case of CF and ICF processes. The SUMRULE model calculation, carried out for the present system, which allow the ICF processes only for $l < l_{crit}$, underestimates the presently measured ICF cross-section data by few order of magnitude. As a typical example the experimentally measured cross-sections for (α3n) and (2α3n) channels are found to be $\approx$ 64.0 $\pm$ 9.6 mb and 5.0 $\pm$ 0.7 mb, however, the theoretically calculated SUMRULE values are 1.32×10^{-2} mb and 3.02×10^{-3} mb at 81 MeV beam energy. These discrepancies indicate the deviations from the assumptions of the model. Similar deviations have also been found by Parker et. al.,[1] in their study on ^{12}C+^{51}V system upto 100 MeV. The SUMRULE model assumes a sharp cut-off l-values for CF and ICF processes. However, the present findings indicate a diffused boundary which may penetrate close to the barrier.

IV. CONCLUSIONS

The recoil range distributions for thirteen residues; ^{194}Tl, ^{193g}Tl, ^{192}Tl, ^{193}Hg^{g}, ^{193}Hg^{m}, ^{192}Hg, ^{191}Hg^{g}, ^{191}Hg^{m}, ^{192}Au^{g}, ^{191}Au^{g}, ^{190}Au^{g} and ^{186}Ir^{g} produced in ^{16}O+^{181}Ta system, at $\approx$ 81, 90 & 96 MeV beam energies have been measured. The measurement and analysis of the FRRDs of reaction products presented in this paper strongly reveal a significant contribution from the partial LMT of the projectile associated with ICF in several α emitting channels. Different partial LMT components are attributed to the ^{12}C and/or ^{8}Be transfer from the ^{16}O projectile to the target nucleus. An attempt has also been made to obtain the relative contribution of CF and/or ICF components. The percentage ICF contributions are found to have an onset from $\approx$ 5% above CB. It has been found that, in general, the residues are not only populated via CF but ICF is also found to play an important role in the production of different reaction products involving direct α-cluster emission at these energies. However, in the case of ^{192}Au^{g}, ^{191}Au^{g}, ^{190}Au^{g} and ^{186}Ir^{g} residues, the RRD data clearly indicate that the ICF reaction mechanism is dominant at the energies of interest in the present work. The results obtained indicate that the forward recoil range distributions of the residues can be an extremly valuable information for establishing the CF and ICF yields at relatively low bombarding energies.

Acknowledgments

Authors also thank the Chairman, Department of Physics, Aligarh Muslim University, Aligarh for providing all the necessary facilities. The authors are thankful to the Prof. Amit Roy, Director, Inter-University Accelerator Centre (IUAC), New Delhi, INDIA for extending all the necessary facilities for performing the experiments and hospitality. We are also thankful to Dr. R. K. Bhowmik, R. P. Singh and S. Muralither for scientific discussions and support during the experiments. Thanks are also due to Mr. Abhilash for help in the target preparation. One of the authors (DPS) thanks to the UGC-DAE, Consortium for Scientific Research Calcutta Centre, INDIA, for providing financial support vide the project No. CRS-076/AMU/P/RP/7409, R. P. thanks to the DST and UGC.

[1] D. J. Parker, J. Asher, T. W. Conlon, N. Naquib; Phys. Rev. C 30, 143 (1984).
[2] J. M. Alexander and L. Winsberg; Physical Review 121, No. 2, 529 (1961).
[3] E. Gadioli et. al.,; Nuclear Physics A 641, 271 (1998).
[4] B. Bindu Kumar, S. Mukherjee, S. Chakrabarty, B. S. Tomar, A. Goswami and S. B. Manohar, Phys. Rev. C 57, 743 (1998).
[5] B. Bindu Kumar, A. Sharma, S. Mukherjee, S. Chakrabarty, P. K. Pujari, B. S. Tomar, A. Goswami, S. B. Manohar and S. K. Datta; Phys. Rev. C 59, 2923 (1999).
[6] K. Siwek-Wilczynska et al., Phys. Rev. Lett. 42, 1599 (1979).
[7] J. Wilczynski et al., Phys. Rev. Lett. 45, 606 (1980).
[8] J. R. Birkelund et al., Am. Phys. Soc. 26, 539 (1981).
[9] H. Morgenstern et al., Phys. Lett. 113B, 463 (1982); Phys. Rev. Lett. 52 No. 13, 1104(1984).
[10] Y. Chan et al., Phys. Rev. C 27, 447 (1983).
[11] K. Siwek-Wilczynska, E. H. Du Marchie van Voorthuysen, J. van Popta, R. H. Siemssen and J. Wilczynski; Nucl. Phys. A 330, 150 (1979).
[12] H. C. Britt and A. R. Quinton, Phys. Rev. 124, 877(1961).
[13] S. E. Arnell et al., Phys. Lett. 129, 23(1983).
[14] H. W. Wilschut et al., Phys. Lett. B 138, 43(1984).
[15] T. Udagawa et al., Phys. Rev. Lett. 45, 1311 (1980).
[16] R. Weiner et al., Nucl. Phys. A 286, 282 (1977).
[17] J.P. Bondrof et al., Nucl. Phys. A333, 285(1980).
[18] H. Tricoire et al., Z. Phys. A- Atoms and Nuclie312, 221(1983).
[19] C. Gregoire et al., Phys. Lett. B127, 121(1983).
[20] F. Sebille et al., Nucl. Phys. A420, 141(1984); Z. Phys. A- Atoms and Nuclie310, 99(1983).
[21] T. Otsuka et al., Phys. Lett. B121, 106(1983).
[22] J. Wilczynski et al., Nucl. Phys. A 373, 109 (1982).
[23] M. K. Sharma et. al., Nucl. Phys. A 776, 83 (2006).
[24] L. Corradi et. al., Phys. Rev. C 71, 014609 (2005).
[25] M. Das Gupta, P. R. S. Gomes, D. J. Hinde, S. B. Moraes, R. M. Anjos, A. C. Berriman, R. D. Butt, N. Carlin, J. Lubian, C. R. Morton, J. O. Newton and A. Szanto de Toledo, Phys. Rev. C 70, 024606 (2004).
[26] S. Chakrabarty, B. S. Tomar, A. Goswami, G. K. Gubbi, S. B. Manohar, A. Sharma, B. B. Kumar and S. Mukherjee, Nucl. Phys. A 678, 355 (2000).
[27] M. Cavinato, E. Fabrici, E. Gadioli, E. Gadioli Erba, P. Vergani, M. Crippa, G. Colombo, L . Redaelli, and M. Ripamonti, Phys. Rev. C 52, 2577 (1995).
[28] D. J. Parker, J. J. Hogan and J. Asher; Phys. Rev. C39, 2256(1989).
[29] Pushpenddra P. Singh, B. P. Singh, Manoj Kumar Sharma, Unnati, Devendra P. Singh, Rakesh Kumar, K. S. Golda and R. Prasad, Phys. Rev. C 77, 014607 (2008).
[30] D. J. Parker, J. Asher, T. W. Conlon, N. Naquib, Phys. Rev. C 35, 161 (1987).
[31] M. K. Sharma et. al., Phys. Rev. C 75, 064608(2007).
[32] Pushpenddra P. Singh, Manoj Kumar Sharma, Unnati, Devendra P. Singh, Rakesh Kumar, K. S. Golda, B. P. Singh and R. Prasad, Eur. Phys. J. A 34, 29 (2007).
[33] S. Sodaye, K. sudarshan, B. S. Tomar, A. Goswami, S. Mukherjee and K. Mehta, Eur. Phys. J. A 14, 371 (2002).
[34] N. Added, R. M. Dos Anjos, N. Carlin, L. Fante Jr., M. C. S. Figueira, R. Matheus, E. M. Szanto, A. Szanto de Toledo, Nucl. Phys. A 540, 328 (1992).
[35] B. S. Tomar, A. Goswami, A. V. R. Reddy, S. K. Das, P. P. Burte, S. B. Manohar, B. John, Phys. Rev. C 49,

941(1994).
[36] B. S. Tomar, A. Goswami, G. K. Gubbi, A. V. R. Reddy, S. B. Manohar, B. John, S. K. Kataria, Phys. Rev. C 58, 3478 (1998).
[37] R. I. Badren, D. J. Parker, N. Naquib, Eur. Phys. Rev. J. A 12, 317 (2001).
[38] Unnati, Pushpenddra P. Singh, Devendra P. Singh, M. K. Sharma, A. Yadav, R. Kumar, K. S. Golda, B. P. Singh, A. K. Sinha and R. Prasad; Nucl. Phys. A811, 77(2008).
[39] M. K. Sharma et. al., Phys. Rev. C 70, 044606(2004).
[40] Devendra P. Singh, Unnati, Pushpendra P. Singh, Abhishek Yadav, Manoj Kumar Sharma, Rakesh Kumar, K. S. Golda, B. P. Singh, A. K. Sinha and R. Prasad; Phys. Rev. C80, 014601(2009).
[41] FREEDOM, Data acquisition and analysis system designed to support the accelerator based experiments at the Nuclear Science Centre, New Delhi, India.
[42] E. Browne and R.B. Firestone, Table of Radioactive Isotopes (Wiley, New York, 1986).
[43] Devendra P. Singh; Ph. D. Thesis, Aligarh Muslim University, Aligarh, India(2009)unpublished.
[44] S. F. Mughabghab, M. Divadeenam and N. E. Holden, Neutron Cross-sections (New York; Academic Press), Part A, 1 89(1981).
[45] J. F. Ziegler, J. P. Biersack and U. Littmark, "Stopping and Range of Ions in Matter", Pergamon Press, New York,(1985).